Technische Universität München

Fakultät für Maschinenwesen
Institut für Luft- und Raumfahrt

Investigating the Dynamic Response of Hybrid-Electric Propulsion Systems for Flight Control Application

Guido Wortmann

Vollständiger Abdruck der von der Fakultät für Maschinenwesen der Technischen Universität München zur Erlangung des akademischen Grades eines
Doktor-Ingenieurs (Dr.-Ing.)
genehmigten Dissertation

Vorsitzender:	Univ.-Prof. Dr.-Ing. Markus Lienkamp
Prüfer der Dissertation:	1. Univ.-Prof. Dr.-Ing. Mirko Hornung
	2. Univ.-Prof. Dr.-Ing. Florian Holzapfel

Die Dissertation wurde am 15.03.2016 bei der Technischen Universität München eingereicht und durch die Fakultät für Maschinenwesen am 18.10.2016 angenommen.

Vorwort

Die vorliegende Arbeit entstand während der Zeit als Stipendiat bei Munich Aerospace sowie meiner Arbeit als wissenschaftliche Hilfskraft bei Bauhaus Luftfahrt. Die Rahmenbedingungen, welche durch dieses Stipendium ermöglicht wurden, trugen wesentlich zum erfolgreichen Abschluss meiner Arbeit bei und ich bin sehr dankbar, dass ich diese Möglichkeit wahrnehmen durfte. In erster Linie möchte ich meinem Doktorvater Herrn Prof. Dr.-Ing. Mirko Hornung danken, welcher mir kontinuierlich mit wertvollen Hinweisen und Gesprächen unterstützend zur Seite stand. Ebenso möchte ich meinem Mentor Herrn Dr. Andreas Sizmann danken, der mich immer wieder mit zahlreichen Anregungen auf neue Ideen gebracht und mich stets hilfbereit durch die Arbeit begleitet hat. Außerdem danke ich Herrn Prof. Dr.-Ing. Florian Holzapfel für die freundliche Übernahme der zweiten Begutachtung dieser Arbeit und seine wertvollen Anregungen sowie Herrn Prof. Dr.-Ing. Markus Lienkamp für die freundliche Übernahme des Prüfungsvorsitzes. Schließlich danke ich Frau Dr. Veronika Gumpinger und Frau Dr. Eva Rogowicz-Grimm für ihre hervorragende Unterstützung in allen organisatorischen Belangen und für ihren unermüdlichen Einsatz für "ihre" Stipendiaten von Munich Aerospace.

Mein besonderer Dank gilt Herrn Dr.-Ing. Arne Seitz, der mich über meine gesamte Zeit als Stipendiat mit zahlreichen Tipps und Ideen zu meiner wissenschaftlichen Arbeit bedingungslos unterstützt und gefördert hat. Darüber hinaus danke ich Herrn Sebastian Herbst und Herrn Oliver Schmitz, welche sich an den Veröffentlichungen im Rahmen meiner wissenschaftlichen Tätigkeit als Koautoren beteiligt haben.

Ich danke den Mitarbeiterinnen und Mitarbeitern des Bauhaus Luftfahrt für ein sehr angenehmes und freundliches Arbeitsklima sowie für zahlreiche inspirierende und befruchtende Gespräche über fachliche Themen und Problemstellungen. In diesem Zusammenhang möchte ich Herrn Askin T. Isikveren hervorheben, dem ich viele wertvolle Einblicke in Zusammenhänge und Wissen aus der Luftfahrt zu verdanken habe und der mich stets mit professionellem Rat bei meinen Problemstellungen unterstützt hat. Im gleichen Zug möchte ich Herrn Dr. Holger Kuhn für seine großartige und geduldige Hilfestellung zum tieferen Verständnis von elektrochemischen Energiespeichern danken. Ferner möchte ich den Kollegen der Abteilung Visionary Aircraft Concepts für zahlreiche inspirierende und konstruktive Diskussionen im Rahmen meiner wissenschaftlichen Arbeit herzlich danken.

Zu guter Letzt möchte ich meiner Frau Mirjam danken, die mich in allen Phasen der Arbeit mit ihrem bedingungslosem Rückhalt gestärkt und begleitet hat.

Abstract

The future development of air traffic brings along an increased demand for autonomy, safety and manoeuvrability in a new generation of Unmanned Aerial Vehicle (UAV) and general aviation aircraft. Future drivers such as increased air traffic density, insertion and growth of UAV traffic, promising applications of cooperative multi-platform missions and tight formation flying as well as near-ground operation in turbulent and limited air space require high manoeuvrability and hands-off or complementary autonomous control mechanisms.

Current research projects address various technologies of environmental sensorics, flight state awareness and flight path prediction, inertial-frame-, computer- and GPS-aided navigation and nonlinear adaptive control. The progress in these disciplines enables a vast variety of new mission tasks that brings up new requirements on aircraft manoeuvrability and performance. The innovation potential of future power systems and technologies in providing maximum agility and yet cost- and energy-efficient mission performance is an important complementary research area. Especially electric power systems will open new design degrees of freedom for radically new propulsion system concepts and enable new ways of integrating distributed propulsion concepts into the airframe, which allows to further increase the overall efficiency of the aircraft. Finally, electric power systems open up new perspectives for flight control by exploiting the synergies of highly agile electric motors and differential thrust with distributed propulsion concepts. These benefits support the significance of focusing on electrically powered aircraft research.

This thesis presents an initial analysis of the thrust response of hybrid-electric propulsion systems for UAVs and general aviation aircraft and assesses the potential application for attitude control of fixed and rotary wing aircraft with distributed propulsion concepts. The work focuses on component modelling as well as the identification of scaling effects, design trade-offs and the sensitivity of the thrust response on component parameters. The objective of the work is the consideration of transient requirements during the preliminary propulsion system design, which is shown in studies on subsystem, system and aircraft level. On subsystem level, the thrust response of an isolated motor-rotor subsystem is investigated to elaborate the sensitivity of the thrust response on the propeller and motor design parameters and the trade-off parameters, which conflict a high efficiency or minimum mass design. On system level, the power response and peak power capability of battery based, fuel cell based and hybrid propulsion systems is assessed to identify power limitations during quick thrust changes. On aircraft level, the manoeuvrability of large quadcopters as well as the yaw control performance of a fixed wing, general aviation aircraft with distributed propulsion is investigated.

Investigations on the motor-rotor subsystem scaling showed an increasing response time for larger systems, while keeping all other design parameters constant. Studies on propulsion system level have shown, that batteries provide superior peak power capability over fuel cell systems, which must be extended with supercapacitors to deliver enough power to enable simple manoeuvres of large quadcopters. An assessment of a distributed thrust concept showed that with four electrically driven propellers or more, a meaningful yaw control performance and a high reliability level is achieved and that the rudder function can be deactivated.

Contents

Contents

List of Figures

List of Figures

List of Tables

Nomenclature

Greek letters

$[\Phi, \Theta, \Psi]$	Euler angles	$[rad]$
α	Angle of attack	$[rad]$
β	Flow angle	$[rad]$
ϵ	Dry porosity, Drag-to-Lift ratio	$[-]$
η	Efficiency	$[-]$
Γ	Circulation	$[\frac{m^2}{s}]$
γ	Inverter control angle	$[rad]$
λ	Membrane water content, pole dispartment	$[-]/[-]$
μ_0	Vacuum permeability	$4\pi \cdot 10^{-7} \, [\frac{N}{A^2}]$
ν	Converter duty cycle	$[-]$
ω	Rotational speed	$[\frac{rad}{s}]$
ϕ	Blade twist angle	$[rad]$
ϕ_0	Variable pitch angle	$[rad]$
ψ	Magnetic flux	$[Wb]$
ρ	Density	$[\frac{kg}{m^3}]$
σ	Stress	$[Pa]$
ξ	Non dimensional radius	$[-]$
ζ	Displacement velocity ratio	$[-]$

Roman letters

$[p, q, r]$	Angular rotation around x,y,z axis	$[\frac{rad}{s}]$
$[u, v, w]$	Velocity	$[\frac{m}{s}]$
$[x, y, z]$	Spatial parameters	$[m]$
A	Current loading	$[\frac{A}{m}]$
a	Linear acceleration	$[\frac{m}{s^2}]$

List of Tables

t	Time	$[s]$
U	Voltage	$[V]$
V	Volume	$[m^3]$
X	Transformation matrix	$[-]$

Sub- and superscripts

1,2	Stator, rotor (electric motor)
act	Active
app	Apparent (power)
B	Bodyfix coordinates
C	Capacitor
carr	Planet carrier
d	Drag
d,q	Direct and quadratic axis (electric motor)
el	Elastic
ind	Induced
L	Inductor
l	Lift
lim	Limit
mech	Mechanic (power)
net	Net
O	North-East-Down coordinates
p	Power
planet	Planet wheel
PM	Permanent magnet
pp	pole pairs
ref	Reference
ring	Ring wheel
rms	root mean square
sun	Sun wheel
sw	Switching
t	Thrust

Acronyms

AC	Alternating Current
CFD	Computational Fluid Dynamics
CG	Center of gravity
DC	Direct Current
DOF	Degrees of Freedom
EASA	European Aviation Safety Agency
ESR	Equivalent Series Resistance
FCTR	Fixed Carrier Train Ratio
GDL	Gas Diffusion Layer
IGBT	Insulated Gate Bipolar Transistor
IM	Induction Motor
MTBF	Mean Time Between Failure
MTF	Motor torque factor
MTOW	Maximum Take Off Weight
NED	North-East-Down
PMAD	Power Management And Distribution
PMSM	Permanent Magnet Synchronous Motor
PPF	Peak Power Factor
RNI	Reynolds Number Index
RPAS	Remote Piloted Aircraft Systems
SAR	Search And Rescue
SOC	State Of Charge
SRM	Switched Reluctance Motor
TWR	Thrust to Weight Ratio
UAV	Unmanned Aerial Vehicle
VTOL	Vertical Take-Off and Landing

1 Introduction

1.1 Evolution and Outlook of Unmanned Aerial Vehicles

It was in 1918 that Charles Kettering constructed the first UAV, which served as a long range artillery weapon. This fixed wing UAV, also known as Kettering Bug, was controlled by a gyroscope and initiated a descend manoeuvre after its propeller has turned a pre set number of times. At ground impact, the vehicle ignited an on board bomb. This UAV was the first version of several flying bombs that were developed and built during both World Wars [8]. The rise of typical UAVs, as we know them today, began in the 1930, when the US Navy began to build dedicated target drones and converted existing aircraft with radio control devices for target practise [8].

Just like manned aviation, UAVs have changed a lot during the last century. Only 100 years ago, aeronautic pioneers examined the basics of aerodynamic flight. Today, large aircraft with up to 600 tons carry more than 850 passengers half around the world; almost at the speed of sound. The driving forces of this evolution have changed during the century. During both World Wars, a huge effort was made to develop more powerful and aircraft to fly faster, higher and longer and to guarantee military predominance. After both wars, the evolution of aircraft was driven by commercial interests, which led to a rapid research progress on the improvement of existing technologies and processes. Today, commercial aviation has reached a high level of safety, which is based on the consolidated knowledge from many experiments and the vast experience in aircraft operation. This requirement for safety and the already highly mature technologies slow the adoption of new technologies in manned aviation. In contrast to manned aviation, unmanned systems have the advantage, that new technologies can be tested easily without risking a test pilot's life. Especially during the last decade, the continuing development and research on UAVs and associated systems has brought up several key technologies, which enable new flying platforms and new applications.

The ongoing miniaturisation and the increasing performance of electronic hardware enables the construction of small, low cost UAVs with enough computational power to test complex flight control algorithms and to provide real-time sensor data processing on board [9]. Especially optical sensors profit from this miniaturisation trend, which enables small and lightweight sensors that provide multi-spectral images in high resolution [10, 11]. By exploiting the gathered information of multiple sensors, sensor fusion technique allows to generate new information that improves the flight state awareness of the vehicle and supports the decision making of autonomous algorithms [12]. Flow field technique allows to derive the movement of the aircraft from optical sensors, which contributes to the flight state awareness and delivers information for flight control and navigation [13, 14]. Moreover, the real-time data processing of optical sensors enables autonomous obstacle recognition and avoidance, tracking of moving objects and autonomous flight manoeuvres like landing or formation flight [15–17].

The research progress in flight and mission control brings up increasingly complex multi-agent cooperation control systems, that enable promising new multi-platform missions [18,19]. More robust flight control algorithms reduce the impact of external disturbances, improve flight performance, allow to fly in severe environments and to react on component failures [20–24]. New optimisation techniques allow for a quick on board calculation of optimum flight path trajectories by considering the envelope limits of the vehicle and discrete configuration changes [25–27].

Thanks to this research progress during the last decade, the number of UAVs and their associated applications has increased significantly. In 2005, UAVs have been mainly utilised by the military for surveillance, target recognition and tracking and logistic tasks. At that time roughly 250 manufacturers and 600 UAVs have been counted [28]. During the last decade, civil and commercial applications have gained significant importance in the UAV market sector and today, these applications represent a large share of all registered UAV and Remote Piloted Aircraft Systems (RPAS) activities. In 2015, the number of UAV manufacturers has increased to 630 and more than 2100 UAV have been registered [1], which reflects the significant commercial interest in new UAV applications. Figure 1.1 shows an annual comparison from UVS International of registered RPAS activities from 2005 to 2015 which confirms these trends very well.
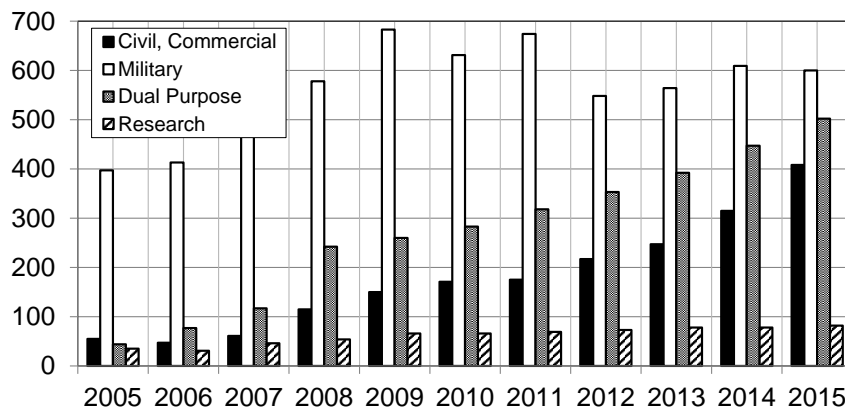
Figure 1.1: Number of registered RPAS activities (data from [1])

A problem that retarded the rise of commercial and civil UAV applications for a long time, was the legal regulation and the integration into airspace. It took until 2015 that the FAA and the EASA published preliminary regulations for the operation of RPAS, which have been elaborated with UAV manufacturers and commercial operators [29, 30]. These regulations represent the first legal basis for the operation of UAV and they define operational limitations as well as operator certification requirements for UAVs.

Today, UAVs are mostly utilised to carry optical sensors and communication equipment. Typical applications are the 3D mapping of small areas [31], photogrammety and remote sensing tasks [32], surveillance, recognition and tracking tasks. Furthermore, UAVs are utilised for monitoring and control tasks in agriculture [33], disaster management [34] and naval and street traffic management [28, 35].

One promising application for UAVs in the near future are high altitude platforms, which combine the advantages of satellite and ground based communication systems and provide broadband wireless communication applications [36]. Airbus is preparing a high altitude pseudo satellite concept named Zephyr for commercial launch [37] and a prototype has already completed its first civil flight in 2014 in Dubai [38]. Another promising application for UAVs are postal and parcel services [39,40]. Amazon has just patented its 'Prime Air' service which is a parcel delivery by UAV within 30 min [41]. However, Amazon is still negotiating with the FAA about experimental certification for their research prototypes. Another field of UAV applications are assembly and manipulating tasks with multiple vehicles. Currently, research projects like ARCAS (Aerial Robotics Cooperative Assembly System) investigate the control, the coordination and operation of multiple UAVs with robotic arms [42, 43]. Another scenario, where UAV contribution is considered to bring a significant benefit are Search And Rescue (SAR) missions. A near future target for UAVs in such missions are local communication applications and the localisation of target persons to support rescue teams on ground. Long-term goals may include dropping first aid equipment as well as transporting a person to a nearby rescue base or the next hospital.

Compared to today's tasks, a lot of new applications take place in different environments and require a significantly higher payload capability. For example, assembly and manipulating tasks require the aircraft to fly between obstacles, which have to be recognised and avoided. As objects have to be picked up or deployed, the UAV must be capable to hover steadily while changing the aircraft mass, inertia and the location of the Center of gravity (CG). The interaction with external objects requires the application of supplementary forces and moments. The environmental conditions may change as well. The SAR mission requires the UAV to operate in bad weather conditions like rain, snow or strong wind, which imposes significant challenges to the aircraft design and raises particular requirements on aircraft performance. UAVs, which are operated in such environments, must cope with strong turbulences and at the same time they must provide a high precision in following curved flight paths. Additionally, autonomous obstacle recognition requires a higher manoeuvrability from the UAV to quickly change the flight path and to avoid collisions. These conditions impose new requirements on the manoeuvrability of the aircraft and the response time of the flight controller and the propulsion system, which have to be considered during aircraft design.

1.2 History of propulsion controlled, fixed wing aircraft

At the beginning of the 1990s, NASA started preliminary investigations on propulsion assisted flight and attitude control of commercial aircraft in emergency situations. The reason for this investigation have been several accidents, where the aircraft hydraulic flight control system has been lost, but pilots often succeeded to stabilise and rudimentarily control the damaged aircraft by applying differential thrust [44]. Some pilots even achieved to perform remarkably precise emergency landings. NASA conducted multiple simulations of aircraft with deactivated control surfaces to find out, whether experienced test pilots where able to perform such emergency landings by manually controlling the engines. Most pilots managed to handle the attitude and flight path control in the air, however the manual landings showed a very low success rate. One of the reasons for the high failure rate is the slow response of the aircraft engines and the therefore slow rotational dynamics of the aircraft. As the experiences proofed, that aircraft can be controlled in a meaningful way by applying differential thrust, NASA developed and tested a dedicated flight controller with the F/A-18 and the MD-11 aircraft, which allowed the pilot to directly control the lateral and the longitudinal movement

as well as the bank angle. The pilot commands where then translated into corresponding thrust commands for the engines. The flight results showed significantly better landing results, however, the poor transient performance of the engines still led to large oscillations and a limited aircraft manoeuvrability [45].

Another technology, which utilises the propulsion system for attitude control augmentation is thrust vector control, which is applied in military fighter aircraft. The concept of this technology is to deviate the engine thrust vector by deflecting the exit gas flow of the engine. This is either achieved by pushing deflection panels into the stream or by using a morphing nozzle, that guides the flow in different directions. With the according lever arm to the aircraft CG, different moments can be applied. The advantage of this technology is its independence from the engine thrust response and it increases the manoeuvrability of the aircraft, especially at low speeds where the flap effectiveness is limited.

1.3 Research targets, applied methods and structure

A rigid body has three translatory Degrees of Freedom (DOF) and three rotatory DOF. By applying external forces and moments, the body is accelerated, which leads to a change of its velocity and its kinetic energy. The required time for a velocity increase of a rigid body depends on the amount of the applied force or moment. A low force or moment requires a long application time to achieve a certain velocity and vice versa.
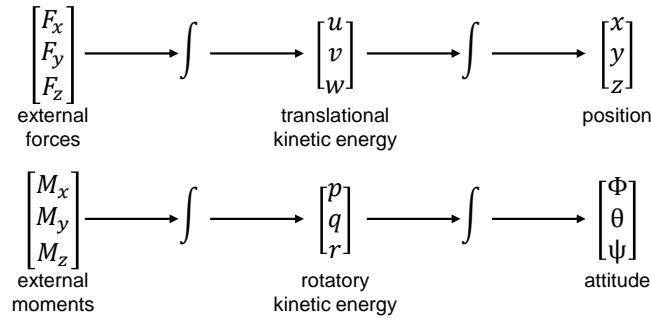
Figure 1.2: Rigid body dynamics

Conventionally, propulsion systems of fixed wing aircraft are utilised to control the translatory velocity and to compensate the aircraft drag. As the available Thrust to Weight Ratio (TWR) of fixed wing aircraft is rather low, the translatory acceleration requires a long application time (e.g. during take-off). In this case, the engine run up time is noticeably faster than the manoeuvre time and, hence, it has no appreciable impact on the duration of the acceleration. However, certification stipulates a minimum transient performance, e.g. time zero requirements [46], which is achieved without any noticeable impact on engine design. Consequently, the engines of fixed wing aircraft are optimised for a high efficiency or a minimum mass; depending on the application. Compared to the translatory movement of fixed wing aircraft, the rotatory movement is a low energy manoeuvre. Thus, the moments are applied only for a short time, which makes the rotatory performance sensitive to the dynamic response of the moment applying device. When differential thrust is utilised for attitude control, the engine thrust is utilised to apply these moments on the aircraft. In this case, the manoeuvrability of the aircraft is sensitive to the thrust response time of its propulsion system.

In rotary wing aircraft, the propulsion system is utilised for vertical as well as rotatory acceleration. The required moments to rotate the aircraft are either generated by a variable pitch control of individual rotor blades (e.g. helicopter) or by generating differential thrust with multiple rotors (multicopter concept). As the kinetic energy of a rotatory manoeuvre is small and the performance of the propulsion system is high (the TWR is at least greater than one), the application interval is short. Thus, the aircraft rotatory acceleration depends significantly on the engine response time. By using variable pitch control, the aircraft rotatory response depends mainly on the agility of the blade actuation mechanism. Consequently, using differential thrust for attitude control implies new requirements on the transient response of the blade actuation mechanism and the propulsion system.

In order to allow the consideration of the transient response of the engines during preliminary propulsion system design, this work presents an approach to include the transient response in the system design process. As the good transient characteristics of electric motors have been the enabling technology for attitude control of multi rotor vehicles, this work focuses on electric and hybrid-electric propulsion systems. Furthermore, the sensitivity of the transient response of electric propulsion systems on component design parameters is analysed to provide ways to further increase the propulsion system agility and to assess possible trade-offs against a high efficiency or minimum mass design.

To analyse the transient performance of electric and hybrid-electric propulsion systems, a framework is developed which allows to generate arbitrary system architectures from individual component models via predefined interfaces. Moreover, chapter 2 describes the utilised models to represent the transient and steady-state performance of all involved components. In a second step, this work investigates the sensitivity of the thrust response on the component design parameters in order to identify synergy and trade-off parameters between high efficiency and fast responding design. As the combination of an electric motor and a propeller represents an isolated mechanical subsystem, chapter 3 investigates the sensitivity of the dynamic response of this isolated subsystem on the propeller design parameters. This study includes the analysis of scaling effects on component and on propulsion system level to derive design considerations for UAV sizing studies. In chapter 4, the peak power capability of batteries and fuel cells is investigated and the performance is assessed on system level. Again, the sensitivity of the system response on relevant design parameters as well as system configurations is analysed. Based on these results, the performance of a hybrid-electric propulsion system, based on a fuel cell and a supercapacitor, is investigated. Chapter 5 presents two studies on aircraft level. In the first study, the impact of component design parameters on the agility of a quadcopter is assessed by simulating translatory, rotatory and combined manoeuvres. The second study investigates the feasibility of yaw control for a fixed wing aircraft, by utilising differential thrust commands on multiple, electrically driven propellers, which are distributed along the wing span.

1.4 Literature survey of related research

The modelling and design of hybrid propulsion systems has been extensively investigated in literature. Especially for automotive applications, a lot of studies have been conducted on the design, the matching, the operational characteristics and the performance of hybrid propulsion systems. Most of the studies, which focus on aerospace and UAV applications, investigate the steady state operating characteristics of the individual components in order

to perform an optimised system design for a given aircraft and mission. Therefore, the transient performance is neglected. The studies, which analyse the transient behaviour of hybrid and electric systems, focus on the prediction of the stability limits of involved components or simply the characterisation of the component response for further control analysis. No research work has been found, which relates the transient performance to the system design. In the following sections, related research work on hybrid propulsion systems for aerospace applications and the agility of multi-rotor and fixed-wing UAV as well as lateral control of fixed wing aircraft via distributed propulsion is briefly summarised.

The Institute of Aircraft Design of the Technische Universität München has investigated hybrid propulsion systems for small UAVs. Schömann developed a design process for hybrid propulsion systems and derived models that predict the mass, the dimensions and the efficiency level of the involved components [47]. Furthermore, he compared conventional and hybrid propulsion systems for multiple reference missions and identified benefits of hybrid systems in terms of energy consumption and low signature capability [48]. The Australian Research Centre for Aerospace Automation of Queensland University of Technology has investigated the design and performance of parallel hybrid propulsion systems for small UAVs. The analysed propulsion system is based on the combination of a small piston engine and an electric motor, which drive one propeller via a gear box system. The system hardware was tested in several wind tunnel experiments and load curve techniques were applied to simulate the performance of the involved components in Simulink [49–51]. Moreover, the Air Force Institute of Technology investigates the design, modelling and simulation as well as control of hybrid propulsion systems for small UAVs, which are based on piston engines [52–55]. Their examinations range from initial architecture comparison over deriving design methods to prototype flight testing.

The School of Aerospace, Mechanical and Mechatronic Engineering in Sydney is investigating fuel cell based hybrid-electric propulsion systems for small UAV [56, 57]. In their recent publications, the transient characteristics of the hybrid power plant and the role of the battery characteristics on the aircraft mission performance are assessed. The Russian Central Institute of Aviation Motors (CIAM) investigates hybrid-electric gas turbine engines for commercial aircraft, which are powered by fuel cells [58, 59]. Besides modelling and simulating hybrid power plants, CIAM operates small UAVs to test the operation and the performance of fuel cell systems. The research institution Bauhaus Luftfahrt e.V. is investigating prerequisites and impacts of electric and hybrid electric propulsion on system and aircraft level. The latest publications present basic analytical studies on hybrid propulsion systems and advanced concept studies on universally electric and hybrid aircraft [60, 61].

The University of Colorado investigated and tested a hybrid propulsion system for the NASA HELIOS aircraft, which consists of a piston engine and an electric motor. The study identified an increased efficiency level of 15% compared to conventional propulsion systems with the same size [62]. Furthermore, the University of Bologna investigated the design of a diesel engine based, hybrid propulsion system for a medium altitude and long endurance UAV. The team conducted an aircraft level comparison between the conventional and the hybrid propulsion system and identified a higher energy specific air range which comes at the price of one percent reduced range capability [63].

NASA is investigating hybrid-electric propulsion systems within several research projects. The Greased Lightning GL-10 concept is a tilt-wing UAV, which utilises distributed hybrid-

electric propulsion to combine Vertical Take-Off and Landing (VTOL) capability and long endurance during aerodynamic flight [64–66]. The UAV is equipped with 10 propellers (8 on the wing and 2 on the empennage) which are utilised for yaw control. In 2015, a battery driven, 50% scale prototype with a wing span of 3.05 m and a take-off weight of 24.9 kg successfully demonstrated VTOL, transition and aerodynamic flight.

Together with Empirical Systems Aerospace and Joby Aviation, NASA is investigating the drag reduction potential and safety benefit of distributed electric propulsion in the Leading Edge Asynchronous Propeller Technology project (LEAPTech) [6, 67, 68]. The general aviation concept plane is based on a four seat Tecnam P2006T fixed-wing aircraft with a gross weight of 1360 kg. 18 electrically driven propellers are distributed along the entire wing span which, according to extensive Computational Fluid Dynamics (CFD) analysis, increase the dynamic pressure on the wing and therefore allow a downsizing of the wing, which reduces the wetted area and aircraft drag. A carbon composite wing prototype has been successfully tested on a truck mount.

The approach of using the engines for flight and attitude control has been picked up again recently by Boeing and NASA. Simulations of failed rudder scenarios show that emergency flight control and flight envelope protection can be achieved with differential thrust of a common commercial aviation aircraft [69–71]. To improve aircraft controllability in emergency situations, NASA is conducting research studies on integrated resilient aircraft control, which is an approach to embed the engine controller in the flight controller. The idea behind this combination is to exploit the engines stability margins in emergency situations and to 'rather sacrifice the engine, but save the aircraft' [72]. Moreover, NASA is working on the project 'Fast Response Engine Research' to improve the engine response time without touching the engine design. One resulting concept is the high speed idle, where the engine is operated at a higher rotational speed, which enables shorter engine run up times during approach [73]. No studies on the performance of lateral or attitude control of fixed wing aircraft with electric propulsion systems have been found. All studies consider conventional engines and focus on damaged rudder or low speed scenarios.

Cutler from the Massachusetts Institute of Technology presented the only known study, which assesses the impact of the propulsion system design on the agility of a quadcopter [74]. In this study he compares the thrust response and the quadcopter agility with fixed and variable pitch propellers. He identified a faster thrust response for variable pitch propellers, which originates from avoiding the motor controller voltage saturation limits in fixed pitch systems. For aggressive manoeuvres, he identified a higher agility level as well as a better path following accuracy. Variable pitch propellers also offer the possibility to increase propeller efficiency and to easily inverse the thrust vector. Riccardi presented multiple control approaches for variable pitch quadcopters, however, he focused on maximising propeller efficiency rather than maximising agility [75]. Pretorius developed a low inertia quadcopter, which is intended to enable highly-agile manoeuvres. However, he did neither present his design methods for the structural layout nor did he present a comparative assessment against other designs. Furthermore, no flight tests have been made with this design [76].

The Institute for Dynamic Systems and Control of the ETH Zürich constructed the Flying Machine Arena, which is a 10 m cube, equipped with a high precision motion capture system and a wireless communication network. This Flying Machine Arena is utilised to investigate adaptive high-performance and high-precision manoeuvres, cooperative tasks with multiple

vehicles and multiple control strategies for quadcopters [77–81]. Many studies examine the agility and high performance capability of quadcopters, however, the focus of these studies are new control algorithms. The impact of hardware design on the quadcopter agility is not investigated.

As prices for small quadcopter platforms are relatively small, many research institutions investigate the design and control of these platforms. Stepaniak from the Air Force Institute of Technology presented a design study of a scaled quadcopter with a take-off mass of roughly 12 kg for testing of navigation sensors [82]. He presents a set of models to predict the dynamics of the involved electric propulsion system components and included these dynamics in the quadcopter dynamics. The flight controller is developed from a simple feed back control architecture and the according gains are adjusted in order to achieve a satisfactory step response. Pounds from the Australian National University developed a large quadcopter to calibrate structural models and to investigate the quadcopter and motor-rotor dynamics [83]. He identified a minimum rise time of the isolated motor-rotor system, which is required for adequate quadcopter control. Moreover, an efficient aeroelastic propeller design was identified as one of the key challenges to build such a large quadcopter. All residual examined studies on transient quadcopter performance did neither consider the dynamics of the propulsion system, nor did they include the propulsion system design parameters in the vehicle dynamics.

2 Modelling of Propulsion System Components

In this chapter the component modelling of electric and hybrid-electric propulsion systems is presented. The scope of the individual models targets a preliminary prediction of the component performance at steady state and transient operation, as well as an estimation of the component dimensions and mass. The models are developed to predict the performance and the dimensions of the involved components with a power level up to 100 kW. Therefore, the models are suitable to simulate propulsion systems of small to medium UAVs and general aviation aircraft.

The composition of electric and hybrid-electric propulsion systems can be divided in two subsystems. The propulsor subsystem consists of a propeller, an optional gear box and an electric motor with a controller. The propulsion system can contain multiple of these mechanic subsystems and they can be distributed within the aircraft. The energy subsystem consists of the electric energy carriers, such as fuel cells, batteries and supercapacitors. By combining two different energy carriers, a hybrid propulsion system is formed. The propulsion system has at least one energy subsystem that provides the required power and energy of all propulsor subsystems. The interface between both subsystems are Power Management And Distribution (PMAD) devices, which distribute the power to all propulsor subsystems via Direct Current (DC) bus systems and control the power share of hybrid energy carriers. This setup represents the most simple and basic architecture which is investigated in this study. To fulfil particular redundancy or operational requirements, this architecture can be extended accordingly to more complex architectures. However, this goes beyond the scope of this thesis.

An architecture framework concept is introduced to simplify the synthesis and the assessment of arbitrary propulsion systems. This framework defines multiple interfaces, which allow to link two components that have the same interface. The interface is utilised to exchange information on the power and energy flow as well as information on the operating state of the component. The following chapters describe the architecture framework as well as the modelling of the involved components.

2.1 Architecture Framework Mapping

As previously described, the propulsor subsystem consists of a propeller, an optional gear box and an electric motor with a controller. Multiple of these propulsor subsystems are integrated in the aircraft structure and produce thrust to accelerate the aircraft. The motor controller represents the interface to the DC power bus and transforms the DC power to AC power, according to the operational state of the motor. The motor then transforms the AC power to mechanical power, which is transformed afterwards by an optional gearbox system. The gearbox enables to operate the motor and the propeller at different rotational speeds. The propeller finally converts the mechanic power into propulsive power. The electric power is distributed by the PMAD devices to all mechanical subsystems. The PMAD devices are con-

nected to the power converters, the motor controllers, to switches and converters, which are required to attain a certain redundancy level and to control mixed Alternating Current (AC)-DC bus systems [84, 85]. Moreover, the PMAD devices control the bus voltage levels and the power flow. For single bus systems with low redundancy requirements, the PMAD devices are omitted and their functionality is transferred to the related DC-DC converters of the energy carriers and the motor controllers. The energy subsystems contain a fuel cell or a battery as a primary energy carrier. To form a hybrid system, a secondary energy carrier can be added to the energy system. Secondary energy carriers are batteries and supercapacitors. As each energy carrier has a certain current loading characteristic, a power converter is added, which conditions the electric power of the energy carrier according to the specifications of the DC power bus.

Figure 2.1 shows the basic propulsion system architecture, which includes all considered components. The upper row shows the propulsor subsystem, the lower row shows the energy subsystem and one single PMAD device. The propeller, the gearbox and the electric motor provide shaft interfaces, that contain information on the rotational speed, the torque and the power flow of the component. By linking the shaft interfaces of the propeller and the motor, a directly driven propeller can be simulated. The electric motor and the controller are connected via an AC interface. The motor controller is supplied from the DC bus via a DC interface. All energy carriers as well as all power converters deliver DC power and are therefore connected with DC interfaces.
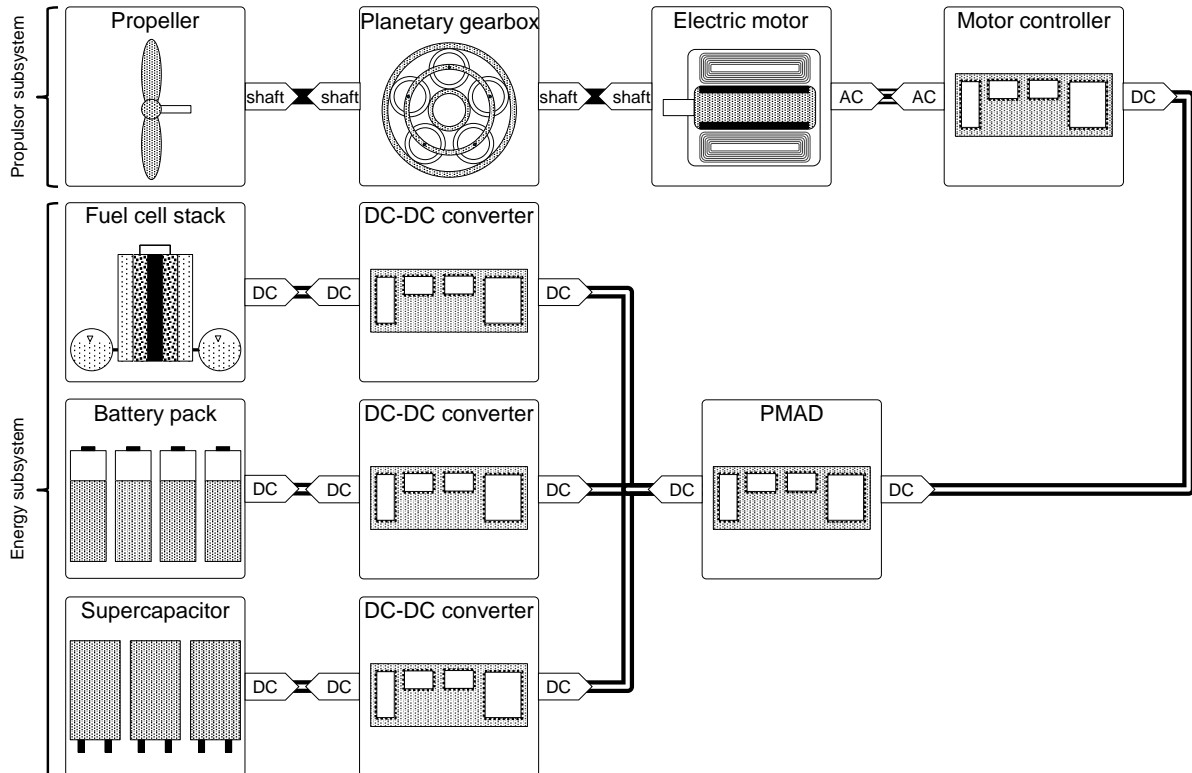
Figure 2.1: Architecture framework layout

2.2 Propeller

A propeller converts mechanical power into a thrust force by rotating multiple blades in a fluid. Propellers consist of multiple blades, that are mounted on a central hub. The rotational movement of the propeller blades creates a pressure increase along the flow, which the fluid converts into a velocity increase. The acceleration of the fluid mass flow creates a force, which is denominated as the thrust of the propeller.

To describe the performance of a propeller, Betz, Glauert and Theodorsen have published baseline theories in the early 20th century. Betz identified the condition for minimum induced losses for screw propellers in 1919 together with Glauert [86]. Glauert published his work on airplane propellers in 1935, where he used a combination of axial momentum theory and blade element theory to predict the performance of an airplane propeller [87]. However, their work was based on the assumption of low propeller loading, small angle approximations and radial flow effects were neglected. Theodorsen showed in 1948, that Betz's condition for minimum induced loss propellers as well as the work of Goldstein [88], who derived an optimum circulation function, are also valid for medium loaded propellers. Based on this work, Larrabee published a procedure for minimum induced loss propeller design in which he included a correction for radial flow effects. As his work was still based on a low loading assumption, Adkins and Liebeck published a corrected design procedure for moderate propeller loadings in 1994 [89].

The axial momentum theory, introduced by Rankine, George and Froude, consists of a 1D balance of the flow velocity and pressure along the flow stream. The propeller itself is considered as a disk within the flow stream that causes a pressure increase in the flow. Although this modelling approach is very simple and does not consider any information on the propeller except for its diameter, it can be used to predict an upper limit for the propeller efficiency and the velocity increase in the downstream wake of the propeller. The ideal efficiency, that is derived from this theory and shown in Equation (2.1), is a basic formulation of the propulsive efficiency of the propeller, which only considers the acceleration of the stream tube flow. At static conditions, a figure of merit can be derived which relates the mechanic power to the thrust of the propeller [90].

$$\eta_{\text{ideal}} = \frac{1}{0.5 + \sqrt{0.25 + \frac{F_t}{2 \cdot \pi \cdot r^2 \cdot \rho \cdot v^2}}} \tag{2.1}$$

As the axial momentum theory neglects a lot of loss mechanisms and just considers the propeller diameter, it is not suitable for an accurate performance prediction. In combination with the blade element theory, which has been presented by Froude and Taylor, and a correction for radial flow effects, the performance prediction can be improved [89]. The approach of the blade element theory is to split the propeller blade into multiple elements from hub to tip (as can be seen in Figure 2.2). The flow conditions at each element are calculated from the propeller rotation, the ambient air conditions and the induced flow angle. With 2D aerodynamic data of the local airfoil, the lift and drag forces are determined for each blade element. To obtain the propeller thrust and torque, the contribution of all elements is determined with the local blade twist angle and the lift and drag forces. Each blade element is considered independently from its neighbour elements, which impedes the consideration of radial flow effects. To consider those effects at the blade tip, a loss factor is implemented, which reduces the circulation distribution at the blade tip to zero [91]. The geometric information which is required for this theory is the local chord length c, the local twist angle ϕ, the blade number

N_{blades} and the propeller diameter. With the design procedure from Adkins and Liebeck, these geometrical parameters are derived from a minimum induced loss design [89].
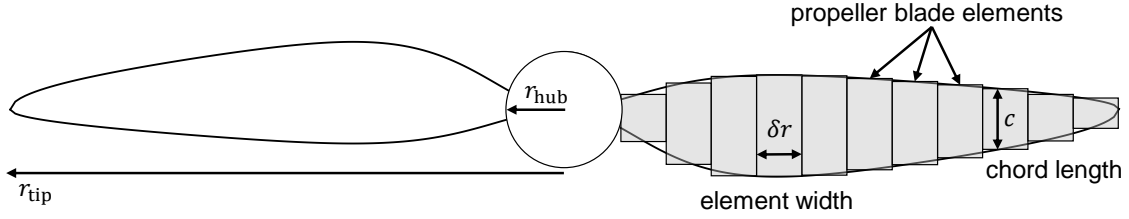
Figure 2.2: Propeller blade element theory

The blade element theory provides good geometrical information of the propeller and requires only low computational effort. The fidelity of the theory is considered adequate for pre-design studies and basic performance estimations. Moreover, the theory can easily be extended to calculate variable pitch propellers, by adding a constant variable pitch angle to all blade elements. Thus, the here proposed model is based on the blade element theory. For detailed design purposes, more complex and computationally more expensive CFD methods can be applied.

The work from Adkins [89] provides an iterative algorithm to calculate the chord length and twist angle distribution for an arbitrary propeller design point. This design point is defined by a thrust or power requirement as well as the environmental conditions, such as the air density and the free stream velocity. Moreover, the diameter, the blade number and the rotational speed of the propeller are required design parameters. The rotational speed is calculated from a design tip speed and the propeller diameter. The air density and temperature are determined from a flight altitude and the standard atmosphere model [92]. In the first step of the design algorithm, the displacement velocity ratio ζ is iteratively calculated with equations (2.2) to (2.6). Therefore, the twist angle of each blade element can be calculated according to equation (2.2), where ξ is the non dimensional radial position of each element [89].

$$\phi = \arctan \left[\frac{v}{\omega \cdot r \cdot \xi} \cdot \left(1 + \frac{\zeta}{2} \right) \right] \tag{2.2}$$

With the twist angle, the circulation distribution along the blade can be calculated with equation (2.3), which includes the tip loss factor for radial flow effects according to Prandtl [89].

$$\Gamma = \frac{2}{\pi} \cdot \arccos \left[\exp \left(-\frac{N_{blades}(1-\xi)}{2\sin(\phi_{tip})} \right) \right] \cdot \frac{\omega \xi r}{v} \cdot \cos(\phi) \cdot \sin(\phi) \tag{2.3}$$

Equation (2.4) and (2.5) provide radial derivatives that are integrated along the non dimensional radius from hub to tip. With the integrated values I_1 and I_2, a new value for ζ can be estimated for the next iteration.

$$I_1' = 4 \cdot \xi \cdot \Gamma \cdot (1 - \epsilon \cdot \tan(\phi)) \tag{2.4}$$

$$I_2' = \frac{v \cdot I_1'}{2 \cdot \xi \cdot \omega r} \cdot \left(1 + \frac{\epsilon}{\tan(\phi)}\right) \cdot \cos(\phi) \cdot \sin(\phi) \tag{2.5}$$

$$\zeta = \frac{I_1}{2 \cdot I_2} - \sqrt{\left(\frac{I_1}{2 \cdot I_2}\right)^2 - \frac{2 \cdot F_t}{I_2 \cdot \rho \cdot v^2 \cdot \pi \cdot r^2}} \tag{2.6}$$

When initialising ζ with zero, the algorithm converges quickly after a few iterations. The iterative part of the algorithm can be reduced to the calculation of ζ if the airfoil coefficients are only available with respect to the angle of attack. When the coefficient sensitivity on Reynolds number is available, the iterative part has to be extended with equations (2.7) and (2.8), in order to consider the Reynolds number effects. With the final value for the displacement velocity ratio, the absolute flow velocity at each blade element can be calculated according to equation (2.7).

$$w = v \cdot \frac{\left(1 + \frac{\zeta}{2} \cdot \cos^2(\phi) \cdot (1 - \epsilon \cdot \tan(\phi))\right)}{\sin(\phi)} \tag{2.7}$$

Finally, the chord length distribution can be calculated with the lift coefficient C_l at the lowest drag-to-lift ratio of the airfoil according to equation (2.8).

$$c = \frac{4\pi \cdot \zeta \cdot v^2 \cdot \Gamma \cdot C_l}{\omega \cdot N_{\text{blades}} \cdot w} \tag{2.8}$$

With the resulting chord length, the propeller mass and inertia are estimated. Therefore, each blade element is approximated by a cuboid. For the cuboid thickness, an average thickness is assumed which results in the same cross sectional area as the airfoil. Adkins and Liebeck use the NACA 4415 profile, whose cross sectional area is determined to 0.103 times the square of its chord length. By assuming a homogeneous material density for all blade elements, the mass and the inertia of the blades can be estimated. The propeller hub is considered as a disk with a diameter-to-thickness ratio of 2 which is made from the same material as the blades. By summing up the mass and inertia of all blade elements and the hub disk, the mass and the inertia of the propeller can be estimated. Therefore, the parallel axis theorem (Steinerscher Satz) has to be considered.

For the validation of the design algorithm, Figure 2.3 shows a comparison of the calculated geometry to the results of the software JavaProp [93] and measurements from the Department of Aerospace Engineering at the University Illinois on 'Thin Electric' series from APC Propellers [94]. The abscissa shows the non dimensional propeller radius from hub to tip. The ordinate of the left figure shows the blade twist angle and the ordinate of the right figure shows the relative chord length. Close to the hub, the calculated chord length and the twist angle of the model and JavaProp differ from the measurement, which is due to the mechanical requirements of the blade mount. A mass calibration has shown that with a material density of 2000 $\frac{\text{kg}}{\text{m}^3}$, the model results are in good agreement with manufacturer data on the APC 'Thin Electric' propellers [95].

To calculate the propeller performance at arbitrary environmental conditions and at different rotational speeds, an algorithm from Phillips is applied [91]. Adkins also provides an off-design algorithm, however, it is not suitable for static conditions. The algorithm from Phillips requires the rotational speed, the free stream velocity and the ambient air conditions. With these parameters, the induced flow angle β_{ind} is iteratively solved for every blade element
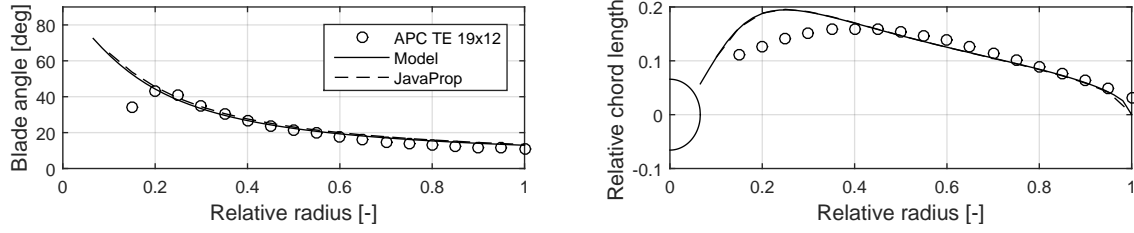
Figure 2.3: Propeller design validation

with equation (2.9) to (2.11). Tests with different solver methods have shown, that Newton's method quickly solves the problem with low computational effort. For the first iteration, the design value of the induced flow angle can be used in order to obtain a quick convergence of the algorithm. The flow angle that results from the rotation of the propeller and the free stream velocity is calculated with equation (2.9).

$$\beta_\infty = \arctan\left(\frac{v}{\omega \cdot \xi \cdot r}\right) \tag{2.9}$$

In the next step, the angle of attack is calculated by subtracting both flow angles from the blade twist angle. The scalar ϕ_0 represents the variable pitch angle, which describes the rotation of the blade around its axis and is an input parameter for variable pitch propellers. For transient simulations, the variable pitch mechanism requires a servo motor and a controller to control the thrust of the propeller. A detailed description of the variable pitch control system is given later in chapter 3.3, where the motor-rotor performance is analysed.

$$\alpha = \phi + \phi_0 - \beta_\infty - \beta_{\text{ind}} \tag{2.10}$$

The angle of attack is required to determine the lift and drag coefficients for each blade element from 2D airfoil data. Finally, Equation (2.11) is utilised to calculate the error for the current induced flow angle.

$$\frac{N_{\text{blades}} \cdot c \cdot C_l}{16 \cdot \xi \cdot r} \cdot \arccos\left[\exp\left(-\frac{N_{\text{blades}}(1-\xi)}{2\sin(\phi_{\text{tip}})}\right)\right] \cdot \tan(\beta_{\text{ind}}) \cdot \sin(\beta_\infty + \beta_{\text{ind}}) = 0 \tag{2.11}$$

When the induced flow angle is solved, the thrust and power coefficients of the propeller can be calculated by integrating the contributions of all aerodynamic forces from hub to tip.

$$C_t = \frac{\pi^2}{4} \cdot \int_{\text{hub}}^{1} \frac{\xi^2 \cdot c \cdot N_{\text{blades}}}{2r} \cdot \left[\frac{\cos(\beta_{\text{ind}})}{\cos(\beta_\infty)}\right]^2 \cdot [C_l \cdot \cos(\beta_\infty + \beta_{\text{ind}}) - C_d \cdot \sin(\beta_\infty + \beta_{\text{ind}})] \; \delta\xi \tag{2.12}$$

$$C_p = \frac{\pi^3}{4} \cdot \int_{\text{hub}}^{1} \frac{\xi^3 \cdot c \cdot N_{\text{blades}}}{2r} \cdot \left[\frac{\cos(\beta_{\text{ind}})}{\cos(\beta_\infty)}\right]^2 \cdot [C_d \cdot \cos(\beta_\infty + \beta_{\text{ind}}) + C_l \cdot \sin(\beta_\infty + \beta_{\text{ind}})] \; \delta\xi \tag{2.13}$$

The thrust and the required mechanical power of the propeller can be calculated with both coefficients according to the next two equations [96].

$$F_t = C_t \cdot \rho \cdot \left(\frac{\omega}{2\pi}\right)^2 \cdot (2r)^4 \tag{2.14}$$

$$P_{\text{mech}} = C_p \cdot \rho \cdot \left(\frac{\omega}{2\pi}\right)^3 \cdot (2r)^5 \tag{2.15}$$

This algorithm calculates the thrust and the power for a given rotational speed, a given variable pitch angle and given environmental conditions. As these input parameters correspond to the available data for transient simulations, this algorithm is implemented in the Simulink model. For steady state calculations, the thrust or power level is the input parameter, which means that the algorithm is executed iteratively. To calculate the performance of fixed pitch propellers at a required thrust or power level, the rotational speed is solved iteratively. For constant speed propellers, the variable pitch angle ϕ_0 is iterated to calculate the performance at a required thrust or power level. Again, Newton's method shows a quick convergence and superior speed. In a last step, the advance ratio J and the efficiency of the propeller can be determined with the equations (2.16) and (2.17).

$$J = \frac{\pi \cdot v}{\omega \cdot r} \tag{2.16}$$

$$\eta = J \cdot \frac{C_t}{C_p} \tag{2.17}$$

To provide a sanity check for the results, the tip speed should not exceed 250 m/s to ensure the mechanical integrity of the propeller. This value has been determined as a meaningful limit from red line speed data from Hoffmann Propellers [97].

To verify the off design performance calculation, Figure 2.4 shows a comparison of the model results to results from JavaProp. The abscissa shows the advance ratio of the propeller and the ordinate shows the thrust coefficient, the power coefficient and the propeller efficiency. The comparison shows that the model results are in good agreement with the performance calculation of JavaProp. The differences in the coefficients arise from visual read-out of the 2D aerodynamic data from JavaProp, which was required for the comparison. Moreover JavaProp uses profile interpolation between four blade sections, which is not considered in the propeller model. A comparison with the APC propellers is not reasonable as geometric shape data is not available and the utilised airfoil is unknown.
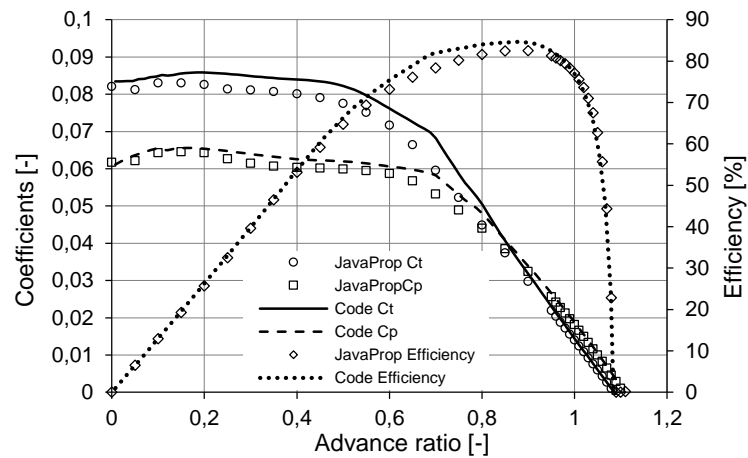
Figure 2.4: Propeller performance validation

A parametric study on the number of blade elements has shown that with 100 elements per blade, the error of the performance results is less than 0.01% compared to 500 elements. The errors on propeller mass and inertia are 0.1% and 0.2% respectively. Thus, a discretisation with 100 elements is considered to be a good trade-off between a sufficiently high accuracy and computational effort.

The accuracy of the model is limited by the quality and validity of the 2D aerodynamic coefficients as well as assumptions like having a constant airfoil profile along the blade and a homogeneous material density. Propellers have a different airfoil profile along the blade. At the hub mount, the cross section is almost circular. Hence, an interpolation between several blade sections and a huge data base of the corresponding coefficients would be required in order to model this effect more accurately. Moreover, an airfoil coefficient database that reflects the sensitivity on angle of attack, Reynolds and Mach number would increase the model accuracy. If no correlation to Mach number is available, it is reasonable to keep the helical Mach number of the blade tip below 0.8, because in excess of this speed, transonic flow regions form on the upper surface of the blade, resulting in a significant deviation of both airfoil coefficients and a lower efficiency [90].

2.3 Gear System

Gear systems are used to transmit mechanical power between two components by transforming torque and speed levels. In the case of an UAV, gear systems can be applied to transform the mechanic power of the propeller from high torque and low speed to high speed and low torque level for a gas turbine engine, a piston engine or an electric motor. Especially, the matching of propellers and gas turbine engines requires reduction gearboxes, as the operational speeds of both components differ significantly. For piston engines, a transmission system can be beneficial for a propeller matching in order to exploit the engines maximum torque capacity, which requires a certain operating speed. Furthermore, as piston engines and electric motors scale with the required torque, the mass and losses of added gearbox systems can be less penalizing for the system mass than the weight of a high torque engine or motor.

A gearbox system for aircraft applications should feature high power and torque densities and be able to modulate at the required rotational speeds of both components. Moreover, the gear system should provide a high efficiency level and have a high reliability. In order to compare different gear types, Looman calculated the force and power density of wheel gears, chain gears, friction gears, belt gears, hydrostatic and hydrodynamic gear systems for equivalent loading conditions [7]. Table 2.1 shows the resulting values for form-locked gear systems, normalized to the wheel gear system. Wheel gears show the highest power density, can operate at high rotational speeds and provide a high reliability, making them the most suitable gear system for aircraft application. For low speed operation and for a connection of multiple shafts, the chain gear is a reasonable competitor for wheel gear systems.

Depending on the installation of the propeller and the relative position to the driving machine, different types of wheel gearbox systems may be applied. Spur gears require parallel shafts with certain shaft offset, while bevel gears imply a certain shaft angle and planetary gears provide a transmission between parallel shafts without offset. Compared to the other wheel gear systems, planetary gear systems show the highest efficiency, the highest force and

	wheel gear	chain gear	friction gear	belt gear
Force density	100%	98%	6%	20%
Power density	100%	37%	2%	7%

Table 2.1: Relative force and power densities of mechanical gear systems (adopted from [7])

power density and the smallest volume for high gear ratios [7,98]. Therefore, planetary gear-box systems are considered as the most suitable gear type for aircraft applications.

Figure 2.5 shows the set-up of planetary gears. In the center of the gearbox is the sun wheel, which is the first shaft of the gearbox. The sun wheel is surrounded by multiple planet wheels, mounted on the planet carrier, which is the second shaft. The third shaft is the ring wheel which encircles the planet wheels. In most cases, the planetary gear is operated with one non-rotating shaft, which is connected to the outer structure. However, operation with three rotating spools is possible. Operating the planetary gear with a fixed sun wheel limits the maximum gear ratio to two and implies high mechanical stress, if the sun wheel supports the gearbox forces.
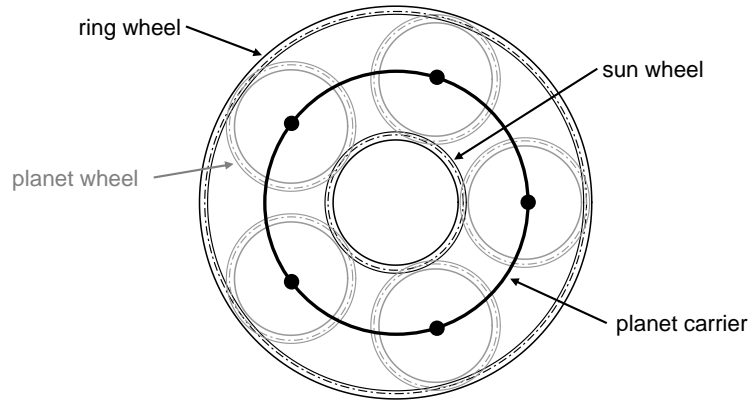
Figure 2.5: Planetary gear system composition

A key parameter of the planetary gear is its Fixed Carrier Train Ratio (FCTR), which describes the speed ratio of the sun wheel to the ring wheel with a non-rotating planet carrier. The FCTR can be calculated using the Willis equation (2.18) which describes the kinematic condition of all three gear shafts (adopted from [99]).

$$\text{FCTR} = \frac{\omega_{\text{sun}} - \omega_{\text{carr}}}{\omega_{\text{ring}} - \omega_{\text{carr}}} \tag{2.18}$$

In the Willis equation, the direction of rotation has to be considered with an appropriate sign. When the carrier is fixed, the sun shaft and the ring shaft rotate in the opposite direction. Moreover, when the size of the planets is reduced towards zero, the gear ratio attains a theoretical lower limit of one. Hence, the FCTR is smaller than -1. When the wheels are considered as cylinders with the corresponding pitch diameters, the FCTR approximates the maximum number of planets that fit into the gear according to equation (2.19).

$$N_{\text{planets}} = \left\lfloor \frac{\pi}{\arcsin\left(\frac{\kappa+1}{\kappa-1}\right)} \right\rfloor \tag{2.19}$$

In order to derive a correlation for the gearbox mass, Ricci derived rated parameters for planetary gear systems and examined the data of available gearboxes [2]. He derived a power function correlation for the mass-to-ring-torque ratio over the rated ring-torque for gearboxes up to six tons. To prove the validity of his correlation for smaller gearboxes from 1 to 100 Nm, the data of planetary gears from Reisenauer Präzisionsantriebe [100], ebm-papst Zeitlauf [101], Tramec Getriebe [102], AHS Antriebstechnik [103] and Wittenstein alpha [104] were added to the graph and shown in Figure 2.6.
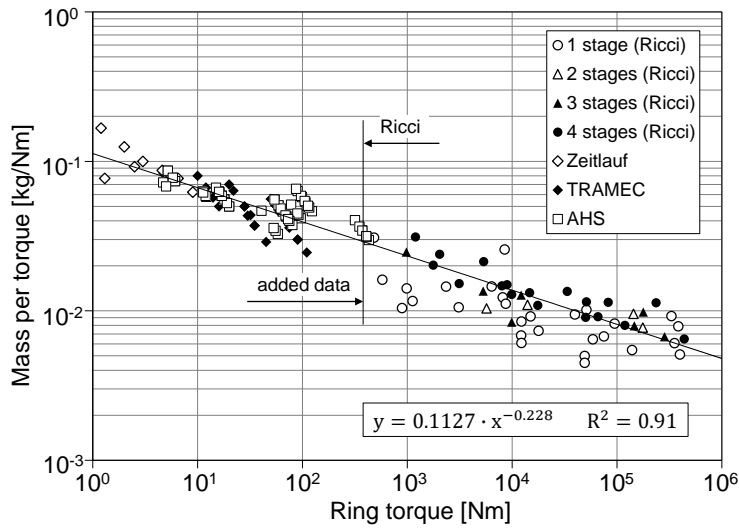
Figure 2.6: Planetary gear mass correlation (extended from [2])

The application of Ricci's correlation to the collected small gearbox data showed that the mass was significantly underestimated. To improve the accuracy for small planetary gear systems, a new correlation is derived, that includes the data from Zeitlauf, TRAMEC and AHS. The resulting correlation is plotted in Figure 2.6 and given in equation (2.20). Neither the study from Ricci nor the data survey has shown a systematic impact of the FCTR on the gearbox mass. A weak trend, that gearboxes with FCTRs from four to six have higher torque ratings than gearboxes with lower and higher FCTRs can be observed and explained with the diameter relations of the sun and planet wheels, however the data of the manufacturers is too scattered to derive a meaningful correlation. For FCTRs lower than four, the planet wheel diameter decreases significantly, resulting in lower torque rating and for FCTR higher than six, the decreasing sun wheel diameter limits the torque rating.

$$\frac{m}{Q_{\text{ring}}} = 0.1127 \cdot Q_{\text{ring}}^{-0.228} \qquad R^2 = 0.91 \tag{2.20}$$

To derive a correlation for the gearbox volume, the volume-to-ring-torque is plotted over the rated ring-torque in Figure 2.7. All examined gear systems show a length-to-diameter ratio close to unity. Hence, a constant length-to-diameter ratio of one is utilized to determine the gear diameter and length from the correlated volume. The identified volume correlation is

shown in equation (2.21).
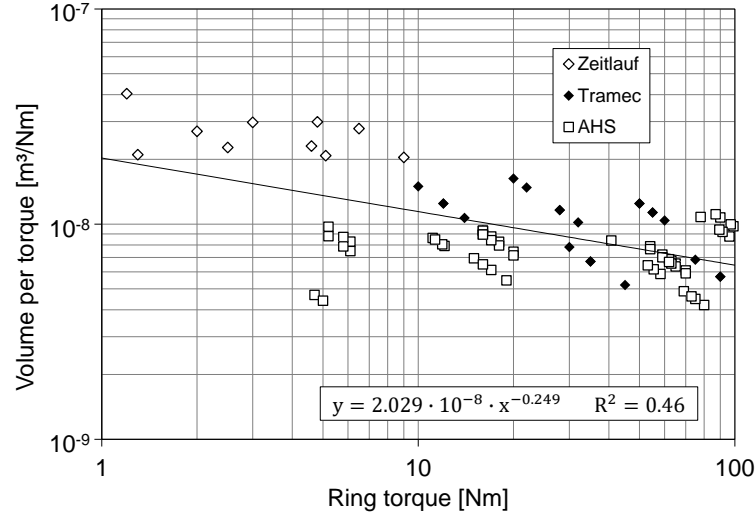
Figure 2.7: Planetary gear volume correlation

$$\frac{V}{Q_{\text{ring}}} = 2.029 \cdot 10^{-8} \cdot Q_{\text{ring}}^{-0.249} \qquad R^2 = 0.46 \tag{2.21}$$

To estimate the efficiency of the gear stage for different loadings, the method from Wittenstein alpha is applied [104]. This method uses a constant fiction torque, which is derived from a 97% efficiency at rated load operation, and subtracted from the sun wheel.

For a dynamic simulation of the planetary gearbox, the inertia of the wheels must be known. In order to estimate this inertia, the pitch circle of the ring wheel is assumed to be 85% of the external gearbox diameter. With this assumption and the FCTR, the pitch diameters of all wheels can be calculated. The width of all wheels is determined from a width-to-diameter ratio of 1.1 of the bevel wheel, which can either be the sun or the planet wheel [105]. The inertia of the wheels is then calculated with a cylinder approximation and an average material density for steel. Finally, the inertia of the wheels is calibrated to the information given from Tramec Getriebe [102]. Furthermore, a kinematic condition is included in order to calculate the rotational speed of the planets [106].

$$\omega_{\text{planet}} = \omega_{\text{carr}} + \frac{2}{\kappa + 1} \cdot (\omega_{\text{sun}} - \omega_{\text{carr}}) \tag{2.22}$$

The equation of motion for the gearbox is obtained with the Lagrangian mechanics. The Euler-Lagrange equation subtracts the potential energy of a system from its kinetic energy. For the planetary gear stage, the potential energy is neglected, so the Lagrangian function is given by equation (2.23).

$$
\begin{aligned}
L = & \frac{J_{\text{sun}} \cdot \omega_{\text{sun}}^2}{2} + \frac{J_{\text{carr}} \cdot \omega_{\text{carr}}^2}{2} + \frac{J_{\text{ring}} \cdot \omega_{\text{ring}}^2}{2} + \\
& \frac{N_{\text{planets}} \cdot m_{\text{planet}} \cdot d_{\text{carr}}^2 \cdot \omega_{\text{carr}}^2}{4} + \frac{N_{\text{planets}} \cdot J_{\text{planet}} \cdot \omega_{\text{planet}}^2}{2}
\end{aligned}
\tag{2.23}
$$

It is important to consider the supplementary inertia of externally connected components in this equation, not only the inertia of the wheel itself. The equation is then derived according to the generalized coordinates of the gearbox to obtain the equation of motion. With one shaft being fixed, the gearbox has one single degree of freedom. For a non-rotating planet carrier, the Euler-Lagrange equation of the planetary gear can be solved for the acceleration of the sun shaft, which is given by equation (2.24).

$$\frac{\delta\omega_{\text{sun}}}{\delta t} = \frac{Q_{\text{sun}} + \frac{Q_{\text{ring}}}{\kappa}}{J_{\text{sun}} + \frac{J_{\text{ring}}}{\kappa^2} + \frac{4 \cdot N_{\text{planets}} \cdot J_{\text{planet}}}{(1+\kappa)^2}} \tag{2.24}$$

For a non-rotating ring wheel, the acceleration of the planet carrier is given by equation (2.25). The shaft speed is obtained by integrating the shaft acceleration.

$$\frac{\delta\omega_{\text{carr}}}{\delta t} = \frac{Q_{\text{carr}} + \frac{Q_{\text{sun}}}{1-\kappa}}{J_{\text{carr}} + \frac{J_{\text{sun}}}{(1-\kappa)^2} + N_{\text{planets}} \cdot m_{\text{planet}} \cdot r_{\text{planet}}^2 + N_{\text{planets}} \cdot J_{\text{planet}} \left(\frac{1-\kappa}{1+\kappa}\right)^2} \tag{2.25}$$

When no gear is used, the acceleration of the shaft is described by Newton's second law for rotational systems, which is given in equation (2.26).

$$\frac{\delta\omega}{\delta t} = \frac{Q_{\text{mot}} - Q_{\text{prop}}}{J_{\text{mot}} + J_{\text{prop}}} \tag{2.26}$$

2.4 Electric Motor

An electric machine transforms electric power into mechanical power and vice versa. There are many machine types with different operating characteristics, however, all electric machines utilise the Lorentz force that is exerted on charged particles as they are moved through electromagnetic fields. Rotatory electric machines consist of a stator and a rotor, whereas one component carries multiple conductors and the other component creates a (electro-)magnetic field. In motor mode, a current flow is sent through the conductors in a defined way, which creates the torque of the electric machine. In generator mode, a torque and an electromagnetic field are applied to the machine, which induces a current flow in the conductor.

The application of an electric motor in a UAV imposes a number of requirements, which include low component mass and dimensions, high efficiency, operability in medium altitude and high reliability. To compare the most common machine types, Finken et al. conducted a pre-design study of a DC motor, an Induction Motor (IM), a Permanent Magnet Synchronous Motor (PMSM) and a Switched Reluctance Motor (SRM) for equal mechanical requirements [3]. The results show, that the PMSM has the highest peak efficiency and the highest power density. This is supported by the results presented in [107–110].

In order to compare the motor types and discuss their advantages for electric aircraft, the operational characteristics of electric motors are visualised in Figure 2.8. For rotational speeds below the rated speed, the motor operation is limited by a maximum continuous torque, which results from thermal limits in the stator coils. At rated speed, the motor controller delivers its maximum output voltage and the motor delivers its maximum power. To further increase the speed, field weakening is applied, which reduces the rotor field intensity and keeps the rotor induced voltage at a constant level. Therefore, controller of the electric machine utilised the stator field to weaken the rotor field, which results in a torque reduction with higher speed. Hence, from the rated speed on, the motor works in a constant power

operation. Figure 2.8 shows the results of the study from Finken et al.
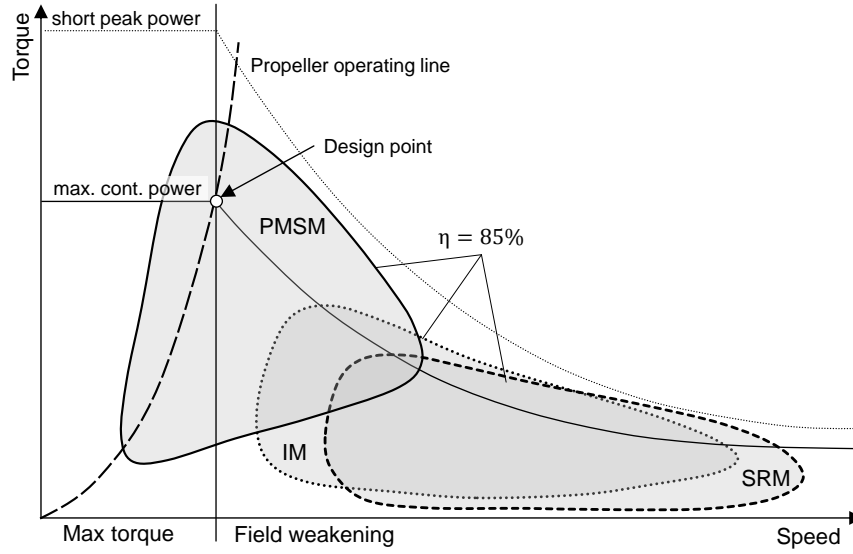
Figure 2.8: Efficiency map comparison of different motor types (adapted from [3])

For fixed pitch propellers, the propeller torque increases with the square of its rotational speed, when the ambient air conditions and flight speed do not change. Hence, the operating line of the propeller is a parabola in the motor efficiency map. To match propeller and motor, it is meaningful to design the most demanding propeller operation point to the rated point of the motor in order to exploit the motor's maximum torque capability and avoid over sizing. The 85% efficiency lines of the three motor types in Figure 2.8 show, that the PMSM is the most suitable type to drive a propeller because it provides the highest efficiency along the propeller operation line.

As the motor is operated at higher altitudes it must be ensured, that the continuous power limit is adapted according to the cooling capacity at lower air density. Therefore the specifications of B&R Automation [111], Baumüller Nürnberg [112], Kollmorgen [113] and Bosch Rexroth [114] have been analysed. The specification of B&R Automation represents an average performance rating and indicates a 10% torque reduction every 1000 m, starting from 1000 m above sea level.

Determining the motor efficiency at rated power is a complex process and requires detailed information on motor geometry and utilised materials. To simplify this process, the motor efficiency is estimated based on the rated mechanical power and efficiency class definitions. Figure 2.9 shows the definition of the four efficiency classes IE1-4 from the IEC 60034-31 [115] standard as well as empiric data of induction motors [116] and permanent magnet motors [117]. For this model, the IE4 class is used, which presents a realistic goal for permanent magnet motors [118].

Beside the rated torque and speed, the bus voltage of the motor controller is a third design parameter. The motor controller architecture is considered as a B6 inverter with six Insulated Gate Bipolar Transistor (IGBT) switches and anti parallel diodes as shown in Figure 2.10. The rms line to line voltage of this inverter can be calculated by its control law in equation
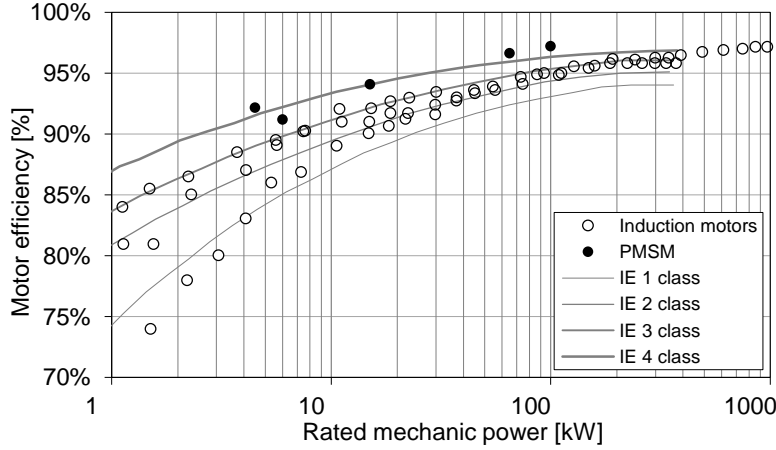
Figure 2.9: Design efficiencies of electric motors

(2.27)(adapted from [119]). The control angle γ is usually limited to 150 deg [119]. With a given voltage U_{DC} and an assumed motor power factor of 0.9, the motor voltage and current at rated power can be calculated. For a performance estimation, the switching and conducting losses of the inverter components are modelled with characteristics from the respective data sheet [120]. The B6 inverter architecture is implemented and the model results are calibrated to the simulation tool SEMISEL from SEMIKRON International [121]. This model neglects the thermal management and assumes that the IGBT modules and diodes operate within their certified temperature range. To estimate the mass of the motor controller, an empirical data fit from Schömann is applied [47]. He identified a constant specific power for motor controllers up to 12 kW of 27 $\frac{\text{g}}{\text{kW}}$.

$$U_{\text{rms,line}} = -\frac{\pi}{3\sqrt{6}} \cdot U_{DC} \cdot \cos(\gamma) \quad (2.27)$$
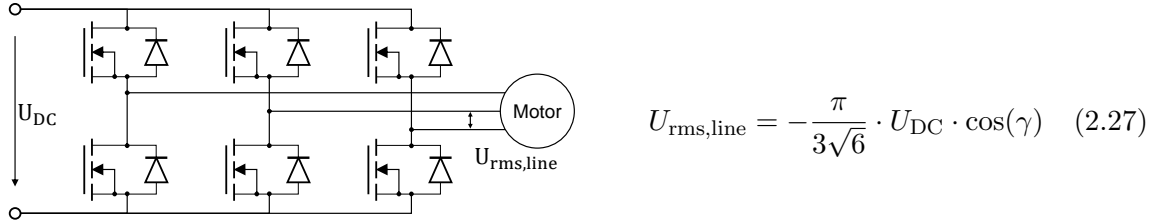
Figure 2.10: Motor controller architecture

To estimate additional motor parameters, which are required for transient simulation, an equivalent circuit is used according to [4]. The equivalent circuit, as it is shown in Figure 2.11, is obtained from a direct-quadratic-zero (dq0) transformation of the three phase electric system. For PMSM, the dq0 transformation is a mathematical transformation of the electric three-phase system of the stator into the rotating frame of the rotor. The benefit of this transformation is the reduction of three linearly dependent AC parameters into two linearly independent DC parameters, which significantly reduces the analysis of three phase systems. The direct axis is parallel to the magnetic field of the rotor and the quadratic axis is perpendicular to the direct axis. By making up the balance of all direct and quadratic components of the circuit elements, the equivalent circuit from Figure 2.11 is obtained. The left circuit contains the terms for the direct axis and the left circuit represents the quadratic

axis. The resistance, R_1, and the inductance, $L_{d/q}$, represent the stator coils. U and I denote the motor input voltage and current level. The voltage sources in the circuit represent the induced voltages from the rotational speed of the rotor. This equivalent circuit considers only the ohmic losses and neglects hysteresis losses in the iron and friction losses. Thus, the equivalent circuit predicts power factors of roughly 0.95 at rated performance, which is too high. As a meaningful assumption, a power factor of 0.9 at rated performance is assumed for all motor designs [5].
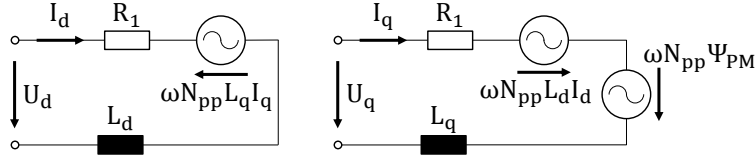
Figure 2.11: Equivalent circuit of a PMSM (adopted from [4])

By applying Kirchhoff's circuit laws on the two equivalent circuits from Figure 2.11, the equations (2.28) and (2.29) can be derived, which describe the time derivative of the magnetic flux ψ in the respective direction of the dq0-frame.

$$\frac{\delta \psi_d}{\delta t} = U_d - R_1 \cdot I_d + \omega \cdot N_{\text{pp}} \cdot \psi_q \tag{2.28}$$

$$\frac{\delta \psi_q}{\delta t} = U_q - R_1 \cdot I_q - \omega \cdot N_{\text{pp}} \cdot \psi_d \tag{2.29}$$

Equations (2.30) and (2.31) balance the magnetic flux components in the dq0-frame. The magnetic flux of the stator coils is simply calculated from the according current term. As the direct axis is oriented along the magnetic flux of the rotor, the permanent magnet flux is only accounted for on the direct magnetic flux.

$$\psi_d = \psi_{\text{PM}} + L_d \cdot I_d \tag{2.30}$$

$$\psi_q = L_q \cdot I_q \tag{2.31}$$

Finally, the torque of the electric motor can be calculated with equation (2.32).

$$Q = \frac{3}{2} \cdot N_{\text{pp}} \cdot [\psi_{\text{PM}} \cdot I_q + (L_d - L_q) \cdot I_d \cdot I_q] \tag{2.32}$$

With these equations, a given rated torque and speed, a given pole pair number N_{pp} and further assumptions on the motor architecture and the control law, the inductances L_d and L_q as well as the magnetic flux of the permanent magnet ψ_{PM} can be calculated. The first assumption is that the motor reluctance is zero, which results in the condition that $L_q = L_d$. An optimized PMSM will show a certain reluctance, as this provides a higher torque and a better efficiency [122]. The second assumption is, that the motor is controlled with the maximum-torque-per-ampere law up to its rated speed [123]. This assumption requires the direct current to be zero $I_d = 0$. By applying a negative direct current, the magnetic field of the permanent magnet can be weakened according to equation (2.30). This reduces the induced voltage in the direct axis and allows to further increase the rotational speed of the machine without exceeding the maximum output voltage of the converter. The ohmic

losses of the electric machine can be estimated from a breakdown of typical motor losses from [116] and the according equivalent stator resistance can be derived. Afterwards, the motor inductance as well as the motor voltage can be calculated. The apparent power of the motor is utilised for estimating the motor dimensions. According to [5], the apparent power, P_{app}, of an electric motor is a function of the Esson factor, C, the air gap diameter, d_{airgap}, the active rotor length, l_{act}, as well as the rotational speed, n.

$$P_{app} = C \cdot d_{airgap}^2 \cdot l_{act} \cdot n \tag{2.33}$$

Figure 2.12 shows the Esson factor of produced PMSM as a function of their apparent power and their pole pair number. The marked areas on the right show typical values for the Esson factor of air cooled and water cooled electric machines with the according pole pair number. The dots on the left show calculated Esson factors of the Plettenberg Predator Series motors[124], which have a rated mechanical power of up to 20 kW and are utilised for large RC aircraft. The Esson factors of the Plettenberg motors are used for a correlation, which is applied in this model.
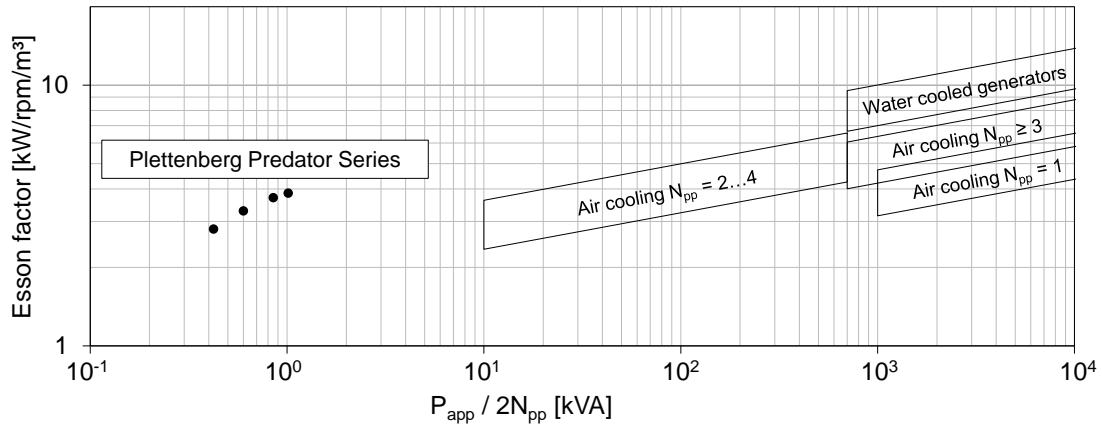
Figure 2.12: Esson factor of PMSM (adapted from [5])

The pole dispartment λ is another design parameter of the electric motor. For a constant pole pair number, it is proportional to the relation between the active length and the air gap diameter of the motor. Empiric values for λ are given between 0.7 and 2.5 (max.5) [5]. Including λ in equation (2.33), the air gap diameter, d_{airgap}, of the motor can be calculated with equation (2.34).

$$d_{airgap} = \sqrt[3]{\frac{2 \cdot N_{pp} \cdot P_{app}}{\pi \cdot \lambda \cdot C \cdot n}} \tag{2.34}$$

For a pole dispartment of 3, the resulting rotor has a length-to-diameter ratio up to 2, which is favourable for a low rotor inertia design. To estimate the outer stator diameter, d_1, some empiric values for the magnetic field intensities, the current density in the stator coil and the filling factors are used from [5].

$$d_1 = d_{airgap} + \frac{2.5 \cdot \bar{A}_1}{j_1 \cdot k_{notch} \left(1 - \frac{\hat{B}_{airgap}}{\hat{B}_{tooth}}\right)} + \frac{\pi \cdot d_{airgap} \cdot \hat{B}_{airgap}}{2 \cdot N_{pp} \cdot \hat{B}_{yoke}} \tag{2.35}$$

To estimate the mass of an electric motor, Schömann analysed a database of small motors and found an average density of roughly 3500 $\frac{kg}{m^3}$ for inrunner motors [47]. A database analysis of

industrial motors has shown that the density of 3400 $\frac{\text{kg}}{\text{m}^3}$ is still accurate (R^2=0.98) for many motors up to 300 kW, which is shown in Figure 2.13. Hence, the mass of the electric motor is estimated by using the outer stator diameter and the active rotor length of the motor multiplied with a calibration factor. The rotor inertia is estimated with the same average density, the air gap diameter and the active length of the motor. The calibration of this model has shown, that a motor length of 1.21 times the active length and an outer diameter of 1.05 times the stator diameter result is a good agreement with manufacturer data on motor mass and rotor inertia [111–113].
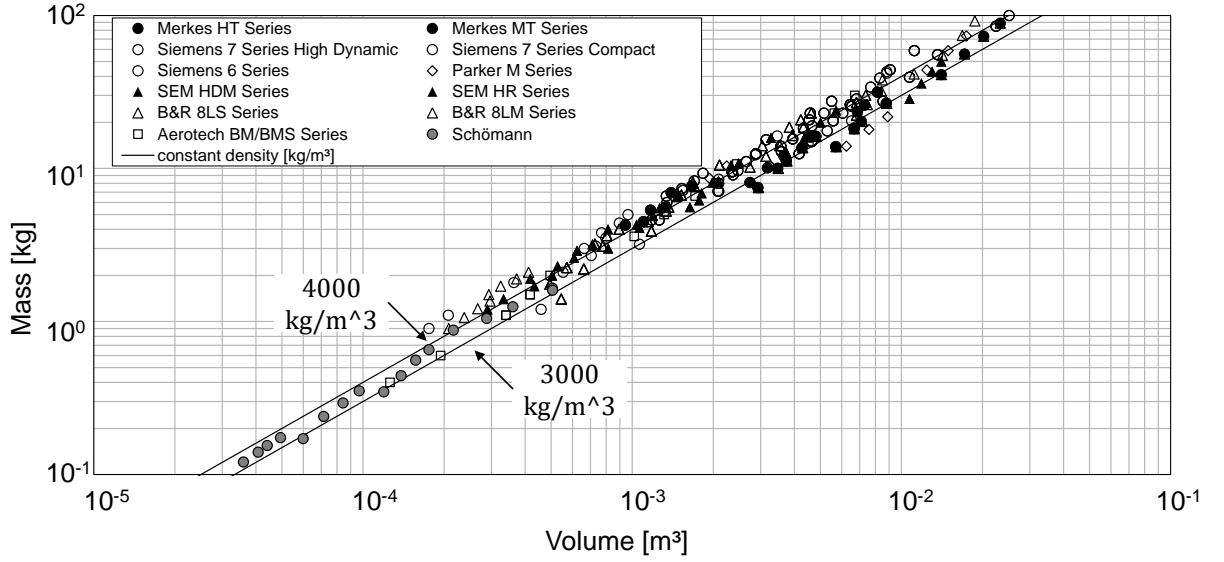
Figure 2.13: PMSM average motor density

To estimate the off design performance of the electric motor and its controller, a generic efficiency map of a PMSM is used [110]. According to methods from Lukic and Emado [125] and Petersheim [126], this map is scaled to the rated point and rated efficiency of the scaled motor. For a given torque and speed, the motor efficiency can be read from the scaled map and the motor voltage and current can be calculated. The voltage and current level are used to calculate the efficiency of the controller. Figure 2.14 shows the efficiency map of the motor, as it was taken from [110]. The dashed lines show the maximum continuous performance for operating altitudes up to 5000 m. Moreover the Figure shows the efficiency of a simulated motor controller with a bus voltage of 200 V. The efficiency of the motor controller is particularly sensitive to the bus voltage level. When the voltage level is reduced and motor current is increased to maintain the same power level (e.g. remote controlled air plane motors), efficiency drops significantly. The characteristics of the controller efficiency map are in good agreement with the map of the Toyota Prius motor controller [127].

For short time manoeuvres, the electric motor torque can be increased over the continuous limit. The upper torque limit of synchronous machines is the stall torque, which occurs at the maximum angular displacement between the stator and the rotor. Figure 2.15 shows the stall torque over the rated torque of the analysed industrial motors from the database. As this data is retrieved from industrial motors, a conservative stall torque ratio of 1.5 to 4 is assumed for aircraft electric motors. Based on their experience with electric motors,
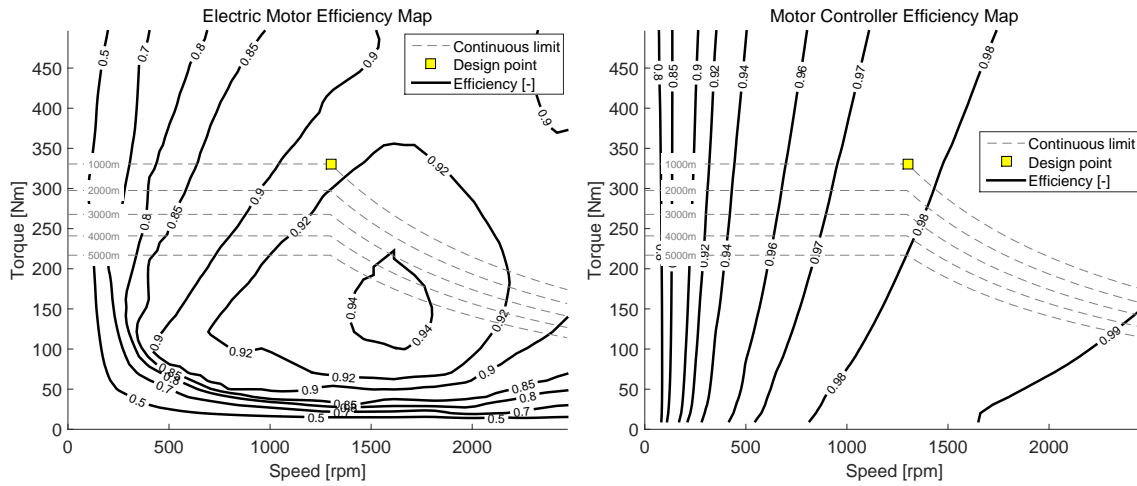
Figure 2.14: Motor(left) and controller(right) efficiency map

NASA assumes, that electric motors for aircraft applications can deliver twice the maximum continuous torque for short time manoeuvres [64].
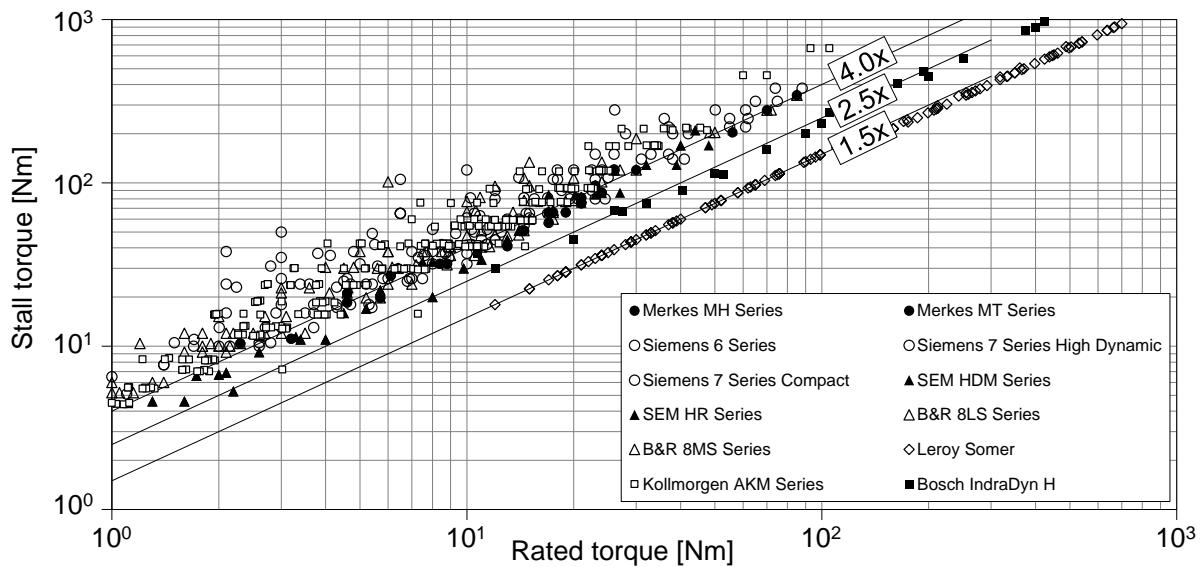
Figure 2.15: PMSM stall torque

The control of the electric motor is implemented in two cascading control loops. The inner loop represents the current controller which is implemented in a simple integrator controller which is fed with a normalised error signal. The outer loop controls the rotational speed of the motor. This controller is implemented in a PI controller, which is fed with the normalised speed. The controller output is scaled with the rated torque of the motor. This normalisation decouples the control parameter from the motor scaling, so that the optimum control parameters can be utilised for all motor designs.

2.5 Buck Boost Converter

DC-DC converters are used to moderate between different voltage levels of two DC components. There are numerous types of DC-DC converters which on a first level can be divided into passive converters and converters with active switching. Passive converters have the drawback that their transmission ratio is dependent on the load state of the connected components and have no relevance any more in today's applications [119], [128]. The basic converters that are used today include the buck converter, the boost converter, the buck boost converter and the Cuk converter. These converters are often used as intermediate stages between a rectifier or inverter and the coupled DC-network to improve the power factor and power quality. Moreover, they are used in DC-networks of renewable energy sources like photovoltaic systems [128]. In hybrid propulsion systems they are used to transform the output voltage of DC-Power sources (e.g. fuel cell, battery or super capacitor) to a defined bus voltage level. The output voltage of these components depends on the load current, therefore, a DC-DC converter is necessary to transform the output voltage to a defined voltage level of the DC bus that the component is connected to.

For the application in hybrid electric propulsion systems for medium size UAVs the buck boost converter was chosen because this topology enables both, higher and lower output voltages than the input voltage level. The converter architecture and a basic equivalent circuit are shown in Figure 2.16. The IGBT and the diode are modelled with normalised operating lines from Infineon components [129]. The inductor and the capacitor are modelled as an ideal inductance L and an ideal capacity C with a parasite series resistance for the inductor R_l and the capacitor R_c. There are no electromagnetic interference (EMI) filters considered in this model. To achieve a better power quality of real converters, those filters are added to the converter in- and output in a detailed design.
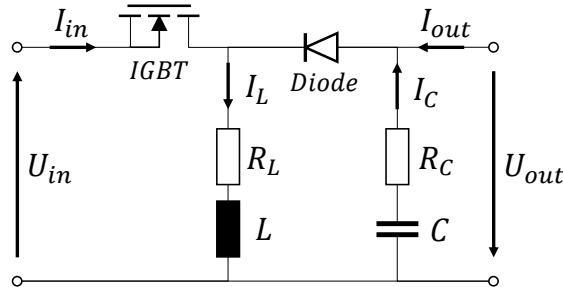
Figure 2.16: Electric circuit of a buck boost converter

By applying Kirchhoff's circuit laws on the three meshes of the equivalent circuit, and by applying time averaging technique, Equation (2.36) can be derived, which describes the performance of the converter [128, 130]. Equation (2.36) can be solved iteratively for the duty cycle ν for any operating point. The duty cycle is a number between 0 and 1, which gives the time share during which the IGBT switch is closed.

$$\nu \cdot (U_{\text{in}} - U_{\text{igbt}} - R_l \cdot I_l) + (1 - \nu) \cdot (-R_l \cdot I_l - U_{\text{diode}} - R_c \cdot (I_l - I_{\text{out}}) - U_{\text{out}}) = 0 \quad (2.36)$$

To solve Equation (2.36), a supplementary relation for the inductor current, I_l, is required, which can be expressed as a function of the duty cycle and the output current I_{out}, according

to equation (2.37). With the inductor current, the IGBT and the diode current can be calculated, which are required to interpolate the voltage drop of both components from the normalised operating lines.

$$I_l = \frac{I_{out}}{1 - \nu} \tag{2.37}$$

For the design of the converter, four design parameters have to be specified:

- the output voltage U_{out}

- the output current I_{out}

- the upper and lower bound of the input voltage

- the switching frequency

With these design parameters the minimum required values for the inductance L and the capacitance C can be calculated. Therefore two methods have been found that consider an arbitrary load type at the output. Many other methods consider only resistive loads at the converter output. The two methods were defined by Texas Instruments [131] and Coilcraft Inc. [132]. Both methods show similar results within the same order of magnitude.

At this stage, the capacitance, the voltage and the current through the capacitor are known. In the next step the Equivalent Series Resistance (ESR), R_c, the volume and the mass of the capacitor is estimated. The results of a database survey of DC-Link capacitors from WIMA [133] is shown in Figure 2.17 and the following equations.
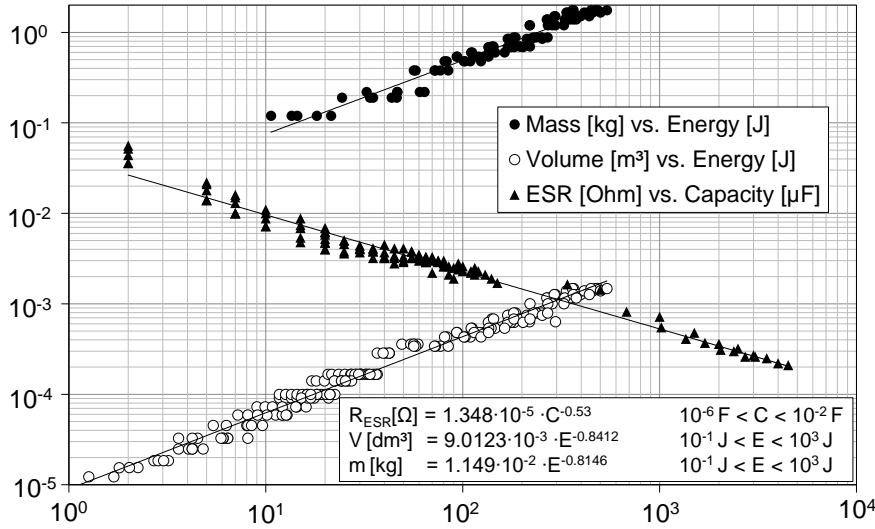
Figure 2.17: Mass, volume and ESR of DC link capacitors

$$R_c[\Omega] = 1.348 \cdot 10^{-5} \cdot C^{-0.53} \qquad 10^{-6}F < C < 10^{-2}F \qquad R^2 = 0.96 \tag{2.38}$$

$$V[dm^3] = 9.0123 \cdot 10^{-3} \cdot E^{-0.8412} \qquad 0.1J < E < 1000J \qquad R^2 = 0.98 \tag{2.39}$$

$$m[kg] = 1.149 \cdot 10^{-2} \cdot E^{-0.8146} \qquad 0.1J < E < 1000J \qquad R^2 = 0.95 \qquad (2.40)$$

For the inductor, the inductance, the voltage and the current are known from the performance calculations. To estimate the resistance, the mass and the volume of the inductor, a method from [134] is applied. The inductor core is considered as a ring with rectangular cross section with the outer diameter, A, the inner diameter, B, and the width, C. A copper wire is wound around the core with N windings. Figure 2.18 shows the set up of the inductor model.
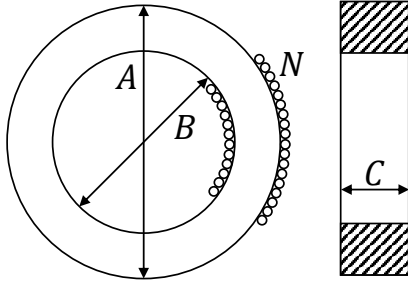
$$L = \mu_0 \cdot \mu_r \cdot N^2 \cdot \frac{C(A - B)}{\pi(A + B)} \qquad (2.41)$$

$$N \leq \frac{\pi(\pi B - d_{\text{wire}})}{3 \cdot 1.15 \cdot d_{\text{wire}}} \qquad (2.42)$$

$$\frac{L \cdot i_{\max}}{N \cdot B_{\max}} \leq \frac{C(A - B)}{2} \qquad (2.43)$$

Figure 2.18: Inductor approximation

A constrained optimization function solves the optimum inductor geometry as well as the optimum wiring for the minimum mass. The data for the ferrite core material is defined according to [135]. The resistance of the copper wire is calculated with the specific resistance of copper, the wire diameter and the total length of the wire. The resulting correlations for minimum mass inductor designs are valid for inductance between 10^{-5} H $< L < 10^{-3}$ H and current between 1 A $< I < 1000$ A and presented in Equations (2.44) to (2.47).

$$R_l[\Omega] = 73.825 \cdot L^{0.6193} \cdot I^{-0.7556} \qquad (2.44)$$

$$d[m] = 0.0645 \cdot L^{0.2883} \cdot I^{0.6235} \qquad (2.45)$$

$$l[m] = 0.0469 \cdot L^{0.2873} \cdot I^{0.6705} \qquad (2.46)$$

$$m[kg] = 1.113 \cdot L^{0.9830} \cdot I^{1.9648} \qquad (2.47)$$

It is considered, that the size and weight of the IGBT and the diode are negligibly small compared to the weight of the inductor and the capacitor. The cooling devices for the IGBT and the diode are neglected in this model. It is assumed that the converter components provide the same peak power capability during short time manoeuvres as electric motors. The switching components are considered to always operate at their rated temperature.

To calculate the off design performance of the converter, the voltage drop of the IGBT and the diode have to be calculated iteratively. The total voltage drop of both components is calculated from the conduction losses and the switching losses. In order to estimate the conduction losses, data sheet information is applied according to the method in [120]. A survey of Infineon IGBT and diode data sheets, that was conducted by the author, has shown, that the operating characteristic is similar for many modules, when it is normalised

to a reference current and voltage. To determine the conduction voltage drop, a reference voltage drop is determined from the maximum collector-emitter voltage (and blocking voltage respectively) of the module according to Table 2.2.

U_{CE} [V]	600	1200	1700	3300	6500
$U_{cond,ref,igbt}$ [V]	1.35	2.00	2.30	2.90	3.10
$U_{cond,ref,diode}$ [V]	1.05	1.75	2.00	2.55	2.95

Table 2.2: Conduction voltage drop of IGBTs and diodes

At part load operation, the voltage drop can be determined from the relative current level according to Figure 2.19.
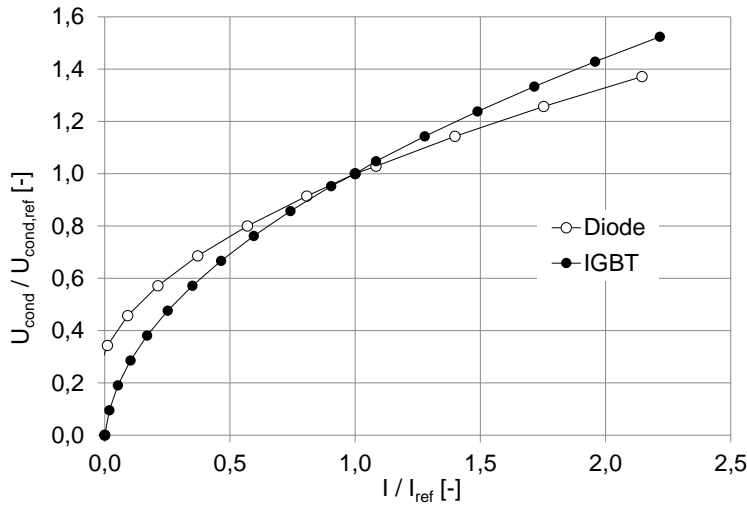
Figure 2.19: IGBT and diode conduction voltage drop

Similar to the conduction losses, the switching losses of IGBT and diode modules can be estimated by normalising the characteristic to rated conditions. In a first step, a reference switching loss energy is calculated with the maximum collector-emitter voltage (and blocking voltage respectively) according to Table 2.3. The table gives specific switching loss energy coefficients per rated current of Infineon modules. To calculate the reference switching loss energy per cycle, the coefficient for the respective collector-emitter voltage is scaled with the rated current of the module. The resulting reference energy is given with respect to the reference voltage U_{ref} in Table 2.3.

U_{CE} [V]	600	1200	1700	3300	6500
U_{ref} [V]	300	600	850	1650	3250
$e_{sw,ref,igbt}$ [J/A]	$8.113 \cdot 10^{-5}$	$4.005 \cdot 10^{-4}$	$6.187 \cdot 10^{-4}$	$4.262 \cdot 10^{-3}$	$1.428 \cdot 10^{-2}$
	(R^2=0.97)	(R^2=0.99)	(R^2=0.97)	(R^2=0.91)	(R^2=0.99)
$e_{sw,ref,diode}$ [J/A]	$1.538 \cdot 10^{-5}$	$7.568 \cdot 10^{-5}$	$3.748 \cdot 10^{-4}$	$2.357 \cdot 10^{-3}$	$4.000 \cdot 10^{-3}$
	(R^2=0.95)	(R^2=0.99)	(R^2=0.94)	(R^2=0.95)	(R^2=0.99)

Table 2.3: Specific switching energy losses of IGBTs and diodes

In order to determine the switching losses at part load operation, the reference energy is scaled with the relative voltage and current according to Equations (2.48) and (2.49) [136]. The switching power loss is calculated with the resulting switching energy and the switching frequency of the module. An equivalent voltage drop is calculated with the power loss and the current level.

$$E_{\text{sw,igbt}} = E_{\text{sw,ref,igbt}} \cdot \frac{I}{I_{\text{ref}}} \cdot \left(\frac{U}{U_{\text{ref}}} \right)^{1.35} \tag{2.48}$$

$$E_{\text{sw,diode}} = E_{\text{sw,ref,diode}} \cdot \left(\frac{I}{I_{\text{ref}}} \right)^{0.6} \cdot \left(\frac{U}{U_{\text{ref}}} \right)^{0.6} \tag{2.49}$$

To calculate the off design performance of the converter, the Equation (2.36) has to be solved iteratively for the duty cycle. The voltage drop of the IGBT and the diode result from adding the voltage drops of the conduction losses and the switching losses. The current level in the components can be calculated from the output current and the duty cycle [130]. Because of the losses in the components, the calculated duty cycle is slightly higher than for the ideal buck-boost converter. Hence, the ideal duty cycle is a suitable initial value for the iteration.

Figure 2.20 shows a calculated efficiency map of a buck-boost converter with a design output voltage of 200 V, a switching frequency of 10 kHz and a design output current of 240 A. This corresponds to an output power of 48 kW. The input voltage range is limited from 200 to 300 V.
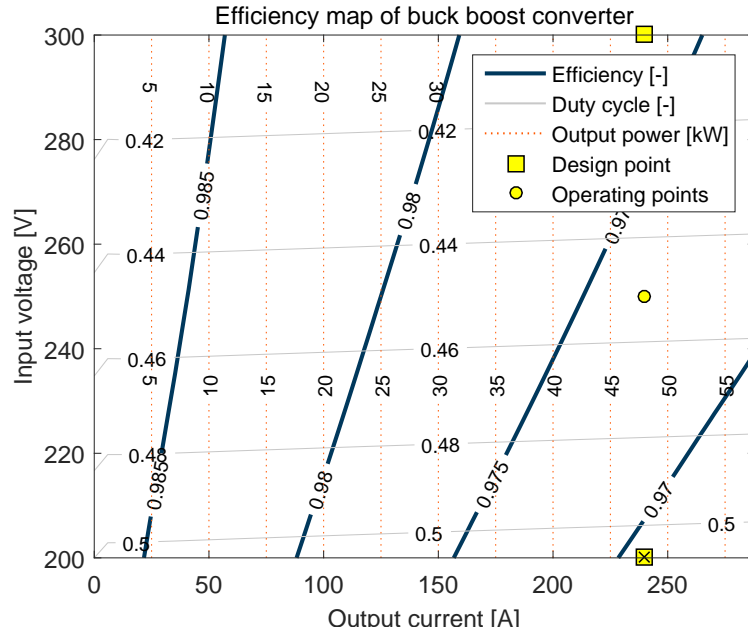
Figure 2.20: Electric circuit of a buck boost converter

The predicted volume of this converter is 4.1 litres which corresponds to a power density of 11.6 $\frac{\text{kW}}{\text{dm}^3}$. A study from Kolar suggested a power density limit of 40 $\frac{\text{kW}}{\text{dm}^3}$ for isolated DC-DC converters and determined the DC-Link capacitor being the limiting component for maximum power density [137]. The estimated weight of the converter is 5.9 kg which corresponds

to a power density of 8.1 $\frac{\text{kW}}{\text{kg}}$.

To simulate a the transient response of the DC-DC converter, a rise time is derived at the system design point [138], which is assumed constant for all operating conditions. The duty cycle is an input parameter of the converter, which requires a controller for transient simulations. As the task of the converter is to deliver a constant output voltage, a PI controller with anti wind-up limitation is implemented, which controls the duty cycle of the IGBT. When the output voltage of the energy carrier changes because of a load change, the controller adopts the duty cycle in order to deliver the voltage level which is required by the DC bus system. This implies that the output voltage is measured and available for the controller.

2.6 Fuel Cell Stack

A fuel cell transforms chemical energy into electrical energy by oxidising a gaseous fuel. This process is split in two separate electrochemical reactions, which are separated by a membrane, which is only permeable for the oxidised fuel. The fuel is oxidised on one side of the membrane, which releases electrons, that run through an electric load to the cathode. At the cathode side, oxygen is supplied, which is reduced and reacts with the oxidised fuel, that diffuses through the membrane. The fuel cell type that is mainly used for vehicles and mobile applications is the proton exchange membrane fuel cell (PEMFC). The advantages of the PEMFC over other fuel cell types are the low operating temperature, the high efficiency and the high power density [139–141]. For aircraft systems with long endurance, the PEMFC is an interesting power device because of its high efficiency in part load operation [142, 143].

The PEMFC must be supplied with hydrogen, which is stored in a pressurized, a hydride or in a cryogenic tank, and oxygen or air. When the fuel cell is supplied with pure oxygen, a supplementary tank is required. When supplying the fuel cell with atmospheric air, the power of the fuel cell decreases with the ambient air density when operated at high altitudes. To counteract this effect, the ambient air can be pressurized with an additional compressor. This however reduces the fuel cell system efficiency, because the power for the compressor has to be delivered by the fuel cell. A further disadvantage of using pressurised air is the high flow rate in the cathode gas channel. This diverts a lot of water from the fuel cell and requires a higher water input at the anode side. Hence, the fuel cell requires a humidifier. When supplied with oxygen, the flow rates in the gas channels decrease and the humidifier is not coercively necessary [144]. Hence the use of pure oxygen can have a system mass benefit for small fuel cell systems. Another advantage of using two pressurised gases is the ease of operating the cell at high pressure levels. This increases the fuel cell output voltage and its efficiency. Figure 2.21 shows the set-up of both fuel cell configurations.

To model the performance and the mass of the compressor, a small radial compressor stage has been modelled with the geometry tool of GasTurb 12 [145]. The compressor efficiency is correlated against the corrected mass flow and Reynolds Number Index (RNI) according to data from Grieb [146].

There do exist different approaches to model the performance of a PEMFC. The standard work for modelling the steady state and transient behaviour of fuel cells was conducted by Amphlett et al. [147]. This model considers a mass flow and a thermal balance. The cell voltage is calculated with the Nernst equation, activation and ohmic losses. However this
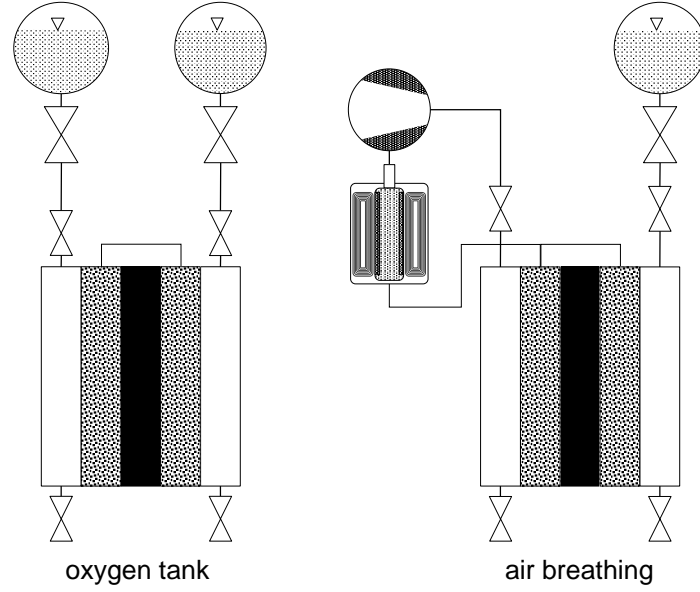
Figure 2.21: Oxygen tank and air breathing configuration of the PEMFC

model uses empiric coefficients, which are related to the analysed fuel cell. More complex models consider two phases in the cathode gas channel and describe the diffusion processes based on the properties of the diffusion layers and the membrane [148].

The fuel cell model, which is utilised for the present work, is based on the work of Loo [149]. The model considers the fuel cell as a one dimensional device with five sections as shown in Figure 2.22. The anode, the membrane and the cathode are discretised into multiple elements to simulate the diffusion. The conditions in the gas channels left from the anode and right from the cathode are derived from a linear gas consumption assumption along the gas path. The movement of hydrogen, oxygen, gaseous water and liquid water through the Gas Diffusion Layer (GDL) and the membrane is modelled with a diffusion process as depicted in Figure 2.22.

Equation (2.50) describes the time dependent progression of the gas concentration, c_j, within the GDL [149]. The index j indicates, that Equation (2.50) is utilised for hydrogen, oxygen and gaseous water, by applying the according concentration, c, and the according effective diffusion coefficient, D^{eff}. The parameter s represents the volumetric share of the GDL, which is occupied by liquid water. The dry porosity of the GDL is represented by the letter ϵ and the parameter D_c constitutes the diffusion coefficient of liquid water [149].

$$\frac{\delta c_j}{\delta t} = \frac{D_j^{\text{eff}}}{\epsilon(1-s)} \cdot \frac{\delta^2 c_j}{\delta x^2} + \frac{c_j \cdot D_c}{\epsilon(1-s)} \cdot \frac{\delta^2 s}{\delta x^2} \qquad (j = H_2, O_2, H_2O_{\text{gas}}) \qquad (2.50)$$

The gas concentrations in the gas channels represent the boundary conditions for the diffusion process at the interface to the GDL. The current density, j, implies a gradient of the hydrogen and oxygen concentration at the interface between the membrane and the GDL, which is calculated using Equations (2.51) and (2.52). In both equations, F constitutes the Faraday constant [149].
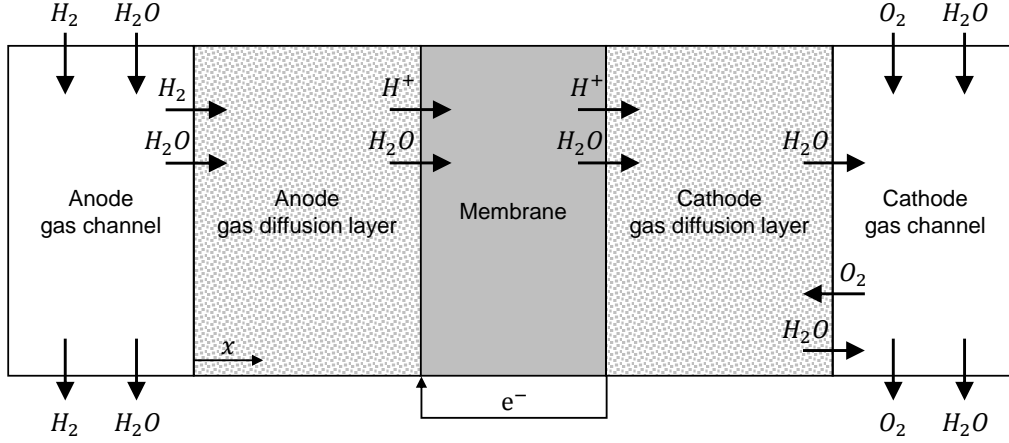
Figure 2.22: 1D, two phase model of a PEM fuel cell

$$-D_{H_2}^{\text{eff}} \cdot \frac{\delta c_{H_2}}{\delta x} = \frac{j}{2F} \tag{2.51}$$

$$-D_{O_2}^{\text{eff}} \cdot \frac{\delta c_{O_2}}{\delta x} = -\frac{j}{4F} \tag{2.52}$$

Equation (2.53) describes the diffusion of liquid water from the membrane through the cathode GDL to the gas channel. It is assumed, that the volume share of liquid water is always zero at the cathode gas channel, as liquid water is drained away by the passing gas flow. At the membrane, liquid water is formed as soon as the water concentrations exceeds its saturation value. Therefore, the gradient of liquid water at the interface between the membrane and the cathode GDL is determined from the diffusion of gaseous water and the formation of water due to the electrochemical reaction [149].

$$\frac{\delta s}{\delta t} = \frac{D_c}{\epsilon} \cdot \frac{\delta^2 s}{\delta x^2} \tag{2.53}$$

Within the membrane, the hydrogen cations imply a water transport from the anode to the cathode side, against the concentration gradient. On the other hand, the water concentration gradient causes water to diffuse back to the anode side. The diffusion of water within the membrane is expressed with the parameter λ, which stands for the number of water molecules held per sulphonic acid group. The spatial diffusion of the water in the membrane is described by equation (2.54). The concentration of sulphonic groups per cubic meter of the membrane material is given by the parameter c_f. Further information on the diffusion processes as well as the numerical description and calculation can be found in [149].

$$\frac{\delta \lambda}{\delta t} = -\left(\frac{2.5}{22} \cdot \frac{j}{c_f \cdot F} \right) \cdot \frac{\delta \lambda}{\delta x} + D_\lambda \cdot \frac{\delta^2 \lambda}{\delta x^2} \tag{2.54}$$

The voltage of the cell is computed with the thermodynamic reversible voltage of the cell reaction minus the activation losses and the resistivity of the membrane according to Equation (2.55) [149].

$$U_{\text{cell}} = -\frac{\Delta g_0}{2F} - U_{\text{activation}} - U_{\text{membrane}} \tag{2.55}$$

The activation loss voltage is calculated with the cell current density, the oxygen concentration and the liquid water share at the GDL-membrane interface according to Equation (2.56) with $j_{ref} = 20\frac{A}{m^2}$ and $c_{O_2,ref} = 41.8\frac{mol}{m^3}$. The index $_{g\text{-}m}$ refers to the interface of the GDL and the membrane.

$$U_{\text{activation}} = \frac{RT}{\alpha_c F} \cdot \log\left(\frac{j}{j_{\text{ref}}} \cdot \frac{c_{O_2,\text{ref}}}{c_{O_2,\text{g-m}}} \cdot \frac{1}{1 - s_{\text{g-m}}}\right) \tag{2.56}$$

The ohmic losses are calculated with the membrane resistance according to Equation (2.57), which is calculated with the water content λ for each membrane element and integrated along the membrane [149]. The letter T constitutes the cell temperature.

$$U_{\text{membrane}} = j \cdot \int_0^{l_{\text{membrane}}} \frac{\delta x}{(0.5139 \cdot \lambda - 0.326) \cdot \exp\left[1268 \cdot \left(\frac{1}{303} - \frac{1}{T}\right)\right]} \tag{2.57}$$

The geometrical and operating parameters of the cell, i.e. the GDL thickness and diffusion coefficients, are adopted from [149] and listed in Table 2.4.

Temperature	T	80	$^\circ$ C
Gas pressure (anode/cathode)	p	5/5	bar
Humidity (anode/cathode)	RH	80/50	%
Stoichiometry (anode/cathode)		1.25/1.25	-
Design current density	j	0.5	$\frac{A}{cm^2}$
Anode GDL thickness		300	μm
Anode GDL porosity	ϵ	0.4	-
Membrane thickness		178	μm
Cathode GDL thickness		300	μm
Cathode GDL porosity	ϵ	0.4	-
Diffusion coefficient water in membrane	D	$2 \cdot 10^{-10}$	$\frac{m^2}{s_2}$
Diffusion coefficient water in GDL	D	$1 \cdot 10^{-9}$	$\frac{m^2}{s}$

Table 2.4: Design and operating parameters of the fuel cell

The steady state performance of the fuel cell is calculated by setting the time derivatives in the preceding equations to zero. The model equation change when liquid water is present in the cathode (s $\neq$ 0). To calculate off design performance, the model equations are first solved for the gaseous water only case. If the calculated water concentration is higher than the saturation value, the equations for the two phase case are considered.

For the design of a fuel cell stack, the required stack voltage and current and the design current density of the fuel cell are necessary. With the design current density, the cell output voltage is calculated for specified operating conditions. The required cell membrane area is calculated from the design current density and the stack current. The number of cells connected in series is determined from the cell output voltage in order to meet the stack voltage level.

The mass and the volume of the fuel cell system is estimated component wise. Because of the detailed information on the stack set up, a lot of parameters from the model can be used for the mass estimation. These are geometry and material parameters of the membrane, the GDL and the gas channels, the active cell area and the number of cells in series. The cell

layers are larger than the active area, because the stack needs to be sealed in order to avoid a gas leakage. The supplementary size of the layers is estimated by a preliminary screw design. Eight screws are considered to bear the force from the operating pressure and the squeezing of the cells. The screw diameter is estimated with a table from [150] and the active membrane area is extended by this diameter to each side. At the ends of the cell stack, two plates are placed to distribute the force of the screws over the cell area. The thickness of the boards is assumed to be equal to the screw diameter. Figure 2.23 shows the structure of the fuel cell stack.
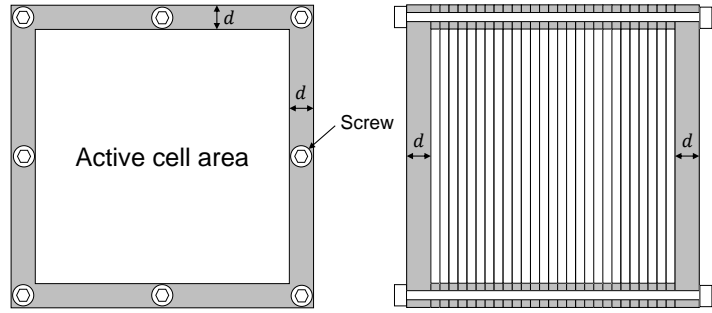
Figure 2.23: Fuel cell stack assembly

The desity of the Nafion N117 membrane is calculated to 1967 $\frac{kg}{m^3}$ from a data sheet from DuPont[151] and the density of the gas diffusion layer is assumed to be 350 $\frac{kg}{m^3}$ which is an average value of the AvCarb series from Fuel Cells Etc [152]. The material of the plates and the gas channels is assumed to be an aluminium alloy. The resulting density of the stack is between 1350 to 1600 $\frac{kg}{m^3}$, which corresponds well to empirical values. Figure 2.24 shows the stack and system densities of several fuel cells. The values from Nedstack, Nuvera and Power Cell are derived from the fuel cell stack without accessories and casing (white dots). Stack densities from 1300 to 1700 $\frac{kg}{m^3}$ with an average value of 1498 $\frac{kg}{m^3}$ have been identified. The lower density values of the other manufacturers (black dots) are evaluated on system level which includes all necessary components and the casing.
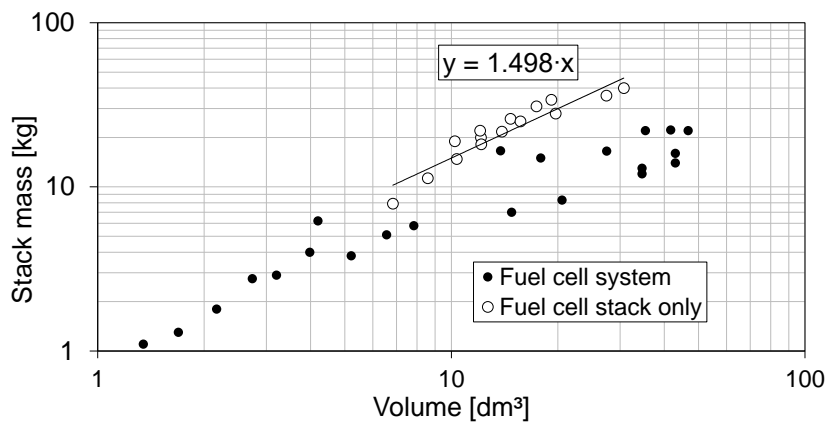
Figure 2.24: Fuel cell stack density

Kellogg presented a fuel cell propulsion system for a small UAV with a detailed mass breakdown of the system components [153]. This breakdown is used to evaluate the mass and the volume of the gas tanks, the high pressure and the low pressure valves. The volume of his reference tanks is calculated from the known gas mass, pressure and an assumed temperature of 288°K to 0.96 litres. The tank masses are then scaled with Barlow's formula and a fixed diameter-to-length ratio of 0.5. The valve data is assumed constant. The mass of oxygen and hydrogen is calculated according to the mission power requirements.

The model performance results have been compared to measurements from the work of Yan et al. [154]. With the given parameters from [149], the model gives good results for fuel cells that are operated at 1 atm (see Figure 2.25 left). The right part of the Figure shows results from a parametric study on the cell operating pressure. For higher operating pressures, the given exchange current density from Loo is invalid, because it depends on the gas concentration [144]. Hence, the exchange current density was scheduled against the operating pressure to meet the measurements from [154] (see Figure 2.25 right). The model performance prediction shows a good agreement to the measurements for low to medium current densities. At high current densities, when liquid water is present in the cell, the model over estimates the cell voltage. The deviation is not critical for the model accuracy, as the maximum output power of the cell is reached at lower current densities and the cell is not operated at these conditions.
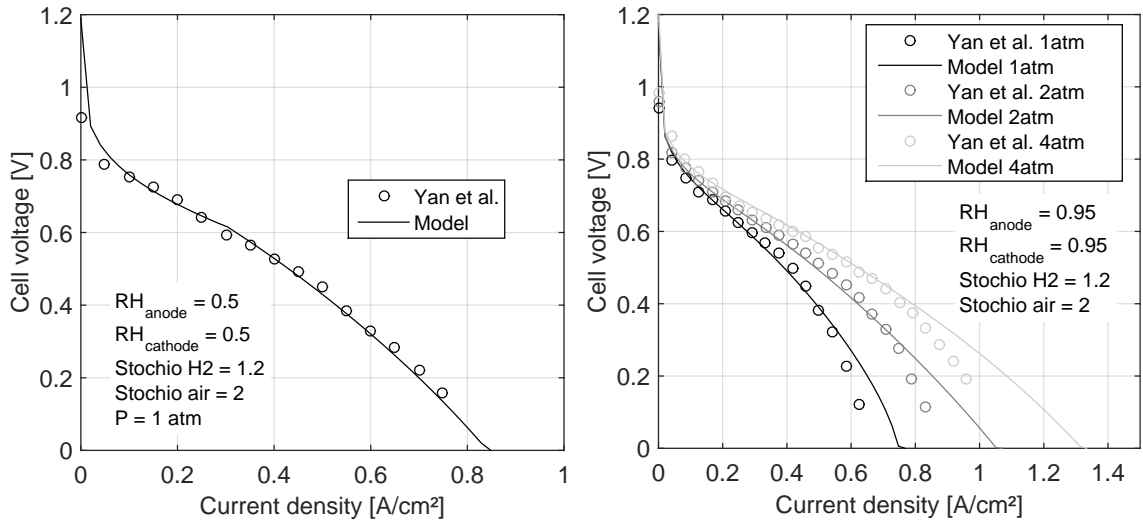
Figure 2.25: Fuel cell performance validation

The error of discretisation is negligible at steady state calculation because the concentration profile is directly calculated from the diffusion equations. However, the number of discrete elements is important for transient simulation. The simulation time step and the number of discrete elements are adjusted according to [149] and to ensure numerical stability of the simulation. For the utilized membrane and GDL thickness, a maximum time step of 20 μs is applied.

For transient simulations, the valves, that control the gas flow into and out of the fuel cell, require a controller. Therefore, a PI controller with a lookup table is implemented, which controls the gas flow through the fuel cell. The fuel cell is equipped with a cut off mechanism, which opens the electric circuit whenever the cell voltage drops below 0.1 V in order to avoid

a cell break down during fast load changes. This removes the current load and the fuel cell can recover. As soon as the cell voltage exceeds 0.1 V, the fuel cell is reconnected again.

2.7 Battery Pack

Similar to fuel cells, batteries transform chemical energy to electric energy. The major difference between both is that fuel cells have to be supplied continuously with fuel, whereas batteries store energy within the cell and there is no material exchange with the environment. Batteries consists of two electrodes that are segregated by a separator which is immersed with an electrolyte. The difference of the electrochemical potential between the two electrodes creates a voltage potential. The electrolyte is an electric isolator and prevents a short circuit between both electrodes. However, it is permeable for ions that are solute in the electrolyte. When the cell is discharged, the anode material is oxidised by emitting electrons. The oxidised ions dissolve in the electrolyte and travel through the separator to the cathode. The cathode material is reduced by absorbing electrons and the dissolved ions from the anode side [155]. For primary batteries, this process is irreversible, which means that the battery must be replaced after discharge. The electrode materials of secondary batteries are chosen to enable recharging of the cell. Modern secondary batteries are not based on chemical reactions but on intercalation of metal ions in complex salts, which results in a change of the electrochemical potential.

Batteries are available in many different shapes and sizes. Most cells have a button, a cylindrical or a coffee bag shape. For low power devices, a few cylindrical or button shaped cells are directly plugged into designated notches in the device. For high power devices, many battery cells are combined to form a battery pack. This pack consists of a casing, a cooling system to remove the heat from the cells and a battery controller, which controls the status of the individual cells and balances them during charge and discharge. In these packs, multiple cells are connected in series to cell strings, which define the voltage of the battery pack. Multiple strings are then connected in parallel, which increases the capacity of the battery pack. The additional weight of the pack casing, the cooling system and the battery controller have to be accounted in battery pack design. Therefore, the resulting energy and power density of the battery pack is lower than for the cell.

There are many types of secondary batteries available. The most favourable battery types for mobile applications are lithium based batteries, because of their high power and energy density. The anode of those batteries mostly consists of graphite. The cathode is made of complex lithium salts that define and limit the energy and the voltage of the cell. Today's lithium-ion batteries reach a mass specific capacity of 250 $\frac{Wh}{kg}$ for high energy cells and a mass specific power of up to 2 $\frac{kW}{kg}$ for high power cells [156–161]. The next generation of lithium based batteries utilise sulphur as a cathode material. These cells are considered to reach a specific energy of 420 $\frac{Wh}{kg}$ on cell level in 2020, however, today, they suffer from low cycle numbers and high prices [162].

The performance modelling of battery cells is similar to fuel cells. Both systems are characterized by diffusion processes through a separator or a membrane and through electrodes. The difference is the way the diffusing particles are supplied to the cell. Whereas the fuel cell is continuously supplied with fuel, the lithium ions are intercalated in the electrode material and there is no external supply [155]. As the cell voltage depends on the amount and the repartition of lithium ions within both electrodes, the battery cell has no steady state operat-

ing behaviour. When a battery cell has been under heavy load and is suddenly disconnected, the lithium concentration in the electrolyte will equalise within in the battery and the cell voltage recovers to a certain level. To correctly capture this effect, the diffusion processes have to be considered in the model, which requires a lot of computational effort [163]. When the cell is only lightly loaded, this effect can be linearised, as the diffusion process of the ions is significantly faster than the current induced movement [164]. In this case, the cell performance can be accurately modelled with an equivalent circuit.

The equivalent circuit of a battery cell model consists of multiple elements. The open circuit voltage is represented by a DC voltage source, U_{OC}, which is correlated to the State Of Charge (SOC) of the cell. A series resistance, R_{series}, represents the ohmic resistance of the cell. To capture short term and long term transient effects from ion diffusion, an arbitrary number of RC members can be added to the circuit. The equivalent circuit in Figure 2.26 was proposed by Chen to model the performance of a lithium-ion secondary battery [165]. Chen proposes two RC members 's' and 'l', which refer to the short term and long term dynamics respectively.
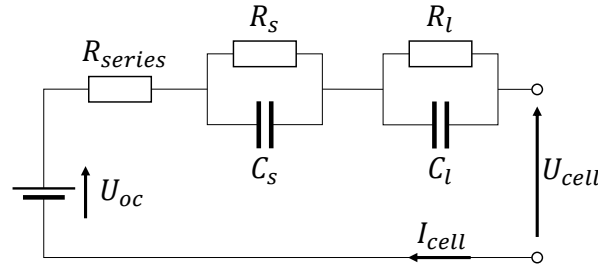
Figure 2.26: Equivalent circuit of the battery model

Chen presents correlations of the equivalent circuit parameters against the cell SOC, which he identified from measurements of the PL-383562 lithium-ion cell, which is produced by AA Portable Power Corp. [166]. The PL-383562 is a high energy cell, which has a standard AA cylindrical shape. The energy and power densities on cell level are listed in Table 2.5 and taken from the battery specification sheet [166].

Mass specific energy	175	Wh/kg
Volume specific energy	433	Wh/dm^3
Mass specific power	350	W/kg
Volume specific power	715	W/dm^3
Max. cont. C-rate	2	1/h
Cut off voltage	2.75	V

Table 2.5: Parameters of the AA PL-383562 Li-Ion cell

With the model of Chen, a discharge chart can be derived for the battery cell, which is shown in Figure 2.27. The abscissa shows the SOC and the ordinate shows the cell voltage. The contour plot represents the load current, expressed in the C-rate. The C-rate is a normalisation of the discharge current with a constant current level, that completely discharges the battery within one hour. The displayed cell voltage corresponds to a quasi steady state operation and

does not consider the dynamic effects of the cell. As a result of the constant inner resistance, the contour lines are spaced equally. However, this assumption is only valid for low discharge current levels. When the diffusion processes were considered, the cell voltage would drop more significantly for higher C-rates. The chart shows that the cell voltage decreases with lower SOC levels and drops considerably below 10% SOC. Hence, 10% is considered as the minimum SOC limit. The dashed line at the bottom represents the cut off voltage, which is a protection mechanism that is similar to the fuel cell. As the cell voltage falls below this value, the controller cuts off the cell in order to avoid a hazardous failure of the cell.
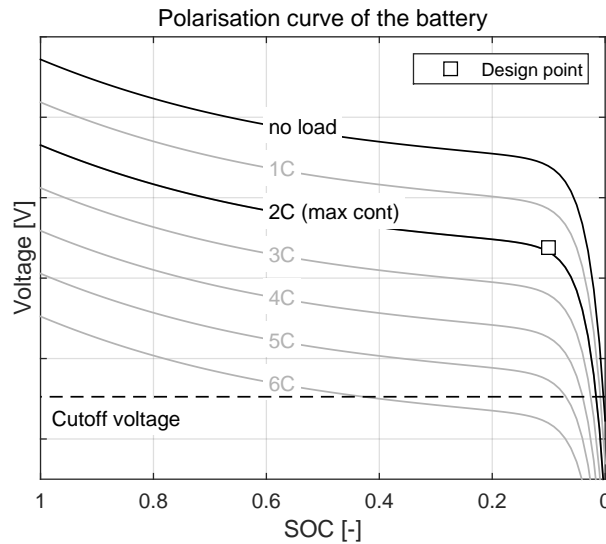
Figure 2.27: Battery performance chart

Figure 2.27 shows that the cell can support higher C-rates at higher SOC. At the minimum SOC of 10%, the cell supports a maximum discharge current of roughly 5C. The thick 2C-line represents the maximum continuous discharge current, that the cell can support. When this current level is exceeded over long periods, the life time and capacity of the cell are affected.

The design of a battery pack requires the stored energy, the maximum continuous power and the voltage level. As the cell performance is affected by the SOC level, the cell is designed to meet the power requirements at the minimum SOC level of 10%. Thus, the number of cells in series is derived from the pack voltage and the cell voltage at 10% SOC. The number of cells in parallel is either calculated by the pack power and the maximum continuous C-rate or by the stored energy. The criterion which results in the higher number of parallel cells is relevant. The total number of cells gives the mass and the volume of the battery pack. To consider the auxiliary components of the battery pack, a constant factor of 0.75 is multiplied with the cell level energy density. A similar modelling approach has been followed by Schömann [47].

By assuming that all cells in the pack are perfectly balanced and that they have the same temperature and identical characteristics, the transient behaviour of the pack can be estimated by the transient behaviour of a single cell. The cell current is calculated by dividing the pack current by the number of cells in parallel. The cell voltage is then multiplied with the number of cells in series to calculate the pack voltage level. For transient simulation,

the battery pack does not require an additional controller. Only the cut off mechanism is implemented.

2.8 Supercapacitor Pack

A supercapacitor is an energy storage device that consists of three main layers. Two porous electrodes enfold an organic separator with a salt dilution. The electric energy is stored in an electrostatic double-layer and an electrochemical red-ox reaction. The separator is very thin to minimise the distance between the two electrodes, which maximises capacity. Moreover, the thin design allows for a large contact area, which is beneficial for the capacity as well. Most supercapacitor cells have a cylindrical shape, which is filled with the rolled sandwich electrodes. However, cubic shapes are available as well. Similar to batteries, multiple cells are combined to form supercapacitor packs. The cells are connected in series to form supercapacitor strings. The supercapacitor pack is assembled from multiple strings to provide the required capacity.

Compared to batteries, the supercapacitor can store much less energy per volume and per mass. However, the peak power level per mass and volume is superior to the one of the battery. Hence, supercapacitors are the favourite device when a lot of power has to be supplied for a short time period. Compared to a battery, the cycle time is much higher [167, 168]. Supercapacitors achieve power densities of 18 kW/kg for short time and up to 10 Wh/kg for low power operation. The capacity of a single supercapacitor module can reach 6500 F. With a typical cell voltage of 2.5 Volts, this corresponds to an energy of roughly 20 kJ. For the design of a supercapacitor pack, the voltage level and energy requirements are required. With the rated voltage of a single cell, the number of capacitors connected in series is calculated. With the required pack energy and the capacity of each cell, the number of parallel connected strings is calculated. The capacity of one cell is assumed to be limited to 6500 F.

Similar to batteries, equivalent circuits can be utilised to model the performance of supercapacitors. As the diffusion kinetics are very fast, there is no significant non-linear effect at high discharge rates. The equivalent circuit in Figure 2.28 has been proposed by [169, 170]. It consists of multiple RC members, which are connected in parallel and a supplementary resistance at the right. The first RC member on the left contains the inner resistance of the supercapacitor, R_i, and a non-linear capacity, C_i, to model the discharge behaviour. The capacity C_i is split into a constant part C_{i0} and a voltage dependant part C_{i1}. The two RC members on the right with the index 'd' and 'l', model the short term and long term voltage response of the supercapacitor cell. The resistance R_{lea} is a high ohm resistance to model the self discharge of the cell.

The parameters of the equivalent circuit have been identified from measurements of two supercapacitors in [170]. The share of the voltage dependant capacity, C_{i1}, of the entire capacity C_i is 0.40 and 0.41. This share is assumed constant at 0.4 for the supercapacitor model. The RC members (d and l) artificially modify the transient behaviour of the cell. The according values of scaled supercapacitors are defined to match the same transient characteristics as identified in [170]. As the supercapacitor is utilised for short time simulations, the resistor R_{lea}, which simulates the self-discharge, can be omitted. An investigation on the simulation time has shown, that the impact of the resistance can be neglected for simulations with a duration less than 1 minute.
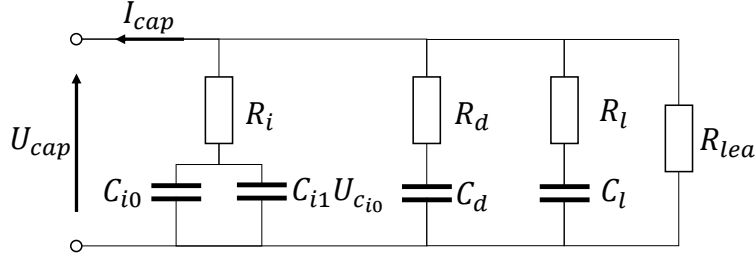
Figure 2.28: Equivalent circuit of the supercapacitor model

Similar to the DC-Link capacitors for the DC-DC converter, the ESR, R_{ESR}, the mass and the volume are correlated from empiric data. For these correlations, the supercapacitors from the WIMA SuperCap series [171], the Maxwell K2 series [172], the VinaTech supercapacitors [173], the CapComp Ultracapacitors [174], the Epcos UltraCap series [175], the Ultracapacitors from Cornell Dubilier Electronics [176] and the Nichicon JD series [177] are considered. The according data of all supercapacitors is shown in Figure 2.29 as well as the derived correlations.
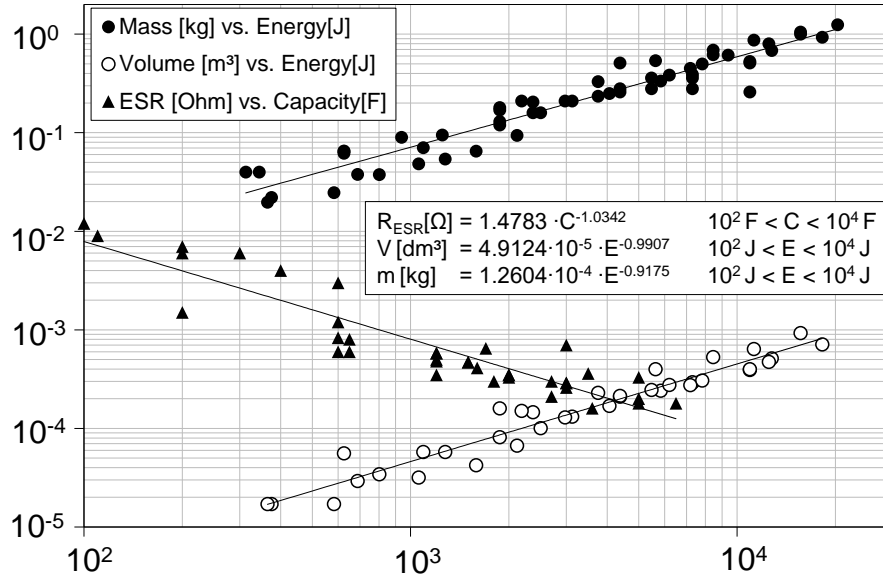
Figure 2.29: Mass, volume and ESR correlation for supercapacitors

The derived correlations for the ESR, the volume and the mass of supercapacitors is given by Equations (2.58) to (2.60).

$$R_{\mathrm{ESR}}[\Omega] = 1.4783 \cdot C^{-1.0342} \qquad 100F < C < 6500F \qquad R^2 = 0.84 \qquad (2.58)$$

$$V[\mathrm{dm}^3] = 4.9124 \cdot 10^{-5} \cdot E^{-0.9907} \qquad 300J < E < 20kJ \qquad R^2 = 0.94 \qquad (2.59)$$

$$m[\mathrm{kg}] = 1.2604 \cdot 10^{-4} \cdot E^{-0.9175} \qquad 300J < E < 20kJ \qquad R^2 = 0.92 \qquad (2.60)$$

The performance of the supercapacitor stack is calculated similar to battery packs. A perfect balancing is assumed for all cells, which allows to calculate the cell current by dividing the pack current by the number of strings. The pack voltage is calculated by multiplying the cell voltage with the number of cells in series. In contrast to the fuel cell and the battery, there is no cut off mechanism required. Furthermore, no controller is required for transient simulations.

2.9 Propulsion system design and offdesign calculation

For propulsion system design, all relevant operating points and the according environmental conditions must be available. The system design starts with the propeller and is executed stepwise in opposition to the power flow up to the energy carrier. The propeller is designed for a set of arbitrary design parameter values and the resulting performance during all operating points is calculated. Afterwards, the gearbox is designed according to the relevant mechanical power requirements of the propeller. Therefore, additional design parameters are required, i.e. the gear ratio. Afterwards, the gearbox performance during all operating points is calculated for the next component. In that way, all involved components are sized step by step. When the aircraft has multiple propellers, the electric power of all motor controllers must be summed up to size the energy subsystems. A design optimisation can be conducted by adjusting all design parameters of the involved components in order to maximise or minimise the respective optimisation target.

The steady state performance of the propulsion system is calculated in the same way as for the component design. The calculation starts with the propeller and is executed stepwise in opposition to the power flow up to the energy carrier. In that way, the power flow through all involved components is calculated, which is required to attain a certain thrust level. During a transient manoeuvre, the system reacts to a changing command signal, which tells the system to operate in a different state. The command signal is computed by the flight controller, which calculate new command signals for each motor controller. These controllers adjust the motor current according to the command signal and the propulsion system components react to this change. Thus, the way of calculation is inverted for the propulsor subsystem models. For example, for steady state calculation, the thrust level is the input for the propeller model and the mechanic power is the output. For transient simulation, the mechanic power is the input and the thrust level is the model output. Thus, to initialise a transient simulation, a steady state starting point is required. This starting point is calculated using a steady state model in Matlab [178]. With the resulting steady state performance parameters, a second component model is initialised, which has been implemented in Simulink to perform the transient simulation.

The command signal which is passed to the propulsion system is passed through multiple controller loops. The outer controller loop is the flight controller, which calculates thrust commands for each propulsor subsystem from the geometrical distribution within the aircraft. The next loop is the motor controller which receives the command from the flight controller and adjusts the propeller thrust accordingly, by accelerating the propeller or adjusting the blade pitch angle. Like this, the original command is computed in multiple cascaded controller loops, which command the power flow in the propulsion system and thereby move the system to its new state.

3 Thrust response of the motor-rotor system

The scope of this chapter is to investigate the impact of the propeller design parameters on the thrust response of the isolated motor-rotor subsystem. The relevant output of the motor-rotor system is its propulsive power and, when a constant free stream velocity is assumed, the thrust level. The thrust response is most interesting for quadcopter vehicles, because they use differential thrust for attitude control. To ensure controllability or even an agile manoeuvrability of the vehicle, a fast thrust response is essential.

The thrust response is assessed with the rise time metric, which is common metric to describe the transient system response of arbitrary processes. It is defined in the following way: the rise time metric is the required time for the system response to rise from 10 to 90% of the steady-state difference during a step command. The rise time unit is seconds. The rise time definition is represented for an arbitrary process in Figure 3.1.
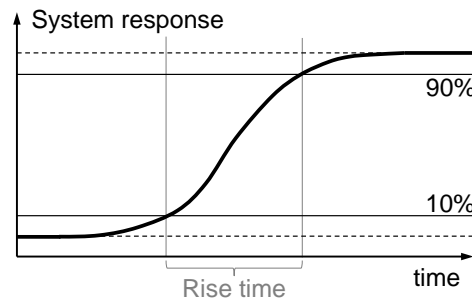
Figure 3.1: Rise time definition

In the following study, two different motor-rotor configurations are investigated. The first configuration consists of a fixed pitch propeller with an electric motor. As the propeller is fixed, the only way to change the thrust level is to change the rotational speed of the system. Thus, the thrust level is directly related to the rotational speed of the system. The second configuration consists of a variable pitch propeller and an electric motor. This system has a supplementary degree of freedom to change the thrust level, which is the variable blade pitch angle. Therefore, the thrust level is no more related only to the rotational speed. In a first approach, both configurations are examined without any supplementary shafts or gear stages. In chapter 3.4, the impact of a gearbox on the system thrust response is investigated. In order to reflect the flight conditions of quadcopters, two transient manoeuvres at levelled hover flight are utilised to assess the thrust response of the two motor-rotor subsystems. In a first manoeuvre, the system is accelerated from part power operation to full power, where the term full power refers to the maximum continuous thrust level. In a second manoeuvre, the system is accelerated from full power to a short time peak power.

For simplicity, the propeller and the motor are designed for a given thrust level at sea level ISA condition [92] according to chapter 2.4. Further on, this design point represents the full

power or maximum continuous thrust level and is later referred to as the rated point. The design parameters of the propeller are:

- the tip speed, v_{tip}

- the free stream velocity or Mach number, v/Ma

- the operating altitude

- the thrust level, F_t

- the blade number, N_{blades}

- the blade loading, f_{load}

The definition of the blade loading is derived from the propeller thrust loading, which represents the thrust per propeller area. The blade loading is defined as the thrust per propeller area and blade number and is a metric which correlates well with the blade shape. The propeller diameter is calculated from the blade loading, the blade number and the thrust level. As a reference design, the design parameters from Table 3.1 are utilised. The Motor torque factor (MTF) of 2 matches the assumption from NASA, which is based on their experience with electric motor systems [64].

f_{load}	Ma	altitude	v_{tip}	F	ρ	MTF
$N/m^2/N_{blades}$	-	-	m/s	N	kg/m^3	-
200	0.08	0	200	400	2000	2

Table 3.1: Reference propeller design parameters

Within the next three chapters, the sensitivities of the performance and the thrust response on the propeller design parameters are examined for both motor-rotor subsystems and both manoeuvres. The purpose of this study is to give a first idea of the rise time magnitude and to identify the basic impact of the design parameters on the thrust response.

3.1 Motor-rotor design

Within this chapter, the design and the steady state performance of the motor-rotor subsystem is discussed, with respect to relevant design parameters of the propeller. This study is introduced to verify the propeller model against well-known trends and correlations as well as to enable trade-off studies between the performance and the thrust response of the system.

Figures 3.2 and 3.3 show the results of a parametric study in the form of a matrix plot of partial dependencies. The propeller design parameters are plotted on the columns and marked at the bottom of the matrix. The output parameters are plotted on the rows and marked on the left side of the matrix. Thus, each plot gives the sensitivity of one design parameter on one output parameter of the system. All remaining design parameters are utilised according to the reference values in Table 3.1. Moreover, each plot contains the results and sensitivities of two blade, four blade and six blade propellers.

The design Mach number is translated to the resulting propeller pitch, which gives the axial distance that the blade tip travels through a non-slip air flow during one rotation. The
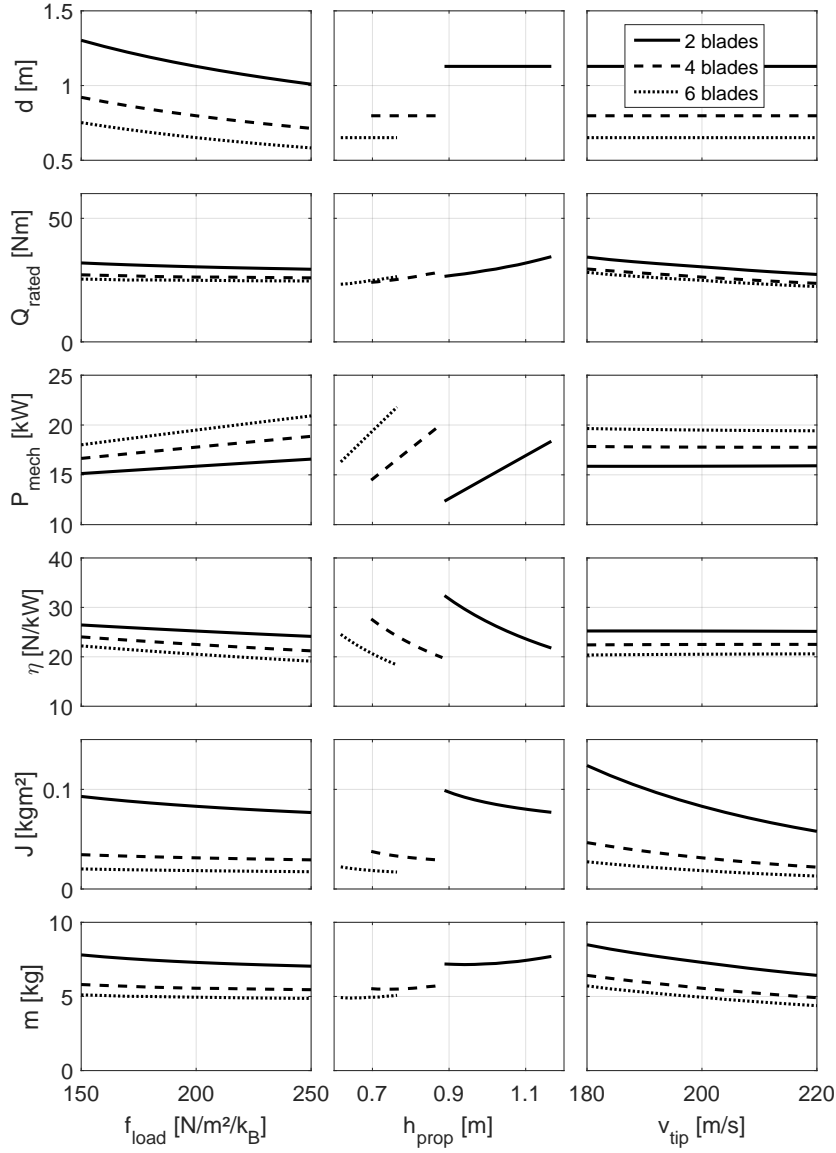
Figure 3.2: Propeller performance and geometry sensitivity on design parameters(1)

propeller pitch correlates with the blade angle and it is a function of the thrust level and the Mach number. The transformation provides a more tangible metric of the propeller shape.

The first row of the matrix plot in Figure 3.2 shows the relation between the propeller diameter and the blade loading. The diameter increases with lower blade loadings and vice versa. Moreover, the diameter of two blade propellers is larger than for four blade and six blade propeller, as the diameter is calculated with the blade loading, the blade number and the thrust level, according to Equation (3.1).

$$d_{\mathrm{prop}} = \sqrt{\frac{4 \cdot F_t}{\pi \cdot f_{\mathrm{load}} \cdot N_{\mathrm{blades}}}} \tag{3.1}$$

As the free stream velocity is zero during hover, the conventional efficiency definition is zero as well. Another figure of merit, which gives the amount of thrust per power, is adopted
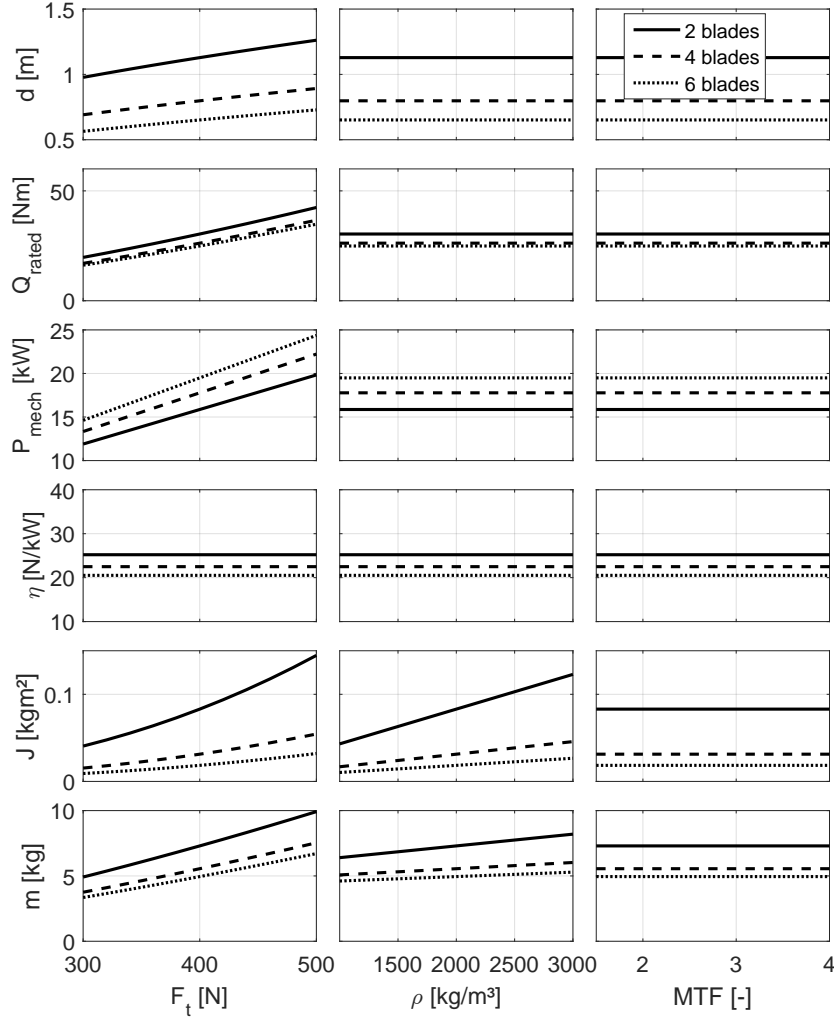
Figure 3.3: Propeller performance and geometry sensitivity on design parameters(2)

from [90]. The simulation results show, that a lower blade loading increases the propeller efficiency and reduces the mechanic power. This relation is well known and can be easily shown with the axial momentum theory and Equation (2.1). Because of the smaller area, four blade and six blade propeller require more mechanic power than two blade propeller and show a lower efficiency. The middle column shows that increasing the pitch results in a higher mechanic power and a lower efficiency. A variation of the design Mach number (propeller pitch) correlates with the flow velocity around the blade elements. In order to maintain a constant thrust level, the blade surface can be reduced when the flow velocity is increased. This is given by the definition of the lift coefficient in Equation (3.2). As the propeller diameter is fixed, the resulting blade is more slender. During hover flight, the torque raises because of the increasing angle of attack and the higher drag coefficient (compare plot above for the torque). The right column plots show that the tip speed has no significant impact on the mechanic power and it is further assumed, that these two parameters are independent. This result depends on the utilised airfoil coefficient data set and the range of the investigated tip speed. Moreover, at high helical Mach numbers, supersonic effects will deteriorate the propeller performance and efficiency [90].

$$F_{\text{lift}} = C_l \cdot \frac{\rho v^2}{2} \cdot S \tag{3.2}$$

The sensitivity of the torque on the blade loading and the pitch can be derived from the previous discussion of the mechanic power results. The impact of the tip speed is significant, as it changes the rotational speed of the propeller, according to Equation (3.3). Hence, as the mechanic power is independent from the tip speed, a higher tip speed results in lower torque. The four blade and six blade propellers require a lower torque level compared to two blade propellers, as the diameter is smaller and the rotational speed is higher.

$$n_{\text{prop}} = \frac{60 \cdot v_{\text{tip}}}{\pi \cdot d_{\text{prop}}} = 30 \cdot v_{\text{tip}} \cdot \sqrt{\frac{f_{\text{load}} \cdot N_{\text{blades}}}{\pi \cdot F_t}} \tag{3.3}$$

The fifth row shows the system inertia, which is the sum of the propeller inertia and the rotor inertia of the electric motor. Calculations have shown, that the inertia of the rotor is between one and two orders of magnitude smaller than the propeller inertia. Therefore, the rotor inertia cannot be neglected in simulations, but the system inertia is mainly driven by the propeller. The left plot shows that higher blade loadings result in lower system inertias. Moreover, four blade and six blade propellers have a lower inertia than two blade propellers. Both trends result from the changing rotational speed, which has a major impact on the chord length and thus on the inertia. The same rationale explains the impact of the tip speed.

The lower row shows the sensitivity of the system mass on the propeller design parameters. Design calculations of the motor-rotor system have shown that the system mass is mainly driven by the electric motor. When no gear stage is utilised, the share of the electric motor mass is between 70 to 80% of the entire subsystem mass. As the motor torque is the relevant parameter for the motor size and mass, the system mass correlates very well with the rated torque of the propeller.

The left column in Figure 3.3 shows the impact of the thrust level. According to Equation (3.1), the diameter increases with the square root of the thrust level. The next two plots show that the required torque and the mechanic power increase with the thrust level, which is intuitive. For the four blade and six blade propellers, the same characteristics as in the previous study can be identified: the smaller propeller diameter results in a higher power and a lower torque. The next row shows that the thrust level has no impact on the efficiency at the rated point. This independence can be explained with the axial momentum theory and Equation (2.1), which says that, for a constant thrust per propeller area, the efficiency is constant too. The fifth plot shows that the system inertia increases significantly with higher design thrust levels. As the system inertia is mainly driven by the propeller size, this trend results from the increasing diameter. The lower plot shows that the system mass correlates well with the rated propeller torque.

The right column shows the sensitivity on the material density. The material density has no impact on the propeller aerodynamics and dimensions. Therefore, the diameter, the required torque, the mechanic power and the efficiency are independent of the material density. As the same material is assumed for the entire propeller, its mass and inertia grow linearly with the material density, which significantly affects the system inertia and shows a little impact on the system mass.

3.2 Fixed pitch propeller system

3.2.1 System setup and control

In this section, the thrust response of an isolated mechanic subsystem with a fixed pitch propeller is analysed. The propeller is directly driven by the electric motor, without considering additional shafts or gearboxes. The motor controller is supplied by an ideal voltage source, which delivers a constant DC voltage. The rotational speed of the system is controlled by a motor controller, which receives a speed command signal.

For the fixed pitch system, the rotational speed is the only degree of freedom to change the thrust level. Hence, a thrust change is realised by accelerating or decelerating the propeller. For acceleration, the motor must compensate the torque that results from the propeller aerodynamics and deliver a supplementary torque to increase the rotational speed, which is described by Equation (2.26). To accelerate up to the rated point, the motor provides a short time peak power capability, which is expressed by the MTF. The torque factor, multiplied with the design torque, represents the pull-out torque, which the motor can deliver for a short time interval (as defined in chapter 2.4).

Within the following two sections, the two transient manoeuvres are analysed. The first manoeuvre is a part load acceleration from 50 to 100% of the rated thrust and the second manoeuvre is an over power acceleration from 100 to 150% of the rated thrust. For each manoeuvre, the motor controller is fed with a step function speed command which corresponds to the respective thrust change.

3.2.2 Part power acceleration

During the part power acceleration, the system accelerates from 50 to 100% thrust. To better describe the manoeuvre, Figure 3.4 shows a plot of the relevant system parameters during the acceleration.
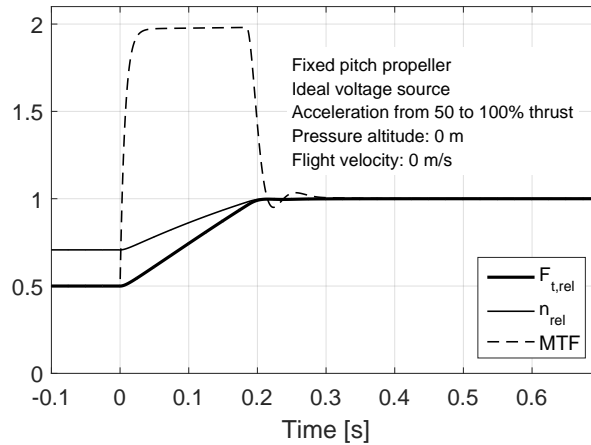
Figure 3.4: Part power acceleration for fixed pitch propellers

The abscissa shows the time axis. The simulation starts at -0.1 seconds in order to give the Simulink models a short time to find an equilibrium state, as the initial point is calculated

with the according Matlab models. At zero seconds, a step command with the new rotational speed is passed to the motor controller, which raises the current to increase the torque to the maximum torque factor. The response of this process takes a few tens of milliseconds and is thus barely visible in the figure. As the motor torque exceeds the propeller torque, the rotational speed and the thrust increase up to their rated values. In order to show all parameters in one figure, the speed and thrust values have been normalised with their design parameters. Similar to the previous chapter, the sensitivity of the thrust response on the propeller design parameters is investigated. The results are shown in Figures 3.5 and 3.6.
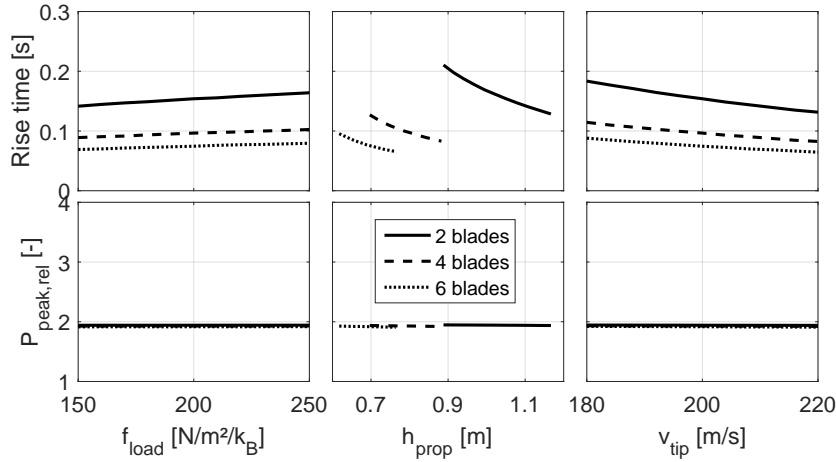
Figure 3.5: Parameter sensitivities for fixed pitch propellers during part power(1)

The upper row shows the rise time of the thrust response. The left plot shows that higher blade loadings results in higher rise times. In contrast to this, the system inertia shows an opposed characteristic and it would be intuitive to say that the reduction of inertia with the blade loading would also result in reduced rise times. The reason for the opposed trend is the power and torque characteristic of the propeller. Increasing the blade loading requires a lower torque and more power (see Figure 3.5). Therefore, the rated motor torque is reduced and the rated speed is increased. This penalty predominates the advantage of a lower system inertia. The middle plot shows that the rise time decreases with higher pitch values. Figure 3.5 shows that this trend is enabled by a reduced system inertia, a higher torque level and the constant rated speed. The right plot shows that the rise time is decreased with higher tip speed values. This trend results from the higher impact on the rotational speed according to Equation (3.3) and the significantly reduced system inertia.

The lower row shows the maximum mechanic power which is delivered by the electric motor. According to Figure 3.4, the maximum power is delivered at the end of the acceleration, when the motor still has a high torque and the rotational speed is close to the rated value. The peak power is utilised as an interface parameter in order to assess the t response time on system level in the next chapter.

Figure 3.6 shows that the thrust response slows down for higher thrust levels, which results from the considerably higher system inertia and the modest increased design torque. This is a quite interesting sensitivity, which is important for the scaling behaviour of small quad-copter vehicles. During a simple up scaling with the same matching points and design laws,
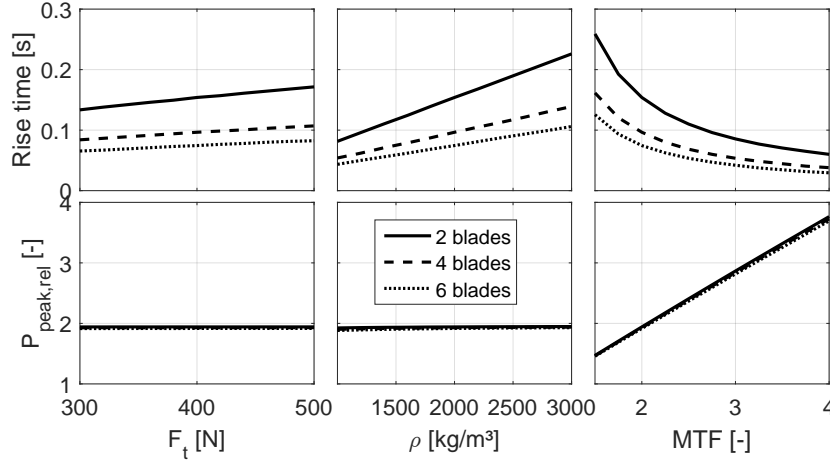
Figure 3.6: Parameter sensitivities for fixed pitch propellers during part power(2)

the thrust response of the motor-rotor system will get slower and might affect the vehicle manoeuvrability and controllability. This effect is further assessed on system and aircraft level later on in this work. As shown before, a change of the system inertia has a significant impact on the transient response of the system. The rise time increases linearly with the material density, which is the parameter that has the most significant impact on the system inertia. Thus, to accelerate the thrust response of a fixed pitch propeller, lighter materials shall be utilised. Of course, the light material must meet the mechanic requirements and provide a similar lifetime expectation. The right column shows that the MTF is directly coupled to the maximum motor power. When the MTF is reduced, less power is available for acceleration and the rise time increases significantly.

To summarise the results, some interesting trends are highlighted. Low blade loading values enable both, a high efficiency design and a fast thrust response. When the propeller size is not limited by aircraft design, the propeller size should be as large as possible to obtain a high efficiency and fast responding motor-rotor subsystem. When the maximum diameter for aircraft design is fixed, the pitch is a second parameter to influence the rise time results. However, the efficiency and the rise time results show conflictive trends. With lower pitch values, the efficiency is increased but the thrust response gets slower and vice versa. The tip speed is a third parameter, which impacts the thrust response but does not significantly affect the propeller efficiency. Finally, the thrust response is improved, when the system has a low inertia and a low kinetic energy.

3.2.3 Over power acceleration

This chapter investigates the over power manoeuvre, during which the system accelerates from 100 to 150% thrust. To describe the manoeuvre, Figure 3.7 shows a plot of the relevant system parameters during the over power acceleration.

For this manoeuvre, the system is initialised at its design point performance. At zero seconds, a step command with the new rotational speed is passed to the motor controller. The controller increases the motor torque to the maximum allowed MTF. As the motor starts to exceed its rated speed, it enters the field weakening operation, which is a constant power
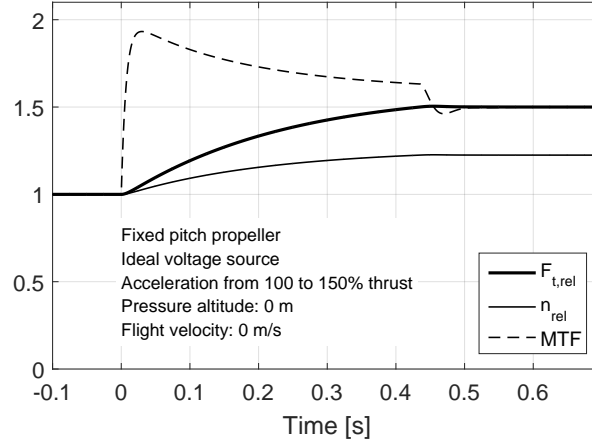
Figure 3.7: Over power acceleration for fixed pitch propellers

mode. Thus, by increasing the rotational speed, the available torque decreases. When the target speed is reached, the motor torque is reduced to the required propeller torque. When high thrust levels are required, the motor torque can be reduced so far that the propeller can not be further accelerated. At this point, the maximum peak thrust is achieved. In order to show all parameters in one figure, the speed and thrust values have been normalised with their design parameters.

In order to investigate the impact of the design parameters on the thrust response, a similar parametric study as for the part power acceleration is conducted. As the design of the propeller is not changed, the results for the propeller geometry and performance parameters is not repeated here. Thus, Figure 3.8 shows the impact of the blade loading, the pitch and the tip speed on the rise time metric and the relative peak power.
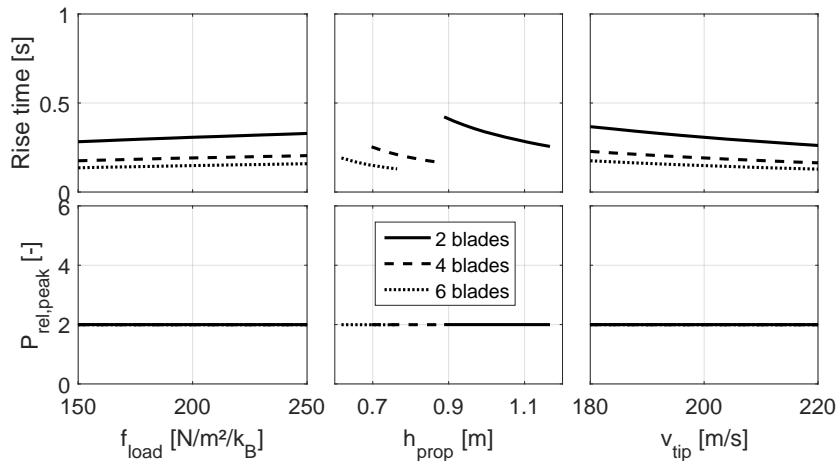
Figure 3.8: Parameter sensitivities for fixed pitch propellers during over power(1)

Figures 3.8 and 3.9 show the same sensitivity characteristics, which have been identified for the part power acceleration. Also the rationale for the resulting trends is the similar. The difference between the rise time results of both manoeuvres is the absolute value. Compared

to the part power acceleration, the over power manoeuvre is significantly slower. One reason for this is the reduction of the motor torque with increasing rotational speed due to the field weakening. This is illustrated by the motor peak power, which is limited to two by the MTF. The second reason is the increased aerodynamic torque of the propeller. Both points lead to a reduction of the torque difference and, thus, result into a slower thrust response and higher rise time. Figure 3.9 shows the rise time sensitivity on the thrust level, the material density and the maximum MTF.
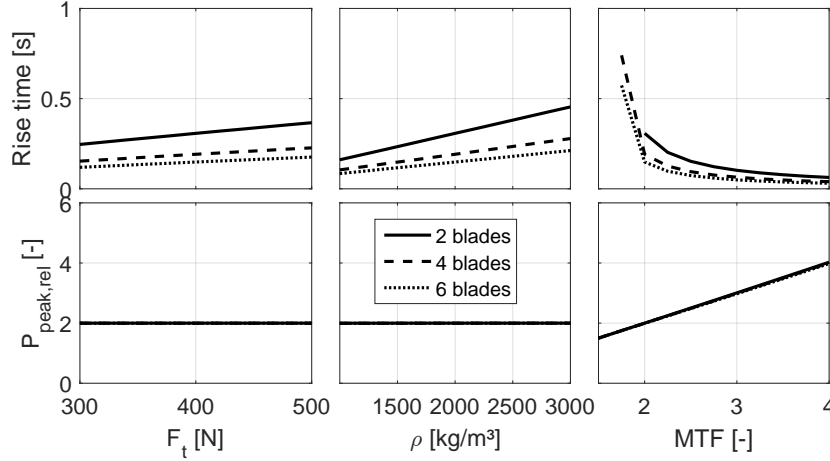
Figure 3.9: Parameter sensitivities for fixed pitch propellers during over power(2)

Similar to the part power manoeuvre, the rise time increases with higher thrust levels and higher material densities. The rationale for both trends is similar to the previous section. The sensitivity on the torque factor shows a vertical asymptotic characteristic, which represents the peak thrust limit. All propellers show excessive rise times for MTFs close to 1.8. With this torque factor, the motor can deliver the propeller torque for 150% thrust, but no more torque is available for further acceleration.

3.2.4 Rise time correlation

In this chapter, a correlation for the rise time of fixed pitch motor-rotor systems is derived, based on a semi analytical approach. Equation (2.26) shows the acceleration of arbitrary motor-rotor systems. As the rise time is a measure of the duration of an acceleration, it is assumed to be inversely proportional to Equation (2.26).

As the propeller torque depends on the rotational speed, the system shows a non linear behaviour. To remove the non linear behaviour, the propeller torque is replaced by its design value. Furthermore, to include the rise time for different part load changes, the $\delta\omega$ is replaced by the speed difference of the acceleration in RPM and the δt is replaced by the rise time t. The motor torque is replaced by the design torque times the MTF.

$$t \sim f \cdot \frac{J_{\text{prop}} \cdot \Delta n}{Q_{\text{prop,design}} \cdot (\text{MTF} - 1)} \tag{3.4}$$

The resulting equation is solved for the rise time and shown in Equation (3.4). This expression is a basic correlation which showed a good agreement to simulated rise time values for small

deviations from a calibrated design parameter set. To improve the correlation accuracy for larger deviations and to include supplementary design parameters, Equation (3.4) is extended with term so that all propeller design parameters are represented in the correlation. These additional parameters are the pitch, design tip speed and thrust level. The resulting Equation (3.5) gives the correlation of the rise time for the acceleration of a fixed pitch motor-rotor subsystem which has been designed according to the previously described design laws.

$$t = f \cdot \frac{J_{\text{prop}} \cdot \Delta n}{Q_{\text{prop,design}} \cdot (\text{MTF} - 1)^{0.7}} \cdot \frac{h_{\text{prop}}^{0.2} \cdot v_{\text{tip,design}}^{0.4}}{F^{0.1}} \qquad (3.5)$$

The correlation captures the impact of all design parameters, as well as the material density, for simulated propellers from 10 to 600 N thrust, a design tip speed from 160 to 220 m/s and a pitch-to-diameter ratio from 0.7 to 1.3. The coefficient of correlation R^2 is better than 0.998 for the given parameter range. The factor f is identified to be constant for a given blade number. It is calculated to 0.0088 for two blade, 0.0097 for four blade, and 0.0104 for six blade propellers.

3.3 Variable pitch propeller system

3.3.1 System setup and control

In this chapter, the thrust response of an isolated motor-rotor subsystem with variable pitch propellers is analysed. The propeller is directly connected to the electric motor, without considering additional shafts or gearboxes. Similar to the fixed pitch propeller, the motor controller is supplied by an ideal voltage source. Supplementary, a servo motor is added to the system, which controls the variable pitch angle of the propeller. Compared to the fixed pitch propeller, the design and matching is not changed.

The variable pitch system has two degrees of freedom to change the thrust level. Similar to the fixed pitch propeller, the thrust can de changed with the rotational speed of the propeller. Moreover, the variable pitch angle is the second degree of freedom to change the propeller thrust. Thus, the system uses two controllers: one motor controller to set a target rotational speed, and one servo controller to set a target pitch angle. Again, the motor provides a short time over power capability in order to counteract deviations of the rotational speed during the manoeuvre.

Most variable pitch propellers are operated at constant speed and the thrust is controlled only by the blade pitch angle. This simple control approach reduces the number of degrees of freedom to one, which makes it easier for pilots to control the thrust level. To maximise propeller efficiency, both parameters have to be adjusted [179]. For a quadcopter, this control strategy results in a power reduction of 1 to 4% compared to fixed speed operation [75]. However, the constant speed operation is assumed for this study. The speed command, which is passed to the motor controller, is the constant design speed. The thrust command for the servo is translated into a pitch angle command via a lookup table.

During dynamic load changes, the rotational speed of the propeller differs from its target value, which will lead to deviations of the propeller thrust, as the lookup table for the variable pitch angle is only valid for the design speed. To correct the lookup table for the rotational speed, a correction term is applied on the thrust command according to Equation

(3.6), which is derived from Equation (2.14). This correction implies, that the rotational speed of the motor is measurable and available for the servo controller.

$$F_{\text{corr}} = F \cdot \left(\frac{n_{\text{design}}}{n_{\text{prop}}} \right)^2 \tag{3.6}$$

The servo dynamics are adopted from measurements from Cutler [180]. He measured a rate limit of 630 $\frac{\text{deg}}{\text{sec}}$ under load and he assumed a delay which corresponds to one update interval of the servo motor at 333 Hz. Similar results are identified by Pretorius, who identified a rate limit of 600 $\frac{\text{deg}}{\text{sec}}$ [76]. Moreover the mechanic link to the propeller blade has a significant impact on the dynamic response. Depending on the relation of the lever arms of the servo and the blade, the angular displacement of the servo is translated to an angular displacement of the blade. This transmission can be used to reduce the torque load on the servo and to increase the blade positioning accuracy. The transfer function of a rigid body connection with different lever arms has a complex non linear behaviour. For sake of simplicity, a constant angular reduction ratio of 2 from the servo to the propeller blade is assumed, as this reflects the kinematic of the non linear system for small angle deflections. Hence, a servo rotation by ten degrees will result in a blade rotation of five degrees.

Similar to the fixed pitch propeller, the two acceleration manoeuvres from 50 to 100% and from 100 to 150% of design thrust are investigated. The servo controller is fed with a step function pitch angle command which corresponds to the respective thrust change. The motor controller is fed with a constant target speed, which corresponds to the design value.

Because the propeller design is not changed compared to the fixed pitch propeller, the sensitivities on the propeller output parameters do not change. Therefore, the investigation of these sensitivities is not repeated in this section. The impact of the supplementary pitching mechanics on the propeller hub design and the propeller mass and inertia is neglected in this study.

3.3.2 Part power acceleration

In this section, the mechanisms of the part power acceleration are further described. For a better understanding, Figure 3.10 shows a plot of the relevant system parameters during the acceleration. The right ordinate shows the delta pitch angle, which represents the angular deviation of each blade from the design point geometry.

The simulation is initialised at design speed and a pitch angle which corresponds to 50% of the rated thrust. Then, the step command is passed to the servo, which begins to increase the pitch angle and the propeller thrust. At the same time, the propeller torque increases, which results in a reduction of the rotational speed. The motor controller increases the motor torque to compensate the higher aerodynamic torque and to re-accelerate the propeller up to its target speed. To show all parameters in one figure, the speed and thrust values have been normalised with their design parameters and the blade pitch angle is shown on the right ordinate.

According to Figure 3.10, the blade pitch shows an overshoot during the acceleration. This is the impact of the speed correction, which compensates the abating rotational speed. The deviation of the rotational speed is generally very low, which enables the motor to quickly
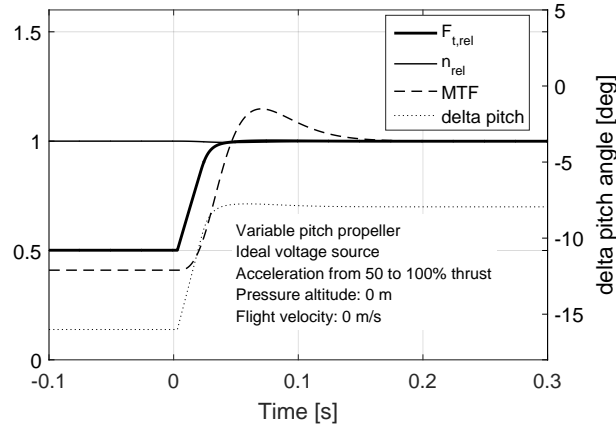
Figure 3.10: Part power acceleration for variable pitch propellers

re-accelerate the propeller. Thus, the required torque factor is very low, compared to the fixed pitch propeller.

The lookup table for the relation between the blade pitch angle and the propeller thrust shows a similar characteristic as the airfoil lift coefficient, which is quite intuitive, as the blade pitch angle changes the angle of attack of all blade elements. The relation shows a linear behaviour up to a region of high pitch angles, where the propeller blade begins to stall and a maximum thrust level is attained. As the design point of the propeller is located at the best lift-to-drag ratio, which is located at low angles of attack, the lookup table shows an almost linear relation for the part power acceleration.

Figure 3.11 shows the impact of the blade loading, the pitch and the tip speed on the various output parameters. The first parameter is the difference in the variable pitch angle, which the blade has to be adjusted in order to change the thrust level. The second and third parameters are the rise time and the maximum required torque factor during the manoeuvre.

The left plot shows that higher blade loadings result in a higher differences of the variable pitch angle. The main reason for this is the slightly non linear characteristic of the airfoil coefficient. As the blade loading has an impact on the rotational speed, it also has an impact on the propeller pitch. Together with the pitch, the angle of attack and, thus, the lift coefficient of both operating points is changed. With a perfectly linear relation between the angle of attack and the lift coefficient, the resulting difference of the pitch angle is constant. Moreover, during hover, the propeller operates closer to the stall region of the airfoil than during design operation. Both points also explain the deviation of the pitch angle difference with the propeller pitch and the tip speed.

The second row shows the dependency of the rise time to the three design parameters. The resulting curves show a discrete characteristic, which results from the simulation time step of 500 μs. A reduction of the simulation time step resulted in smoother curves, however, the calculation effort increased considerably. The 500 μs time step has been chosen as a compromise between simulation accuracy and calculation effort. As the thrust response depends only on the dynamics of the servo motor, the trends of the rise time directly depend on the pitch angle difference. In general, the results show a rise time between 22 and 26 ms, which
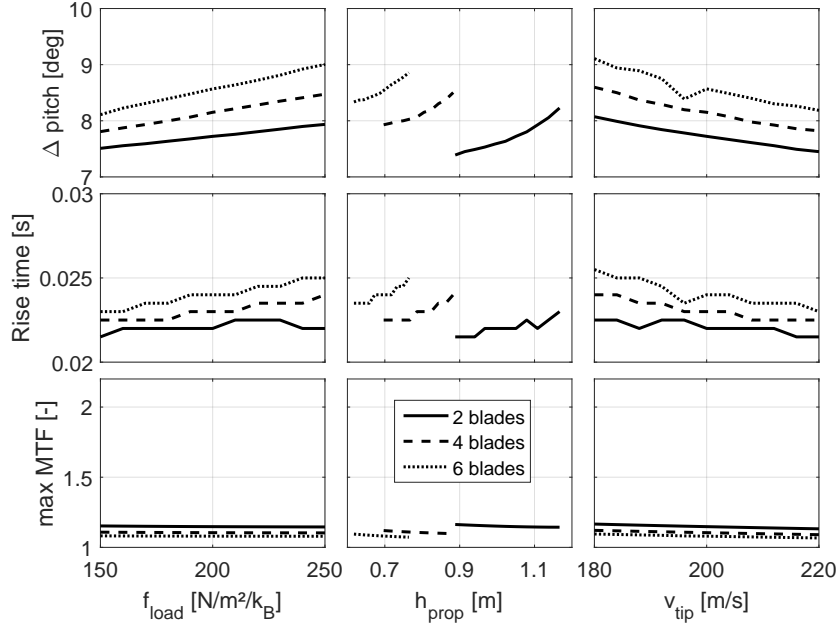
Figure 3.11: Parameter sensitivities for variable pitch propellers during part power(1)

is significantly faster than the fixed pitch propeller.

The required torque factor depends on the motor control parameters, the speed error, the rated motor torque and the system inertia. The simulation results show, that higher blade loadings results in a higher maximum torque factor. This trend results from the reduction of the rated motor torque and the modest reduction of the system inertia, which has been identified earlier in the previous chapter. The same rationale explains the behaviour of the maximum torque factor on a pitch variation. A higher pitch requires a high torque motor and, hence, the resulting torque factor is reduced. The increase of the tip speed shows a reduction of the rated motor torque and a considerable reduction of the system inertia. The combination of both trends lead to a reduction of the torque factor with increasing tip speed. It is remarkable that the required torque factor does not exceed a value of 1.2, which significantly reduces the requirements on the electric motor design. Figure 3.12 shows the dependency of the thrust response on the thrust level, the material density and the MTF.

The left column shows that the rise time is independent from the thrust level. However, the thrust level influences the system inertia and, thereby, the required torque factor. As higher thrust level result in elevated system inertia, the kinetic energy is increased. Thus, to re-accelerate the propeller with a higher system inertia, a higher torque factor is required. Similar to the thrust level, the material density does not impact the pitch angle difference or the rise time. Finally, all output parameters are independent of the allowed torque factor, because the part power acceleration does not require values higher than 1.2.

3.3.3 Over power acceleration

In this section, the over power acceleration is investigated. Similar to the part power manoeuvre, Figure 3.13 shows a plot of the relevant system parameters during the acceleration.
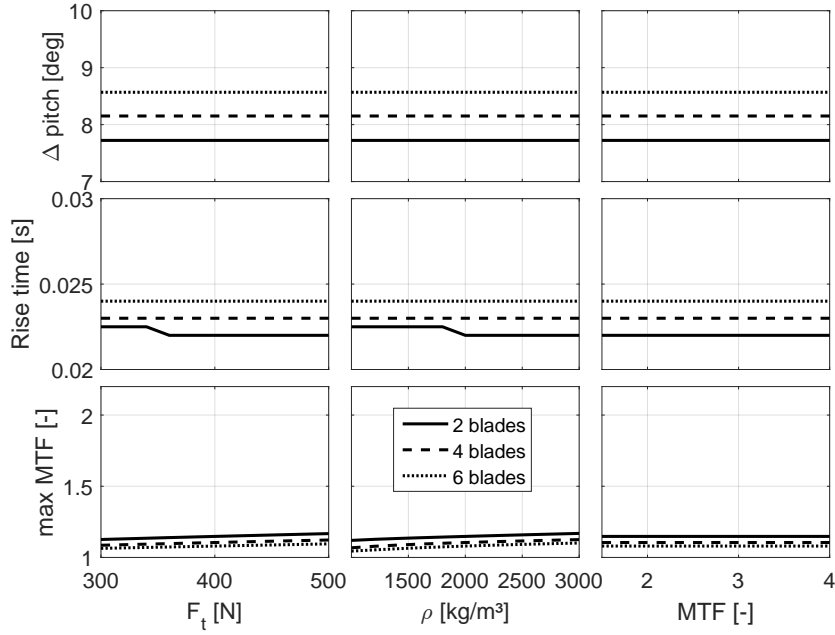
Figure 3.12: Parameter sensitivities for variable pitch propellers during part power(2)
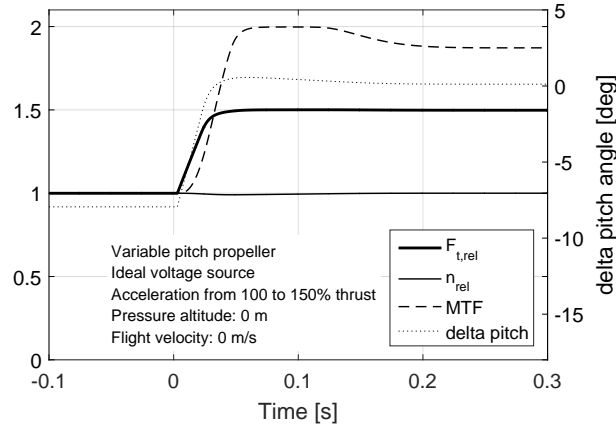
Figure 3.13: Over power acceleration for variable pitch propellers

The system is initialised at design speed and a pitch angle which corresponds to the rated thrust level. At zero seconds, a step command is passed to the servo, which adapts the pitch angle accordingly. The resulting higher propeller torque reduces the rotational speed of the system and the motor controller increases the motor torque to re-accelerate the propeller. Again, the speed and thrust values have been normalised with their design parameters and the blade pitch angle is shown on the right ordinate.

The blade pitch shows the overshoot, which originates from the speed correction. The deviation of the rotational speed is again very low. Compared to the part power acceleration, the aerodynamic torque of the propeller is significantly higher which requires a higher MTF and the acceleration of the propeller requires more time. The matrix plot in Figure 3.14 shows

the dependency of the rise time and the maximum MTF on the blade loading, the pitch and the tip speed.
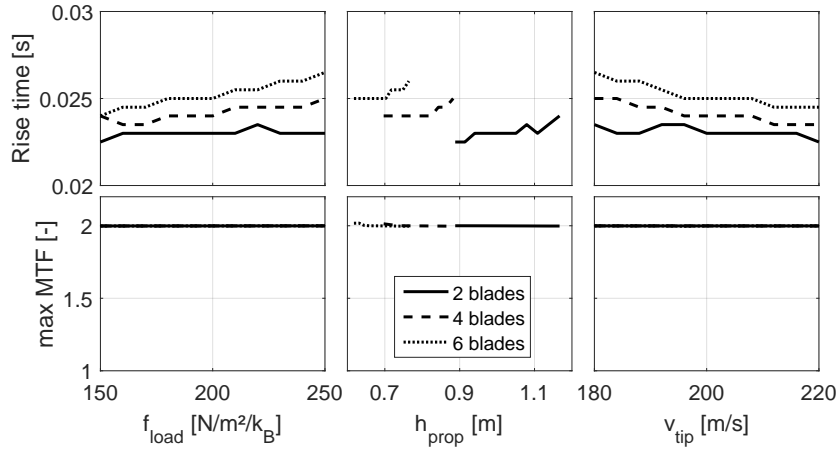
Figure 3.14: Parameter sensitivities for variable pitch propellers during over power(1)

The figure shows that all propeller designs reach the maximum MTF of two during the acceleration. The rise time characteristics are similar to the part power acceleration. Because of a slightly higher abatement of the rotational speed and the therefore increased overshoot of the variable pitch command, the rise time values are slightly higher.

To deliver a higher propulsive power, a variable propeller requires more torque than a fixed pitch propeller, as the variable propeller is operated at a constant speed, whereas the fixed pitch propeller is accelerated. When the peak thrust level is exceeded, the motor can no longer deliver the propeller torque and the system decelerates. In this case, the speed correction further increases the pitch angle, in order to maintain the required thrust, which further increases the propeller torque. In this way, the system gets unstable and the propeller decelerates to a very low rotational speed. Simulations have shown, that this thrust level is beyond 150% of the rated thrust.

Again, the rise time results show a similar characteristic to the part power acceleration and the main difference remains the slightly higher values. Moreover, the simulations have shown, that higher thrust levels and higher material densities increase the system inertia. This increases the kinetic energy and reduces the abatement of the rotational speed. The variation of the available torque factor shows that a value of 2.2 is sufficiently high for a 150% thrust demand for all blade numbers. The according value for the fixed pitch propeller was 1.8.

To conclude the analysis of variable pitch propellers, the most important findings are briefly summarised. The variable pitch mechanism allows to decouple the thrust response from the speed response of the mechanical subsystem. By adding a speed correction term on the thrust command, the precision of the lookup control of the variable pitch angle can be improved significantly and the thrust response can be decoupled completely from the rotational speed. In contrast to fixed pitch propellers, variable pitch propellers benefit from a high inertia design, as this reduces the speed deviation during thrust changes and the required MTF of the electric motor. Finally, thrust changes only require a change of the motor torque and no change of the system kinetic energy, which is by far much more responsive. The thrust
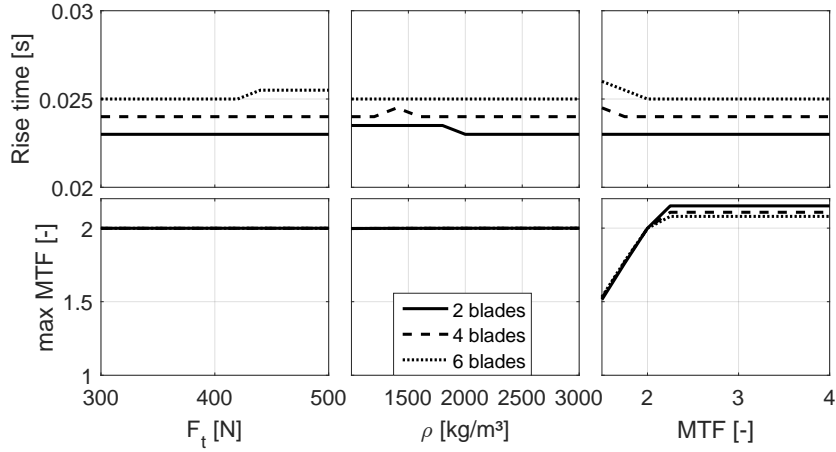
Figure 3.15: Parameter sensitivities for variable pitch propellers during over power(2)

response of the variable pitch propeller is roughly ten times faster than the response of the fixed pitch system.

3.4 Impact of a supplementary gear stage

In this chapter the impact of a supplementary gear stage is analysed. Therefore, a planetary gear stage is placed between the motor and the propeller. The propeller is connected to the planet carrier, the motor is connected to the sun wheel and the ring wheel is fixed to the non rotating structure. This arrangement allows high gear ratios and a simple connection to the surrounding structure via the ring wheel. Both acceleration manoeuvres have been simulated with the same design laws and matching conditions. Figure 3.16 shows the variation of the rise time and the system mass in dependency on the gear ratio for the part power acceleration of a fixed pitch propeller.
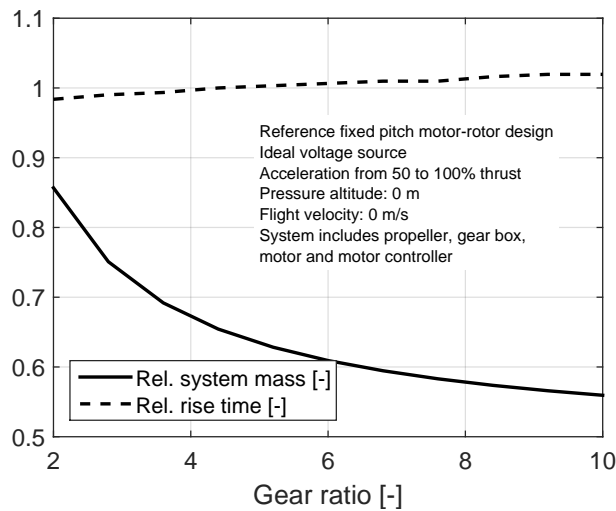
Figure 3.16: Impact of gearbox on thrust response and system mass

The abscissa shows the gear ratio and the ordinate shows the rise time and system mass results for the geared system relative to the system without gearbox. The results show that the inclusion of a gear stage does not significantly change the thrust response. For low gear ratios, the effect of the reduced motor inertia dominates over the supplementary inertia of the gearbox. At higher gear ratios, the planet wheel size and, thereby, the system inertia increases. Thus, the thrust response is slightly slowed down and the resulting rise time increases. A significant advantage of including a gear stage is the reduction of the system mass. As the gearbox mass is correlated against the propeller torque level, which is constant, the variation of the system mass originates only from the reduction of the motor torque and mass. The disadvantage of the gearbox are the supplementary gearbox losses which require more input power and hence a higher system mass of the upstream components. Moreover, a higher mission energy may be required, if the efficiency levels of the upstream components do not noticeably improve.

3.5 Sensitivities on model errors

Within this section, the sensitivity of the simulation results on the remaining model output parameters is investigated to assess the sensitivity on modelling inaccuracies. For the fixed pitch motor-rotor system, the most relevant model output parameters are the motor and the propeller inertia. Moreover, the off design calculation may lead to an inaccurate rotational speed which results into a higher or lower speed difference between the starting and the target point. To assess the sensitivity on these three parameters, a motor-rotor system is designed according to the reference conditions from Table 3.1. The system is accelerated from 50 to 100% thrust. Figure 3.17 shows the rise time results in dependency on the motor and propeller inertia variations as well as varying speed differences, relative to the reference system results.
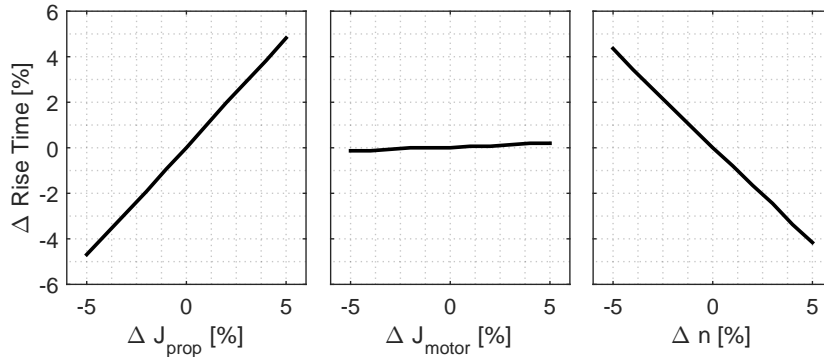
Figure 3.17: Error sensitivity of fixed pitch simulation results

The abscissa of the left plot shows the variation of the propeller inertia by +/- 5%. The ordinate shows the resulting rise time variation. The plot shows that the error characteristic is linear and that a one percent error on the propeller inertia translates into a one percent error in the rise time results. The motor inertia is shown in the middle plot. The figure shows that a small variation of the motor inertia does not significantly impact the rise time results, as the propeller inertia is one to two orders of magnitude larger than the motor inertia. Finally, the right plot shows the difference of the rotational speed of the starting and the target point. The plot shows that the speed difference has a similar impact on the rise time as the propeller

inertia. The characteristic is linear as well and a 5% error in the speed difference results into a 4% percent change of the rise time result. Hence, for fixed pitch systems it is essential that the propeller model provides a high accuracy for the rotational speed and the inertia, as they have a significant impact on the simulation results. For the variable pitch motor-rotor system the thrust is changed with the propeller servo, which changes the blade pitch angle. Thus, the servo speed and the distance to adjust the blade pitch angle are relevant model output parameters. Again, a reference system is designed and accelerated from 50 to 100% thrust and the rise time results are examined according to variations of these two parameters. The results are shown in Figure 3.18.
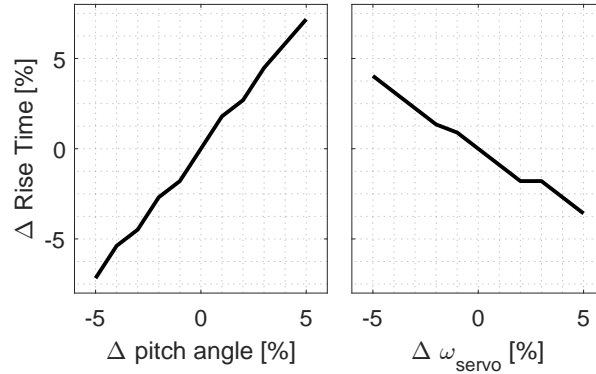
Figure 3.18: Error sensitivity of variable pitch simulation results

The left plot shows the impact of a deviation of the blade pitch angle. The error characteristic is linear and the impact on the rise time results is significant. A distance variation of 5% results in a rise time variation of 7%. The right plot shows the speed of the servo motor which is no output parameter from the here presented models, but from the modelling of Cutler and Pretorius [76, 180]. In comparison to the pitch angle distance, the rotational speed of the servo motor has a lower impact on the rise time results. Again, the characteristic is linear, but a 5% variation of the servo speed results in a 4% variation of the rise time. For variable pitch systems it is mandatory to provide a high accuracy for the blade pitch angle and the servo motor speed.

4 Propulsion System Peak Power Analysis

In the previous chapter, the thrust response of an isolated propulsor subsystem has been analysed and the according peak power requirements have been derived. The scope of this chapter is to investigate the sensitivity of component and system parameters on the peak power capability of battery and fuel cell based propulsion systems. Therefore, the motor-rotor subsystem is extended with power converters, batteries, fuel cells and supercapacitors to synthesise electric and hybrid electric propulsion systems.

To set up a DC bus network with multiple sources and multiple consumers, a bus voltage level is defined to simplify the network control and to provide defined requirements for component suppliers. For the system architectures which are examined in this work, the bus voltage level is derived from the motor controller requirements at the design point. The propulsion system design point is a hover operation with 400 N thrust per propeller at sea level static conditions. At this design point, the controller voltage is correlated to the motor power level by the following expression:

$$U_{\text{controller}} = P_{\text{mech,prop}}^{0.6} \tag{4.1}$$

During over power manoeuvres, the ohmic resistance of the stator armature requires a higher controller output voltage than at the design point. Especially for small motors the ohmic loss share is large [116] and therefore the voltage drop is significant. To be able to deliver the required voltage for an over power manoeuvre, the controller is designed at 90% of its maximum output voltage.

For the reference motor-rotor system, whose properties have been presented in Table 3.1, the resulting reference electric network properties are shown in Table 4.1. For the simulations in chapter 3, this reference bus voltage has been utilised for the ideal voltage source. In this chapter, all systems are designed with this reference bus voltage and the electric power of one motor.

Electric power (one motor)	Bus voltage
kW	V
9.82	235

Table 4.1: Reference electric network parameters

4.1 Battery based Systems

In this section, the basic motor-rotor system is extended with a power converter and a battery, to evaluate the thrust response of battery based propulsion systems. The ideal voltage source, that supplied the motor controller is replaced by a combination of a battery pack and a power converter. The converter is plugged between the battery and the motor controller to

compensate variations of the battery output voltage and supply the constant bus voltage to the motor controller. Figure 4.1 shows the system setup.
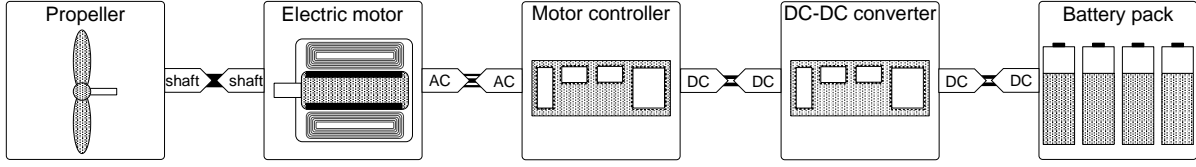
Figure 4.1: Battery based system setup

4.1.1 System Design

By adding a converter to the system, a supplementary degree of freedom is added to the system design, which is the pack voltage level. For the battery pack, the maximum continuous power and the available energy are the two major design parameters. The battery pack is assembled from multiple single cells which are connected in series and in parallel. As the number of cells in series and in parallel must be integers, the battery pack voltage, power and energy can only attain discrete values, whose spacing is defined by the cell parameters. A basic design process for batteries is to derive the number of series cells from the pack voltage and the number of parallel cells from the power and energy requirements. When batteries are designed in this way, they can store more energy than required, which results from the integer number of cells condition. Thus, the battery stack is oversized and heavier than necessary. In order to obtain a minimum mass layout, the voltage level must be optimised on component level. For example, an energy specification requires 37 battery cells. This design can be realised with a 5x8, 4x10, a 3x13 or a 2x19 layout. The pack voltage differs for every layout. So does the number of cells and the available energy storage. Figure 4.2 shows a comparison of fixed voltage and optimised voltage design of two battery packs for the reference power and bus voltage requirements.
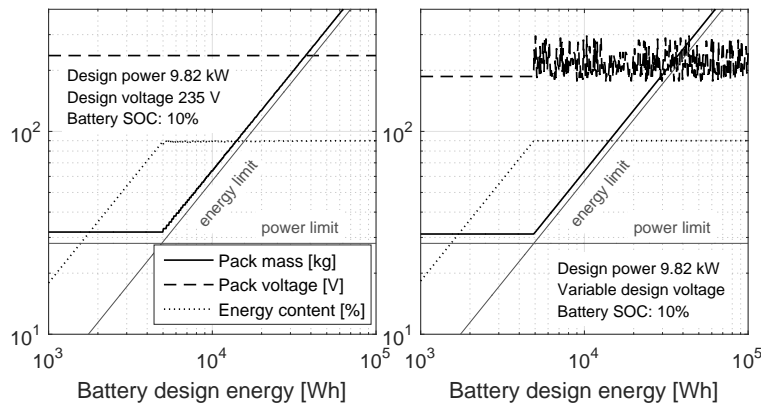
Figure 4.2: Battery design space

The left plot shows the design for the constant bus voltage. The abscissa of the plot shows the available energy of the battery pack, when a minimum SOC limit of 10% is considered.

The plot shows the constant battery design voltage, the pack mass and the energy content, which gives the amount of the design energy to the resulting installed energy. As the SOC level is limited to 10%, up to 90% of the battery energy content can be utilised. Moreover the plot shows the energy and power limits, which are given by the data sheet of the PL-383562 battery [166]. For low energy designs, the battery is designed according to the power specification, which results in a constant pack mass. As soon as the ratio of the pack power to the pack energy reaches or exceeds the maximum continuous cell C-rate, the battery pack is designed according to the energy specification. The maximum continuous C-rate of the PL-383562 cell is 2. For a design power of 9.82 kW and the C-rate limit of 2, the intersection point of both design limits is at 4.91 kWh. A variation of the maximum continuous C-rate results in a displacement of the intersection point of both design limits and thus to a vertical movement of the power limit. A low power limit is beneficial for battery packs that are designed for short time power profiles. For batteries that are designed for a given energy requirement, the maximum continuous cell C-rate is of minor interest.

The integer condition for the cell numbers causes the subordinated stair case shape of the pack mass curve. At each step, the energy content falls slightly under 90%, which means that the battery pack is oversized. For large battery packs with many cells, the step size decreases and the optimisation benefit of the pack voltage level declines. Consequently, for large battery packs, the pack voltage has no impact on the pack mass. For small batteries, there is a reasonable benefit.

The right plot shows the same design study with a variable pack voltage design. In this case, the pack voltage is optimised in order to obtain a minimum mass design and to exploit the battery capacity to the maximum of 90%. The plot shows that the pack voltage differs around 10% from the bus voltage level. The pack mass and the energy content show that the stair case shape has been removed and the available energy content of 90% is exploited from all battery packs, that are designed according to the energy requirement. The achieved mass benefit for the reference power level is 2-3%. For further studies on battery systems, the optimum design with a variable pack voltage level is applied in order to analyse.

4.1.2 Peak Power Performance

A high C-rate capability is beneficial for applications which require short time peak power. To assess the peak power capability of batteries, Figure 4.3 shows the cell voltage during an over power manoeuvre, which is initialised at the minimum SOC level of 10%. This represents the battery performance at the end of a mission. This configuration is most critical, as the battery voltage is already very low and the margin to the cut off level is small. The ordinate shows the Peak Power Factor (PPF), which is the ratio of the peak power to the maximum continuous power. The abscissa shows the duration, for which the peak power is delivered. The black contour plot shows the cell voltage and the grey contour plot the SOC level. The battery is designed for the reference power requirements with pack voltage level optimization.

When the cell voltage reaches its minimum limit, the cell is cut off to avoid structural transformation of the electrode material, which is an irreversible damage of the cell. This protection mechanism is important at low SOC values, as the battery open circuit voltage is already at a low level. When the cell is loaded with high current levels, the cell voltage is further reduced and the cut off voltage level is reached quickly. Figure 4.3 shows the peak power capability of the PL-383562 battery with an initial SOC level of 10%. The black contour plot shows for how long a certain power can be provided before the cell reaches the according cut
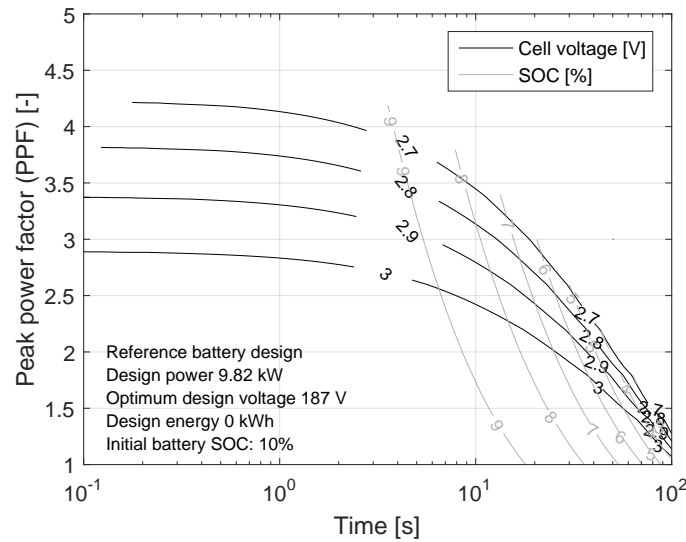
Figure 4.3: Battery over power capability

off voltage. For the cut off voltage of 2.75 V, which is given by the data sheet of the cell, the peak power is limited to a factor of 4 for very short power peaks and a PPF of 3 can be supplied for roughly 20 seconds. After almost two minutes, the SOC has decreased to such a low level, that the battery is not able to deliver more than the maximum continuous power.

For the fixed pitch propeller, a PPF of 4 has been identified in chapter 3. Figure 4.3 shows that, with a cut off voltage of 2.75 V, a PPF of 4 can be supplied only for a split of a second. Thus, the battery already affects the thrust response of the motor-rotor system at a SOC level of 10%, which takes half a second. In order to increase the voltage margin and to enable a longer peak power capability, the battery must be either resized for higher energy and power specifications or the minimum SOC level must be augmented. Both measures result in larger and heavier battery design. For the variable pitch propeller, a PPF slightly above two has been identified. This peak power can be supplied for around one minute, down to a SOC level of 4 percent. This means that the utilisation of a variable pitch propeller enables a lower minimum SOC level than a fixed pitch propeller. In this example, roughly 6% more energy can be drawn from the cell, which means that the battery pack is also roughly 6% lighter. At the same time, the thrust response is ten times faster than with the fixed pitch propeller, according to the results of chapter 3.

To demonstrate the limiting behaviour of the battery, the over power acceleration of the reference fixed pitch motor-rotor system with a MTF of 4 is simulated. Figure 4.4 shows the plot of the relevant system parameters during the manoeuvre. The left plot shows the parameters of the motor-rotor subsystem and the right plot the battery cell voltage and C-rate.

The simulation shows that the C-rate increases with the motor torque from the maximum continuous power towards the required peak power level. At the same time, the cell voltage drops towards the cut off voltage. As soon as the cut off voltage is reached, the controller cuts off the battery and the motor torque is reduced. After a short time, the battery voltage recovers and the battery is reconnected. During the acceleration, the battery is cut off multiple times. The cut off process limits the average power and prohibits the system to deliver
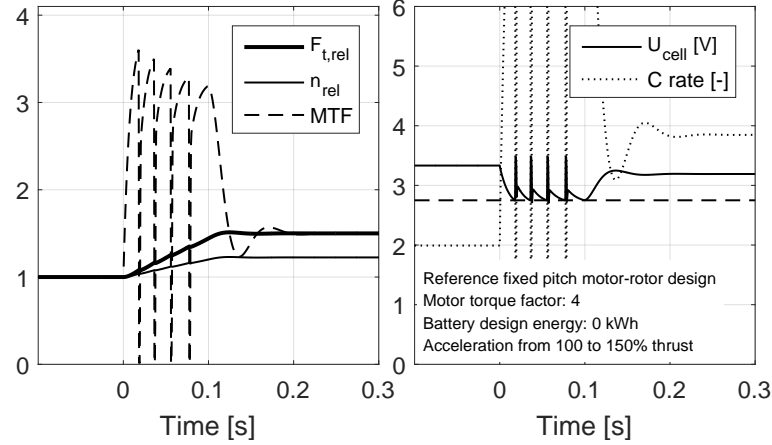
Figure 4.4: Over power acceleration of fixed pitch propeller with battery(1)

the required MTF target. This results in a slower acceleration and higher rise time results. To further investigate the sensitivity of the rise time on the peak power requirements, a parametric study on the MTF and the battery cut off voltage is conducted. Figure 4.5 shows the rise time (left plot) of the reference system and the minimum battery cell voltage (right plot), which is observed during the acceleration.
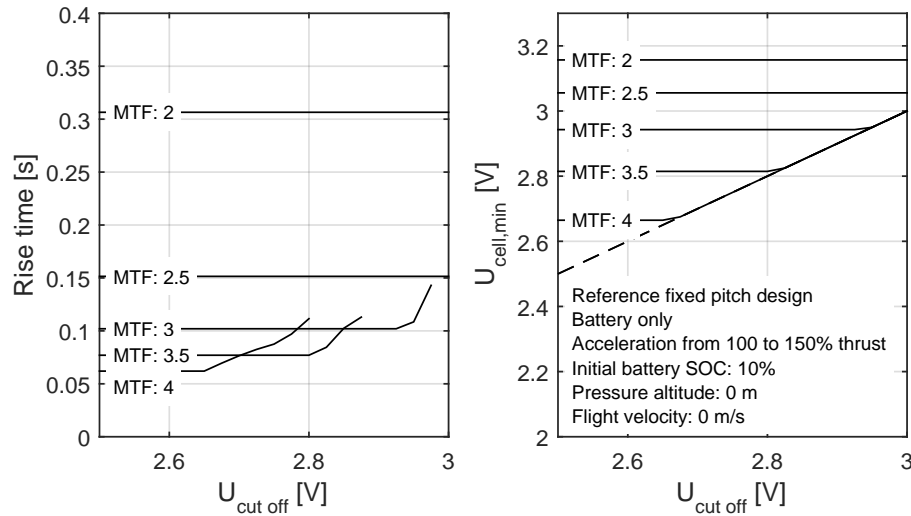
Figure 4.5: Over power acceleration of fixed pitch propeller with battery(2)

The abscissa of both plots shows the battery cut off voltage. The left plot shows, that for very low cut off voltages, the acceleration gets faster with increasing MTF and the rise time results are reduced. At the same time, the current level is increased, which results in a lower minimum cell voltage during the acceleration, which is shown by the right plot. When the minimum cell voltage reaches the cut off voltage, the system power is limited and the rise time results are affected. At this point, the power specifications must be increased or a high power cell, which provides a lower internal resistance must be applied to avoid the power limitation. The shape of the rise time results in the left plot show that there is an optimum

MTF for each cut off voltage, which draws the maximum power from the battery without causing the cells to be cut off. The application of this optimum MTF results into the fastest acceleration and the lowest rise time. Equation 4.2 shows a correlation of the maximum MTF in dependency on the cut off voltage level.

$$\text{MTF}_{\text{max}} = -2.424 \cdot U_{\text{cut off}}^2 + 10.000 \cdot U_{\text{cut off}} + 5.403 \tag{4.2}$$

By defining the bus voltage and the battery pack voltage as system design parameters, the voltage transmission ratio of the buck-boost converter is defined as well. Design calculations of the buck-boost converter have shown that the resulting time constants are faster than the response times of the propulsor subsystem. Consequently, the buck-boost converter does not noticeably affect the system response.

To conclude this chapter, the interesting findings on battery based system are briefly summarized. For small batteries, the pack voltage level represents an optimisation parameter for the battery mass. The mass of larger batteries is independent from the pack voltage level. The analysis of the peak power capability of battery based systems has shown, that the average high-energy cell PL-383562 can deliver a PPF of up to almost 4 until a SOC level of roughly 10% is reached. Until this SOC level, the thrust response is not limited by the battery. The reduced peak power requirements of variable pitch propellers enable a higher utilisation of the battery energy. Simulations with the PL-383562 cell model have shown that 6% more energy could be delivered by the cell, which translates into an equivalently lower battery weight. In the next section, the design of the buck-boost converter is investigated together with the fuel cell.

4.2 Fuel Cell based Systems

In this chapter, the design and the peak power capability of a fuel cell based propulsion system is investigated.

4.2.1 Fuel Cell Configuration Comparison

Before analysing the peak power capability of the fuel cell, the two fuel cell configurations, which have been presented in the modelling chapter 2.6, are compared in order to identify the better configuration for UAV application. Therefore, both configurations are designed for equal electric power levels and equal environmental conditions. The design voltage level is derived from the electric power level according to the correlation from Equation (4.1). The fuel cells are operated at full power for a certain operating time. The system mass of both configurations is calculated in dependency on the power level and on the operating time. The oxygen configuration contains two gas tanks, whose size and mass depend on the amount of stored gas. The air breathing configuration only requires a hydrogen tank and the air is taken from the environment to supply the cathode. The gas tanks are designed in that way, that at the end of the operating time, the tank pressure equals the operating pressure of the fuel cell. The oxygen tank configuration includes the fuel cell stack, two gas tanks and four pressure valves. The air breathing configuration consists of the fuel cell stack, one radial compressor stage, a gearbox, an electric motor and three pressure valves. The required power of the electric motor is subtracted from the fuel cell power output. Figure 4.6 shows a comparison of the system mass of both configurations at different pressure altitudes. The abscissa shows

the operating time and the ordinate shows the design net electric power.
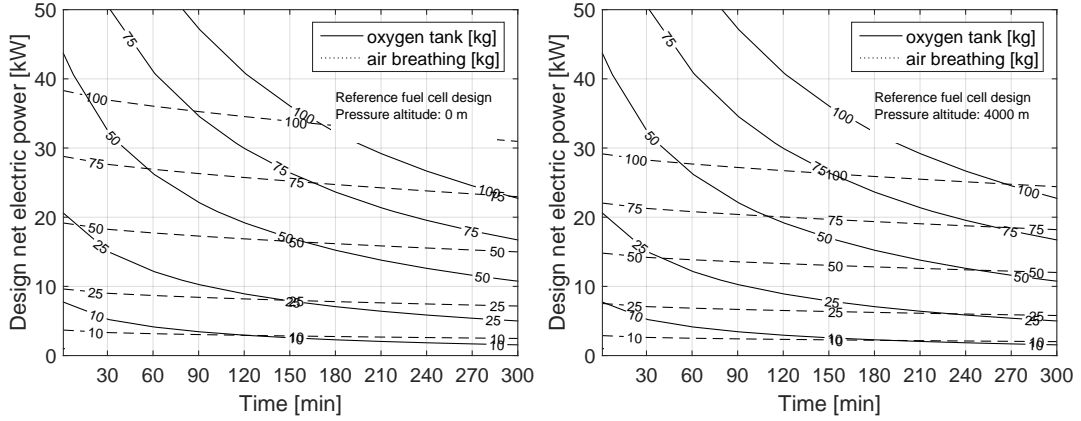
Figure 4.6: Comparison of air breathing and oxygen tank configuration

The left figure shows the results for operation at sea level ISA conditions. Both configurations show an increasing system mass for longer operating times. The gradient of the system mass versus the operating time is greater for the oxygen configuration than for the air breathing configuration because of the oxygen tank, which grows with the operating time. For short operating times, the oxygen tank configuration has a lower system mass than the air breathing configuration, which results from the additional mass of the auxiliary components and the power consumption of the compressor stage. The break even of the system mass is attained at an operating time between 150 and 180 minutes. The right figure shows the results for operation at an pressure altitude of 4000m. Because of the reduced air pressure, the air breathing configuration suffers from the mass and the power consumption of an additional compressor stage, which is required to attain the target operating pressure in the fuel cell. Moreover, the low air density requires larger compressors, which further increases the mass of the auxiliary components. Therefore, the break even is delayed to roughly 5 hours of operating time. As the targeted operating times are well below the identified break even points and because of the results of the discussion in chapter 2.6, the oxygen tank configuration is favoured over the air breathing configuration.

4.2.2 System Design

In the following section, the impact of the fuel cell design parameters on the peak power performance of fuel cell based propulsion systems is investigated. Therefore, a basic fuel cell based system is designed according to Figure 4.7. The system contains the reference motor-rotor system, a DC-DC power converter and a fuel cell stack. Similar to battery based systems, the converter is utilised to compensate variations of the fuel cell voltage, which introduces the fuel cell stack voltage level as a new degree of freedom into the system design.

To analyse the sensitivity of the buck-boost converter and the fuel cell peak power capability on the main design parameters, a parametric study is conducted. As Table 2.4 shows, there are numerous parameters of the cell geometry and operating conditions which influence the performance of the fuel cell. To keep the numbers of parameters in a reasonable range, the current density, the membrane thickness and the stack voltage and power level are utilised
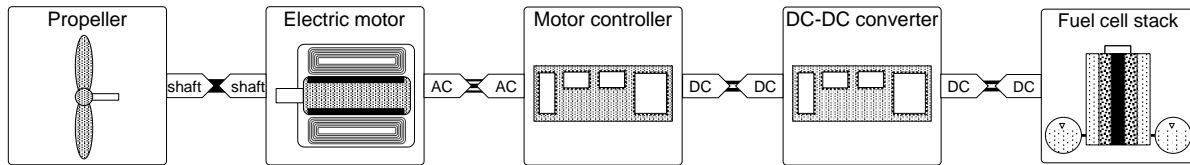
Figure 4.7: Fuel cell based system setup

as the most relevant parameters, which show an impact on the peak power performance of the fuel cell. The fuel cell is designed for reference power specification and the bus voltage level which are listed in Table 4.1. The result is shown in a matrix of partial dependencies in Figure 4.8.

According to Figure 4.8, the current density and the membrane thickness have no impact on the design of the buck-boost converter. As the current density is inversely proportional to the active membrane area, it has a considerable impact on the fuel cell stack size and mass. A high current density results in a low membrane area and a small and light weight fuel cell. On the other hand, a high current density decreases the cell efficiency. To achieve a high efficiency, a low current density is required. Thus, the current density represents a very important trade-off between system mass and efficiency and has to optimised on aircraft level. The membrane thickness is directly related to the inner resistance of the fuel cell. Thus, a thinner membrane results in a lower resistance and a higher cell voltage and efficiency. The impact on the fuel cell mass and volume is rather low, as the membrane represents only a small part of the fuel cell stack.

Figure 4.8 shows that the buck-boost converter mass and efficiency depends on the stack voltage and power level. For higher power levels, the converter mass and efficiency increase. The mass increases because of the increasing mass of the coil and the capacitor. As the voltage level is kept constant, the power level is increased with higher current levels. The higher current level results in a lower coil resistance, which improves the converter efficiency. The study on the voltage level shows a kink in the curves of the converter mass and efficiency. The transition point marks the rated voltage of the motor controller. For lower fuel cell voltage levels, the converter design is dominated by the boost requirements and for higher voltage levels, the buck requirements dominate the design.

Both, the voltage and power level have no impact on the fuel cell efficiency. Similar to batteries, the stack voltage level determines the number of series cells. However, there are no parallel cells considered in the fuel cell stack design. The membrane area is derived from the current level and is not limited to discrete values. Thus, the stack voltage level has no impact on the stack mass. As a sealing rim and two backplates are considered in the mass calculation, there is a minor impact on the voltage level, because the fuel cell dimensions and, thus, the surface area is changed. The subordinated discrete levels originate from the discrete screw design, which is related to the sealing rim thickness. Similar to large batteries, the stack mass is independent on the design voltage level. However, the voltage level has an impact on the efficiency of the buck-boost converter, which will influence the amount of energy that is required for given mission specifications. Thus, on aircraft level, the aircraft will benefit from a high fuel cell voltage.
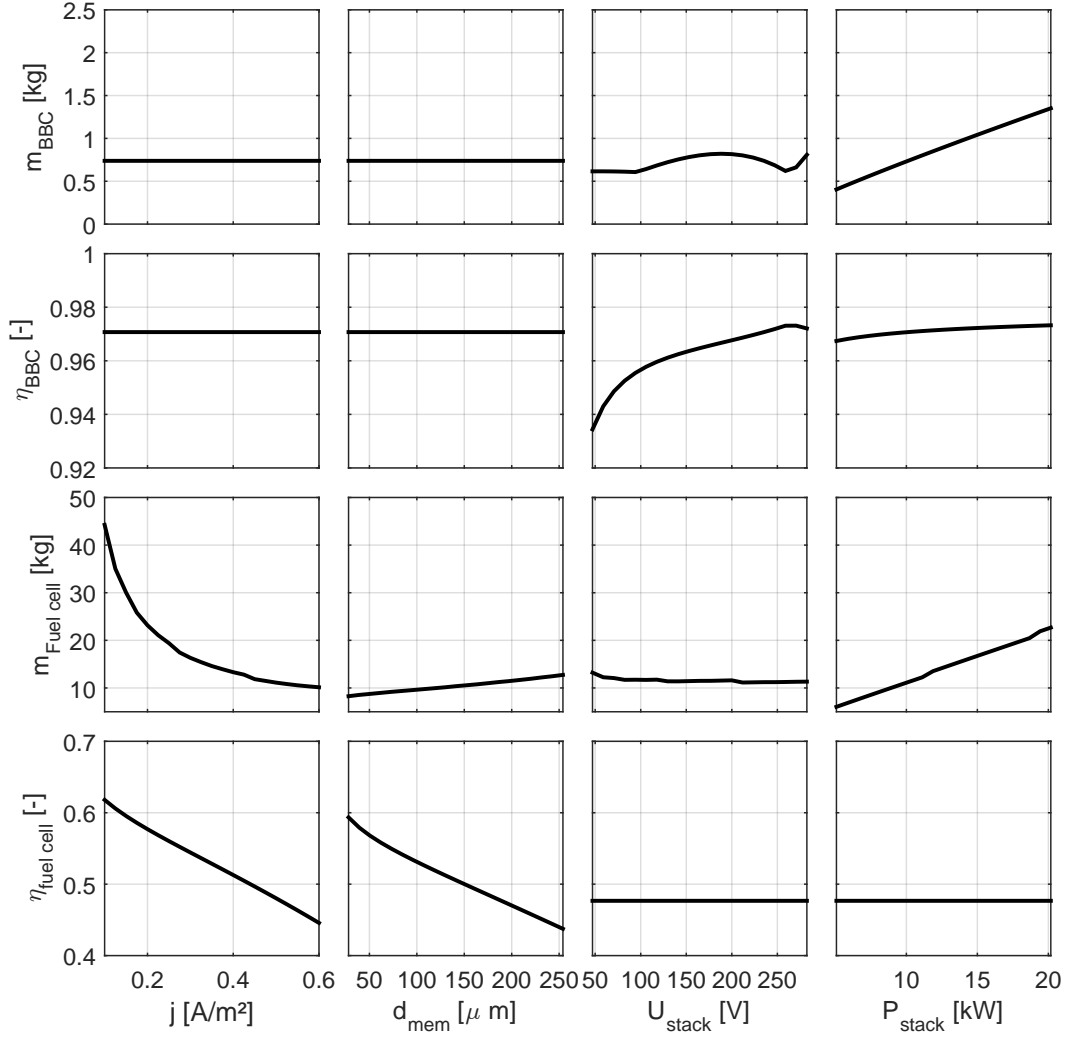
Figure 4.8: Fuel cell design space

4.2.3 Peak Power Performance

In contrast to the battery, the fuel cell is continuously provided with gas, which means that, in a first approach, its peak power does not vary with time. Of course, as impedance spectroscopy studies have shown, the diffusion processes and capacitive effects influence the dynamic response of the fuel cell in different time scales [144]. Moreover, at high current loadings, liquid water is formed at the cathode, causing cathode flooding. However, there is no dependency on a charge level like in batteries or supercapacitors. For a first assessment of the fuel cell peak power capability, a quasi steady state operation is calculated, which neglects the diffusion processes and the capacitive effects. The result of the study is shown in Figure 4.9.

The abscissa shows the current density and the ordinate shows the cell voltage, the efficiency and the relative electric power. The cell voltage and the efficiency are coupled and show the same characteristic over the current density. With higher current densities, the relative power increases up to a maximum value of roughly 1.3. From this point on, the voltage drop of the cell dominates over the higher cell current and the relative power decreases. As the
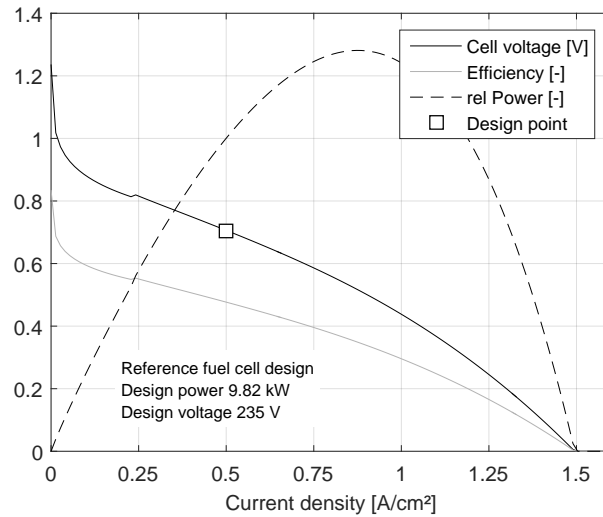
Figure 4.9: Fuel cell over power capability

power output of the cell is fixed for given operating conditions, the relative power output can only be changed with the design current density. By reducing the design current density, the relative peak power can be increased. However, this results in a higher stack mass according to the findings from Figure 4.8. To illustrate the system response during a transient load change, Figure 4.10 shows the relevant parameters for the part power acceleration of the reference fixed pitch motor-rotors system with a fuel cell.
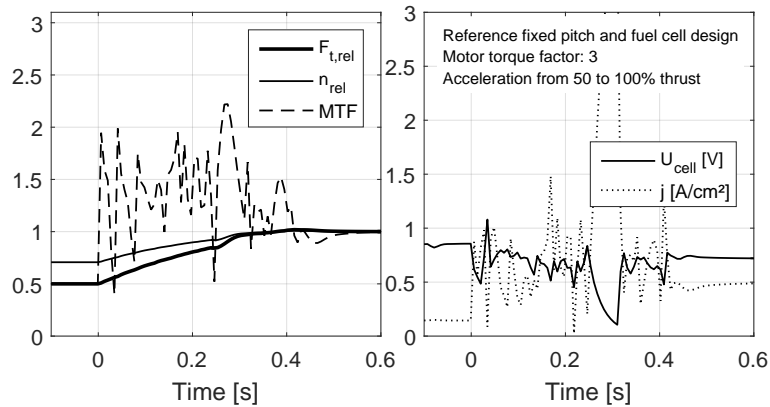
Figure 4.10: Fuel cell part power acceleration

The abscissa of both plots shows the time. At zero seconds, a step command for the new target rotational speed is passed to the motor controller. The maximum allowed MTF is set to 3. The left plot shows that the MTF and the current density are quickly increased. At the same time, the fuel cell voltage declines and reaches the lower limit of 0.1 V, where the cell is cut off. The voltage drops so quickly, that the cell is cut off before the MTF reaches its target value. After the cut off, the cell voltage recovers immediately and the cell is reconnected. During the acceleration, the fuel cell is cut off several times, before the system reaches the rated operating point.

The diffusion processes and the capacitive effects introduce dynamics into the change of the fuel cell state, which enables higher peak power levels for short periods and extends the time of over power operation. To further analyse this impact, the part power acceleration of the reference fixed-pitch motor-rotor system is simulated with different peak power levels. Figure 4.11 shows the result of this study.
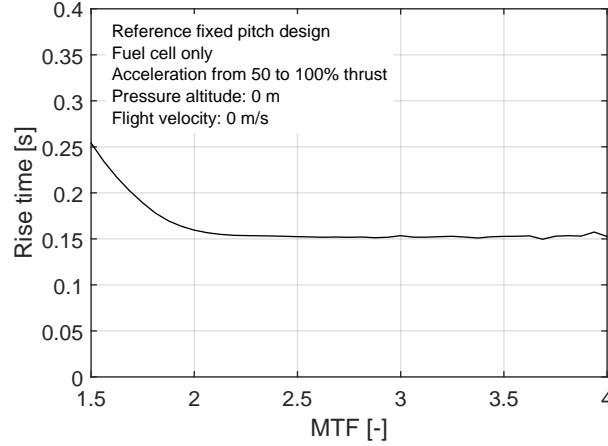
Figure 4.11: Fuel cell over power capability(2)

The abscissa shows the MTF and the ordinate shows the rise time of the part power acceleration. The smooth decline of the rise time for up to a MTF of 2 shows that the fuel cell can deliver the required PPF. For higher MTF, the required power increases and the fuel cell is cut off. Thereby the fuel cell power is limited, which results in constant rise time results.

Although, under the defined operating conditions and design points, the fuel cell can deliver a continuous PPF of 1.3, the diffusion processes enable a short time PPF of slightly above 2. Therefore, the fuel cell is able to accelerate both reference motor-rotor systems up to 150% of thrust when low MTF are utilised. However, higher power levels can not be sustained.

In this final section, the key findings from this chapter are summarized. A system mass comparison of both fuel cell configurations has shown that the oxygen tank configuration has a mass benefit up to 180 minutes at sea level ISA operation. At 4000m pressure altitude, this mass benefit is extended and the break even point is delayed to 5 hours of operating time. According to the studies in this chapter, the fuel cell has a poor dynamic behaviour, which originates from internal diffusion processes and a higher internal resistance, compared to batteries. The design current density is an optimisation parameter to trade the peak power capability and the efficiency against the fuel cell mass and has to be optimised on aircraft level. Moreover, the stack voltage level is a relevant parameter to trade the stack mass against the converter efficiency, which has to be optimised at aircraft level.

To enable a better peak performance of fuel cell based systems, a second energy storage with a higher peak power performance is necessary. Therefore, in the next chapter, the design and the peak power performance of a hybrid propulsion system is analysed, which consists of a fuel cell and a supercapacitor.

4.3 Hybrid Fuel Cell System

In this chapter, the design and the dynamic performance of a hybrid fuel cell system is analysed. Therefore, the basic motor-rotor system is extended with two power converters which are supplied by a fuel cell and a supercapacitor. The hybrid system involves an additionally PMAD unit, which controls the power split of both components. However, there is no physical hardware associated to this component. In this work, the PMAD is considered as a logical unit which controls the power network. The system architecture is shown in Figure 4.12. The fuel cell is matched for the rated power of the electric motor and the supercapacitor is sized to deliver the full rated motor power for 10 seconds. The purpose of the supercapacitor is to support the fuel cell during peak power manoeuvres to obtain a similar performance as battery based systems.
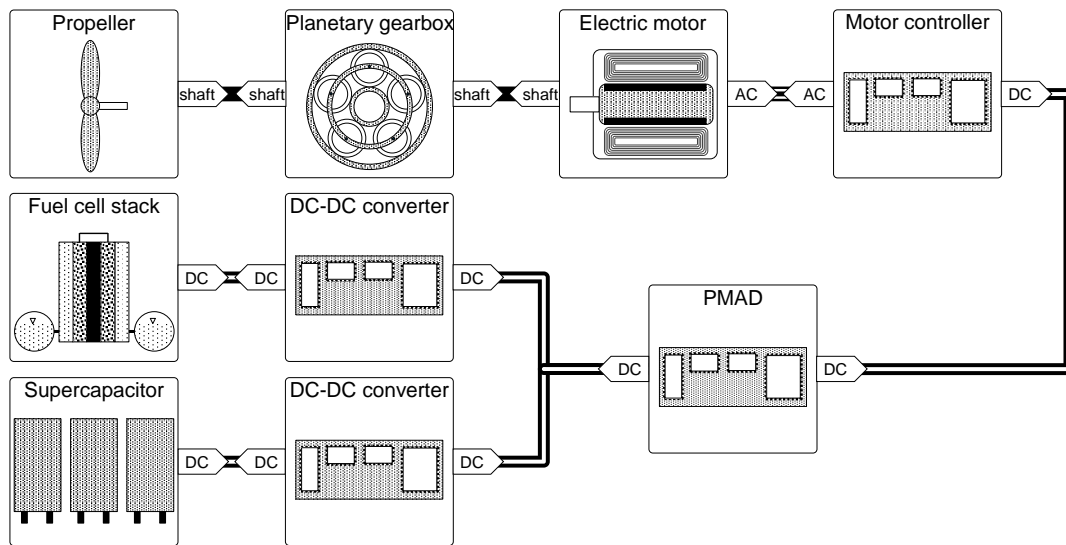
Figure 4.12: Hybrid fuel cell based system setup

4.3.1 Hybrid System Design

In this section the design of the supercapacitor is further investigated. Similar to batteries, the supercapacitor pack is composed of multiple single cells, which are connected in series and in parallel. Therefore, as it has been shown for batteries, its pack voltage is a parameter, that can be optimised on component level to obtain a minimum component mass. For the supercapacitor, the benefit of this optimisation is more interesting than for batteries, as the number of cells is significantly lower than for batteries. The essential difference to batteries is the power rating of the single cell. The design parameters of the battery are the voltage, power and energy level. Because of the very low inner resistance of supercapacitors, there is no significant power limitation of supercapacitors and, hence, the pack power is no design parameter. The relevant design parameters are the voltage and energy level of the stack. Similar to batteries, the energy limit of the stack results from the specific energy of one single cell. The second limitation is the pack voltage level, which defines a minimum number of cells and has the same characteristics as the power limit of batteries. The location of the intersection point of both limits is defined by the cell capacity. Whenever the pack capacity is superior to the cell capacity times the number of series cells, the pack is designed according to the energy requirements. When the pack energy is lower, the supercapacitor is designed

according to the voltage requirements. Figure 4.13 shows the same design study which has been conducted for battery systems. The supercapacitor is designed for the reference specifications in Table 4.1. The stair case shape of the curve originates from the integer condition for the number of cells. Compared to the battery, the stair steps are significantly larger, because the pack energy (and therefore the number of cells in parallel) is very low in this design.
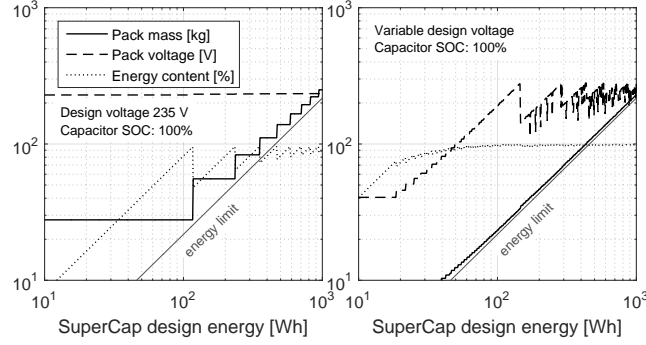
Figure 4.13: Supercapacitor design space

The left plot shows the design for the bus voltage and the right plot shows the design with an optimised pack voltage. The comparison of both plots shows, that especially for small energy designs, the pack mass can be reduced by more than 80% by optimising the pack design voltage. The pack mass curve for the optimised design is much closer to the energy limit and the energy content shows, that with a lower pack voltage level, the supercapacitor can be designed closer to the required energy specification. However, reducing the pack voltage is only feasible within a limited range. To further analyse this limit and the resulting trade-off, the discharge characteristic of a capacitor is briefly explained. The discharge behaviour can be plotted in a polarisation curve, similar to a battery. Figure 4.14 shows the polarisation curve of the non linear supercapacitor model from [170]. The abscissa shows the state of charge and the ordinate shows the cell voltage. The contour plots show the cell voltage for different C-rate loadings. Compared to the polarization curve of the battery, the supercapacitor shows a significant voltage drop with decreasing SOC levels. When fully discharged, the supercapacitor voltage is zero.

In theory, the supercapacitor can be discharged to zero without any damage to the system. However, the capacitor voltage drops down to zero at complete discharge and most electric systems only work in a specified voltage range. Moreover, a very low current is required to completely discharge the supercapacitor, which significantly reduces the available power. In practice, the capacitor is discharged to a lower voltage limit, which is referred to as cut off voltage in analogy to the previous models. Hence, the available energy, which can be drawn from a capacitor depends on the cut off voltage according to Equation (4.3).

$$E_{\text{cap}} = \frac{1}{2} \cdot C \cdot \left(U_{\text{rated}}^2 - U_{\text{cutoff}}^2 \right) \tag{4.3}$$

The transmission ratio of the converter can limit the design values of the cut off and the rated voltage and a power conversion must be feasible at both voltages. As the transmission ratio of a buck-boost converter is limited to roughly 10, a trade-off between the pack voltage level and the extractable energy has to be made. This trade-off is included in the design study
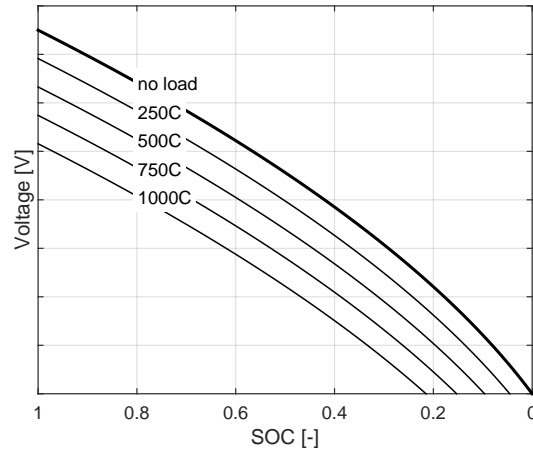
Figure 4.14: Supercapacitor polarisation curve

from Figure 4.13 by utilising the maximum transmission ratio of the converter at the cut off voltage of the supercapacitor.

4.3.2 Peak Power Performance

Within the next section, the peak power performance of the supercapacitor is investigated. Figure 4.15 shows the peak power capability under constant power operation. The abscissa shows the time and the ordinate shows the C-rate of the capacitor. As there is no rated power available for supercapacitors, the C-rate is utilised instead of the PPF. The contour plot shows the cell voltage, which correlates to the SOC level. The simulation is initialised with a SOC level of 95%.
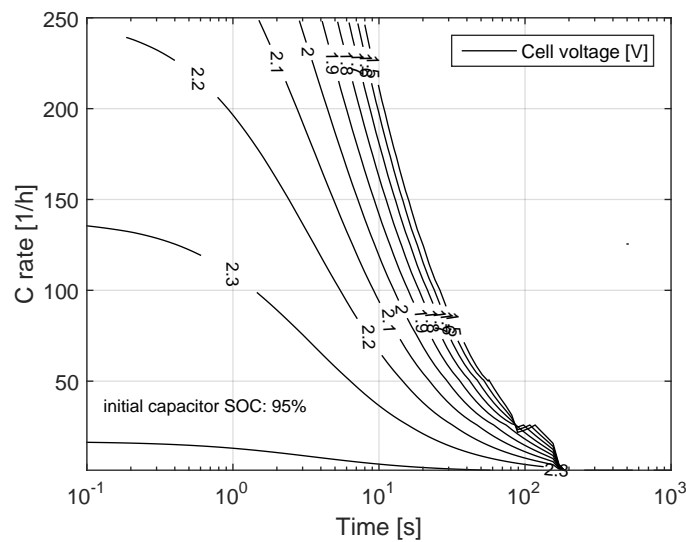
Figure 4.15: Supercapacitor over power capability

The results show that the short time peak power performance is superior to batteries and

fuel cells. The capacitive effects from the model can hardly be identified in the plot and the duration of the power supply is only limited by the capacitor energy. After roughly two minutes, as soon as the cut off voltage is reached, the capacitor can not supply any more power.

In the last section, the peak power performance of the hybrid system is investigated. In order to show the benefit of the supercapacitor and to compare the performance to the fuel cell system, Figure 4.11 shows the part power acceleration of the reference fixed-pitch motor-rotor system. The relevant motor-rotor parameters are plotted in the left plot of Figure 4.16. The right plot shows the electric power of the motor, the fuel cell and the capacitor.
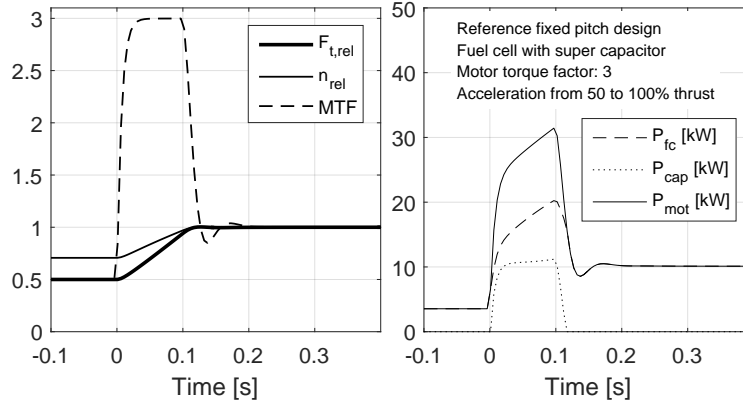
Figure 4.16: System characteristics for part power acceleration

The left plot shows that, in contrast to the fuel cell, the hybrid system is able to deliver the available PPF of 3 throughout the acceleration. The fuel cell is not cut off during the simulation and the achieved rise time is similar to the battery system. Further simulations have shown, that the hybrid system is able to achieve the same rise time results that have been obtained for the fixed pitch motor-rotor system in chapter 3 for both manoeuvres with MTF up to 4. Thus, the hybrid system enables both; the utilisation of a fuel cell for long endurance and high peak power performance. On the other hand, the supercapacitor and its converter add 7.8 kilograms to the system mass, which is, compared to the 12.0 kg of the fuel cell stack (without gas tanks), a considerable penalty.

The introduction of the PMAD device adds a new degree of freedom to the propulsion system control, which is the power split between both components. Three different approaches have been identified to control the power split. The first method is a passive device, which consists of two diodes that are connected to the two converters of the fuel cell and the supercapacitor. In this configuration, the power split depends on the output voltage of both converters and, therefore, on the component part power characteristics. By choosing a lower output voltage design for the supercapacitor converter, the continuous power level is entirely supplied by the fuel cell as its converter produces a higher output voltage. As the power load is increased, the fuel cell and converter output voltage drop until current is also drawn from the supercapacitor. This passive method has been utilised for the simulation shown in Figure 4.16. The other two methods consist of actively controlling the power split or the current split. Just to control the power split does not prevent the cut off of the fuel cell, as this process is triggered with the voltage level of the fuel cell. Simulations with the current split device have proven it a

reliable method to avoid the fuel cell cut off and keep the fuel cell within a save operational envelop.

5 Aircraft Level Manoeuvre Performance

In this chapter, the impact of the thrust response on aircraft manoeuvrability is investigated. As the thrust response is most relevant for distributed thrust configurations, the performance of a multicopter as well as a fixed wing aircraft with multiple propellers is investigated. The first vehicle is a symmetric quadcopter, which utilises four electrically driven propellers for attitude and vertical speed control. The quadcopter agility is assessed with one rotary, one translational manoeuvre as well as an arbitrary combination of both. The second aircraft is the Tecnam P2006T, a twin engine general aviation aircraft, which is the basis for the LEAPtech concept. This concept has 18 electrically driven propellers at the leading edge of the wing, which increases the dynamic pressure on the wing. This technology enables a smaller wing design, whereas the low speed manoeuvre performance of the original aircraft is conserved and the drag is reduced. The high agility of electric motors gave birth to the idea to investigate the yaw control performance by applying differential thrust, which is conducted in the second part of this chapter.

5.1 Quadcopter Manoeuvre Performance

A quadcopter vehicle is a flying platform with four rotors, which are positioned in a common plane and the rotors point upwards, which enables the quadcopter to lift off vertically like a helicopter. In the center of the vehicle, an energy storage, the payload and the flight control hardware are mounted. With the VTOL capability, the mission profiles are similar to those of helicopters. In aeronautical science, quadcopters are mainly utilised to test new flight control algorithms. Typical commercial applications are camera based maintenance and surveillance of power lines, buildings and major events. In both fields, the quadcopter had a breakthrough because of its mechanical simplicity and the recent miniaturisation of payload sensors and computer hardware, which results in small vehicles with low-cost hardware. For this study, the quadcopter concept has been chosen as it utilises differential thrust for attitude and flight control. This requires a good thrust response of the propulsion system in order to stabilise the vehicle and perform highly agile manoeuvres. Within the next two sections, a basic structural design and an analysis of the flight dynamics and the flight control system is conducted. Afterwards, a quasi steady state mission performance and the peak power performance are investigated, based on the design parameters of the mechanical subsystem and the system design parameters.

5.1.1 Structure Modelling

In this section, a basic structure model of a quadcopter is derived and explained. Figure 5.1 shows a top view of the modelled quadcopter configuration. The plotted coordinate system represents the bodyfix coordinates (index $_B$), whose origin is located in the center of gravity of the vehicle. The positive x- and y-axis show towards the front and the right side of the vehicle. The positive z-axis shows downwards and is not plotted in Figure 5.1.

It is assumed, that the quadcopter is symmetric to its x- and y-axis. Thus, the center of gravity is located at the intersection of both diagonal rotor arms. This results in equal lever
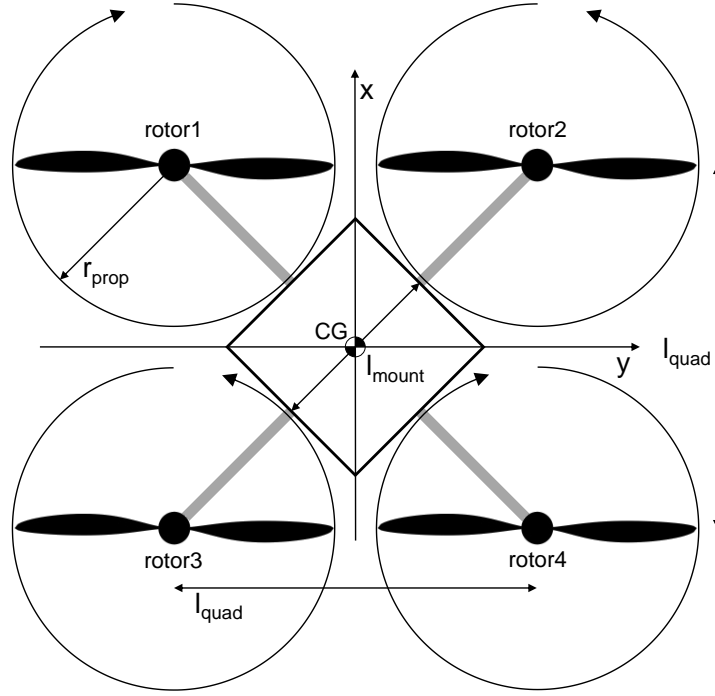
Figure 5.1: Quadcopter configuration

arms for all four rotors and therefore in an equal thrust level. As shown in chapter 3, the thrust response depends on the design thrust level. Hence, for a non symmetric design, the balance of forces and unequal thrust responses of the motor-rotor systems must be considered for vehicle design. This either results in a complicated motor-rotor design or a complex flight control system.

The lever arm length defines the distance between the propellers and it therefore has an impact on the quadcopter mass and inertia. At the same time, longer arms increase the resulting moments of the propeller thrust and therefore boost the manoeuvrability of the vehicle. The distance between the propellers and therefore the length of the arms is correlated to the propeller radius by a linear factor k_{quad} according to Equation (5.1). The reference value for k_{quad} is set to 1.05 according to design investigations for quadcopters for aggressive manoeuvres [76].

$$l_{\text{quad}} = 2 \cdot r_{\text{prop}} \cdot k_{\text{quad}} \tag{5.1}$$

The four arms reach from the vehicle center to the center of each propeller. The tip of each arm carries an electric motor and a propeller. The maximum bending moment at the root depends on its length and the maximum thrust level of the propeller. Therefore, the double hover thrust level is considered for the arm design. The arm is considered as a hollow aluminium tube with a thickness of 2mm, a material density of 2780 $\frac{\text{kg}}{\text{m}^3}$ and a yield elastic limit of 300 MPa [181]. The average radius of the tube is calculated with a security factor S of 2 according to Equation (5.2).

$$r_{\text{arm}} = \sqrt[3]{\frac{2 \cdot S \cdot F_{t,\text{hover}} \cdot l_{\text{arm}}}{\pi \cdot \text{thick} \cdot \sigma_{\text{el,lim}}}} \tag{5.2}$$

The resulting free space between the propellers is utilised to mount the flight control equipment and the payload. Therefore a mounting plate with the same thickness and the same aluminium properties as the arms is positioned at the vehicle center. The quadcopter mass and inertia is calculated from the four arms, the mounting plate, the electric motors and the propellers, which are located at the arm tips, the propulsion system components and the payload. The inertia of the electric motors and the propellers is corrected by the parallel axis theorem (Steinerscher Satz), since they are not located in the center of gravity. Simulations with this structure model have shown, that the four motors and propellers represent between 70 to 80% of the quadcopter inertia. The payload, the energy storages and their power converters are considered to be mounted at the vehicle center of gravity. Thus, their inertia is not corrected with the parallel axis theorem. The inertia of the payload is calculated from a cuboid model with a homogeneous material density of 2000 $\frac{\text{kg}}{\text{m}^3}$.

5.1.2 Flight Dynamics and Control

The thrust vectors of all four propellers point upwards in the negative direction of the bodyfix z-axis. In order to perform a vertical movement, which is the most simple manoeuvre, the thrust level of all four rotors is changed at the same time. To perform a lateral movement, the quadcopter must apply a bank or pitch angle to tilt the thrust vectors in the appropriate direction. To attain a certain bank or pitch angle, the distributed thrust capability is utilised to create bank and pitch moments by changing the thrust level of the propellers accordingly. To describe the flight dynamics of the symmetric quadcopter, the balance of forces and moments is derived in Equations (5.3) and (5.4), where x and y denote the lever arm components of the propellers. F_z is the resulting vertical force and M_x, M_y and M_z represent the resulting roll, pitch and yaw moments. Q_i denotes the aerodynamic torque of the propellers.

$$\begin{bmatrix} F_z \\ M_x \\ M_y \end{bmatrix} = \begin{bmatrix} -1 & -1 & -1 & -1 \\ -y_1 & -y_2 & -y_3 & -y_4 \\ x_1 & x_2 & x_3 & x_4 \end{bmatrix} \cdot \begin{bmatrix} F_{t,1} \\ F_{t,2} \\ F_{t,3} \\ F_{t,4} \end{bmatrix} \tag{5.3}$$

$$M_z = \sum_{i=1}^{4} Q_i \cdot \text{sign}(n_i) \tag{5.4}$$

During hover flight, the yaw torque of the propellers must be cancelled to avoid an acceleration of the quadcopter. Therefore, two propellers rotate clockwise and the other two propellers rotate anticlockwise. To avoid yaw moments during bank and pitch manoeuvres, two diagonally opposed propellers rotate in the same direction. Thus, propellers 1 and 4 rotate in the opposite direction as propellers 2 and 3. By replacing the thrust and the torque of each propeller with the relations in Equations (2.14) and (2.15), the forces and moments of the propulsion system can be expressed as a linear function of the square rotational speed of the rotors according to Equation (5.5). The matrix in Equation (5.5), shows a column vector for one propeller. The index i indicates the entries that must be adapted to the according propeller value.

$$\begin{bmatrix} F_z \\ M_x \\ M_y \\ M_z \end{bmatrix} = \begin{bmatrix} -C_{t,i} \cdot \rho \cdot \frac{1}{60^2} \cdot d_i^4 \\ y_i \cdot C_{t,i} \cdot \rho \cdot \frac{1}{60^2} \cdot d_i^4 \\ -x_i \cdot C_{t,i} \cdot \rho \cdot \frac{1}{60^2} \cdot d_i^4 \\ C_{p,i} \cdot \rho \cdot \frac{30}{\pi \cdot 60^3} \cdot d_i^5 \cdot \text{sign}(n_i) \end{bmatrix} \cdot \begin{bmatrix} n_1^2 \\ n_2^2 \\ n_3^2 \\ n_4^2 \end{bmatrix} \tag{5.5}$$

This approach is utilised for fixed pitch propellers. For variable pitch propellers, the rotational speed is constant and the thrust is controlled by the variable pitch angle β. In order to

convert Equation (5.5) for variable pitch propellers, the lookup tables for the thrust and power coefficient are linearised at the current pitch angle according to Equation (5.6).

$$C_t = C_{t,1} \cdot \beta + C_{t,0} \qquad C_p = C_{p,1} \cdot \beta + C_{p,0} \tag{5.6}$$

With the linearisation of both coefficients, Equation (5.5) is modified in order to solve the variable pitch angle. The resulting equation is solved iteratively. In each step, the lookup table is linearised at the new beta value. Because of the linear and quadratic characteristic of the air foil lift and drag coefficients, the iteration converges quickly after a few steps.

$$\begin{bmatrix} F_z \\ M_x \\ M_y \\ M_z \end{bmatrix} = \begin{bmatrix} \sum_i -C_{t,i,0} \cdot \rho \cdot \left(\frac{n_i}{60}\right)^2 \cdot d_i^4 \\ \sum_i y_i \cdot C_{t,i,0} \cdot \rho \cdot \left(\frac{n_i}{60}\right)^2 \cdot d_i^4 \\ \sum_i -x_i \cdot C_{t,i,0} \cdot \rho \cdot \left(\frac{n_i}{60}\right)^2 \cdot d_i^4 \\ \sum_i C_{p,i,0} \cdot \rho \cdot \left(\frac{n_i}{60}\right)^3 \cdot \frac{\text{sign}(n_i)}{\omega_i} \cdot d_i^5 \end{bmatrix} + \begin{bmatrix} -C_{t,i,1} \cdot \rho \cdot \left(\frac{n_i}{60}\right)^2 \cdot d_i^4 \\ y_i \cdot C_{t,i,1} \cdot \rho \cdot \left(\frac{n_i}{60}\right)^2 \cdot d_i^4 \\ -x_i \cdot C_{t,i,1} \cdot \rho \cdot \left(\frac{n_i}{60}\right)^2 \cdot d_i^4 \\ C_{p,i,1} \cdot \rho \cdot \left(\frac{n_i}{60}\right)^3 \cdot \frac{\text{sign}(n_i)}{\omega_i} \cdot d_i^5 \end{bmatrix} \cdot \begin{bmatrix} \beta_1 \\ \beta_2 \\ \beta_3 \\ \beta_4 \end{bmatrix} \tag{5.7}$$

For fixed pitch propellers, the rotational speed command is calculated by solving Equation (5.5) for given vertical force and given moments. For a variable pitch propeller, Equation (5.7) is solved for a variable pitch angle command, β. During hover flight, the advance ratio of the propellers is zero and the thrust and power coefficients are independent from the rotational speed.

After describing the forces and moments of the propellers, the equations of motion of a 6 DOF model are set up according to [182]. As the duration of the simulated manoeuvres is short and the vehicle speed is low, the assumptions of a flat and non rotating earth are included to simplify the equations. To describe the movement of the quadcopter, a second coordinate system is utilised, which is the North-East-Down (NED) system (index $_O$). As the name already reveals, the positive x-, y- and z-axis point towards north, east and downwards respectively. The origin of the NED system is fixed to the quadcopter center of gravity. This allows to track the travelled distance of the quadcopter in a more convenient way. For further simplification, the propulsive forces and moments and the gravitational force are the only considered effects and aerodynamic drag is neglected. The balance of forces is shown in Equation (5.8).

$$\begin{bmatrix} \dot{u} \\ \dot{v} \\ \dot{w} \end{bmatrix}_O = \frac{1}{m} \cdot X_{OB} \cdot \begin{bmatrix} 0 \\ 0 \\ F_z \end{bmatrix}_B + \begin{bmatrix} 0 \\ 0 \\ g \end{bmatrix}_O \tag{5.8}$$

The equation describes the linear acceleration of the quadcopter in the NED system. The left side of the equation shows the velocity components [u,v,w]. The vertical force F_z has been derived in the bodyfix coordinates. Thus, the transformation matrix X_{OB}, which is a function of the euler angles, is necessary to transform the force into the NED system [182]. The gravitational acceleration is modelled by a constant one dimensional acceleration perpendicular to the surface. The balance of moments is shown in Equation (5.9).

$$\begin{bmatrix} \dot{p} \\ \dot{q} \\ \dot{r} \end{bmatrix}_B = J^{-1} \cdot \left(\begin{bmatrix} M_x \\ M_y \\ M_z \end{bmatrix}_B - \begin{bmatrix} p \\ q \\ r \end{bmatrix}_B \times J \cdot \begin{bmatrix} p \\ q \\ r \end{bmatrix}_B \right) \tag{5.9}$$

The left side of Equation (5.9) describes the time derivatives of the bodyfix turn rates of the quadcopter [p,q,r]. The right side represents the bodyfix moments and the turn rates. By integrating all accelerations, the velocity and turn rates are obtained. To calculate the time

derivative of the euler angles, the turn rates are utilised in the strap down relation, which are given in Equations (5.10) and (5.11).

$$
\begin{bmatrix} \dot{\Phi} \\ \dot{\Theta} \\ \dot{\Psi} \end{bmatrix} = X \cdot \begin{bmatrix} p \\ q \\ r \end{bmatrix}_B
\tag{5.10}
$$

$$
X = \begin{bmatrix} 1 & \sin(\Phi) \cdot \tan(\Theta) & \cos(\Phi) \cdot \tan(\Theta) \\ 0 & \cos(\Phi) & -\sin(\Phi) \\ 0 & \frac{\sin(\Phi)}{\cos(\Theta)} & \frac{\cos(\Phi)}{\cos(\Theta)} \end{bmatrix}
\tag{5.11}
$$

These equations describe the quadcopter flight dynamics on a flat and non rotating earth with constant gravitation and without wind and aerodynamic drag.

In the following section the design of an appropriate flight controller is described. Conventionally, the flight controller of quadrocopters is implemented in cascaded loops. The inner loop is an attitude controller, which controls the orientation of the vehicle. This controller utilises the error between target euler angles and measured euler angles from an on board inertial measurement unit. Based on this error, the attitude controller calculates target moments, which are translated into a speed command for the electric motors according to Equation (5.5). To remove the coupling terms in Equation (5.9), the controller is based on non linear dynamic inversion of the system dynamics [183]. This significantly reduces the complexity of the controller design and improves the utilisation of linear controllers. To apply non linear dynamic inversion, the system dynamics must be known in detail. With this knowledge, the controller input is adjusted in order to cancel out the coupled system dynamics and to obtain a linear system, which is then controlled by a linear controller. Equation (5.12) shows the resulting target moments, which are commanded by the controller. The linear target moment $\tilde{M}$ is calculated from the euler angle error by the attitude controller, which is implemented as an PD controller.

$$
M = \begin{bmatrix} p \\ q \\ r \end{bmatrix}_B \times J \cdot \begin{bmatrix} p \\ q \\ r \end{bmatrix}_B + J \cdot X^{-1} \cdot \left(-\frac{\delta X}{\delta t} \cdot \begin{bmatrix} p \\ q \\ r \end{bmatrix}_B + \tilde{M} \right)
\tag{5.12}
$$

The attitude controller controls three degrees of freedom. Equation (5.5) additionally requires a vertical force to solve the rotational speed of four propellers. The fourth parameter is the vertical force of all propellers and is obtained by a vertical speed controller. This controller is based on the equilibrium condition of the vertical forces. During hover, the vertical forces can be calculated with the quadcopter mass and the orientation according to Equation (5.13).

$$
F_z = \frac{m_{\text{quad}} \cdot g}{\cos(\Phi) \cdot \cos(\Theta)}
\tag{5.13}
$$

To perform a vertical climb manoeuvre, the resulting thrust force must be increased over the value from Equation (5.13) and vice versa. The vertical speed controller is implemented as a PI controller. The gain parameters of both controllers are defined to obtain a short oscillating system response to show the effects and limitations of the propulsion system and to exclude dynamic effects from the controller.

5.1.3 Mission performance

In this section, the quadcopter mission performance is analysed to assess the applicability of the three propulsion systems that have been introduced in chapter 4. During operation, the

quadcopter only hovers at the same position at constant altitude. The mechanical subsystem is designed according to the reference values from Table 3.1. The propeller thrust level is derived from a TWR of 1.1. The resulting propeller diameter is the basis for the sizing of the quadcopter structure according to Equation (5.1). The propulsion system is designed according to the power requirements of the four motor-rotor systems, the reference values for each component, the reference values from Table 4.1 and a hover time specification. According to the findings in chapter 3.4, a gear stage is included in the motor-rotor system in order to reduce the mass of the electric motor.

The mission performance of a quadcopter is defined by the payload capability and the available hover time. To assess the applicability of the three propulsion systems, three different quadcopters are designed for a given payload and hover time combination. The resulting quadcopter mass is the metric to compare the three propulsion systems with each other. Figure 5.2 shows the result of the mission performance analysis. The abscissa and the ordinate show the hover time and the payload capability respectively. The figure shows three contour plots, which represent the quadcopter masses for battery based, fuel cell based and hybrid propulsion systems. In the study, quadcopter masses up to 160 kg have been investigated.
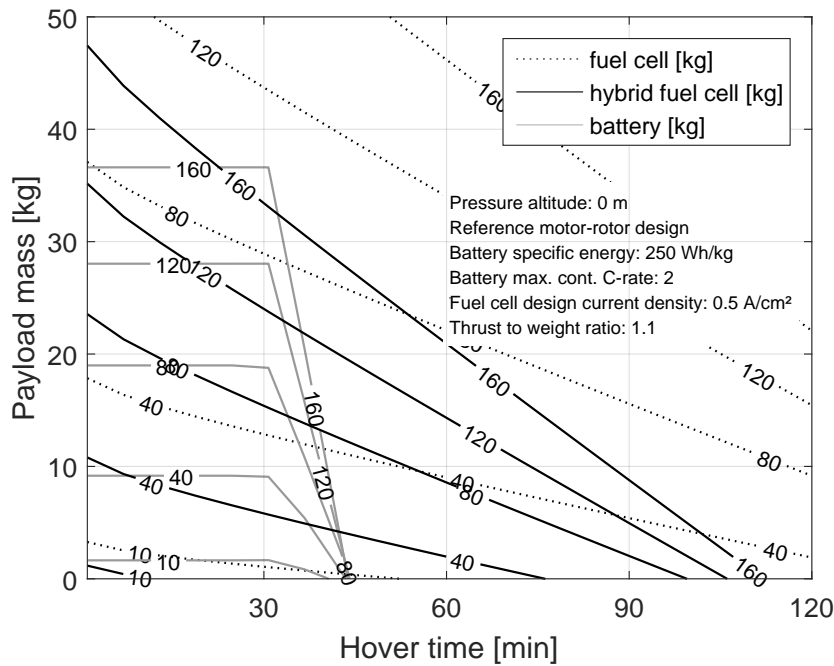
Figure 5.2: Quadcopter payload hover time diagram

The study revealed, that the reference energy density of batteries is too low to converge to a meaningful payload design. Thus, the battery energy density is increased from 175 to 250 $\frac{Wh}{kg}$, which corresponds to the latest state of the art, high energy lithium battery cells. All remaining battery parameters are not modified. The plot shows that battery based systems provide a constant payload capability up to a hover time of roughly 30 minutes. Within this range, the battery is designed according to the power requirements. For longer hover times, the battery is designed according to the energy requirements and the payload capability decreases significantly. A hover time of roughly 45 minutes is the ultimate hover time for battery based quadcopters, which are designed and operated according to the presented assumptions.

According to the findings on fuel cell design in chapter 4.2, the design current density is optimised within the range of 0.2 to 0.5 $\frac{A}{cm^2}$. Fuel cell based systems show significantly higher payload capabilities and longer hover times than battery based systems. The plot shows that the higher the payload requirements are, the higher is the mass benefit of fuel cell based systems. For small quadcopters with less than 10 kg, battery based systems show a mass benefit over fuel cell based systems. The significant drawback of fuel cell based systems is the poor peak power performance, as identified in the assessment of fuel cell systems 4.2.3. The investigations on hybrid propulsion systems has shown that the supplementary supercapacitor enables the system to provide similar peak power as battery systems. Therefore it is assumed, that the hybrid propulsion system is very competitive to battery systems in terms of manoeuvrability. The mission performance shows that the supplementary supercapacitor reduces the payload capability and the available hover time of fuel cell based quadcopters. For small systems, the battery shows a clear mass benefit over the hybrid system. Even for high payload specifications, both systems show similar system masses. The significant benefit of the hybrid propulsion system is the longer available hover time. Whereas battery systems can not exceed 45 minutes, the hybrid propulsion system achieves hover times up to roughly 100 minutes.

Figure 5.2 clearly shows the advantage of fuel cell based quadcopters, when long hover times are required. The drawback compared to the battery is its high price, which has a significant impact on the choice of the energy storage. The author supposes that, although the quadcopter mass of fuel cell based systems is lower for high payload designs, the currently high prices of fuel cells will have a higher impact on the quadcopter price than the higher cost for larger electric motors, propellers and converters for battery based systems. Thus, the high cost of fuel cells will make battery based propulsion systems the first choice, whenever the mission time is short enough. In the next section, the applicability of the three propulsion systems is assessed with respect to the dynamic performance requirements of quadcopters.

5.1.4 Performance with and without motor-rotor dynamics

For quadcopter control design, it is conventionally assumed, that the motor-rotor dynamics are significantly faster than the vehicle dynamics and, therefore, the propulsion system dynamics are neglected. In order to proof the validity of this assumption, especially for large vehicles, the manoeuvrability of the quadcopter with propulsion system dynamics is further investigated in this chapter.

The agility of the quadcopter is determined by two manoeuvres with three quadcopter configurations. Similar to the previous studies, the rise time metric is utilised to measure the required time to fly the manoeuvres. The first manoeuvre is a roll movement, where the quadcopter must attain a 20 degrees bank angle, starting from a levelled hover flight condition. The rise time is assessed on the quadcopter bank angle response. The second manoeuvre is a vertical climb, where a target vertical velocity of 3 $\frac{m}{s}$ is commanded. Again, this manoeuvre starts from a steady and levelled hover flight operation. For this simulation, the rise time is derived from the vertical velocity response of the quadcopter. All three quadcopter configurations are designed according to the method from chapter 5.1.1 with battery based propulsion system, which is designed for a flight time of 20 minutes and a battery energy density of 250 $\frac{Wh}{kg}$. The motor-rotor system is designed according to the reference values from Table 3.1 and the propulsion system is designed according to the reference values from Table 4.1. Drag forces, which arise from wind or the quadcopter movement are not considered. The

only forces that act on the vehicle are the propulsive forces and the gravitational acceleration. For the first configuration, the propulsion system dynamics are entirely neglected. The commanded thrust signals of the flight controller are directly fed into the 6 DOF model. The second configuration is equipped with fixed pitch motor-rotor systems which are supplied by an ideal voltage source. The motor-rotor dynamics are included in the model, whereas the dynamics of the battery and the power converter are neglected. The third configuration is equipped with variable pitch motor-rotor systems which are supplied by an ideal voltage source, as well. Thus, only the dynamics of the variable pitch motor-rotor system is included for the propulsion system.

Simulations of the fixed pitch motor-rotor system in chapter 3.2 have shown, that the rise time increases with higher design thrust levels, which translates into slower flight dynamics of larger quadcopters. To analyse the impact of this trend on the quadcopter manoeuvrability and to investigate scaling effects, a parametric study on the quadcopter size and the proportional gain of the PD attitude controller is conducted for the bank manoeuvre. For the climb manoeuvre, the parametric study is conducted on the quadcopter size and the proportional gain of the PI altitude controller. The derivative and the integral gain values are kept constant. By increasing the proportional gain, the controller output increases, which results in a higher thrust output and a more agile flight dynamics. When the proportional gain is increased to high values, the system will show an oscillating response and even get unstable, when the gain is further increased. For both controllers, the reference gain values are selected in order to attain an oscillating, but converging system response, in order to reduce the impact of the controller dynamics on the system response and to show the limitations of the propulsion system. Moreover, the rise time can be measured more easily, when the target value is exceeded in an oscillation. Figure 5.3 shows the results of the parametric study on the roll manoeuvre.
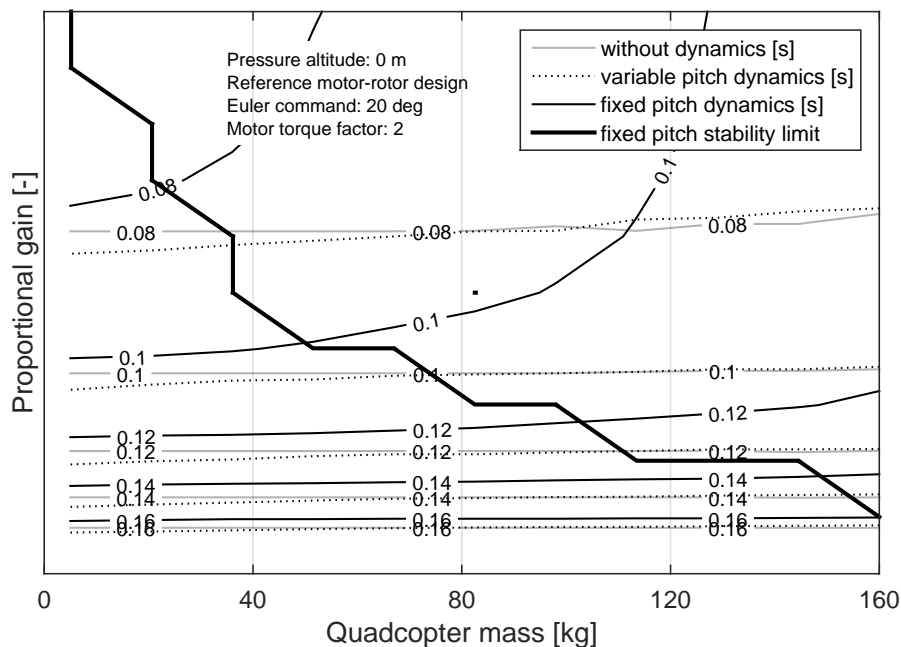

Figure 5.3: Rise time results for roll manoeuvre without, with fixed and with variable pitch motor-rotor dynamics

The abscissa shows the quadcopter mass. As the quadcopter mass changes, the propeller diameters change too, which results in a larger quadcopter dimensions according to the design method in chapter 5.1.1. Thus, the quadcopter inertia changes with the vehicle mass. The ordinate shows the proportional gain of the PD attitude controller. For this study, a maximum MTF of 2 is assumed. The system response of the first configuration (without propulsion system dynamics) is almost independent on the quadcopter size. As expected, higher proportional gains increase the thrust output and therefore reduce the required rise time to attain the 20 degree bank angle. The third configuration with variable pitch propellers shows a similar performance as the first configuration in the entire parameter space. This result is confirmed by the simulations of the variable pitch motor-rotor system in chapter 3.3, which show very quick thrust responses with rise times of a few milliseconds. The dynamics of the variable pitch mechanism is independent of the propeller design parameters, which means that it does not change with the quadcopter size. This mechanism represents an additional delay with an integrator in the closed loop system, which leads to a higher thrust output and therefore a higher roll rate. As the rise time metric only considers the change from 10 to 90% of the system response, it does not measure initial delays. Consequently, the rise time results of configurations with variable pitch propellers are a little bit lower than for the configuration without propulsion system dynamics. The fixed pitch configuration shows a slower system response than the other two configurations. This results from the inertia of the motor-rotor systems, which must be accelerated to a different speed. In agreement to the findings from the fixed pitch system simulations, the deviation from the first configuration is very low for small quadcopters. As the quadcopter size and mass increase, the dynamic performance of the fixed pitch system declines and so does the manoeuvrability of the quadcopter. Especially for high proportional gains, the deviation is significant, which shows the stability limit of the fixed pitch system.

At a certain proportional gain, the thrust response is so strong, that the flight controller cannot recover the roll rate and the quadcopter enters an unstable roll movement. The solid black line shows this stability limit of the roll manoeuvre. The line shows that the quadcopter gets unstable as soon as the fixed pitch system operates at its fastest thrust response. Up to the stability limit, the fixed pitch system delivers a similar performance as the other two configurations. Fixed pitch quadcopters cannot be operated beyond this stability limit, which shows that the dynamic performance and the agility of a quadcopter is a function of its mass. The stability limit of the variable pitch system has not been encountered in the examined parameter space.

For the vertical climb manoeuvre, a similar parametric study is conducted. The simulation is initialised at a levelled hover flight. A step command for a vertical climb with $3 \frac{\text{m}}{\text{s}}$ is passed to the flight controller and the rise time is utilised to assess the required time to achieve the vertical velocity. The available MTF is set to three. Figure 5.4 shows the results of the parametric study.

Again, the abscissa shows the quadcopter mass, which also represents the quadcopter size and inertia. The ordinate shows the proportional gain of the PI altitude controller. The three contour plots show the three quadcopter configurations without motor-rotor dynamics and with fixed pitch and variable pitch dynamics. Similar to the previous manoeuvre, the rise time results of the configuration without motor-rotor dynamics shows a constant performance, independent from the quadcopter size. For low proportional gains, the rise time results of all three configurations is similar, which indicates that the speed response is governed by the
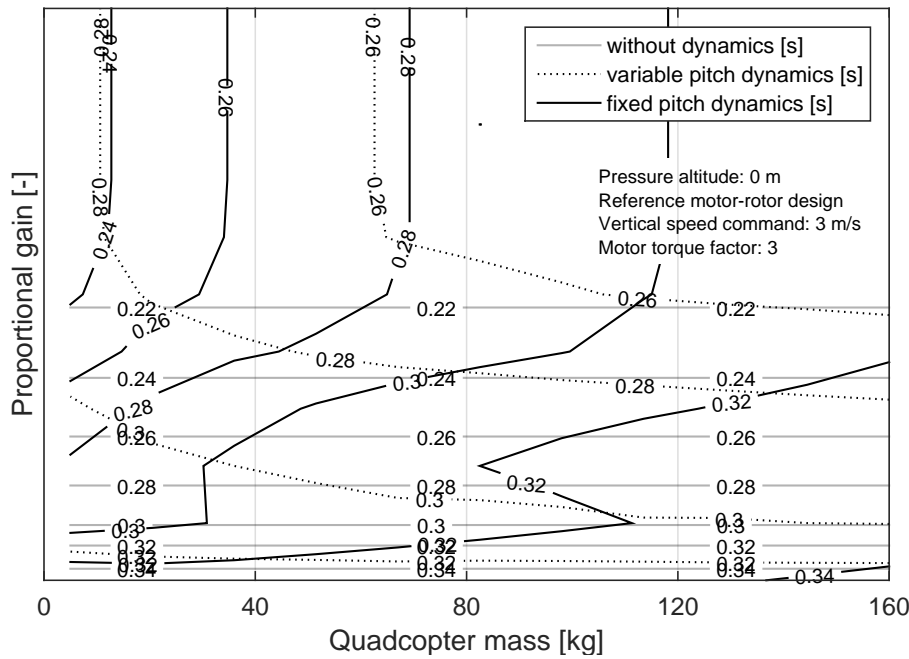
Figure 5.4: Rise time results for climb manoeuvre without, with fixed and with variable pitch motor-rotor dynamics

controller dynamics. As the proportional gain is increased, both configurations with motor-rotor dynamics show a transition zone up to a level where the rise time gets independent from the proportional gain. At this level, the propulsion system delivers its maximum output power during the acceleration of the vehicle. According to the contour plot for fixed pitch systems, the quadcopter size has an impact on the climb response. The plot shows that larger quadcopter require more time to reach the target vertical speed. The ragged shape of the contour lines in the transition zone of fixed pitch systems originates from the logarithmic scale of the ordinate. Similar to the fixed pitch configuration,the variable pitch configuration shows a transition and a maximum power zone. In contrast to the fixed pitch propeller, small and light quadcopters require a higher rise time for the vertical climb manoeuvre than large ones. This trend inversion originates from the lower motor design torque for variable pitch propellers. The design motor torque is smaller as the rotational speed of the propeller is constant and the motor is designed for this speed. During hover at rated thrust, the rotational speed of the fixed pitch propeller is lower than its design speed. Therefore, the motors of variable pitch propellers are designed for a higher speed and a lower torque.

5.1.5 Impact of Propeller Design Parameters on Quadcopter Agility

In this section, the impact of the propeller design parameters on the quadcopter agility is investigated. To measure the agility of the quadcopter, the rise time metric is applied on the bank and the vertical climb response, similar to the previous section. For this study, a battery based propulsion system is designed with the reference design parameters from Table 4.1. Based on this reference design, a parametric study on the propeller design parameters is conducted. The take-off mass is kept constant in this study. The payload inertia is calculated by a cuboid assumption with a homogeneous density of $2000 \frac{kg}{m^3}$. The quadcopter design parameters are the reference values from Table 5.1. The motor-rotor system is designed ac-

cording to the reference values from Table 3.1 and the structure is designed according to the method from chapter 5.1.1.

Take-off weight	TWR	altitude	max. MTF	Hover time	Size factor k_{quad}
kg	-	m	-	min	-
100	1.1	0	2	20	1.05

Table 5.1: Reference design for constant mass design study

In a first step, the impact of the three main propeller design parameters is analysed with a battery based propulsion system. These are the blade loading, f_{load}, the pitch h_{prop}, and the tip speed, v_{tip}. The thrust level is given by the quadcopter mass and the TWR. Figure 5.5 shows the results of the sensitivity study in the form of a matrix plot of partial dependencies.
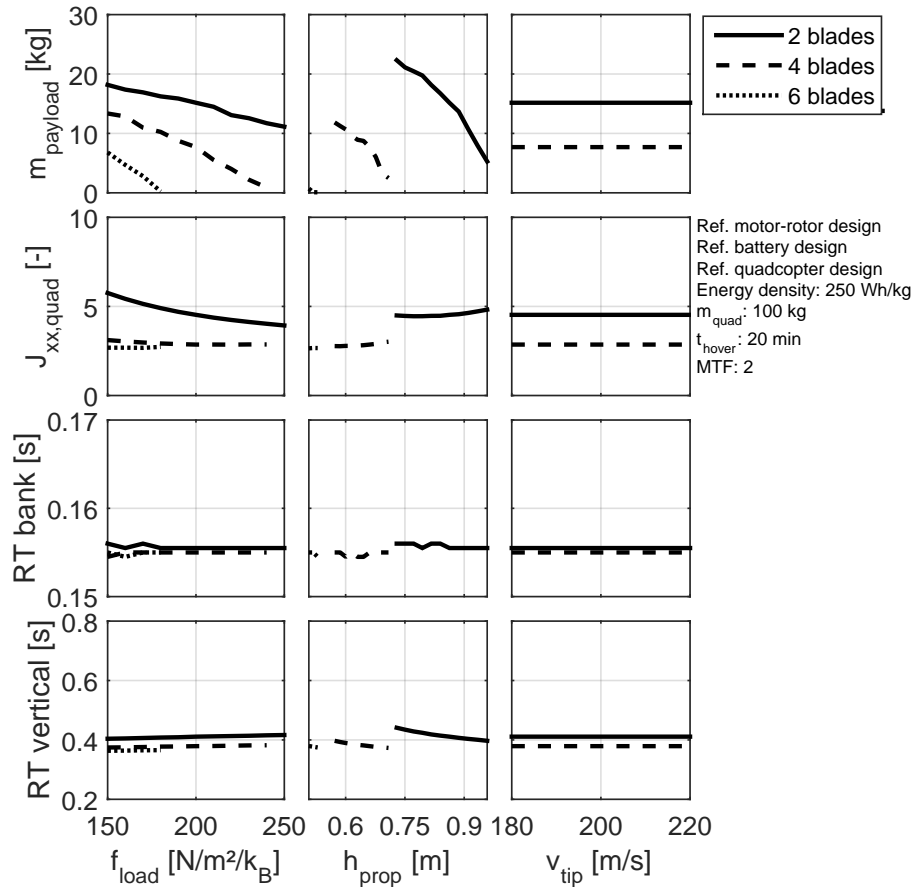
Figure 5.5: Impact of fixed pitch propeller design on dynamic performance

The three propeller design parameters are plotted in the three columns. Figure 5.5 shows four output parameters, which are the payload mass, m_{payload}, the quadcopter inertia around the x-axis of its bodyfix coordinate system, $J_{\text{xx,quad}}$, which is relevant for the roll manoeuvre, the rise time for attaining a 20 degrees bank angle and the rise time to accelerate to a vertical speed of 3 $\frac{\text{m}}{\text{s}}$ from levelled hover flight. Furthermore, each plot shows the results for two blade, four blade and six blade propellers. As previously defined, the blade loading is related

to the propeller diameter and, therefore, it has an impact on the quadcopter mass and inertia. As the blade loading is reduced, the required mechanical power is reduced, which leads to a reduction of the propulsion system mass and a higher payload capacity. Moreover, as the blade loading is reduced, the propeller and the quadcopter size increase, which results in a higher inertia around the bodyfix x-axis. An increasing propeller diameter results in a larger lever arm to the quadcopter CG, which results in a higher moment. The third plot shows the rise time for the roll manoeuvre, which is a rotatory manoeuvre that is characterised by low kinetic energy. Therefore, the application time as well as the amplitude of the roll moment is small and the according differential thrust level is low. Consequently, the impact of the propeller design parameters tends to be low on this manoeuvre. However, the design parameters have a double impact on the roll manoeuvre rise time, as they impact the vehicle inertia and the thrust response. The plot shows, that the rise time result is almost independent from the blade loading. This indicates as well, that the effect of the larger inertia is compensated by the larger lever arm of the propellers. The fourth plot shows the rise time results for the vertical climb manoeuvre, which is a translational manoeuvre, that requires a higher kinetic energy and a long application time of the according thrust. In contrast to the roll manoeuvre, the trends of the vertical manoeuvre only account for the thrust response, as the quadcopters are designed with a constant mass. The lower plot shows an increasing rise time for higher blade loadings, which confirms the simulations of the motor-rotor subsystem with fixed pitch propellers in chapter 3.2. The interval from 150 to 250 $\frac{N}{m^2}$ translates into a relative change of 2.8% of the rise time. In summary, the blade loading has to be minimised to maximize payload and to enable a quick climb response. The blade loading has only a minor impact on the agility of roll manoeuvres, as the required kinetic energy is very low.

The middle column shows sensitivity on the propeller pitch. The results from chapter 3.2 show that the propeller pitch is a trade-off parameter between low power requirements and a fast thrust response. On aircraft level, this result is confirmed. A low propeller pitch is favourable for a low power design, which results in a low battery mass and a high payload capability. On the other hand, the more powerful motor design of high pitch propellers is advantageous for a quick acceleration and low rise times, especially for the vertical climb manoeuvre. Within the investigated velocity span from Ma 0.05 to 0.1, the rise time varies about 10.8% for the vertical climb manoeuvre. The right column shows that the propeller tip speed does not have any noticeable impact on the quadcopter payload and inertia. Thus, the tip speed does not impact the power requirement and the efficiency of the propeller, which reflects previous results from chapter 3.2. This previous study on component level showed, that the tip speed has a considerable impact on the rise time results. The constant rise time results for both flight manoeuvres show, that the motor-rotor dynamics only have a minor impact on the agility of the quadcopter. Consequently, the variations of the rise time primarily result from variations of the quadcopter inertia, rather than the thrust response of the mechanical subsystem. To investigate the impact of the design parameters of variable pitch propellers, the same parametric study is conducted on variable pitch quadcopters and the results are shown in Figure 5.6.

The sensitivity characteristics of variable pitch quadcopters on the propeller design parameters are similar to the fixed pitch quadcopters. However, the blade loading results show that the variable pitch propeller is more efficient during hover than the fixed pitch propeller, which results in a higher payload capacity. The pitch results show a similar characteristic to fixed pitch quadcopters. Similar to the fixed pitch configuration, the propeller tip speed has no impact on the quadcopter design or agility. The main difference to the fixed pitch
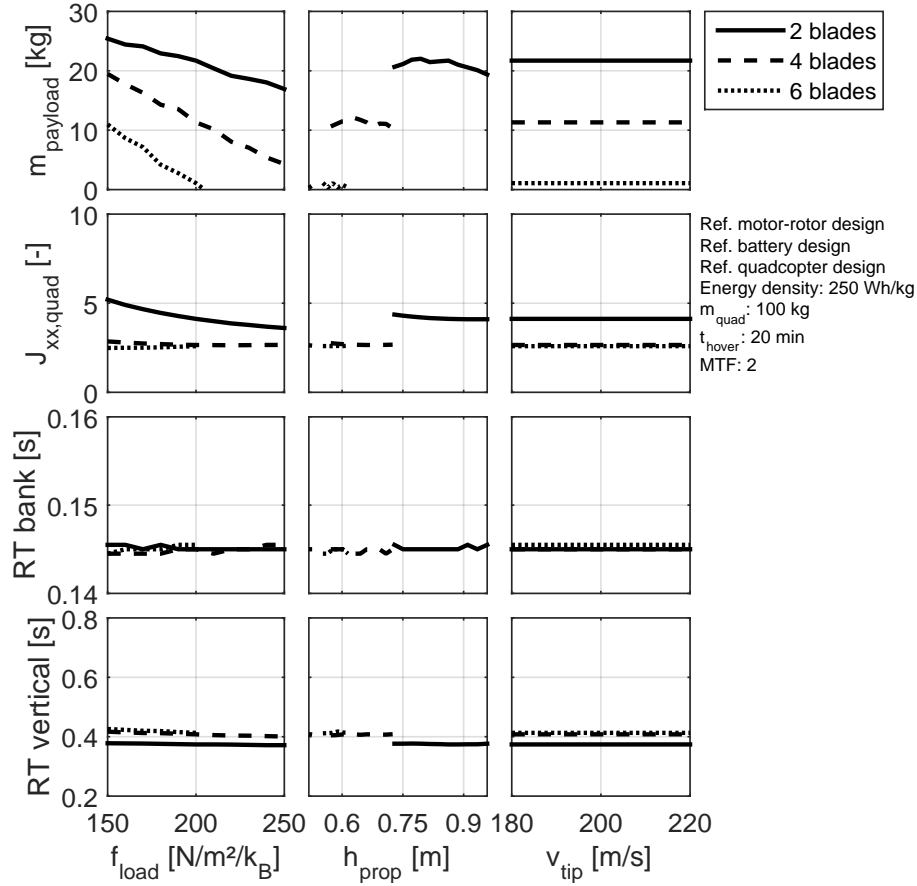
Figure 5.6: Impact of variable pitch propeller design on dynamic performance

propeller version is that the rise times results of both manoeuvres are almost decoupled from the propeller design parameters. This is reasonable, as the thrust response of the motor-rotor system is independent from the design parameters. Compared to the agility of fixed pitch quadcopters, the roll manoeuvre requires less time. In average, the variable pitch version is 6.5% faster than the fixed pitch version, which originates from the faster thrust response of the motor-rotor system. The rise time results for the vertical climb manoeuvre are 16.5% faster that the rise time results for the fixed pitch version. This reflects the component level simulations from chapter 3. Compared to the results of fixed pitch quadcopters, the variable pitch propeller configuration shows a significantly lower impact on the payload capacity. This originates from the variable pitch mechanism, which adjusts the blade angle of attack for the required thrust level, no matter how much the blade is twisted. The detailed shape of the curves is the result of the propeller design and the aerodynamic coefficients of the propeller airfoil. Similar to the blade loading, the propeller pitch has no noticeable impact on the rise time results for both manoeuvres. The tip speed shows no impact on the quadcopter design and its performance, just like for fixed pitch propellers. Figure 5.7 shows the results for a parametric study on the TWR, the quadcopter mass and the maximum allowed MTF.

The left column shows the sensitivities on the design TWR. The upper plot shows that higher TWRs result in lower payload capacities. The reason is the increasing propulsion system mass and a lower efficiency during hover, which leads to larger batteries. The same rationale explains the significant increase of the inertia with higher TWRs. As four blade
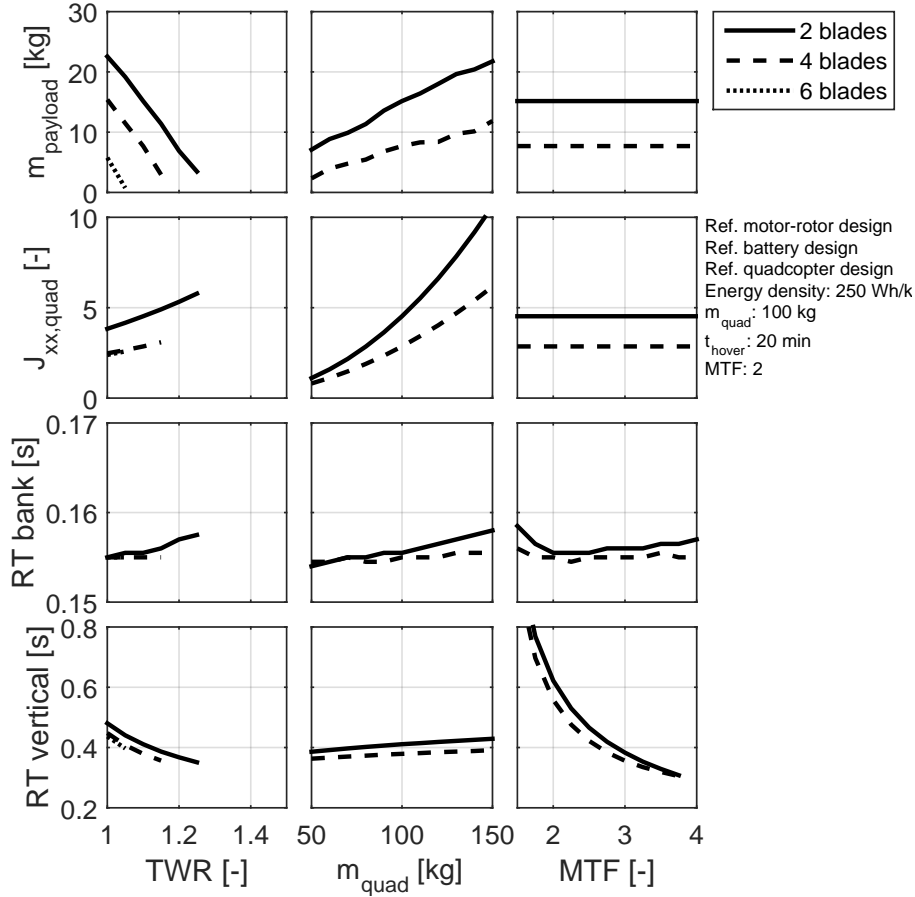
Figure 5.7: Impact of fixed pitch quadcopter design parameters on dynamic performance

propellers have a smaller diameter and a lower payload capacity, the effect is most significant for two blade propellers. The third plot confirms that the rise time of the roll manoeuvre depends significantly on the inertia. The rise time for the climb manoeuvre benefits from higher TWRs, as more thrust is available to accelerate the quacopter. As soon as the payload capacity drops to zero, the design calculation is aborted. Similar to the propeller pitch, the TWR is a trade-off parameter between high payload capacity and high agility.

The middle column shows the impact of the quadcopter mass on the output parameters. The payload capacity shows an almost linear characteristic versus the quadcopter mass. The inertia, however, increases considerably with the quadcopter mass, which originates from the relation between the quadcopter mass and size. The strong increase of the quadcopter inertia results in higher rise time results for the bank manoeuvre. This trend is further supported by the larger motor-rotor systems and the associated slower thrust response. The results for the vertical climb manoeuvre show increasing rise times for larger quadcopter masses. As the TWR and the quadcopter mass are constant, the reduced climb performance results only from the reduced thrust response of the motor-rotor system. The right column shows the impact of the MTF on the dynamic performance. As it has no impact on the quadcopter design, the payload capacity and the inertia are not affected. The bank manoeuvre rise time does not change noticeably with the MTF, which originates from the low kinetic energy characteristic and the fact that only two propellers are accelerated and the other two are de-

celerated. Consequently, a high power motor does not improve the roll agility considerably. The lower plot shows that the required rise time for the vertical climb manoeuvre can be significantly reduced by increasing the MTF. In contrast to the roll manoeuvre, a lot more energy is required and all propellers are accelerated. Therefore, a higher MTF results in a faster thrust response as well as a higher thrust level, which leads to significantly reduced rise times. By increasing the MTF from 2 to 3.3, which is the highest value before the battery is cut off, the rise time can be reduced by 30%. The same parametric study is conducted on variable pitch quadcopters and the results are shown in Figure 5.8.
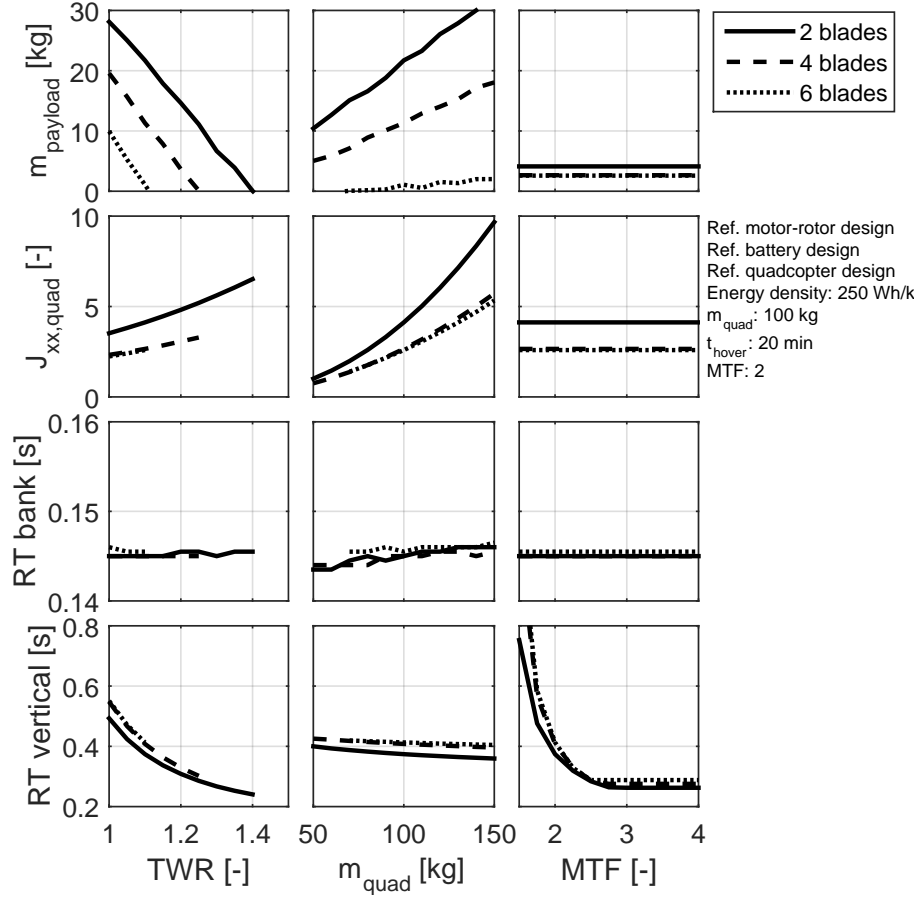
Figure 5.8: Impact of variable pitch quadcopter design parameters on dynamic performance

The results for the TWR show, that the payload capacity is more sensitive to the TWR, which results from the higher efficiency of the variable pitch propellers during hover operation. As the quadcopter size is related to the propeller design thrust, the quadcopter inertia is increased with higher TWR values. Similar to the previous findings, the bank manoeuvre of the variable pitch propeller is about 6.5% faster than for fixed pitch propellers. A rise time deviation for high TWR values is not observed, because the inertia is smaller than for fixed pitch propellers. The rise time for the vertical climb manoeuvre shows higher values as for the fixed pitch version, which results from the lower thrust output with the same maximum MTF. Similar to the fixed pitch version, the characteristic of the payload capacity over the quadcopter size is almost linear and the inertia grows non linearly with the quadcopter size. The rise time results for the bank manoeuvre show a similar characteristic as for the fixed

pitch version with the identified reduction of 6.5%. Again, the trend towards longer rise times results from the increasing inertia. As the thrust response depends only on the dynamics of the variable pitch mechanism, the climb rise time does not change with the quadcopter size. Thus, utilising variable pitch propellers can reduce the rise time for climb manoeuvres by up to 25% for large quadcopter vehicles. For roll manoeuvres, the variable pitch propeller does not offer significant advantages. The MTF has no impact on the design of the quadcopter, whereby the payload capacity and the inertia are independent from the MTF. Similar to the fixed pitch version, the MTF has no significant impact on the roll manoeuvre rise time. The vertical climb rise time is very sensitive to the MTF because of the faster thrust response and the higher thrust level. Increasing the MTF from 2 to 4 is not as beneficial as for the fixed pitch propeller, however it still yields a reduction of 22%.

For the battery system, the pack voltage level is the only relevant design parameter, which is not related to the cell characteristics. As the simulations in chapter 4.1.1 have shown, that, for large battery packs, the battery voltage has no impact on the pack mass, there is no battery design parameter that is of further interest for the quadcopter agility.

5.1.6 Agility of Fuel-Cell Based Quadcopters

In this chapter, the agility of quadcopters with fuel cell based propulsion systems is investigated and the sensitivity on fuel cell design parameters is assessed. The fuel cell is the only energy storage in the propulsion system and it must deliver the entire electric power. Like in the previous section, the agility is measured with the roll and the vertical climb manoeuvre. The mechanical subsystems and the quadcopters are designed according to the respective reference values. In chapter 4.2.2, the impact of the fuel cell design parameters on the component mass and efficiency as well as the power converter mass and efficiency are investigated. The result of this analysis was that the design current density is an important trade-off parameter and has to be optimised on aircraft level. Moreover the fuel cell stack voltage was identified to have a minor impact on the mass of the stack and the power converter. To investigate the impact of the stack voltage level, the TWR as well as the MTF, a parametric study is conducted on these parameters. For this study, only two blade propellers are simulated. The payload capacity, the x-axis inertia of the bodyfix frame and the two rise times for the roll and the vertical climb manoeuvre are the output parameters. Figure 5.9 shows the results of the parametric study and each plot contains the simulation results of fixed pitch and variable pitch propellers.

The left column of the matrix plot shows the impact of the design TWR on the output parameters. The characteristics are similar to the results of previous chapter, which where obtained with battery based propulsion systems. The higher specific energy of hydrogen increases the payload capacity of fuel cell based quadcopters over the ones with batteries. Fuel cell based quadcopters have a 34% higher payload capacity as battery based quadcopters. The result for the inertia is very similar to battery based systems and can be explained with the same rationale. As the thrust response of fixed pitch propellers get slower with higher design thrust levels, an increasing TWR results into a reduced agility and longer rise times for the roll manoeuvre, as shown in the third plot. The variable pitch propeller has a constant thrust response, which results in constant rise time results. Also the rise time results for the vertical climb manoeuvre show no considerable difference to the results of battery based quadcopters. With higher TWRs, more thrust is available to accelerate the quadcopter. Consequently, the rise time results are reduced for higher TWR. The kink in the curve of the fixed pitch propeller at low TWRs indicates, that the first cut off limitation is reached and
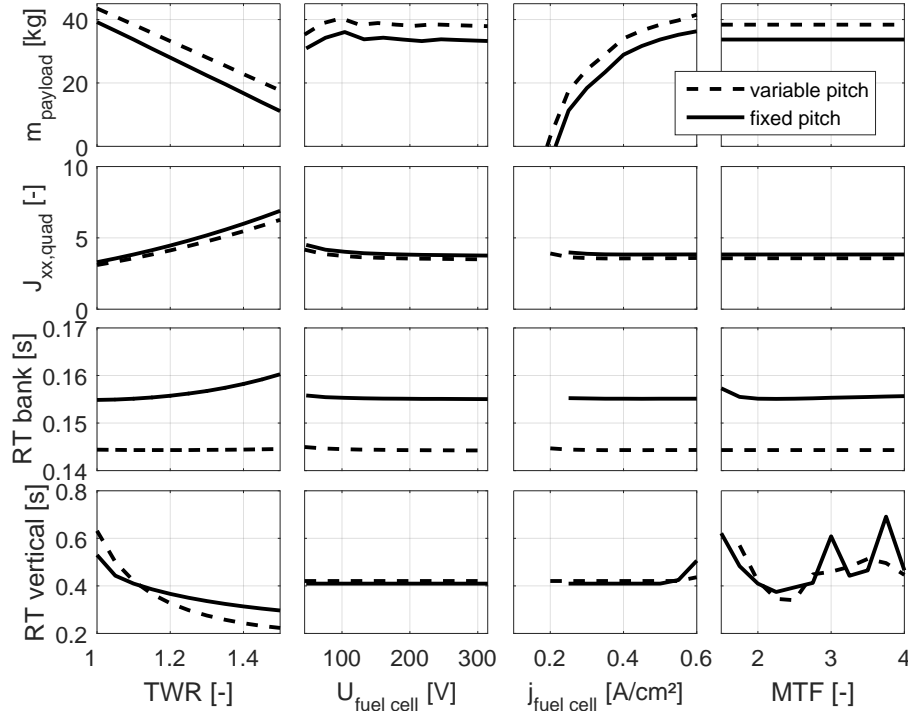
Figure 5.9: Impact of fuel cell design parameters on dynamic performance

that the available power is reduced.

The second column shows the impact of the fuel cell stack voltage. The results for the payload capacity reflect the same characteristics as for the fuel cell stack mass and the power converter mass, which were presented in Figure 4.8. The variable pitch quadcopter shows higher payload capacities than its fixed pitch counterpart. The sensitivity of the inertia on the stack voltage is very low. The stack voltage has no noticeable impact on the rise time for the roll manoeuvre, which can be seen from the rise time results, which only reflect the trend of the vehicle inertia. Within the examined stack voltage interval, the rise time for fixed pitch propellers varies less than 0.5%, whereas variable pitch configurations are even less sensitive to the stack voltage level. The simulation of the vertical climb manoeuvre shows that the rise time is independent from the stack voltage level. This confirms as well, that the rise time results for the roll manoeuvre just reflects the inertia variation of the quadcopter. Consequently, the fuel cell stack voltage level has no impact on the thrust response.

The third column shows the sensitivity on the fuel cell design current density. Previous studies on system level in chapter 4.2.2 showed, that the current density has a significant impact on the stack mass and efficiency. The strong sensitivity of the fuel cell mass on the design current density is directly reflected by the payload capacity. As the current density is reduced, the membrane area and therefore the stack dimensions increase significantly, which results in a higher fuel cell stack mass and lower payload capacity. The design current density does not contribute significantly to the vehicle inertia, as the fuel cell is mounted at the quadcopter CG. The results for both manoeuvres show that the design current density has no impact on the quadcopter agility. The rise time results for the roll manoeuvre show the typical offset that has been identified for battery based systems, which results from the faster

thrust response of variable pitch propellers.

The right column shows the impact of the MTF on the four output parameters. The payload capacity and the inertia are independent from the MTF, as the MTF is no design parameter. Similar to the findings for battery based propulsion systems, the MTF has no significant impact on the roll performance of the quadcopter. For fixed pitch propellers, a slightly higher rise time is observed at low MTF of 1.5, which also has been identified for battery based systems. The variable pitch propeller shows constant rise time results, as the thrust response does not depend on the rotor kinetic energy. As the MTF defines the required peak power level, it has a significant impact on manoeuvrability of fuel cell based configurations. As identified in chapter 4.2.3, the fuel cell has a poor peak power capability, when designed at high current densities. Therefore, the high MTF values cause the fuel cell to run into the cut off limitation, which is reflected by the rise time results of the vertical climb manoeuvre. For MTFs up to 2, the continuous rise time results indicate that the fuel cell can deliver the peak performance. For higher MTFs, the fuel cell power is limited and the result curves show a scattered shape.

In summary, the design parameters of the fuel cell have no direct impact on the quadcopter agility. The manoeuvrability is mostly affected by secondary effects, that have an impact on the quadcopter mass and inertia. This, however, depends significantly on the integration of the fuel cell into the vehicle. The studies on the design TWR and the MTF have shown that these two parameters influence the performance during vertical climb manoeuvres. Moreover, the simulations have shown that the peak power limitation of the fuel cell admits MTFs up to 2 during short time intervals. In order to achieve a certain climb performance, the TWR must be increased accordingly, which results in a larger fuel cell design and a reduction of the payload capacity. In contrast to the lower agility, fuel cell based systems provide a 34% higher payload capacity as battery based systems, which can be a considerable benefit. In conclusion, fuel cell based propulsion systems provide enough peak power to stabilise quadcopters and perform slow manoeuvres. However, when highly agile manoeuvres are required, another propulsion system is required.

5.1.7 Manoeuvrability of Quadcopters with Hybrid Propulsion System

In this section, the manoeuvrability of quadcopters with hybrid propulsion system is discussed. The hybrid system consists of a fuel cell that is designed for the average power load and an additional supercapacitor, which delivers short time peak power for roll and climb manoeuvres. The system setup is further explained in chapter 4.3. For this study, the supercapacitor pack voltage is optimized for a minimum component mass. For the hybrid system, the same parametric study that has been conducted for the fuel cell system, is performed. The results are shown in Figure 5.10.

The upper row shows the sensitivity of the payload capacity on the TWR, the fuel cell design parameters and the MTF. The characteristics of all four plots are very similar to the results from the fuel cell based system. However, because of the additional supercapacitor, the propulsion system mass is higher, which results in a lower payload capacity. Compared to the battery based configuration, the hybrid system has a 4% lower payload capacity, which is the lowest of all three systems. The results for the quadcopter inertia and the rise time for the roll manoeuvre are identical to the results from the assessment of fuel cell based systems. The last row shows the results for the vertical climb manoeuvre. The rise time results of the hybrid system show, that similar manoeuvrability as for battery based quadcopters can be
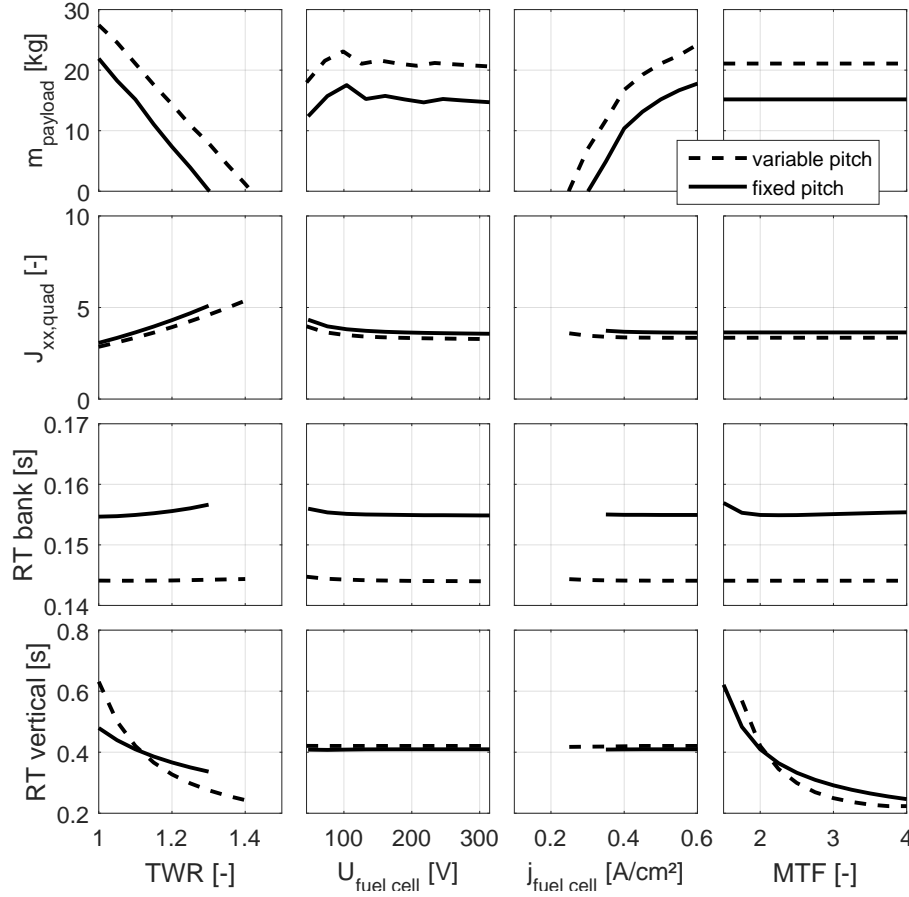
Figure 5.10: Impact of hybrid fuel cell parameters on dynamic performance

achieved. The right plot shows that the rise time for the vertical climb manoeuvre declines continuously up to a MTF of 4. The results of both propeller configuration do not show any cut off effects from the fuel cell.

In summary, by extending the fuel cell based propulsion system with an additional supercapacitor, the peak power performance of the propulsion system can be significantly increased and a similar manoeuvrability as of battery based configurations can be achieved. However, the mass of the supercapacitor represents a considerable drawback for the payload capacity of the quadcopter. In the last chapter, the performance of the three propulsion systems is investigated for combined manoeuvres with multiple step commands for all euler angles and the vertical speed, to assess the performance during arbitrary manoeuvres.

5.1.8 Combined manoeuvre performance

In the previous chapter, the agility of the quadcopter has been assessed with two simple and short time manoeuvres. In order to assess the agility and the command tracking capability for arbitrary or 'real life' manoeuvres, four multiple step command profiles, three for the euler angles and one for the vertical speed, are superposed and passed to the flight controller. The step commands for the bank and the pitch angle vary from -20 to 20 degrees and the yaw angle is varied from -10 to 10 degrees. The vertical speed command ranges from a descent with $1 \frac{m}{s}$ to a climb with $-3 \frac{m}{s}$ (given in the bodyfix coordinates). Similar to the previous

investigations, the control parameters are designed to cause a small overshoot and the maximum MTF is limited to 2. In this study, the examined quadcopters are designed according to the reference parameters from Table 5.1 and have a take-off mass of 100 kg. Figure 5.11 shows a comparison of fixed pitch quadcopters with the battery based, the fuel cell based and the hybrid propulsion system.
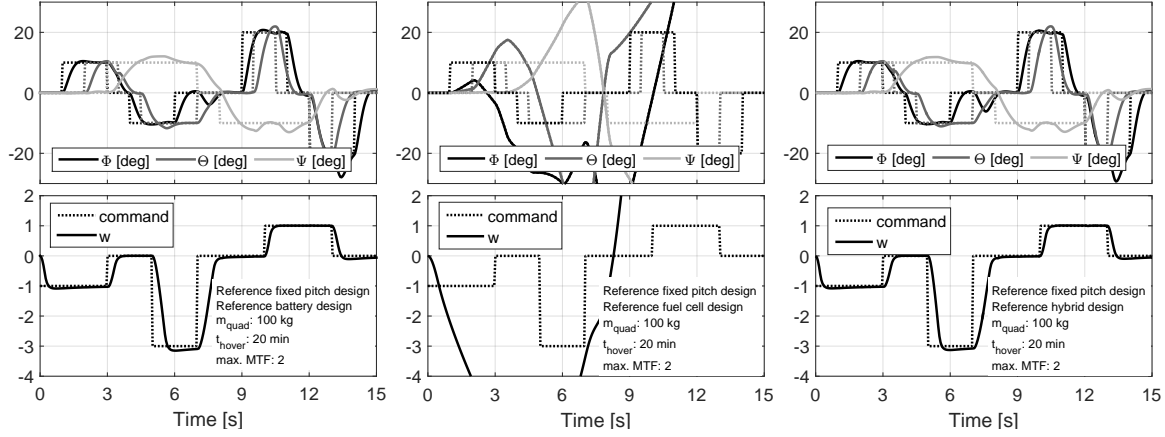
Figure 5.11: Combined manoeuvre performance of a fixed pitch quadcopter

The abscissa of the three plots shows the simulation time of the manoeuvre. The upper plots show the attitude command and the actual euler angles of the quadcopter in degrees. The lower plot shows the vertical speed command and the actual vertical speed of the vehicle, w, represented in the bodyfix coordinates. The command signals are plotted with the dotted lines and the vehicle euler angles and velocities are represented by the solid lines. The left plot shows the performance of the battery based quadcopter system, which is able to follow all commands with a meaningful precision. The middle plots show the performance results of the fuel cell based propulsion system. In contrast to the simulation of the basic manoeuvres, the fuel cell system gets unstable as the flight controller tries to follow two superposed attitude and one climb command. This results in a quick drop of altitude and heavy attitude oscillations, that cannot be recovered by the flight controller. The performance of the hybrid system is plotted on the right. The graphs show, that the hybrid system is able to follow the command with a similar precision as the battery based system. This is enabled by the additional supercapacitor of the propulsion system. The same study has been conducted on variable pitch systems with the same reference design. The results of this study is shown in Figure 5.12.

For the variable pitch quadcopter, the same controller parameters are utilised as for fixed pitch quadcopters. The abscissa shows the simulation time, the upper plots show the attitude command and the actual euler angles and the lower plots show the vertical speed of the quadcopter. The performance of the battery based system shows, that the system can follow all commands. The faster thrust response of the variable pitch propellers results in rise time reductions of up to 45% and the system overshoot is increased from 5 to 11% in average. Furthermore, the variable pitch version shows a more oscillatory response. The middle plot shows the performance of the fuel cell system. Similar to the fixed pitch version, the system gets quickly unstable and is not able to perform the commanded manoeuvre or even to maintain the flight altitude. However, the upper plot shows, that the variable pitch
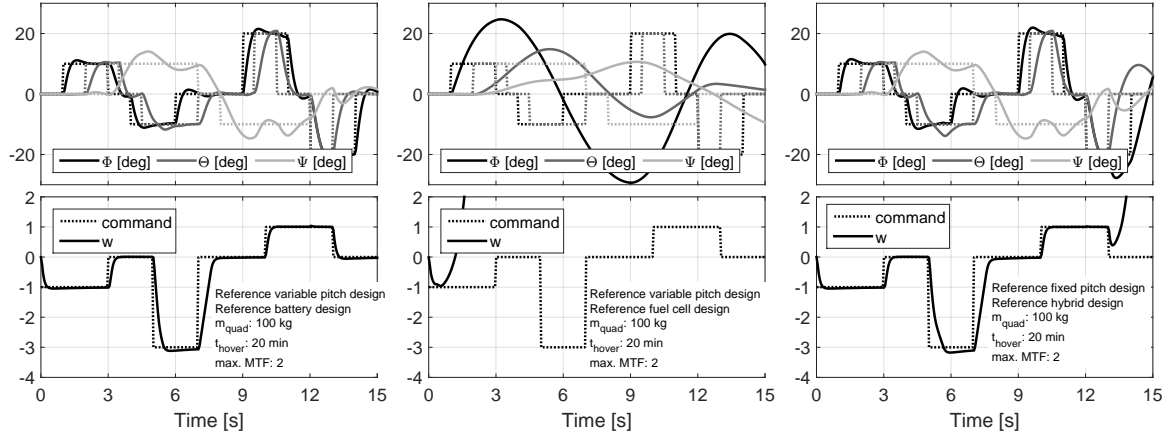
Figure 5.12: Combined manoeuvre performance of a variable pitch quadcopter

configuration is at least enable to prevent the attitude angles from diverging. The hybrid system on the right shows a similar performance as the battery based system. As the simulation proceeds, the supercapacitor state of charge decreases, which results in a lower output voltage and, therefore, a higher current drain from the fuel cell. As the supercapacitor is designed to deliver the system power for 10 seconds, the supercapacitor quickly discharges to a low level, which means that the current is mostly drained from the fuel cell. The last two seconds of the manoeuvre shows that the supercapacitor is deeply discharged and that the fuel cell cannot supply the required power for the last acceleration manoeuvre.

The investigation of the combined manoeuvre shows that fuel cells alone are not suitable for quadcopter performance requirements. Even a slow climb manoeuvre leads to the breakdown of the fuel cell. The battery based and the hybrid system can supply high enough peak power for aggressive manoeuvres up to the stability limit of the quadcopter controller. In the next chapter, the yaw control investigations for the Tecnam P2006T aircraft are presented.

5.2 Fixed wing aircraft performance

NASA and Joby Aviation are currently investigating the potential of distributed electric propulsion for general aviation aircraft. In their Leading Edge Asynchronous Propeller Technology project (LEAPtech), a concept aircraft is derived from the Tecnam P2006T twin engine aircraft and equipped with 18 electrically driven propellers, which are distributed along the leading edge of the wing. The benefit of this installation is that the propellers artificially increase the dynamic pressure on the wing, which is especially interesting during low speed manoeuvres [67]. This allows for a smaller and more slender wing design, which reduces the wetted area and the associated drag and leads to higher aircraft L/D ratios during cruise. During a 200 mph cruise flight, the L/D of the aircraft is claimed to increase from roughly 12 to 20 [6]. Figure 5.13 shows the original Tecnam P2006T on the left and the derived LEAPtech concept plane on the right.

As electric motors have a larger torque characteristic compared to internal combustion engines, their dynamic response to speed changes is much faster. The previous investigations on quadcopters has shown, that the dynamic response of electric motors is fast enough to stabilise large quadcopters and to perform agile manoeuvres. Because of the fast response

Figure 5.13: The Tecnam P2006T and the derived LEAPtech concept plane [6]

and the distribution along the wing, electric propulsion may be sufficiently agile to perform yaw stabilisation and control of a fixed wing a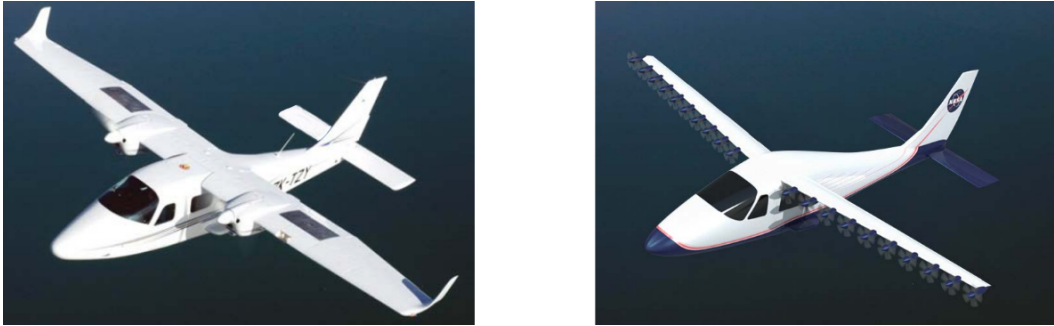ircraft by quickly producing high moments by differential thrust. To investigate the feasibility of this approach, the following chapter presents flight performance simulations of an electrified Tecnam P2006T aircraft which utilises 18 distributed propellers on the wing leading edge, just like the LEAPtech concept. In a first step, the Tecnam P2006T reference aircraft is briefly described and a model for the longitudinal and lateral movement of the electrified aircraft is derived from literature.

5.2.1 Tecnam P2006 Aircraft Modelling

The Tecnam P2006T is a four seat aircraft with a Maximum Take Off Weight (MTOW) of 1230 kg and a maximum range of 742 nm. The aircraft is driven by two Bombardier-Rotax 912 S3 piston engines, which provide a maximum take-off power of 73.5 kW each. The engines drive two MTV-21 variable pitch propellers from MT Propellers with a diameter of 1.8 m [184–187]. A detailed mass break down of the engine and its accessory components as well as a detailed performance analysis are published by Rotax [188, 189]. The mass breakdown gives a total weight of 76.5 kg per engine, including all accessory components and oil. The mass of the nacelle is estimated in combination with a mass break down from Nicolosi on the P2006T aircraft, which indicated a total weight of 197 kg for the engines group [190]. MT Propeller indicate a total mass of 12.5 kg for the variable pitch Propeller MTV-21, including the pitch governor.

A dynamic model for the longitudinal and lateral movement of the electrified version of the P2006T is derived from a state space model from Nicolosi, which he identified from flight test data and wind tunnel experiments [191]. This model is utilised in its original form to model the flight performance of the reference P2006T aircraft. For the electrified version, the model is modified to account for the changes of the propulsion system. Therefore, the bodyfix coordinates are utilised, which have their origin in the CG of the aircraft. Figure 5.14 shows the configuration of the basic P2006T model, which has been taken from the manufacturer specification sheet [185]. The position of the fuel tank is assumed to be in the center wing.

The CG is assumed to be located in the xz-plane of the aircraft. To obtain the x- and z-position of the CG, the longitudinal model of the P2006T aircraft is utilised. The x-position is derived from Nicolosi, who indicated that the flight test was conducted with the CG being at 19% of the mean aerodynamic chord. The z-position is calculated from a trim analysis. The flight test data show a trimmed flight condition with a stabiliser deflection of -5
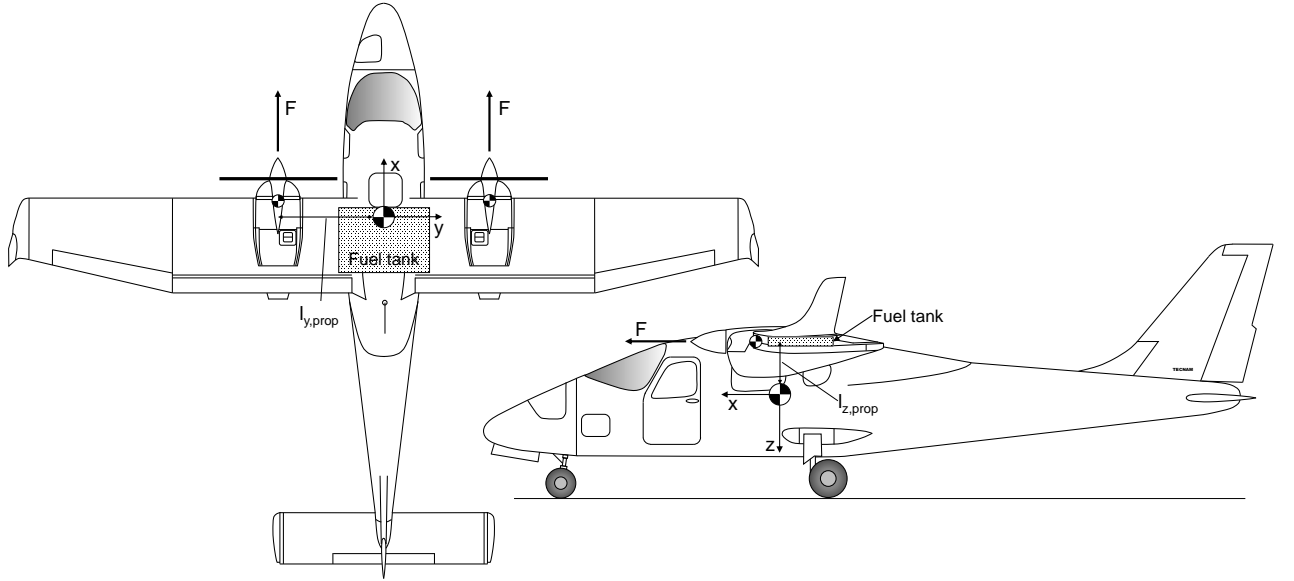
Figure 5.14: Model of the Tecnam P2006T Aircraft

degrees. With the state space model and the given aircraft data, the angle of attack, the required engine thrust as well as the aerodynamic moment can be calculated for a trimmed flight condition and the given stabiliser deflection. The condition, that the moment of the propulsion system must compensate the aerodynamic moment, finally gives the z-position of the CG. The identified Cm0 coefficient of -0.0922 from Nicolosi results in a lever arm that places the CG on the bottom of the aircraft cabin, which is no reasonable result for a high wing configuration with wing mounted engines. To obtain a meaningful position of the CG, the Cm0 coefficient is changed to -0.12, which results to a CG position in the center of the cabin, as indicated in Figure 5.14. The CG position of the fuel tank is considered to be in the xz-plane. The z-position is considered to be equal to the thrust vector and the tank thickness is chosen in that way that the tank fits well within the center wing. The x-position is small and has a minor impact on the aircraft CG position and the y-inertia. The tank has a capacity of 200 litres, which corresponds to roughly 160 kg of fuel. The CG of the engine-propeller combination is assumed to be located on the thrust vector line and in the yz-plane. The z-position is given by the previous trim analysis and the y-position is read out from the aircraft top view to +/- 1.7 m.

The propulsion system of the electrified P2006T aircraft is designed in order to enable the same flight performance as the reference aircraft. The P2006T has a practical ceiling of 15000 ft, where the aircraft must be capable to climb 100 ft/min. To meet the take-off distance specifications the aircraft requires a certain thrust level during take-off. To derive the take-off thrust of the P2006T, the here presented propeller model is utilised to predict the performance of the MTV-21 variable pitch propeller at minimum control speed and the maximum take-off power of the Rotax 912 S3 engine. A parametric study on the unknown propeller design parameters has shown, that the impact of these parameters on the take-off performance is very small. Figure 5.15 shows an average result of the MTV-21 propeller performance at sea level ISA condition at the minimum control speed.

At maximum take-off performance, the propeller delivers 1500 N of thrust at an efficiency
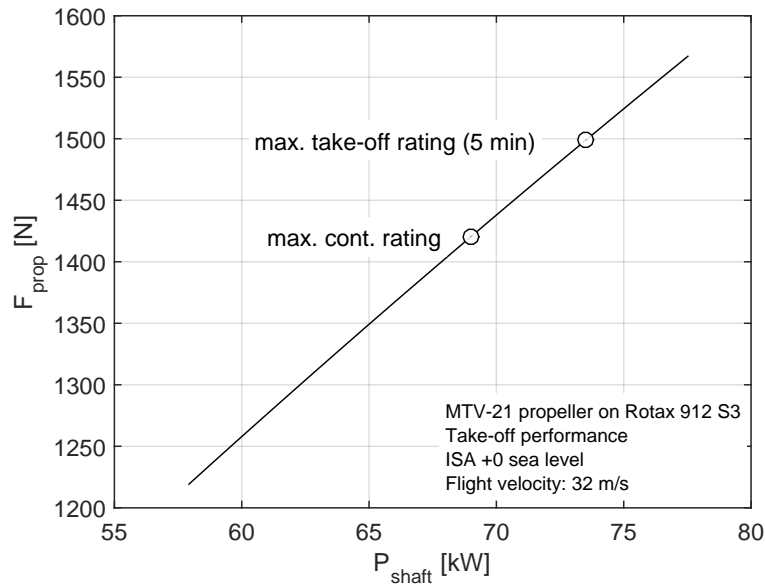
Figure 5.15: Performance of MTV-21 propeller on Rotax 912 S3 engine during take-off

level of roughly 68%. This corresponds to 3 kN take-off thrust at aircraft level. NASA presented the results of a test run of one of the LEAPtech propellers, which showed 164.4 N thrust at the same take-off conditions. This translates into 2.96 kN thrust on aircraft level for the LEAPtech aircraft. As the LEAPtech aircraft and the P2006T have a similar MTOW, a take-off thrust requirement of 3 kN is assumed for the electrified aircraft versions. The propellers of the electrified version are designed as fixed pitch propellers. When the thermal management of electric motors is neglected, the performance of electric motors does not decrease with altitude. Therefore, the gearbox, the electric motor and all succeeding components of battery based propulsion systems are sized to the maximum power operation. The propellers are designed for a minimum installed power by considering three operating points: take-off rotation, cruise and the top of climb performance at the ceiling altitude. Similar to the propellers of the LEAPtech aircraft, the fixed propellers are designed with three blades and a low tip speed for reduced noise emissions. Figure 5.16 shows the propeller performance for the minimum installed power condition for a two propeller configuration. The plot shows that the propeller reaches a peak efficiency at the cruise condition of the flight test.

To assess the manoeuvrability of the aircraft, the dynamic response of the control surface actuators has to be considered. Dorobantu measured and identified a model for the dynamic response of electric actuators, which is applied for aileron, stabiliser and rudder dynamics [192]. The aircraft model with the actuator dynamics has been validated against the flight test data from Nicolosi.

5.2.2 Impact of multiple electric propellers

In the next section, a parametric study on the number of propellers is conducted. The 18 propellers of the LEAPtech aircraft are considered as an upper limit. The lower limit is two, since the reference aircraft is a twin engine configuration. To keep aircraft symmetry according to the xz-plane, only even numbers of propellers are considered, and the thrust level is kept constant in order to achieve a similar take-off performance as the reference aircraft. The
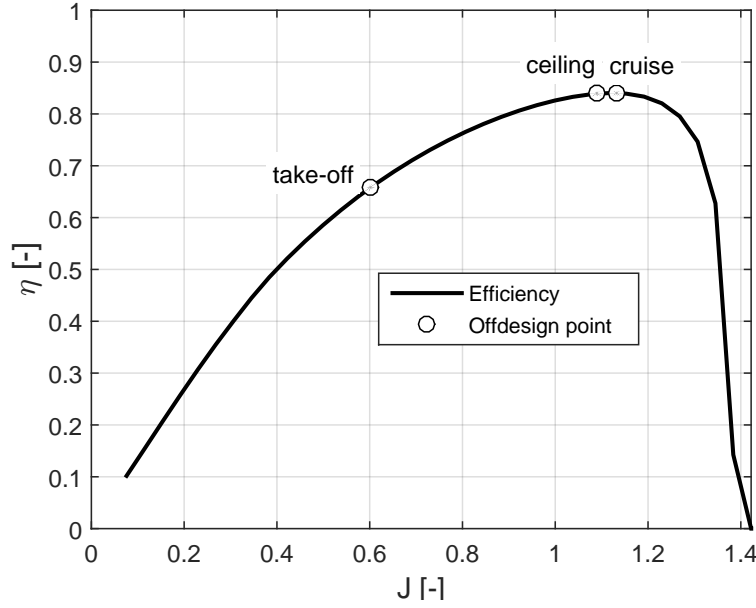
Figure 5.16: Fixed pitch propeller design and performance

propeller diameter is limited by two factors. The first limit is a maximum diameter of 1.8 m, which is the diameter of the reference propeller. The second limit is the semi wing span of the P2006T aircraft. It is assumed that the outer propeller does not exceed the wing tip and the inner propeller must not touch the cabin. The available semi wing span from the cabin to the wing tip is derived from the aircraft top view to 5 m, which must not be exceeded by the sum of all propeller diameters. Figure 5.17 shows a front view of the P2006T aircraft, where the left wing shows the maximum propeller size for 18 propellers and the right wing for six propellers. The plot shows very well that the available propeller disk area decreases as the number of propellers increases.
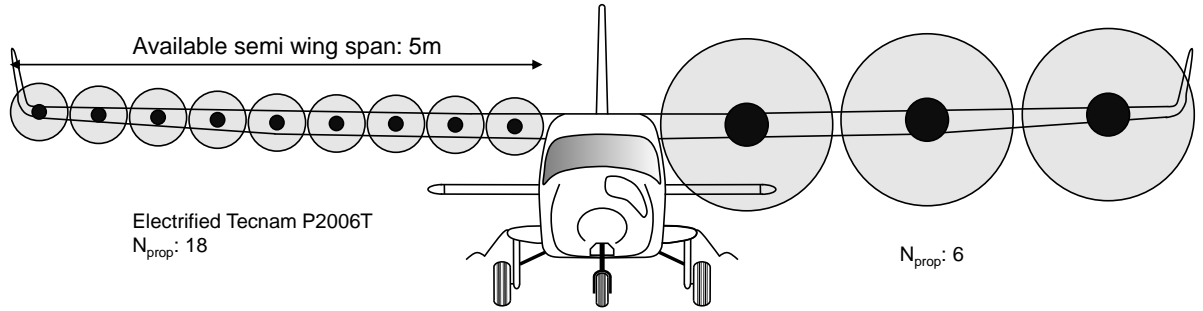
Figure 5.17: Multiple electric propeller installation

The propeller diameters should be as large as possible to obtain the lowest thrust loading and therefore the most efficient design. Figure 5.18 shows the thrust loading depending on the number and the diameter of the propellers. The abscissa shows the total number of propellers and the ordinate shows the propeller diameter. The contour lines show the thrust loading. The two black lines represent both diameter limits. Propeller designs exceeding one of the

limits are not feasible.
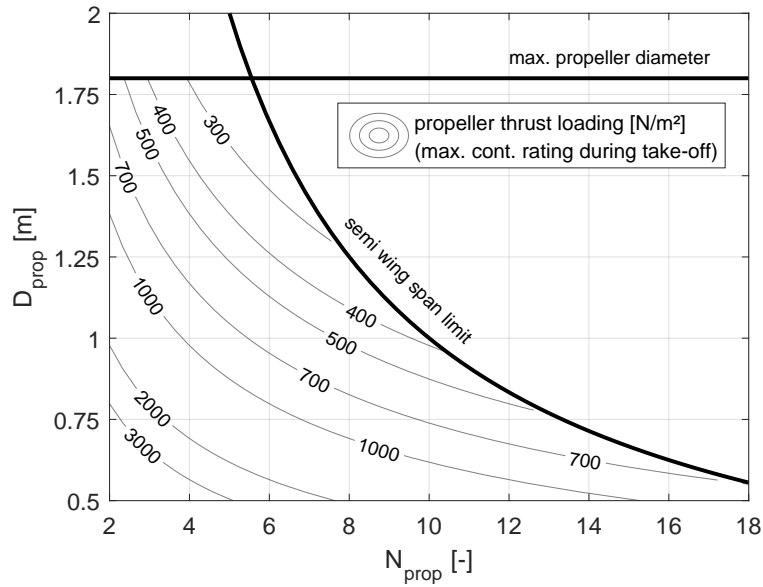
Figure 5.18: Multiple electric propeller thrust loading

The plot shows that from two to six propellers, the available propeller area increases as the thrust loading decreases. When the number of propellers is further increased, the available propeller area declines and the thrust loading increases again. Hence, from an efficiency point of view, six propellers represent an optimum number. Besides the thrust loading, the number of propellers has an impact of several parameters of the aircraft. For the electrified P2006T aircraft, the engines and the fuel tank are subtracted from the aircraft mass and inertia. Then, the new propellers, the gearbox, the electric motor and the battery are added to the aircraft mass and inertia. Depending on where the components are installed on the aircraft, the position of the CG will change. As this has a noticeable impact on the state space model, it is assumed that the component replacement always results in the same aircraft MTOW and the same CG position. As system components are only removed from the wing, the battery must be installed in the wing as well. The electric motors are designed to fit within the hub diameter of the propeller and the nacelle dimensions are adjusted accordingly. The supplementary surface of the reference engine nacelles to the clean wing has been estimated from the manufacturer drawings to roughly 4.6 m^2 per engine. With the estimated mass of the engine nacelles, a notional surface density of 2 $\frac{kg}{m^2}$ is derived for the nacelles, which is utilised to estimate the mass of the new motor nacelles.

Besides the CG location, the electrification has an impact on the system efficiency, the system mass and the available battery mass. Moreover, the smaller motors reduce the size of the nacelles and therefore reduce the wetted area of the aircraft, which reduces the viscous drag. As shown in chapter 3.2, the design thrust levels of the propeller has an impact on the thrust response of the motor-rotor system. Consequently, the number of propellers also influences the thrust response of the propulsion system. Figure 5.19 shows the sensitivity of several propulsion system and aircraft parameters on the number of propellers.

The first plot on the left shows the sum of the installed power, which is a function of the
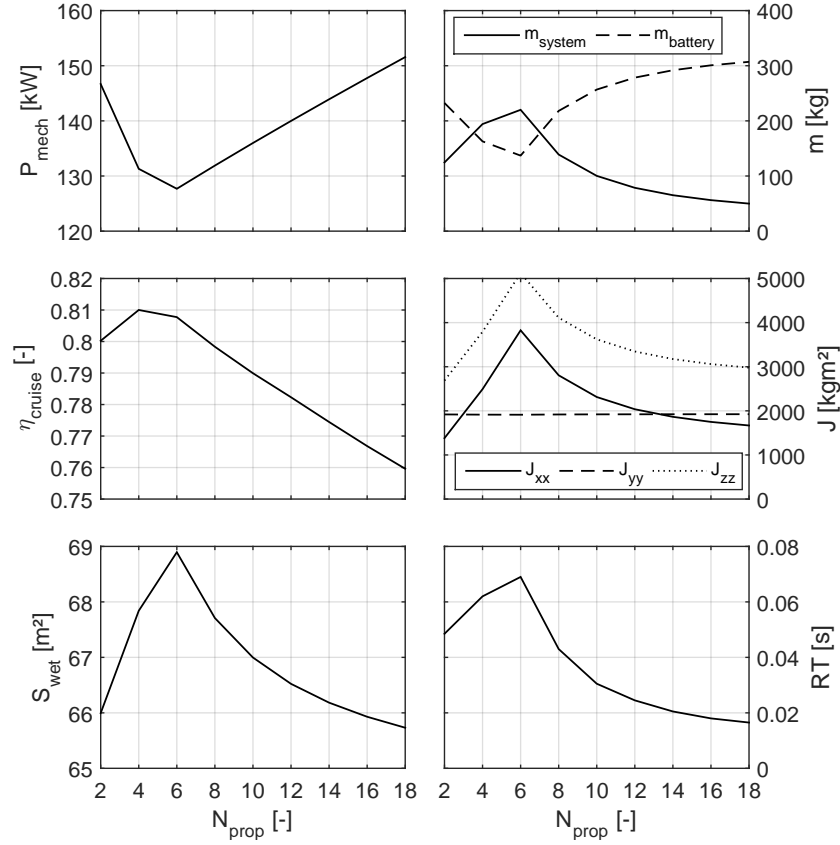
Figure 5.19: Impact of propeller number on system and aircraft parameters

propeller thrust loading and therefore of the propeller area. The larger the propeller area, the lower the thrust loading and the required mechanical power. Hence, the installed power of the six propeller configuration shows the lowest installed power. The first plot on the right shows the propulsion system mass and the available mass of the battery. Because of the constant MTOW design, both curves are mirror-inverted. Although the six propeller configuration has the lowest installed power, it has the highest propulsion system mass and the lowest available battery mass. This originates from the propeller design, which results in a higher required torque for large propellers. As the weight of electric motors is mainly driven by the required torque, the six propeller configuration has the highest motor mass. Moreover, the six propeller configuration has the maximum propeller diameter and, therefore, large and heavy motor nacelles. The second plot on the left shows the propulsion system efficiency at the cruise condition of the flight test. The change of the system efficiency is mainly driven by the propeller efficiency. The plot shows that the four and six propeller configuration have the highest efficiency. As the number of propellers is increased, the system efficiency is decreased, because of the reduced propeller diameter and efficiency. For 18 propellers, the system efficiency has decreased by 5% points compared to the 4 propeller configuration, which is quite significant. For the LEAPtech concept, a lower propeller efficiency might even be favourable, as it increases the dynamic pressure on the wing. The available battery mass shows considerably higher sensitivity on the number of propellers. The higher the number of propellers, the lower is the mass of the motor-rotor systems and the larger the available weight of the battery. The second plot on the right shows the aircraft inertia around the three bodyfix axis. The inertia around the x- and the z- axis show a noticeable and similar

sensitivity on the number of propellers. For two to six propellers, the inertia increases up to a maximum, which results from the supplementary propellers and motors that are added to the wing with an increasing lever arm to the CG. For more than six propellers, the inertia decreases again, as the mass of the motor-rotor systems decreases and the average lever arm is not changed. The inertia around the y axis has a minor sensitivity on the number of propellers, because all propulsion components are removed and added to the wing with a similar lever arm in the x and z position. The lower plot on the left shows the total wetted area of the aircraft. The total wetted area of the reference P2006T with the two piston engines has been estimated with the manufacturer drawings to roughly 73 m^2. This results in a wetted area to reference wing area ratio of 4.9, which matches well with correlations from Raymer for twin engine general aviation aircraft [193]. The diameter of the motor nacelles is set to the hub diameter of the propellers and the length is set to 1.5 times the length of the electric motor in order to house the gearbox and the motor controller. The results show that the wetted area of the electrified P2006T aircraft is significantly reduced compared to the reference aircraft. The wetted area increases from two to six propellers, which is quite intuitive as all propellers, and therefore the motor nacelles, nearly have the same diameter. For more than six propellers, the propeller diameter is decreased and the propeller speed is increased. Both trends lead to a reduction of the motor size and therefore to a reduction of the motor nacelle area. The lower plot on the right shows the rise time of the motor-rotor systems for an acceleration from 50 to 100% of cruise thrust. These results cannot be compared to the investigations in chapter 3, because at cruise thrust, the electric motor is still in part load operation, whereas in chapter 3, the rise time was measured for the acceleration from 50 to 100% of the maximum continuous thrust level. The results show that for two to six propellers, the rise time increases. As the thrust is distributed to multiple propellers, the required torque to drive the propeller is reduced. At the same time, the diameter stays constant, which keeps its inertia on a high level. For more than six propellers, the thrust loading of each propeller is increased with the number of propellers, as shown in figure 5.18. Therefore, the required torque increases. Additionally, the propeller diameter is decreased, which reduces its inertia and enables a faster thrust response.

5.2.3 Yaw control with multiple electric propellers

The vertical tail of an aircraft is a passive device that provides weathercock stability. When an external disturbance causes a side slip angle, the vertical tail creates a restoring force that reduces the developed side slip angle. This function is an important requirement for aircraft certification. The rudder is a control surface at the trailing edge of the vertical tail, which allows to apply yawing moments for lateral movement. As the passive weathercock stability is an important function of the aircraft, the vertical tail is not modified or resized for the following investigations. Thus, the minimum control speed airborne as well as the dutch roll and the spiral dive eigenmodes are not modified. Only the rudder is fixed to the neutral position, which means that the hardware for rudder deflection can be omitted.

Another way to apply moments on the aircraft is the application of differential thrust with the propulsion system. Depending on the lever arm of each propulsor to the aircraft CG, the thrust force creates a moment on the aircraft. During normal operation of a fixed wing aircraft, the sum of all yaw moments is zero as all engines are installed symmetrically and operated at the same thrust level. By applying different thrust levels, the total thrust level and the resulting moment can become positive or negative. The total thrust and the resulting moment are determined according to the equations (5.14) and (5.15).

$$F = \sum F_i \tag{5.14}$$

$$M = \sum F_i \times \vec{l_i} \tag{5.15}$$

With more than two propellers, these two equations form an under-determined problem that requires additional assumptions for a unique solution. For the electrified P2006T aircraft it is assumed, that all engines on one wing are operated at the same thrust level. This allows to calculate the total thrust force of all propellers on one wing according to equation (5.14) and an equivalent lever arm for the total thrust force according to equation (5.16). With both total thrust levels and both equivalent lever arms, the thrust command for each propeller can be calculated from a given thrust and moment command.

$$\vec{l}_{\text{left}} = \frac{\sum \vec{l}_{i,\text{left}}}{Z_{\text{left}}} \tag{5.16}$$

This concept works very well as long as each propeller can deliver the required thrust. Especially during take-off, when each motor is running near its maximum take-off power, this control approach can result in thrust commands, that the motor can not deliver. At that point, both command requirements cannot be satisfied and one command must be prioritised over the other. For this study, the yaw moment command is prioritised over the thrust command. To implement this control approach, a saturation limit is included. The flight controller admits thrust levels that require the motor to operate at a PPF of 2, which is the reference assumption from table 3.1. As soon as the motors on one side of the aircraft reach the maximum PPF, the thrust level of the opposite side is reduced in order to deliver the required yaw moment. Consequently, the thrust command cannot be met and the aircraft acceleration or climb performance is degraded, which is critical during take-off and initial climb manoeuvres.

One advantage of electric motors is that the motor status can be easily monitored in real time with motor current signature analysis [194]. Thus, the motor controller can quickly detect motor failures and provide this information to the flight controller. The information of propulsor failures can be considered in equations (5.14) and (5.15). In that way, the flight controller can compensate the resulting moment with the remaining motors. For the following investigations it is assumed, that the flight controller recognises and considers the failure of an electric motor one second after the failure occurred.

5.2.4 Critical motor failure cases

Utilising differential thrust for yaw control throws up new requirements for the reliability of the propulsion system, as the system now has a double function for aircraft control. A propulsion system failure may lead to a thrust reduction, or to a reduced yaw controllability, or even both. As the yaw command has been chosen to be prioritised over the thrust command, a failure of one or multiple propulsors can lead to a considerable thrust reduction of the remaining propulsors, as they may have to be throttled back. This may affect the acceleration and climb performance of the aircraft. Especially during take-off and the initial climb, the aircraft requires a high thrust level, which makes a propulsion system failure critical during this manoeuvre.

There exist two critical failure cases for each aircraft configuration: one, where the thrust target cannot be sustained, and one where the yaw moment cannot be supplied any more. By prioritising the yaw command, the number of critical failure cases, where yaw control is lost, can be reduced significantly. Simulations have shown that with at least one operating propulsor on each wing, the propulsion system can produce a meaningful yaw moment to control the aircraft. However, in all failure cases, where only minimum yaw controllability was achieved, the remaining thrust level was too low for steady state flight. Consequently, the available thrust level falls below a minimum limit before a minimum yaw controllability is reached. As the propulsion system failure is most critical after exceeding the decision speed during take-off, the take-off and initial climb performance is further investigated for the electrified Tecnam P2006T aircraft.

According to the certification specifications of the European Aviation Safety Agency (EASA), the Tecnam P2006T aircraft must be able to maintain a steady climb gradient of at least 1.5% up to a pressure altitude of 1524 m and a minimum climb speed of 1.2 times the minimum stall speed [195]. To simulate the take-off performance of the aircraft, the identified aerodynamic derivatives of Nicolosi are utilised to linearise a state space model at take-off conditions with minimum control speed. As the aerodynamic derivatives of the state space model have been identified at low subsonic speeds, where incompressible effects can be neglected, the derivatives are utilised for take-off simulations without corrections. The major issue of utilising the same derivatives is that the flight test was conducted at cruise conditions in a clean configuration. During take-off, the flaps and the landing gear are extracted, which has an impact on the lift and drag characteristic of the aircraft. To account for the drag of inoperative propellers and the flight with an increased side slip angle, the state space model is extended with appropriate methods from Torenbeek [196].

In a first step, the performance of the reference Tecnam P2006T is simulated with one engine inoperative during take-off at minimum control speed. The simulation is initialised at ISA sea level conditions at minimum control speed with both engines running at maximum take-off thrust. One second after the rotation, the thrust of the right engine is instantly set to the according engine inoperative drag force. It is assumed that no sensor data on the side slip angle is available to the flight controller. The controller receives information about the yaw rate, which is derived from the inertial measurement unit of the aircraft. The flight controller operates the rudder in order to maintain a zero yaw rate. To stabilise the attitude of the twin engine aircraft at low speeds, a significant rudder deflection is required. For this simulation, the rudder deflection is limited to +/- 30 degrees. Figure 5.20 shows the rudder deflection and the side slip angle, β, over time.

The side slip angle increases instantaneously as the right engine is set inoperative and the flight controller tries to compensate the resulting yaw rate with a rudder deflection, which quickly runs into its saturation limit. After a few oscillations, the side slip angle converges at 26 degrees, which is considered too high for a one engine inoperative scenario. To test the impact of the added drag prediction method on the resulting side slip angle, the simulation was run only with the state space model. However, in this second run, the side slip angle also clearly exceeded 20 degrees.

The first step for the electrification of the P2006T aircraft was the replacement of the two internal combustion engines by two electric motors. The rudder is fixed in its neutral position and the yaw control is realised by differential thrust of the two electric propulsors. The
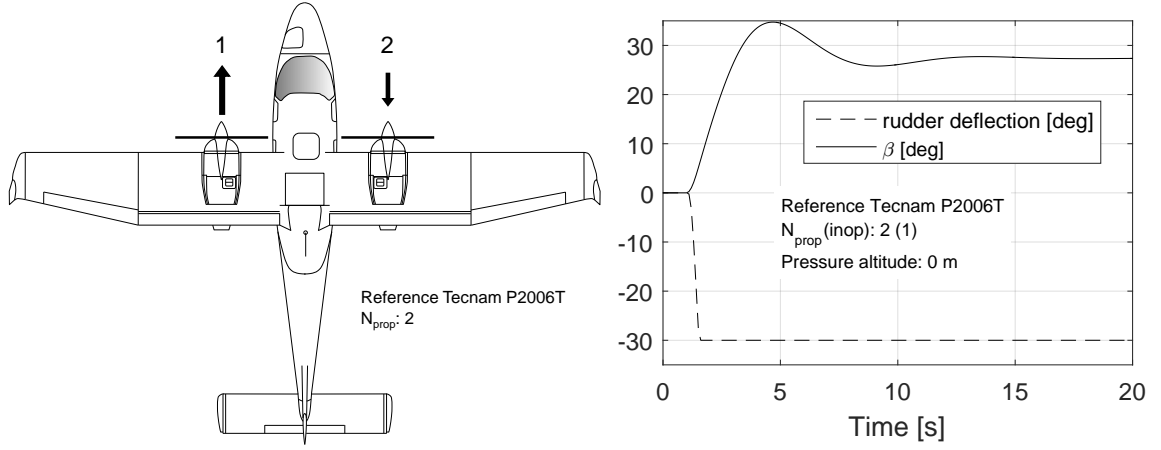
Figure 5.20: Reference Tecnam P2006T take-off performance

simulation of the reference aircraft already showed, that the twin engine aircraft requires a significant rudder deflection in order to stabilise the aircraft when one engine is inoperative. Thus, yaw control via an electrified propulsion system with a deactivated rudder is not feasible for twin propeller aircraft. There are at least four propellers required to allow a one motor inoperative case.

For yaw control, the failure of motors near the wing tip is more critical than the failure of motors close to the wing root, as they have a larger lever arm to the aircraft CG. Consequently the remaining propulsors near with smaller lever arms have to compensate the lacking yaw moment of the inoperative motor, which requires a higher thrust level. When the thrust limit of the remaining propulsors is reached, the thrust level is decreased by throttling back the propulsors on the opposite wing, which deteriorates the aircraft's performance. To identify the critical configuration of inoperative propulsors, motor by motor is shut down, starting from the right wing tip. At a certain number of inoperative motors, the remaining motors on the right wing operate at their maximum MTF and the motors on the left wing are considerably throttled back, so that the aircraft is hardly able to accelerate during the initial climb. In the following section, this critical configuration is investigated for different number of propellers. Figure 5.21 shows the failure case with the minimum thrust capability of the four propeller version and its initial climb performance.

The left plot in Figure 5.21 shows the failure case configuration. Similar to the reference aircraft, the simulation is initialised at minimum control speed with all motors running at maximum take-off thrust. One second after rotation, the right motor (number 4) is set inoperative. The black arrows in the left plot represent the net thrust or drag of each propulsor. The right plot of Figure 5.21 shows a time plot of the aircraft velocity, v, the yaw moment of the propulsion system on aircraft level, $M_{propulsion}$ and the side slip angle, β. To plot all parameters in one plot, the scale of the moment is divided by 100. As motor 4 is set inoperative after one second, the propeller speed decreases and the propulsion system exerts a negative yaw moment on the aircraft. Consequently, the aircraft begins to yaw and the side slip angle increases. The flight controller commands a positive yaw moment in order to maintain a zero side slip angle. This can be seen by the small increase of the propulsion system moment just before two seconds. At two seconds of simulation time, the flight controller receives the information of the motor failure and considers it in the motor command. Immediately, the
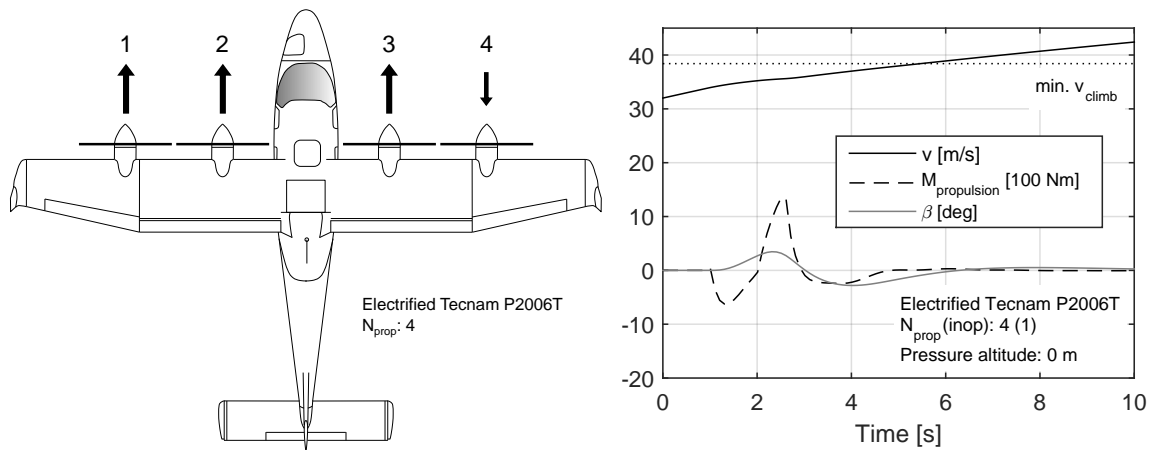
109

Figure 5.21: Electric Tecnam P2006T take-off performance with 4 propellers

propulsion system applies a large positive moment to recover the yaw rate. The side slip angle reaches its maximum of 4 degrees after 2.5 seconds. As the side slip angle is non-zero, the vertical tail creates a yaw moment, which reduces the side slip angle down to zero. This implies a yaw rate in the opposite direction, which causes the flight controller to command a negative yaw moment. As the flight controller works against the yaw rate, which is created by the vertical tail, the side slip angle shows and oscillatory characteristic. However, the excitation of the dutch roll is considerably reduced, which is shown by the amplitude and the quick attenuation of the side slip angle. The kink in the velocity curve shows the reduced acceleration capability of the aircraft with one inoperative motor. The aircraft performs the minimum required climb angle and exceeds the minimum climb speed, min v_{climb} which is required by the EASA certification specifications and indicated by the dotted line, after 5.5 seconds. Thus, under the assumed circumstances, an electric propulsion system is able to stabilise and further accelerate a four propeller electrified P2006T according to the certification requirements, with an asymmetric motor failure of one motor.

The maximum take-off thrust requires the maximum continuous power of the electric motor. As the maximum MTF is set to 2, the electric motor will overheat after a certain time. This time limit depends on the cooling method and may be extended by the increasing velocity, if the motor is cooled by the ambient air flow.

The next three figures show the results for the six propeller, the 12 propeller and the 18 propeller configuration of the electrified P2006T aircraft. All figures show the worst failure configuration, where the remaining motors provide enough thrust to accelerate the aircraft up to the minimum required climb speed within ten seconds after rotation. Figure 5.22 shows the results for the six propeller aircraft.

The left plot of Figure 5.22 shows the worst failure configuration for the six propeller aircraft. With six propellers, the aircraft can perform the initial climb manoeuvre with two inoperative motors. However, a simultaneous failure of motor 5 and 6 (or 1 and 2) decreases the available thrust level so much, that the aircraft cannot reach the minimum climb speed within 10 seconds after rotation. When at least one motor (5 or 6) stays operative, the propulsion system can produce enough thrust to accelerate the aircraft. The right plot shows that the moment of the propulsion system as well as the side slip angle show the same characteristics
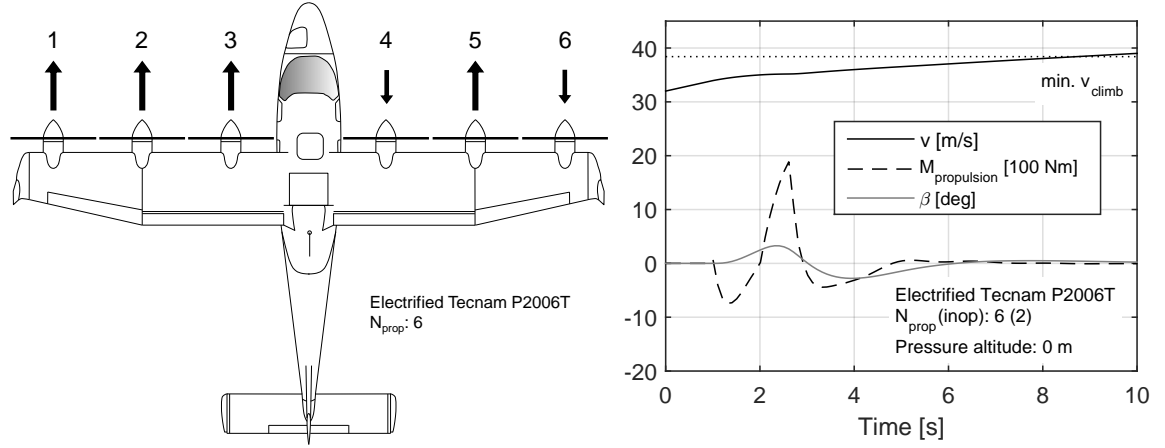
Figure 5.22: Electric Tecnam P2006T take-off performance with 6 propellers

as for the four propeller aircraft, however, the moment amplitude has increased. This results from the larger lever arms of the inoperative propellers and the fact that more thrust is cut off compared to the four propeller configuration. The side slip angle shows a similar characteristic, which results from the increased inertia around the z-axis as found in Figure 5.2.2. The velocity plot shows that the aircraft requires the nine seconds to reach the minimum climb speed. Figure 5.23 shows the results for a 12 propeller aircraft.
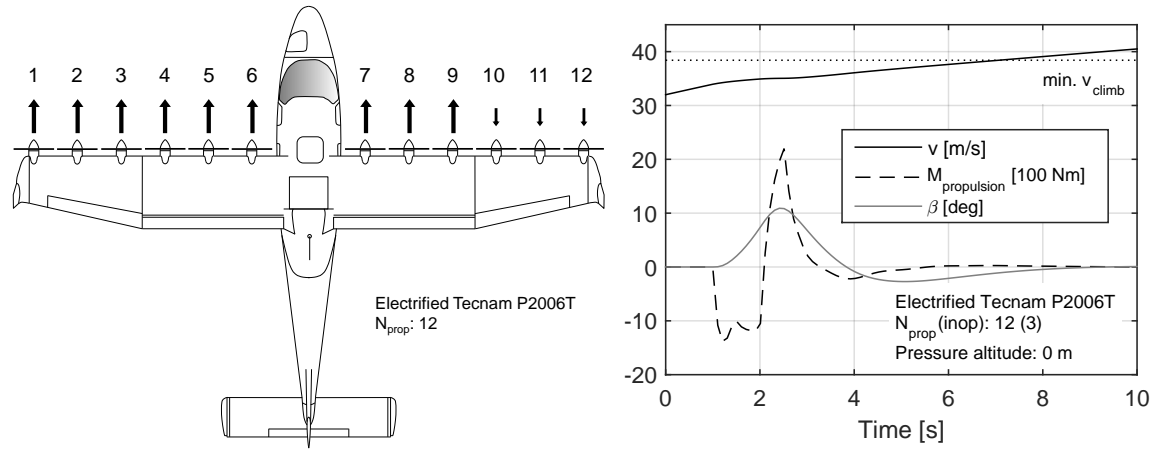
Figure 5.23: Electric Tecnam P2006T take-off performance with 12 propellers

The left plot shows the critical asymmetric failure case for the 12 propeller aircraft. The plot shows, that a minimum of three propellers is required for a successful initial climb. The right plot of Figure 5.23 shows that the peak of the side slip angle exceeds 10 degrees. As the three outer propellers are set inoperative, the moment of the propulsion system is quite large. As, furthermore, the inertia of the aircraft is relatively low, the high moment leads to a high yaw rate and a high side slip angle. Figure 5.24 shows the results for the electrified P2006T with 18 propellers, which is similar to the LEAPtech configuration.

The left plot shows, that the configuration can cope with a remarkable five motor asymmetric
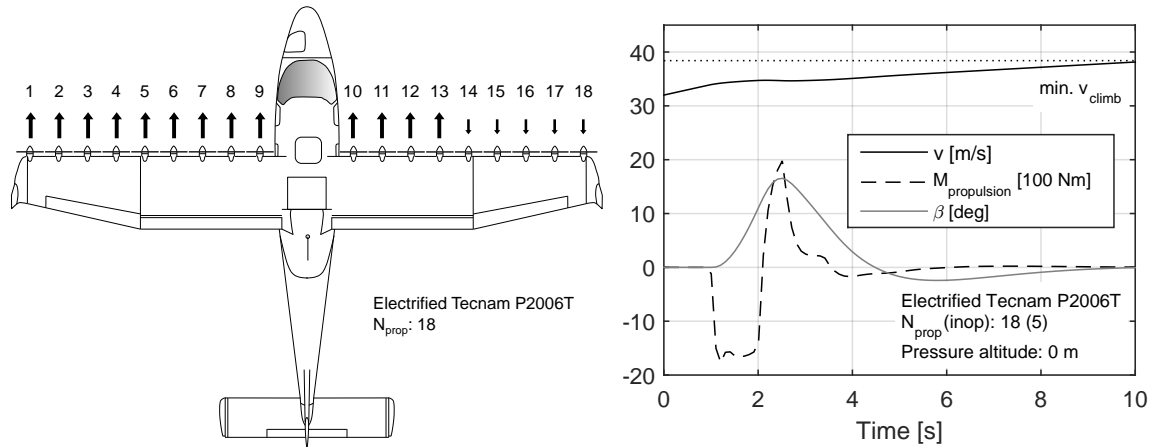
Figure 5.24: Electric Tecnam P2006T take-off performance with 18 propellers

failure case. The right plot shows that the moment of the propulsion system, which results from the asymmetric failure case, is similar to the 12 propeller configuration. As the inertia is smaller compared to the 12 propeller configuration, the side slip angle has a higher maximum of roughly 16 degrees. The velocity profile shows, that this configuration takes the maximum time of ten seconds to accelerate to minimum climb velocity, which is longer than for the 12 propeller configuration, which requires only seven seconds.

After investigating the critical take-off failure scenarios, a brief reliability analysis is conducted, to assess the probability of critical failure cases. For certification, the aircraft must prove a maximum critical failure rate of $10-9$ per hour. In general, the loss of thrust that results from a complete propulsion system failure is not relevant for the critical failure of the aircraft as long as no parts of the engine damage vital systems of the aircraft (i.e. disk burst in gas turbine engines). By taking over the yaw control and by deactivating the rudder, a failure of the propulsion system can cause the loss of control of the aircraft and, hence, contribute to a critical failure. Thus, the propulsion system must prove a certain reliability in producing the required yaw moments under the failure of individual motors or propellers. The electric propulsion system consists of a planetary gearbox, an electric motor with controller and a battery system. Conventional brushless electric motors have a high reliability level an failure rates of down to $5 \cdot 10^{-6}$ [197]. Villani investigated the design of an electric motor for aircraft actuator applications with a particular high reliability and predicted a Mean Time Between Failure (MTBF) of $31.3 \cdot 10^9$ for the motor [198]. For gearbox systems, Gieras indicates a failure rate of down to $2 \cdot 10^{-6}$ per hour [197]. The battery is assembled from multiple single cells that are lined up in series and parallel strings. This structure makes the battery tolerant against the failure of single cells, especially, when the battery is operated in part load power. When the battery is sized according to the energy specification, the battery generally works in part load operation. As a short circuit failure of a few cells does not affect the reliability of its series string, and the battery can bare multiple inoperative series strings during part load operation. The reliability of the battery pack is considered good enough and is, therefore, not analysed in detail [199]. The following table shows the failure probability of the electrified propulsion systems, by considering the planetary gearbox and the electric motor.

The upper line of Table 5.2 shows the number of propellers and the second line gives the minimum number of inoperative propellers, that lead to a critical failure. The third line gives

N	2	4	6	12	18
N_{inop}	1	2	2	4	6
critical cases [-]	2/2	2/6	2/15	495/495	18564/18564
critical failure rate [1/h]	$7.00 \cdot 10^{-6}$	$1.63 \cdot 10^{-11}$	$6.53 \cdot 10^{-12}$	$2.40 \cdot 10^{-21}$	$1.18 \cdot 10^{-31}$

Table 5.2: Critical failure rate of the electric propulsion systems

the number of combinations, which lead to critical failure. For example, for six propellers, the loss of 2 tip propellers represents a critical failure. There are 15 possible combinations to choose two out of six and only the two cases, where the two tip propellers fail, lead to a critical failure. For 12 and 18 propellers, all combinations are considered as critical. The lower line gives the resulting critical failure rates per hour. The result show, that for a twin engine aircraft, a particular motor and gearbox design has to be considered in order to achieve an acceptable failure rate. With four propellers or more, the probability for a critical propulsion system failure is less than 10−9 per hour, which is a reasonable level for aircraft certification.

To conclude the investigation on the critical motor failure cases during take-off and the initial climb, the identified results are briefly summarised. The simulation of the initial climb of the reference Tecnam P2006T aircraft showed a significant side slip excursion of 26 degrees with one engine inoperative. To stabilise the aircraft, the flight controller commanded the maximum rudder deflection of 30 degrees. The results for the electrified configurations showed that the maximum side slip oscillations can be reduced compared to the reference aircraft. A comparison of the critical failure cases shows that the side slip excursion increases with the number of propellers. The failure case gets critical as soon as the average lever arm of the remaining motors (on the right wing) gets to small. The more motors are installed, the more discrete values are possible for the average lever arm. Consequently, more motors allow to approach the average lever arm towards its critical value, which increases the side slip angle excursion of the aircraft. This trend is further supported by the decreasing aircraft inertia with more propellers. As the propulsion system takes over the yaw control of the aircraft, specific failure cases can cause loss of control of the aircraft. A brief reliability analysis of the gearbox and the motor has shown that the critical failure rate is significantly reduced with increasing number of propellers. With four propellers or more, a reasonable critical failure rate can be demonstrated for aircraft certification.

5.2.5 Side slip excursion during roll manoeuvres

In the last study, the dutch roll excitation by the electric propulsion yaw control is investigated. The flying qualities of piloted aircraft specify maximum side slip excursions for roll manoeuvres, during which the bank angle is varied by at least 90 degrees. The lower the resulting side slip angle after the manoeuvre, the better is the classification of the aircraft. For level 1, the resulting side slip angle must be lower than 6 degrees for adverse yaw and lower than 2 degrees for proverse yaw characteristic. The level 2 category requires side slip angles of less than 10 degrees for adverse yaw and less than 3 degrees for proverse yaw characteristics [200]. As the $C_{n\beta}$ coefficient of the identified state space model is positive, the P2006T has adverse yaw characteristics.

To investigate the impact of electrification and to determine the impact of the number of propellers, the state space model from Nicolosi is utilised, which was measured and identified at a medium cruise speed. The state space model is corrected for the impact of the new

propulsion system configuration, noticeably the aircraft inertia, the wetted area, the lever arm and the number of the propellers. As the propellers are mounted in a pull configuration in front of the wing, they will increase the dynamic pressure on the wing, which increases the lift of the wing. Consequently, changing the thrust level asymmetrically on both wings, which is required to apply a yaw moment, will also result in an asymmetric lift condition and cause a roll movement. This effect is not modelled for this study, as the roll response is dominated by the aileron deflection and the side slip response is the relevant output for the aircraft categorisation.

In the simulation, a roll manoeuvre with multiple step commands is calculated. One second after the simulation has started, a step command for a bank angle of +45 degrees is issued. This command is held for six seconds so that the resulting oscillations have abated. After seven seconds, a step bank angle command for -45 degrees is passed to the flight controller. This represents the required 90 degrees change of the bank angle. This command is also held for a few seconds. Finally, the aircraft returns to levelled flight condition. During the entire manoeuvre, all motors are operative. The yaw controller targets a given azimuth angle and its input is the error of the side slip angle. This requires the assumption, that the side slip angle is measurable and available to the flight controller. Figure 5.25 shows the simulation of the reference Tecnam P2006T with rudder yaw control.
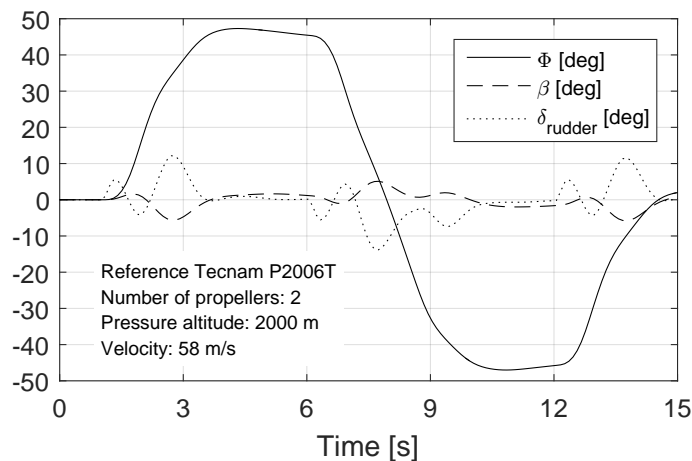
Figure 5.25: Reference Tecnam P2006T roll performance

The abscissa shows the simulation time and the ordinate shows the bank angle (Φ), the side slip angle, β, and the rudder deflection, δ_{rudder}, in degrees. After the 90 degrees roll manoeuvre, the reference Tecnam P2006T shows a maximum side slip angle of 6 degrees, which corresponds just the limit value for the level 1 category. Of course, the aircraft performance depends not only on the aerodynamic characteristics, but on the flight controller parameters. The controller gains are chosen in that way to obtain a low overshoot together with a minimum oscillatory response of the aircraft. As the same controller gains are utilised for all aircraft, the system response changes with the number of propellers and the inertia of the aircraft. The next three figures show the results for the four propeller, the six propeller, the 12 propeller and the 18 propeller configuration. Figure 5.26 shows the results for the four propeller configuration.
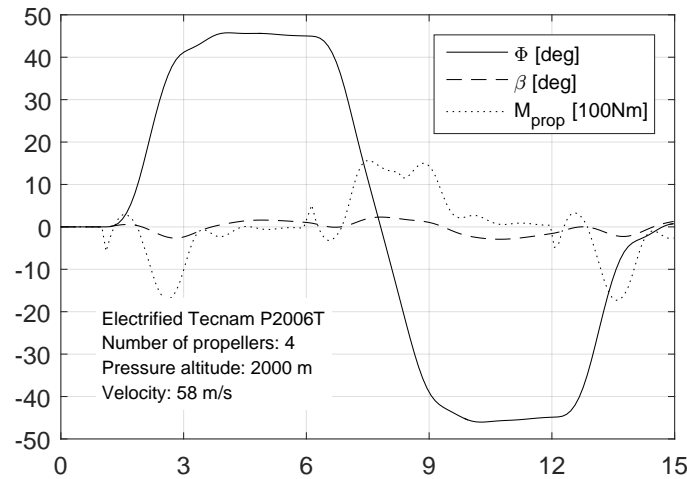
Figure 5.26: Electric Tecnam P2006T roll performance with 4 propeller

The scale of the propulsion system yaw moment is divided by 100 to plot all parameters in one single plot. The peaks of the yaw moment curve show that the propulsion system applies a moment during the roll manoeuvre of the aircraft, to compensate the aerodynamic moment of the vertical tail. During the 90 degrees roll manoeuvre, the aircraft shows a maximum side slip angle of 3 degrees, which is considerably lower than for the reference aircraft. As the propulsion system does not apply any roll moment on the aircraft, the dutch roll mode is less excited, which results in a lower side slip angle excursion compared to the conventional rudder controlled aircraft. Figure 5.27 shows the results of the six propeller configuration.
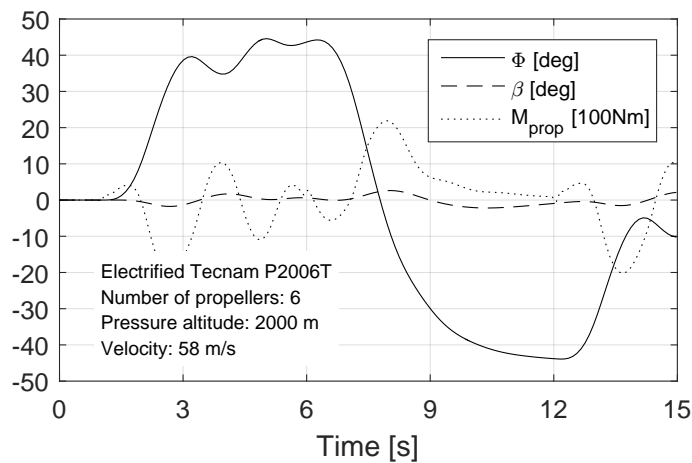
Figure 5.27: Electric Tecnam P2006T roll performance with 6 propeller

The six propeller configuration shows a much more oscillatory behaviour of the bank angle and the moment of the propulsion system as the four propeller configuration. This results from the high level of inertia around the x- and z-axis of the aircraft (see Figure 5.19), which influences the aircraft dynamics. The benefit of the high inertia is a higher damping of the yaw motion and therefore a reduced side slip excursion. The results show that the larger oscillation approximately annuls the higher damping, and a maximum side slip angle of

3 degrees is found. Figure 5.28 shows the simulation results for the 12 propeller configuration.
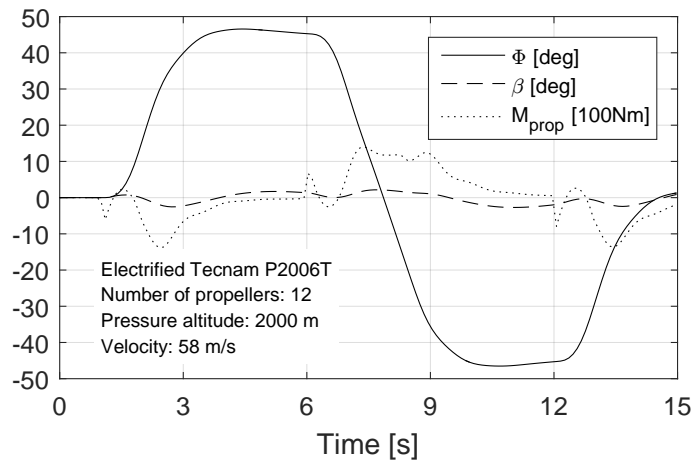
Figure 5.28: Electric Tecnam P2006T roll performance with 12 propeller

According to Figure 5.19, the 12 propeller configurations has a slightly lower inertia, which results in a more smooth roll manoeuvre with a minimum overshoot. Again, the curve of the propulsion system moment shows that the yaw control quickly counteracts the yaw acceleration that results from the roll manoeuvre. The resulting side slip excursion stays well below 3 degrees. Finally, Figure 5.29 shows the simulation results for the 18 propeller configuration.
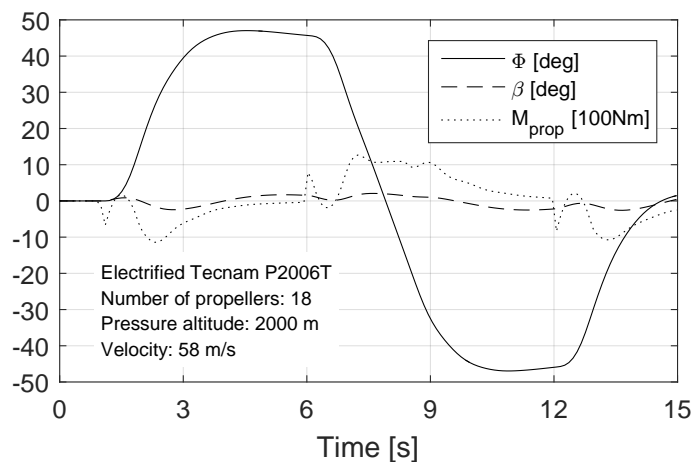
Figure 5.29: Electric Tecnam P2006T roll performance with 18 propeller

Compared to the other configurations, this version has the lowest inertia around the bodyfix x- and z-axis. The bank angle shows the same smooth and non oscillatory roll manoeuvre as the previous configurations. The response of the propulsion system is fast enough to quickly react on the resulting yaw rates and keep the side slip excursion below 3 degrees.

To conclude the investigations on the side slip excursion during a 90 degrees roll manoeuvre, the reference Tecnam P2006T aircraft shows an excursion of 6 degrees, which is just the limit value of the level 1 categorisation. All electrified configurations show a maximum side slip

angle that is only half of the reference aircraft, which qualifies them for the level 1 category. Comparisons between the rudder deflection of the reference aircraft to the propulsion system moment shows a similar dynamic response, which enables the good yaw response of the electrified versions. The number of propellers has no noticeable impact on the yaw response of the aircraft. All configurations show a similar side slip angle. Thus, the thrust response of distributed, electrically driven, fixed pitch propeller is suitably fast to perform yaw control by differential thrust on a general aviation aircraft.

6 Conclusions and Outlook

This thesis presents a preliminary analysis of the thrust response of hybrid-electric propulsion systems for flight control applications. The first part of the thesis is dedicated to the development of appropriate models that allow to predict the steady state and the transient performance of propulsion system components during a preliminary design phase of hybrid-electric propulsion system. In a step-by-step approach, the sensitivity of the thrust response on the system component design parameters investigated on propulsor level, which consists of an isolated motor-rotor combination. In the second step, the peak power capability of battery based, fuel cell based and hybrid propulsion systems is investigated with respect to the most relevant component and system design parameters. Finally, an aircraft level assessment is conducted with two applications, which utilise differential thrust for attitude and flight control. The first application are large quadcopter vehicles, which require fast responding propulsion systems for attitude stabilisation and for performing agile manoeuvres. The second application is a fixed wing concept, which is equipped with a distributed electric propulsion system and utilises differential thrust for yaw control. The aircraft is derived from the Tecnam P2006T and the LEAPtech concept from NASA. The studies on aircraft level focus on critical failure cases as well as manoeuvre performance.

6.1 Important findings

A constant thrust design analysis of the thrust response of an isolated motor-rotor system with fixed pitch propellers showed that low thrust loadings result in high a high propeller efficiency as well as a fast thrust response. The propeller pitch is a trade-off parameter between a high efficiency level during hover flight and a fast thrust response. For the investigated parameter space, the propeller efficiency showed a minor sensitivity on the design tip speed, however, a higher tip speed results in significantly faster thrust responses. In summary, the thrust response of fixed pitch motor-rotor systems benefits from low inertia designs, as this reduces the kinetic energy, that the motor has to supply to the system in order to change the thrust level. Adding a supplementary gearbox between the propeller and the motor showed a minor impact on the thrust response of fixed pitch propellers. The main advantage of the gearbox is the reduction of the motor mass and inertia, which enables a slightly faster thrust response for low gear ratios. For higher gear ratios, the gear wheel inertia increases, which leads to longer response times of fixed pitch systems. The scaling of the motor-rotor system to higher design thrust levels showed slower thrust responses, which indicates that the agility of small aircraft is superior to large aircraft with similar design parameters. The analysis of variable pitch propellers showed, that the thrust response is roughly 10 times faster compared to fixed pitch propellers. The major advantage of variable pitch propellers is that the thrust level and the thrust response are decoupled from the kinetic energy and the design parameters of the motor-rotor system. Furthermore, variable pitch propellers require less peak power as the deviation of the rotational speed during thrust changes is much smaller than the difference of the rotational speed, that is required by fixed pitch propellers.

The analysis of battery based propulsion systems showed that the pack voltage level can be

optimised to obtain a minimum battery mass. The optimisation benefit decreases for larger battery packs, as the increasing number of cells allows more discrete steps of the pack energy. A battery pack, which was optimised for the reference power of roughly 10 kW, a benefit of 2-3% was found for the pack mass. Transient simulations showed, that the minimum cell voltage is the main limiting parameter for the battery peak power capability. A comparison of fixed and variable pitch propellers showed that variable pitch systems can extract up to 6% more energy from the battery, which originates from the reduced peak power requirements. A comparison of air breathing and gas tank fuel cells has shown that gas tank configurations have lower system masses for operation times up to 150 - 180 min at sea level. When the operating altitude is increased to 4000 m, the break even operating time is extended to 270 minutes. A parametric study on the design parameters showed that the design current density is the most relevant trade-off parameter between the stack mass on the one hand and the efficiency level and the peak power capability on the other hand. For a low mass design, a high design current density is required, which reduces the efficiency level as well as the peak power capability of the fuel cell. The design for the reference power of almost 10 kW showed a quasi steady-state peak power factor of roughly 1.3 times on the design power. During very short acceleration manoeuvres, the investigated fuel cell is able to supply up to twice the design power, which is related to the internal diffusion processes in the cell, which buffer the power loading. Thanks to the superior energy density of hydrogen over batteries, the fuel cell based systems provide a higher endurance potential over battery based system. To profit from this better endurance potential and to boost the peak power capability of the fuel cell, a hybrid system of a fuel cell and a supercapacitor is examined. Investigations showed, that this hybrid system can deliver even higher peak power levels than battery based systems, if the supercapacitor takes over the peak power loads and the fuel cell only supplies the average power level. For supercapacitors, the pack voltage level is an optimisation parameter for minimum pack mass, just like for batteries. However, as supercapacitor packs are mostly designed for short operation intervals, they only consists of a few cells which increases the optimisation potential for the pack mass up to 80%. The drawback of the excellent peak power of the hybrid system is the additional mass of the supercapacitor and the associated converter, which increase the system mass by 64%.

A steady-state mission analysis of quadcopters showed that the initially assumed battery energy density of 175 $\frac{Wh}{kg}$ had to be increased to 250 $\frac{Wh}{kg}$ to achieve a meaningful payload capacity. The maximum hover time with battery based propulsion systems was calculated to 45 minutes, which is affected by a rather conservative mass model for the quadcopter. Fuel cell systems provide flight times up to 240 minutes for quadcopters, which originates from the high energy density of hydrogen. Moreover, large quadcopter vehicles show higher payload capacities with fuel cell based systems than with battery based systems, which results from the superior power and energy densities of the fuel cell stack and hydrogen over batteries. The hybrid propulsion systems provide similar payload capacities as battery based systems, however, they enable hover times up to 100 minutes, which shows a clear benefit of the hybrid propulsion system. A comparison of the roll and climb agility of quadcopter models with fixed pitch dynamics, variable pitch dynamics and without motor-rotor dynamics showed, that neglecting the motor-rotor dynamics is a valid assumption for variable pitch configurations. For fixed pitch propellers, the motor-rotor dynamics must be considered in the quadcopter dynamics, when highly agile manoeuvres are targeted. Additionally to a slower thrust response, the slow motor-rotor dynamics of fixed pitch systems reduce the stability limit of the quadcopter. The simulation of individual roll and climb manoeuvres confirmed that the peak power capability of fuel cells is high enough to stabilise the quadcopter and to perform

slow manoeuvres. However, high power manoeuvres as well as combined manoeuvres showed that fuel cells alone are not suitable for the application in quadcopters. The battery and the hybrid system can deliver the required power to fly aggressive manoeuvres but, especially for the hybrid system, the peak power capability is limited in time.

A study on the yaw control performance of a modified Tecnam P2006T aircraft with an electric distributed propulsion system was conducted to assess the feasibility of the concept. An initial parametric study on the number of propulsors showed that for more propellers, the available propeller area decreases, which results in higher thrust loadings and lower efficiency levels. On the other hand, the higher thrust loading results in a faster thrust response. At the same time, the total wetted area as well as the propulsion system inertia and mass decrease, which is beneficial for reduced drag and better manoeuvrability. The flight controller is extended by a module which calculates an asymmetric thrust command for each motor, according to a given thrust and yaw moment command on aircraft level. During critical failure cases, the propulsion system may not be able to fulfil both, the thrust and the moment command. In this case, the yaw control is prioritised over the thrust command, as the time scale of the rotational movement is much shorter than the translational movement of the aircraft. For simplification, the same command level is passed to all propulsors on one wing side, which is not the optimum control strategy for minimum energy consumption, but it results in the maximum available thrust level for a given yaw moment command during failure cases. A simulation of an inoperative engine scenario during take-off rotation of the reference aircraft showed that the side slip angle converged to 26 degrees with a maximum rudder deflection of 30 degrees. The benefit of the electrification is the removal of the rudder deflection hardware and the integration of yaw control into the existing distributed propulsion system. As the conventional aircraft requires a rudder kick for stabilisation, an electrified aircraft with two propulsors and a deactivated rudder is not feasible. Simulations with multiple propulsors have shown that the side slip angle can be kept well below 20 degrees in critical inoperative motor scenarios during take-off and initial climb. A reliability analysis showed that already with 4 propellers, the yaw control failure rate is less than $10-9$ per hour and with 18 propellers, the failure rate is less than $10-30$ per hour. Simulation of roll manoeuvres at cruise condition showed, that the resulting side slip excursions are reduced from 6 to 3 degrees, which classifies the electrified aircraft for level 1 of the handling qualities of piloted aircraft. In summary, the thrust response of the electric propulsion system is fast enough for yaw control with differential thrust and the flight performance can even be improved over the reference aircraft.

6.2 Perspectives for Future Work

The here presented models are developed for the preliminary design of hybrid electric propulsion systems for medium size UAVs and general aviation aircraft. The target of these component models is to predict the steady-state performance as well as the transient response and peak power capability. As parameter and optimisation studies require short execution times of the modelling code, only the most relevant component characteristics are considered. Future studies may include more sophisticated models for the propulsion system components, which are suitable for detailed component design by including more component details, which have been neglected in this work to keep the models simple.

In this study, one basic system architecture has been investigated for each energy storage system. For the design of these architectures, reliability requirements have not been consid-

ered. The consideration of there requirements as well as the investigation of different system architecture layouts are interesting points for follow-up studies. Moreover, future studies may investigate the impact of component and system control on the thrust response. An interesting point for the motor-rotor system is the control of the rotational speed of fixed pitch propellers. In this study, the deceleration of fixed pitch propeller is achieved only by the aerodynamic torque of the propeller, which can be a limiting factor for very agile configurations. By applying breaking torques with the motor, the deceleration time of the motor-rotor system can be further reduced.

As simulation results of fuel cell based propulsion systems showed significantly higher payload capacities over battery based and hybrid propulsion systems, a sophisticated fuel cell design should be investigated, which focuses on high peak power and elevated transient performance capability. If the fuel cell was able to supply the required power profile of quadcopters, without additional high power energy storages, this would make fuel cell based propulsion systems far more attractive for multicopter applications.

On aircraft level, future studies should consider more detailed models for quadcopter flight mechanics that consider drag and moment contributions from the vehicle velocity or wind. This would allow to investigate the flight performance of quadcopters in turbulent environments. Therefore, the propeller model should be extended to consider the forces and moments that result from cross flow conditions. The simulation of the electrified Tecnam P2006T aircraft may be enhanced by utilising flight mechanic models that consider the flap deflection during take-off as well as the additional lift from the increased dynamic pressure on the wing from the pull propellers.

As differential thrust can be used not only for yaw control but for pitch and roll control as well, the investigation of unconventional aircraft configurations would reveal how far the differential thrust concept is applicable. Especially mixed configurations, which have four rotors for hover and vertical take-off and a fixed wing for efficient aerodynamic flight, represent promising applications, that can exploit the benefit of differential thrust control during the entire mission. As the study on yaw control with multiple distributed, electric propulsors showed good control performance and reliability results, follow-up studies may investigate tailless aircraft configurations, which entirely rely on the propulsion system for attitude stabilisation and control.

Bibliography

[1] Blyenburgh & Co. Remotely Piloted Aircraft Systems - The Global Perspective - Yearbook 2015-2016. *http://uvs-info.com*, 2015.

[2] G. Ricci. Mass and rated characteristics of planetary reduction units. *Meccanica*, Vol. 27, No. 1, pp. 35-45, 1992.

[3] T. Finken and M. Felden and K. Hameyer. Comparison and design of different electrical machine types regarding their applicability in hybrid electrical vehicles. *18th International Conference on Electrical Machines, ICEM 2008*, Vilamoura, September 2008.

[4] D. Schröder. Elektrische Antriebe - Regelung von Antriebssystemen. *Springer Verlag*, 3rd edition, 2009.

[5] G. Müller and K. Vogt and B. Ponick. Berechnung elektrischer Maschinen. *Wiley-VCH*, 6th edition, 2007.

[6] M.D. Moore and B. Frederics. Misconceptions of Electric Propulsion Aircraft and Their Emergent Aviation Markets. *52nd AIAA Aerospace Sciences Meeting*, National Harbor, Maryland, January 2014.

[7] J. Looman. Zahnradgetriebe. *Springer-Verlag*, 2nd edition, 1988.

[8] J.M. Sullivan. Revolution or evolution? The rise of the UAVs. *International Symposium on Technology and Society*, Ithaca, USA, June 2005.

[9] J.S. Jang and D. Liccardo. Automation of Small UAVs using a Low Cost Mems Sensor and Embedded Computing Platform. *25th Digital Avionics Systems Conference*, Portland, USA, 2006.

[10] S. Nebiker et al. A light-weight multispectral sensor for micro UAV—Opportunities for very high resolution airborne remote sensing. *The International Archives of the Photogrammetry, Remote Sensing and Spatial Information Sciences*, 2008.

[11] H. Saari et al. Novel miniaturized hyperspectral sensor for UAV and space applications. *Sensors, Systems, and Next-Generation Satellites XIII*, Berlin, Germany, August 2009.

[12] C. Pohl and J.L. van Genderen. Multisensor image fusion in remote sensing: Concepts, methods and applications. *Journal of Remote Sensing*, Vol. 19, No. 5, pp. 823-854, 1998.

[13] H. Chao and Y. Gu and M. Napolitano. A Survey of Optical Flow Techniques for UAV Navigation Applications. *International Conference on Unmanned Aircraft Systems*, Atlanta, USA, May 2013.

[14] G. Chowdhary et al. GPS-denied Indoor and Outdoor Monocular Vision Aided Navigation and Control of Unmanned Aircraft. *Journal of Field Robotics*, Vol. 30, No. 3, pp. 415-438, 2013.

[15] V. Kunchev et al. Path Planning and Obstacle Avoidance for Autonomous Mobile Robots: A Review. *Knowledge-Based Intelligent Information and Engineering Systems*, Vol. 4252, pp. 537-544, 2006.

[16] B.M. Albaker and N.A. Rahim. Unmanned aircraft collision detection and resolution: Concept and survey. *5th IEEE Conference on Industrial Electronics and Applications*, Taichung, China, June 2010.

[17] J. Shang and Z. Shi. Vision-based Runway Recognition for UAV Autonomous Landing. *International Journal of Computer Science and Network Security*, Vol. 7, No. 3, pp. 112-117, 2007.

[18] A. Ryna et al. An Overview of Emerging Results in Cooperative UAV Control. *43rd IEEE Conference on Decision and Control*, Atlantis, Bahamas, December 2004.

[19] M. Pechoucek and V. Marik. Industrial deployment of multi-agent technologies: review and selected case studies. *Autonomous Agents and Multi-Agent Systems*, Vol. 17, No. 3, pp. 397-431, 2008.

[20] S. Karim and C. Heinze. Experiences with the Design and Implementation of an Agent-based Autonomous UAV Controller. *4th International Joint Conference on Autonomous Agents and Multiagent Systems AAMAS*, Utrecht, Netherlands, July 2005.

[21] M.L. Cummings et al. Automation Architecture for Single Operator, Multiple UAV Command and Control. *The International C2 Journal*, Vol. 1, No. 1, pp. 1-24, 2007.

[22] S. Martinez. UAV Cooperative Decision and Control - Challenges and Practical Approaches. *IEEE Control Systems Magazine*, April, pp. 104-108, 2010.

[23] I. Sadeghzadeh and Y. Zhang. A Review on Fault-Tolerant Control for Unmanned Aerial Vehicles (UAVs). *Infotech at Aerospace*, Louis, Missouri, USA, March 2011.

[24] Z.T. Dydek and A.M. Annaswamy and E. Lavretsky. Adaptive Control of Quadrotor UAVs: A Design Trade Study With Flight Evaluations. *IEEE Transactions on Control Systems Technology*, Vol. 21, No. 4, 2012.

[25] N. Xu et al. Minimum-time trajectory planning for helicopter UAVs using computational dynamic optimization. *IEEE International Conference on Systems, Man, and Cybernetics*, Seoul, South Korea, October 2012.

[26] J.F. Horn et al. Neural Network-Based Trajectory Optimization for Unmanned Aerial Vehicles. *Journal of Guidance, Control, and Dynamics*, Vol. 35, No. 2, pp. 548-562, 2012.

[27] V. Roberge and M. Tarbouchi and G. Labonte. Comparison of Parallel Genetic Algorithm and Particle Swarm Optimization for Real-Time UAV Path Planning. *IEEE Transactions on Industrial Informatics*, Vol. 9, No. 1, pp. 132-141, 2012.

[28] P. van Blyenburgh. UAVs — Current Situation and Considerations for the Way Foreward. *European Unmanned Vehicle Systems Association*, Paris, 2000.

[29] Federal Aviation Administration. Overview of Small UAS Notice of Proposed Rulemaking. *http://www.faa.gov/regulations_policies/rulemaking/media/021515_sUAS_Summary.pdf*, February 2015.

Bibliography

[30] European Aviation Safety Agency. Concept of Operations for Drones. *http://www.easa.europa.eu/system/files/dfu/204696_EASA_concept_drone_brochure_web.pdf*, March 2015.

[31] F. Nex and F. Remondino. UAV for 3D mapping applications: a review. *Applied Geomatics*, Vol. 6, No. 1, pp. 1-15, 2013.

[32] I. Colomina and P. Molina. Unmanned aerial systems for photogrammetry and remote sensing: A review. *ISPRS Journal of Photogrammetry and Remote Sensing*, Vol. 92, pp. 79-97, 2014.

[33] C. Zhang and J.M. Kovacs. The application of small unmanned aerial systems for precision agriculture: a review. *Precision Agriculture*, Vol. 13, pp. 693-712, 2012.

[34] S.M. Adams and C.J. Friedland. A survey of unmanned aerial vehicle (UAV) usage for imagery collection in disaster research and management. *9th International Workshop on Remote Sensing for Disaster Response*, Stanford, USA, September 2011.

[35] K. Kanistras. A Survey of Unmanned Aerial Vehicles (UAV) for Traffic Surveillance. *Handbook of Unmanned Aerial Vehicles*, pp. 2643-2666, 2014.

[36] A.K. Widiawan, R. Tafazolli. High Altitude Platform Station (HAPS): A Review of New Infrastructure Development for Future Wireless Communications. *Wireless Personal Communications*, Vol. 42, No. 3, pp. 387-404, 2006.

[37] B. Stevenson. Airbus D & S focuses on commercialisation of Zephyr HAPS. *http://www.flightglobal.com/news/articles/airbus-damps-focuses-on-commercialisation-of-zephyr-410820/*, 02.04.2015.

[38] Airbus Defence & Space.

[39] L. Kumar and M.M. Crisostomo and K. Bousson. VTOL UAV for Postal and Parcel Services. *17th ITS World Congress*, Busan, South Korea, October 2010.

[40] R. Haque et al. Autonomous Quadcopter for Product Home Delivery. *International Conference on Electrical Engineering and Information and Communication Technolog*, Dhaka, Bangladesh, April 2014.

[41] Amazon Technologies. Unmanned Aerial Vehicle Delivery System. *US Patent, Family ID: 52993365, Appl. No.: 14/502707, Filed: September 30, 2014*, 30.04.2015.

[42] G. Arleo et al. Control of quadrotor aerial vehicles equipped with a robotic arm. *21st Mediterranean Conference on Control & Automation*, Platanias-Chania, Greece, June 2013.

[43] F. Caccavale et al. Adaptive control for UAVs equipped with a robotic arm. *19th IFAC World Congress*, Cape Town, South Africa, August 2014.

[44] F.W. Burcham et al. A Preliminary Investigation of the Use of Throttles for Emergency Flight Control. *NASA Technical Memorandum 4320*, 1991.

[45] F.W. Burcham et al. Development and Flight Test of an Emergency Flight Control System Using Only Engine Thrust on an MD-11 Transport Airplane. *NASA Technical Publication TP-97-206217*, 1997.

[46] P.P. Walsh and P. Fletcher. Gas Turbine Performance. *Blackwell Science*, 2nd edition, 2004.

[47] J. Schömann. Modeling of Hybrid Electric Propulsion Systems for Small Unmanned Aerial Vehicles. *12th AIAA Aviation Technology, Integration, and Operations (ATIO) Conference*, Indianapolis, September 2012.

[48] J. Schömann. Hybrid-Electric Propulsion Systems for Small Unmanned Aircraft. *Lehrstuhl fuür Luftfahrtsysteme*, Technische Universität München, 2014.

[49] R.R. Glassock et al. Design, modelling and measurement of a hybrid powerplant for unmanned aerial systems. *50th Australasian Congress on Applied Mechanics (ACAM 2007)*, Brisbane, Australia, Descember 2007.

[50] R.R. Glassock and J.Y. Hung and L.F. Gonzalez. Multimodal hybrid powerplant for unmanned aerial systems (UAS) Robotics. *24th Bristol International Unmanned Air Vehicle Systems Conference*, Bristol, United Kingdom, April 2009.

[51] J.Y. Hung and L.F. Gonzalez. On parallel hybrid-electric propulsion system for unmanned aerial vehicles. *Progress in Aerospace Sciences*, Vol. 51, pp. 1-17, 2012.

[52] R.M. Hiserote. Analysis of Hybrid-Electric Propulsion System Design for Small Unmanned Aircraft Systems. *Air Force Institute of Technology*, Wright-Patterson Air Force Base, 2010.

[53] J. Lieh et al. Design of Hybrid Propulsion Systems for Unmanned Aerial Vehicles. *47th AIAA/ASME/SAE/ASEE Joint Propulsion Conference & Exhibit*, San Diego, California, August 2011.

[54] T.A. Rotramel. Optimization of Hybrid-Electric Propulsion Systems for Small Remotely-Piloted Aircraft. *Air Force Institute of Technology*, Wright-Patterson Air Force Base, 2011.

[55] J.K. Ausserer. Integration, Testing, and Validation of a Small Hybrid-Electric Remotely-Piloted Aircraft. *Air Force Institute of Technology*, Wright-Patterson Air Force Base, 2012.

[56] D. Verstraete et al. Characterisation of a hybrid, fuel-cell-based propulsion system for small unmanned aircraft. *Journal of power sources*, Nr. 250, pp. 204-211, 2014.

[57] D. Verstraete et al. Experimental investigation of the role of the battery in the AeroStack hybrid, fuel-cell-based propulsion system for small unmanned aircraft systems. *International Journal of Hydrogen Energy*, Nr. 40, pp. 1598-1606, 2015.

[58] P. Ryabov. Research of Efficiency of the Mid-Flight Power Plant Based on the Hybrid Engines for Advanced Airliners. *29th Congress of the International Council of the Aeronautical Sciences*, St. Petersburg, 2014.

[59] A.V. Lukovnikov et al. The Hybrid Propulsion Systems for the Advanced Aircraft. *29th Congress of the International Council of the Aeronautical Sciences*, St. Petersburg, 2014.

[60] H. Kuhn and A. Sizmann. Fundamental Prerequisities for Electric Flying. *61th German Aerospace Congress*, Berlin, September 2012.

[61] M. Hornung et al. Ce-Liner - Case Study for eMobility in Air Transportation. *Aviation Technology, Integration, and Operations Conference*, Los Angeles, August 2013.

[62] J. Koster. Hybrid Electric Integrated Optimized System (HELIOS) Design of a Hybrid Propulsion System for Aircraft. *49 th AIAA Aerospace Sciences Meeting including the New Horizons Forum and Aerospace Exhibition*, Orlando, FL, 2011.

[63] S. Bagassi. Design Analysis for Hybrid Propulsion. *28th International Congress of the Aeronautical Sciences*, Brisbane, Australia, 2012.

[64] P.M. Rothhaar et al. NASA Langley Distributed Propulsion VTOL Tilt-Wing Aircraft Testing, Modeling, Simulation, Control, and Flight Test Development. *14th AIAA Aviation Technology, Integration, and Operations Conference*, Atlanta, GA, June 2014.

[65] P.C. Murphy and D. Landman. Experiment Design for Complex VTOL Aircraft with Distributed Propulsion and Tilt Wing. *AIAA Atmospheric Flight Mechanics Conference*, Kissimmee, Florida, January 2015.

[66] G. Frank et al. Artificial Intelligence Based Control Power Optimization on Tailless Aircraft. *NASA Technical Report*, NASA/TM-2014-218671, L-20510, NF1676L-20404, 2015.

[67] A.M. Stoll et al. Drag Reduction Through Distributed Electric Propulsion. *14th AIAA Aviation Technology, Integration, and Operations Conference*, Atlanta, GA, June 2014.

[68] N.K. Borer and M.D. Moore and A.R. Turnbull. Tradespace Exploration of Distributed Propulsors for Advanced On-Demand Mobility Concepts. *14th AIAA Aviation Technology, Integration, and Operations Conference*, Atlanta, GA, June 2014.

[69] J.M. Urnes and Z.A. Nielsen. Use of Propulsion Commands to Control Directional Stability of a Damaged Transport Aircraft. *Infotech Aerospace Confrence*, Atlanta, Georgia, April 2010.

[70] J.M. Urnes and T.A. Smith. Use of Propulsion Commands to Prevent Loss-of-Control Aircraft Accidents. *Infotech Aerospace Confrence*, St. Louis, Missouri, March 2011.

[71] R.D. May et al. The Effect of Faster Engine Response on the Lateral Directional Control of a Damaged Aircraft. *AIAA Guidance, Navigation, and Control Conference*, Portland, OR, August 2011.

[72] T.-H. Guo and J. Litt. Resilient Propulsion Control Research for the NASA Integrated Resilient Aircraft Control (IRAC) Project. *Infotech Aerospace Confrence*, Rohnert Park, California, May 2007.

[73] R.D. May et al. Improving Engine Responsiveness during Approach through High Speed Idle Control. *AIAA Joint Propulsion Conference & Exhibit*, San Diego, CA, August 2011.

[74] M.J. Cutler et al. Comparison of Fixed and Variable Pitch Actuators for Agile Quadrotors. *AIAA Guidance, Navigation, and Control Conference*, Portland, Oregon, August 2011.

[75] F. Riccardi et al. Control of variable-pitch quadrotors. *19th IFAC Symposium on Automatic Control in Aerospace*, pp. 206-211, September 2013.

[76] A. Pretorius and E. Boje. Design and Modelling of a Quadrotor Helicopter with Variable Pitch Rotors for Aggressive Manoeuvres. *The World Congress*, Vol. 19, no. 1, pp. 12208-12213, 2014.

[77] S. Lupashin et al. A simple learning strategy for high-speed quadrocopter multi-flips. *IEEE International Conference on Robotics and Automation*, Anchorage, AK, May 2010.

[78] S. Lupashin and R. D'Andrea. Adaptive fast open-loop maneuvers for quadrocopters. *Autonomous Robots*, Vol. 33, no. 1-2, pp. 89-102, 2012.

[79] D. Brescianini and M. Hehn and R. D'Andrea. Quadrocopter pole acrobatics. *IEEE/RSJ International Conference on Intelligent Robots and Systems*, Tokyo, November 2013.

[80] F. Augugliaro et al. Building Tensile Structures with Flying Machines. *IEEE/RSJ International Conference on Intelligent Robots and Systems*, Tokyo, November 2013.

[81] M. Hamer et al. Knowledge Transfer for High-Performance Quadcopter Manoeuvres. *IEEE/RSJ International Conference on Intelligent Robots and Systems*, Tokyo, November 2013.

[82] M.J. Stepaniak and F. van Graas and M.U. de Haag. Design of an Electric Propulsion System for a Quadrotor Unmanned Aerial Vehicle. *Journal of Aircraft*, Vol. 46, no. 3, pp. 1050-1058, 2009.

[83] P. Pounds and R. Mahony. Design Principles of Large Quadrotors for Practical Applications. *IEEE International Conference on Robotics and Automation*, Kobe, Japan, May 2009.

[84] H. Kuhn et al. Progress and Perspectives of Electric Air Transport. *28th Congress of the International Council of the Aeronautical Sciences*, Brisbane, Australia, September 2012.

[85] G.V. Brown. Weights and Efficiencies of Electric Components of a Turboelectric Aircraft Propulsion System. *49th AIAA Aerospace Sciences Meeting including the New Horizons Forum and Aerospace Exposition*, Orlando, January 2011.

[86] A. Betz. Schraubenpropeller mit geringstem Energieverlust. *Göttinger Nachrichten*, 1919.

[87] H. Glauert. Airplane Propellers. *Aerodynamic Theory*, 1935.

[88] S. Goldstein. On the vortex theory of xcrew propellers. *Proceedings of the Royal Society of London, Series A*, Vol. 123, pp. 440-465, 1929.

[89] C.N. Adkins and R.H. Liebeck. Design of Optimum Propellers. *Journal of Propulsion and Power*, Vol. 10, No. 5, p. 676-682, 1994.

[90] H.V. Borst. Summary of propeller design procedures and data. Volume I. Aerodynamic design and installation. *National Technical Information Service, U.S. Department of Commerce*, Springfield, 1973.

[91] W.F. Phillips. Mechanics of flight. *John Wiley & Sons*, 1st edition, 2004.

Bibliography

[92] International Civil Aviation Organisation. Manual of the ICAO Standard Atmosphere. *Secretary General of the International Civil Aviation Organization*, 1993.

[93] M. Hepperle. JavaProp. *Version 1.65*, 2014.

[94] Department of Aerospace Engineering, University Illinois. UIUC Propeller Database. *http://aerospace.illinois.edu/m-selig/props/propDB.html*, 31.03.2014.

[95] APC Propellers. APC Thin Electric propeller series. *http://www.apcprop.com/ProductDetails.asp?ProductCode=LP19012E.html*, 31.03.2014.

[96] H. Wainauski et al. Prop-Fan Performance Terminology. *SAE Technical Paper 871838*, 1987.

[97] Hoffmann Propeller. Hoffmann Propeller data sheets. *http://www.hoffmann-prop.com/UserFiles/Documents*, 14.07.2014.

[98] H.W. Müller. Die Umlaufgetriebe. *Springer-Verlag*, 2nd edition, 1998.

[99] M. Stangl. Methodik zur kinematischen und kinetischen Berechung mehrwelliger Planeten-Koppelgetriebe. *Lehrstuhl für Maschinenelemente, Technische Universität München*, 2006.

[100] Reisenauer Präzisionsantriebe. Reisenauer Motor Chief and Super Chief gear series. *http://www.reisenauer.de/artikelauswahl.php5?kid=42*, 24.04.2014.

[101] ebm-papst ZEITLAUF GmbH & Co KG. ebm-papst ZEITLAUF - Planetengetriebe. *http://www.zeitlauf.de/produktinfo/produktprogramm/planetengetriebe.html*, 24.04.2014.

[102] Tramec Getriebe GmbH. Tramec Getriebe Planetengetriebe REP/EP. *http://www.tramec-getriebe.de/pdf/Planetengetriebe/TRAMEC-Planetengetriebe-REP-EP.pdf*, 24.04.2014.

[103] AHS Antriebstechnik. TRUE Planetary Gearheads. *http://www.ahs-antriebstechnik.de/pdf-dateien-e/gears/Micron_TRUE_EN.pdf*, 25.05.2014.

[104] Wittenstein alpha GmbH. Wittenstein Produktkatalog 2014/2015. *http://www-alt.alphagetriebe.de/pdf/alpha_gesamtkatalogd1014.pdf*, 24.04.2014.

[105] G. Niemann and H. Winter. Maschinenelemente Band 2, 2nd edition. *Springer-Verlag*, 2003.

[106] F. Mulzer. Systematik hoch übersetzender koaxialer Getriebe. *Lehrstuhl für Maschinenelemente, Technische Universität München*, 2009.

[107] M. Zeraoulia and M.E.H. Benbouzid and D. Diallo. Electric Motor Drive Selection Issues for HEV Propulsion Systems: A Comparative Study. *IEEE Transactions on Vehicular Technology, Vol. 55, No. 6, p. 1756-1764*, 2006.

[108] C. Farr. Hybrid Electric Drive Electric Machine Topology Comparison. *Electric Machines Technology Symposium (EMTS) 2010 Proceedings*, Philadelphia, May 2010.

[109] D.G. Dorrell et al. Comparison of different motor design drives for hybrid electric vehicles. *Energy Conversion Congress and Exposition (ECCE)*, Atlanta, September 2010.

[110] E. Odvarka. Electric Motor-Generator for a Hybrid Electric Vehicle. *Engineering Mechanics*, Vol.16, Nr. 2, pp. 131-139, 2009.

[111] Bernecker Rainer Industrie Elektronik. Drehstrom-Synchronmotoren 8LS Anwenderhandbuch V1.1. *http://www.br-automation.com/download.php?type=download&folder=BRP4440000000000000036248&file=MAMOT2-GER_V11_11_2005.pdf*, 27.03.2014.

[112] Baumüller Nürnberg. Drehstrom-Synchronmotoren DSD2 28-100 Katalog. *http://www.kollmorgen.com/zu-za/products/motors/servo/akm-series/_manuals/kollmorgen-akm-synchron-servomotor-manual-de-en-it-es-fr-ru/*, 27.03.2014.

[113] Kollmorgen Europe. Kollmorgen AKM Synchron-Servomotor Manual de-en-it-es rev04-2013. *http://www.kollmorgen.com/zu-za/products/motors/servo/akm-series/_manuals/kollmorgen-akm-synchron-servomotor-manual-de-en-it-es-rev04-2013.pdf*, 27.03.2014.

[114] Bosch Rexroth. Rexroth IndraDyn H Synchron-Bausatz-Spindelmotoren Projektierung. *http://www.boschrexroth.com/modules/BRMV2PDFDownload.dll/R911297894_03.1.pdf*, 27.03.2014.

[115] P. Waide. Energy-Efficiency Policy Opportunities for Electric Motor-Driven Systems. *International Energy Agency Paris, http://www.iea.org/publications/freepublications/publication/ee_for_electricsystems.pdf*, 26.01.2015.

[116] H. Auinger. Determination and designation of the efficiency of electrical machines. *Power Engineering Journal*, Vol. 13, No. 1, pp.15-23, 1999.

[117] A.T. de Almeida. Standards for Super-Premium Efficiency class for electric motors. *Industrial & Commercial Power Systems Technical Conference - Conference Record 2009 IEEE*, Calgary, AB, May 2009.

[118] M. Lindegger. Wirtschaftlichkeit, Anwendungen und Grenzen von effizienten Permanent-Magnet-Motoren. *Bundesamt für Energie BFE, http://motorsummit.ch/data/files/MS_2010/unterlagen/permanent-magnet-motors_de.pdf*, Bern, Switzerland, 26.01.2015.

[119] D. Schröder. Leistungselektronische Schaltungen. *Springer Verlag*, 3rd edition, 2012.

[120] U. Drofenik. A General Scheme for Calculating Switching- and Conduction-Losses of Power Semiconductors in Numerical Circuit Simulations of Power Electronic Systems. *Power Electronic Systems Laboratory (PES), ETH Zurich*, 2005.

[121] SEMIKRON International. SEMISEL Calculator and Simulator. *http://www.semikron.com/service-support/semisel-simulation.html*, 26.01.2015.

[122] S. Morimoto. Trends of Permanent Magnet Synchronous Machines. *TRANSACTIONS ON ELECTRICAL AND ELECTRONIC ENGINEERING*, Vol. 2, pp. 101-108, 2007.

[123] D. Schröder. Elektrische Antriebe – Grundlagen. *Springer Verlag*, 5th edition, 2013.

[124] Plettenberg Elektromotoren. Plettenberg Predator Series. *http://www.plettenberg-motoren.net/index.php/de/plettenberg-motoren/plettenberg-brushless-motoren/predator*, 02.04.2014.

[125] S.M. Lukic and A. Emado. Modeling of electric machines for automotive applications using efficiency maps. *Electrical Insulation Conference and Electrical Manufacturing & Coil Winding Technology Conference*, September 2003.

[126] M. Petersheim. Scaling of hybrid-electric vehicle powertrain components for Hardware-in-the-loop simulation. *Mechatronics*, Vol. 19, pp. 1078-1090, 2009.

[127] R.H. Staunton. Evaluation of 2004 Toyota Prius Hybrid Electric Drive System . *http://www.engr.uvic.ca/~mech459/Pub_References/890029.pdf*, 27.08.2014.

[128] M.H. Rashid. Power Electronics Handbook. *Academic Press*, 3rd edition, 2010.

[129] Infineon Technologies. Technical Information FP75R06KE3. *http://www.infineon.com/dgdl/ds_fp75r06ke3_2_0_de-en.pdf?folderId=db3a304412b407950112b408e8c90004&fileId=db3a304412b407950112b43330245a87*, 13.03.2014.

[130] B. Johansson. Improved Models for DC-DC Converters. *Department of Industrial Electrical Engineering and Automation*, Lund University, Sweden, 2003.

[131] Texas Instruments. Design Calculations for Buck-Boost Converters. *http://www.ti.com/lit/an/slva535a/slva535a.pdf*, 2012.

[132] Coilcraft. Design tool for buck-boost converter. *http://www.coilcraft.com/apps/selector/selector_2.cfm*, 02.04.2014.

[133] WIMA. DC-Link Capacitors. *http://www.wima.com/DE/products_dclink.htm*, 02.04.2014.

[134] B. Wen. Weight Estimation of Electronic Power Conversion Systems. *Virginia Polytechnic Institute and State University*, 2011.

[135] Chen Yang Technologies. ChenYang Ferritkern Werkstoffe. *http://www.softferrite.de/DE-SoftFerriteMat.pdf*, 2006.

[136] A. Wintrich. Comparing the Incomparable - Understanding and Comparing IGBT Module Datasheets. *http://www.electroline.com.au/white_papers/64798-Comparing-the-incomparable-understanding-and-comparing-IGBT-module-datasheets*, Semikron, 2011.

[137] J. Kolar et al. PWM Converter Power Density Barriers. *Power Conversion Conference*, Nagoya, April 2007.

[138] S. Ben-Yaakov and D. Adar. Average Models as Tools for Studying the Dynamics of Switch Mode DC-DC Converters. *Power Electronics Specialists Conference*, Taipei, June 1994.

[139] J. Larminie and A. Dicks. Fuel Cell Systems Explained. *Wiley-VCH*, 2nd edition, 2003.

[140] S. Basu. Recent Trends in Fuel Cell Science and Technology. *Springer*, 2007.

[141] P. Adcock and A. Kells and C. Jackson. PEM Fuel Cells for Road Vehicles. *EET-2008 European Ele-Drive Conference*, Geneva, March 2008.

[142] T. Bradley. Design Studies for Hydrogen Fuel Cell Powered Unmanned Aerial Vehicles. *26th AIAA Applied Aerodynamics Conference*, Honolulu, 2008.

[143] A. Himansu. Hybrid Solid Oxide Fuel Cell/Gas Turbine System Design for High Altitude Long Endurance Aerospace Missions. *NASA Technical Memorandum*, TM-2006-214328, 2006.

[144] H. Kuhn. In-Situ Charakterisierung von Polymer-Elektrolyt Brennstoffzellen mittels Elektrochemischer Impedanzspektroskopie. *Eidgenössische Technische Hochschule Zürich*, Zurich, 2006.

[145] J. Kurzke. GasTurb 12. *Compiled with Delphi XE3 on 5. March 2013*, 2012.

[146] H. Grieb. Projektierung von Turboflugtriebwerken. *Springer Basel*, 2004.

[147] J. Amphlett. A model predicting transient responses of proton exchange membrane fuel cells. *Journal of Power Sources*, Vol. 61, pp. 183-188, 1996.

[148] C. Siegel and J.J. Scheuren. Vergleich und Bewertung unterschiedlicher Polymer-Elektrolyt-Membran Brennstoffzellen Modellierungsansätze. *Revue Technique Luxembourgeoise*, Vol. 3, pp 117-134, 2006.

[149] K. Loo. Characterization of the dynamic response of proton exchange membrane fuel cells - A numerical study. *International Journal of Hydrogen Energy*, Vol. 35, pp. 11861-11877, 2010.

[150] H. Hoischen. Technisches Zeichnen. *Cornelsen Verlag Scriptor*, 30th edition, 2005.

[151] DuPont. DuPont Nafion PFSA Membranes. *http://www2.dupont.com/FuelCells/en_US/assets/downloads/dfc101.pdf*, 04.05.2014.

[152] Fuel Cells Etc. Gas Diffusion Layer Comparison Table. *http://fuelcellsetc.com/store/DS/gas-diffusion-layer-properties.pdf*, 04.05.2014.

[153] J. Kellogg. Fuel Cells for Micro Air Vehicles. *Joint Service Power Expo*, Tempa, May 2005.

[154] Q. Yan. Steady state and dynamic performance of proton exchange membrane fuel cells (PEMFCs) under various operating conditions and load changes. *Journal of Power Sources*, Vol. 161, pp. 492-502, 2006.

[155] D. Linden and T.B. Reddy. Handbook of Batteries. *McGraw-Hill*, 3rd edition, 2002.

[156] K. Aifantis and S.A. Hackney and V. Kumar. High Energy Density Lithium Batteries: Materials, Engineering, Applications. *Wiley-VCH*, 2002.

[157] Y. Lin. The Evolution of Electric Vehicle Lithium Battery Technology - Towards SSI Perspective. *35th DRUID Celebration Conference*, Barcelona, June 2013.

[158] H. Chen et al. Progress in electrical energy storage system: A critical review. *Progress in Natural Science*, Vol. 19, pp. 291-312, 2009.

[159] X. Luo et al. Overview of current development in electrical energy storage technologies and the application potential in power system operation. *Applied Energy*, Vol. 137, pp. 511-536, 2014.

[160] A. Rahman and X. Wang. A review of high energy density lithium–air battery technology. *Applied Electrochemistry*, Vol. 44, pp. 5-22, 2014.

Bibliography

[161] Panasonic. Panasonic NCR 18650B Specification Sheet. *http://www.batteryspace.com/ prod-specs/8678_specification.pdf* , 27.02.2015.

[162] A. Thielmann et al. Technologie-Roadmap Energiespeicher für die Elektromobilität 2030. *Fraunhofer-Institut für System- und Innovationsforschung*, Karlsruhe, 2012.

[163] V. Ramadesigan. Modeling and Simulation of Lithium-Ion Batteries from a Systems Engineering Perspective. *Journal of The Electrochemical Society*, Vol. 159, No. 3, pp. R31-R45, 2012.

[164] P. Arora. Comparison between computer simulations and experimental data for high-rate discharges of plastic lithium-ion batteries. *Journal of Power Sources*, Vol. 88, pp. 219-231, 2000.

[165] M. Chen and G.A. Ricon-Mora. Accurate Electrical Battery Model Capable of Predicting Runtime and I–V Performance. *IEEE Transactions on Energy Conversion*, Vol. 21, No. 2, pp. 504-511, 2006.

[166] AA Portable Power Corp. Polymer Li-Ion Cell PL-383562 Specification Sheet. *http: //www.batteryspace.com/prod-specs/1120_UN.pdf* , 27.02.2015.

[167] J. Kowal. Elektrochemische Doppelschichtkondensatoren. *MTZ - Motortechnische Zeitschrift*, Nr. 02/2013, pp. 158-163, 2013.

[168] R. Kötz. Doppelschichtkondensatoren – Technik, Kosten, Perspektiven. *Kasseler Symposium Energie-Systemtechnik*, Kassel, 2002.

[169] R. Niu. Modeling and Identification of Electric Double-Layer Supercapacitors. *IEEE International Conference on Robotics and Automation (ICRA)*, shanghai, 2011.

[170] L. Zubieta. Characterization of Double-Layer Capacitors for Power Electronics Applications. *IEEE Transactions on Industry Applications*, Vol. 36, No. 1, pp. 199-205, 2000.

[171] WIMA. SuperCap C,R series. *http://www.wima.cn/DE/supercap_construction.htm*, 07.08.2012.

[172] Maxwell Technologies, Inc. Datasheet K2 Series Ultracapacitors. *http://www.maxwell. com/products/ultracapacitors/docs/K2SERIES_DS_1015370-4.PDF* , 07.08.2012.

[173] Vinatech. Hy-Cap / VinaTech Supercapacitor. *http://www.perel.fi/files/518/ Supercap_catalogue(12_page_version).pdf* , 07.08.2012.

[174] Capcomp. NESSCAP zylindrische Hochleistung ULTRACAP. *http://www.capcomp. de/fileadmin/document_download/NESSCAP_Specifications/8_Cylindric_large_cells/ ESHSR_V5_Gewindeausfuehrung/Spec_Family_ESHSR-0650C0-3000C0_-_ 002R7A5T_20100825.pdf* , 07.08.2012.

[175] Epcos. Epcos UltraCap series. *http://media.digikey.com/pdf/Data%20Sheets/ Epcos%20PDFs/B49410B2276Q000.pdf* , 07.08.2012.

[176] Cornell Dubilier Electronics. Type CDLC Carboncap High-Power Axial-Terminal Ultracapacitors. *http://www.cde.com/resources/catalogs/CDLC.pdf* , 07.08.2012.

[177] Nichicon Corporation. Electric Double Layer Capacitors EVerCAP. *http://datasheet. eeworld.com.cn/pdf/NICHICON/202657_JJLOE557MSE.pdf* , 07.08.2012.

[178] The Mathworks Inc. Matlab with Simulink. *Version 8.4.0.150421 (R2014b)*, 2014.

[179] J.H. Steiner. An Investigation of Performance Benefits and Trim Requirements of a Variable Speed Helicopter Rotor. *The Pennsylvania State University*, Department of Aerospace Engineering, 2008.

[180] M.J. Cutler. Design and Control of an Autonomous Variable-Pitch Quadrotor Helicopter. *Massachusetts Institute of Technology*, Cambridge, 2010.

[181] C.T. Sun. Mechanics of Aircraft Structures. *Wiley-VCH*, 2nd edition, 2006.

[182] F. Holzapfel. Nichtlineare adaptive Regelung eines unbemannten Fluggerätes. *Lehrstuhl f"ur Flugmechanik und Flugregelung*, Technische Universität München, 2004.

[183] G.P. Falconí et al. Admissible Thrust Control Laws for Quadrotor Position Tracking. *American Control Conference (ACC)*, Washington, DC, USA, June 2013.

[184] European Aviation Safety Agency. TCDS EASA.A.185 Tecnam P2006T. *http://easa. europa.eu/system/files/dfu/EASA-TCDS-A.185_Tecnam_P2006T-04-21112013.pdf*, 2013.

[185] Costruzioni Aeronautiche TECNAM S.r.l. Specification & Description. *http://tecnam. com/Documents/Brochures/P2006t.pdf*, 2006.

[186] European Aviation Safety Agency. TCDS EASA.E.121 Rotax 912 series engines. *http://easa.europa.eu/system/files/dfu/EASA-TCDS-E. 121_BRP--Powertrain_Rotax_912_Series_engines-04-10082012.pdf*, 2012.

[187] MT Propeller. MTV-21-() Verstellpropeller. *http://www.mt-propeller.com/pdf/ datsheet/mtv-21.pdf*, 2005.

[188] BRP Rotax GmbH & Co. KG. 912 ULS / ULSFR / S. *http://www. rotax-aircraft-engines.com/portaldata/5/data/Techn.Data_912_S_ULS.pdf*, 2006.

[189] BRP Rotax GmbH & Co. KG. Rotax 912 S DCDI Performance. *http://www. rotax-aircraft-engines.com/portaldata/5/data/perf912s.pdf*, 2006.

[190] F. Nicolosi. Aircraft Design Research and Education at University of Naples. *9th European Workshop on Aircraft Design Education*, Sevilla, May 2009.

[191] F. Nicolosi and A. De Marco and P.D. Vecchina. Stability, Flying Qualities and Parameter Estimation of a Twin-Engine CS-23/FAR 23 Certified Light Aircraft. *AIAA Guidance, Navigation, and Control Conference*, Toronto, Canada, August 2010.

[192] A. Dorobantu et al. Frequency Domain System Identification for a Small, Low-Cost, Fixed-Wing UAV. *AIAA Guidance, Navigation, and Control Conference*, Portland, Oregon, August 2011.

[193] D.P. Raymer. Aircraft Design: A Conceptual Approach. *AIAA Education Series*, 2nd edition, 1992.

[194] G.B. Kliman and J. Stein. Methods of Motor Current Signature Analysis. *Electric Machines & Power Systems*, vol. 20, no. 5, 1992.

Bibliography

[195] European Aviation Safety Agency. Certification Specifications for Normal, Utility, Aerobatic, and Commuter Category Aeroplanes CS-23. *http://easa.europa.eu/system/files/dfu/CS-23%20Amdt%203.pdf*, Amendment 3, 20.07.2012.

[196] E. Torenbeek. Synthesis of Subsonic Airplane Design. *Kluwer Academic Publishers*, 1982.

[197] J.F. Gieras. Permanent Magnet Motor Technology. *CRC-Press*, 3rd edition, 2010.

[198] M. Villani et al. High Reliability Permanent Magnet Brushless Motor Drive for Aircraft Application. *IEEE Transactions on Industrial Electronics*, vol. 59, no. 5, 2012.

[199] J. McDowall. Lies, Damed Lies and Statistics: The Statistical Treatment of Battery Failures. *Saft America Inc.*, 2005.

[200] D.J. Moorhouse. Background Information and User Guide for the MIL-F-878SC, Military Specification - Flying Qualities of Piloted Aircraft. *Air Force Systems Command Wright-Patterson Air Force Base Ohio*, 1982.